Fundamental Studies on Model Catalyst Systems: Energetics of Metal Nanoparticles Supported on Oxide Surfaces and Microkinetic Analysis Using Degree of Rate Control

Zhongtian Mao

A dissertation

submitted in partial fulfillment of the

requirements for the degree of

Doctor of Philosophy

University of Washington

2020

Reading Committee:

Charles T. Campbell, Chair

Bo Zhang

Bruce Robinson

Program Authorized to Offer Degree:

Chemistry

University of Washington

Abstract

Fundamental Studies on Model Catalyst Systems: Energetics of Metal Nanoparticles Supported on Oxide Surfaces and Microkinetic Analysis Using Degree of Rate Control

Zhongtian Mao

Chair of the Supervisory Committee:
Professor Charles T. Campbell
Chemistry

This dissertation includes the study of metal nanoparticles supported on oxide surfaces and the microkinetic analysis of complex reaction mechanisms using the degree of rate control (DRC).

In Chapters 2-5, the energetics, structure and electron transfer of Ni nanoparticles supported on MgO(100) and $CeO_{2-x}(111)$ are studied using Single Crystal Adsorption Calorimetry (SCAC), He^+ low-energy ion scattering (LEIS), X-ray photoelectron spectroscopy (XPS) and density functional theory (DFT).

Both experiments and DFT calculation shows that the extent of reduction and the presence of step edge sites on $CeO_{2-x}(111)$ can strongly affect its interaction with the supported Ni nanoparticles. At 300 K, Ni atoms nucleate preferentially on the step edges of $CeO_{2-x}(111)$,

and the initial heat of adsorption is higher than that measured at 100 K where Ni atoms nucleate mainly on terraces. The initial heat of adsorption of Ni on $CeO_{1.8}(111)$ is lower than that on $CeO_{1.95}(111)$, no matter for step edges or terraces. It suggests the bonding between the Ni atoms and the lattice O dominates the interaction between Ni and $CeO_{2-x}(111)$. Upon adsorption, Ni can transfer electrons to stoichiometric ceria and form Ni cations at low coverages. DFT shows that adsorbed Ni monomers are in a +2 oxidation state on $CeO_2(111)$. As the Ni coverage and particle size increases, both XPS and DFT shows the charge transfer per Ni atom sharply decreases. The perturbation of the ceria support to the electronic property of Ni is crucial to understanding the nature of the active sites on the surface of Ni/CeO_2 catalysts.

On MgO(100), Ni has different growth modes at 300 and 100 K. At 300 K, Ni grows 3D nanoparticles. The Ni atoms form a metastable phase when the nanoparticles are smaller than 2.5 nm in diameter. At 100 K, the Ni atoms form single adatoms and then 2D islands with a thickness of 0.17 nm at low coverage. The 2D islands cover the entire surface rapidly before thickening. The initial heat of adsorption measured at 100 K is 148 kJ/mol, which corresponds to the binding energy of a single Ni atom on MgO(100). The XPS Ni $2p_{3/2}$ peak binding energy for 0.21 ML Ni on MgO(100) at 100 K is 2.2 eV higher than that for bulk Ni(solid), suggesting charge transfer from Ni to MgO(100) and formation of Ni^{2+} at very low coverage.

The heat of adsorption and growth morphology of Ni on MgO(100) and $CeO_{1.95}(111)$ are then used to calculate the adhesion energy of Ni to MgO(100) and $CeO_{1.95}(111)$. Due to Ni’s high oxophilicity, the adhesion energy of Ni to MgO(100) and $CeO_{1.95}(111)$ is higher than any other metal that has been measured previously. The reported adhesion energy of Ni fits well in the trend, which states that the adhesion energy increases linearly from metal to metal with increasing heat of formation of the most stable oxide of the metal.

In Chapters 6-8, the DRC analysis is applied to understand the kinetics of simple model reactions and real reaction mechanisms. In Chapter 6, we show the DRC for any catalyst-bound intermediate is proportional to its fractional population of catalyst sites, where the proportional constant is given as the DRC-weighted average of the site requirements for all the elementary steps. This relation offers opportunities to measure DRC experimentally since the fractional population of catalyst-bound intermediates can be measured. In Chapter 7, the DRC analysis is used for the interpretation of the kinetic isotope effect (KIE). The DRC analysis shows that the KIE of a multistep reaction results from the energy change of kinetically-relevant species upon isotope substitution. Considering the rate-determining step only is not enough to obtain a full understanding of KIE, and it can lead to conceptual mistakes. In Chapter 8, a general expression for the apparent activation energy is given via DRC. It shows that the apparent activation energy equals a weighted average of the standard-state enthalpies of all species in the reaction mechanism, each weighted by its DRC. This equation provides deep insights into the connection between the reaction energy diagram and the apparent activation energy.

TABLE OF CONTENTS

LIST OF FIGURES

LIST OF TABLES

ACKNOWLEDGEMENTS

Funding for this work was provided by the Department of Energy, Office of Basic Energy Sciences, Chemical Sciences Division grant number DE-FG02-96ER14630.

First, I would like to show respect to my advisor Dr. Charles T. Campbell. As my research advisor, Charlie has strict requirements for my research, but he also allows me to work at my own pace. This helps me keep productive and creative. He has a library of catalysis and surface science in his brain. When I have questions, he can usually give the answer and reference papers, or offer helpful ideas that inspire me to find the solution by myself. In the past five years, Charlie always encourages me to learn and think like a scientist, and he offers me many opportunities to practice, writing scientific papers, peer-reviewing journal articles and giving oral presentations. I cannot extend enough gratitude to Charlie, for all the trust and patience he has given to me.

I would also like to thank the members of my committee, Dr. David Castner, Dr. Bruce Robinson, and Dr. Bo Zhang, for their time and support.

The members in Campbell group lend me helping hands in my research. I had a tough time when I just started to work on the instrument. Dr. Spencer J. Carey, Dr. Trevor E. James, Dr. Wei Zhao, and Dr. Wei Zhang helped me to overcome the challenges and trained me to be an expert on Cal 3. Ziareena Almualem joined Cal 3 in 2018. She helped me finish the Ni/MgO project. Then John Rumptz came. We worked together and completed a series of amazing projects. I am glad that Cal 3 will have a master after I leave. Elizabeth Harman and Griffin Ruehl on Cal 2 help Cal 3 a lot in our daily work. I hope they all enjoy their life and work and keep making progress on Cal 2.

I received help from the Chemistry Department administrative staff and the faculty members that I have interacted with in courses and in my research. I have my sincerest appreciation for them. Particularly I would like to thank the Chemistry and Physics machine shop, the Chemistry electronic shop, and James Gladden. It is hard to keep Cal 3 running smoothly without their technical support.

Finally, I would like to say thank you and sorry to my family in China. I spent only two months with them in the past five years. All my progress is only possible with their encouragement and understanding. They are always the most solid backing for me.

Chapter 1. Introduction

Heterogeneous catalysis typically involves the reactions with solid-phase catalysts and fluid phase reactants. It plays an essential role in every aspect of human life. A good example is the Haber-Bosch process. In the first decade of the 20th century, Fritz Haber and Carl Bosch invented the famous Haber-Bosch process, which converts nitrogen N_2 and hydrogen H_2 to ammonia using solid metal catalysts. The Haber-Bosch process allows large-scale production of ammonia and nitrates as fertilizers and other industrial feedstocks. It helps improve the food supply to keep up with the need from the growing population, and addresses the concern demonstrated in the “Malthusian catastrophe”. In the 21st century, the need for food, sustainable energy, and all other products required for maintaining high-quality life grows exponentially. Heterogeneous catalysis becomes even more critical for satisfying the growing demand. Heterogeneous catalysts have wide applications in modern industry for clean energy, bulk chemical production, and environmental technologies. The production of ~90% of chemicals is assisted by heterogeneous catalysts. The search never stops for better heterogeneous catalysts with efficiency, durability, and selectivity. In order to design better catalysts, people need quantitative measurements and understanding at a molecular level about the structure of heterogeneous catalysts and the reaction mechanisms catalyzed on heterogeneous catalysts.

Late-transition metal nanoparticles dispersed on oxide support materials with a high surface area form a common group of heterogeneous catalysts. The bonding strength between the metal nanoparticles and the oxide support is crucial to their behavior for catalyzing reactions. By changing the metal-support interactions, people can tune the electronic and structural properties of the supported metal nanoparticles, which leads to different reactivity and selectivity.[1, 2] One of the main drawbacks of using metal nanoparticles as catalysts is that the metal nanoparticles can easily deactivate under reaction conditions due to sintering and coke formation.[3-6] The interaction between the metal nanoparticles and the support materials helps the metal nanoparticles to maintain their sizes as small nanoparticles instead of forming large particles with lower exposure, and the metal nanoparticles gain sinter resistance and coke resistance.[7-16] However, understanding the nature of the interfacial chemical bonding between the metal nanoparticles and the oxide support is difficult. Studies about the bonding strength between the metal nanoparticles or overlayers and the substrates are usually performed by measuring the adsorption energies.[15, 17] Temperature-programmed desorption (TPD) is a typical indirect method, [18] but it requires the adsorption-desorption process to be reversible, which is not always valid. It usually fails for the systems consisting of late-transition metals and oxide supports. As the temperature ramps up, the metal overlayers aggregate into large 3D particles. The surface structure has been changed before the metal atoms desorb from the surface, and the adhesion energies extracted from TPD measurements can only be considered as upper limits.[15]

To overcome the disadvantages of indirect measurements of adsorption energies, David King’s group at Cambridge University developed a method for direct measurement of adsorption energies called Single Crystal Adsorption Calorimetry (SCAC).[19-22] In a SCAC experiment, the adsorbates are dosed onto the single-crystal sample in a pulsed molecular beam. The heat released upon adsorption causes a tiny temperature increase on the sample, and an infrared detector can detect it. The SCAC method provides opportunities to measure accurate, coverage-dependent adsorption energies directly. Partially based on King’s method, the Campbell group built a SCAC apparatus for measuring the adsorption and adhesion of metal on solid surfaces. [17, 23] The infrared detector is replaced with a pyroelectric polyvinylidene fluoride (PVDF) ribbon that is pushed against the backside of the single-crystal sample for heat detection. The calorimeter and other instruments for surface characterization are attached to an ultrahigh vacuum (UHV) chamber. An e-beam evaporator is also attached for generating metal vapor, so this apparatus is capable of measuring the adsorption energies of metal atoms onto oxide surfaces. Model catalyst systems consisting of metal nanoparticles supported on single-crystal oxide surfaces are studied using this apparatus. The surface order of the single-crystal sample, the coverage of metal dosage, the size and number density of metal nanoparticles, and the surface cleanliness are all precisely controlled in the UHV chamber. Thus, it simplifies the complexity of real catalysts, and the scientific questions of interest are focused. In Chapter 2, this improved SCAC apparatus and the process for measuring the adsorption and adhesion of metals on oxide surfaces are described in detail.

Ni-based heterogeneous catalysts have wide applications with promise for catalyzing important industrial reactions. However, Ni nanoparticles deactivate via sintering and coke formation under reaction conditions.[3, 24] A common strategy to extend the lifetime of Ni nanoparticles is anchoring the Ni nanoparticles on selected oxide surfaces. The interaction between the Ni nanoparticles and the oxide supports not only keeps the Ni nanoparticles from sintering and coke formation but also perturbates the electronic properties of Ni atoms, which can lead to better performance for catalyzing reactions.[25-34] In Chapter 3 and Chapter 4, Ni nanoparticles supported on reducible ceria $CeO_{2-x}(111)$ and magnesia MgO(100) are studied using SCAC and other surface spectroscopies at 300 and 100 K. The coverage-dependent heats of adsorption of Ni on oxide surfaces were first measured using SCAC by depositing Ni onto the oxide single-crystal surfaces in a pulsed molecular beam. The growth morphology of Ni nanoparticles on oxide surfaces was monitored using He^+ low energy ion scattering (LEIS) spectroscopy. When the Ni atoms grow as 3D nanoparticles, the particle number densities can be determined by fitting the LEIS data points.

Combining the energetic information from SCAC and the structural information from LEIS, the measured heat of adsorption is correlated with the particle size. The heat of adsorption can also be converted to the chemical potential of Ni atoms in the nanoparticles with a given size, which provides direct and quantitative measurements of the size effect of metal nanoparticles.

Conditions were controlled in the experiments to study the factors that can affect the Ni nanoparticle growth. In Chapter 3, three cases are shown for Ni growth on $CeO_{2-x}(111)$: $CeO_{1.95}(111)$ at 300 K, $CeO_{1.8}(111)$ at 300 K, $CeO_{1.95}(111)$ at 100 K . The comparison among these three cases shows that Ni atoms bind most strongly on the step edges of $CeO_{1.95}(111)$. When the Ni atoms can diffuse to the favored step edges, they prefer to nucleating on step edges instead of terraces. Ni atoms bind the reduced ceria $CeO_{1.8}(111)$ more weakly than the stoichiometric ceria $CeO_{1.95}(111)$, which suggests that the lattice oxygen of ceria plays a key role in the interaction between Ni and ceria. X-ray photoelectron spectroscopy (XPS) gave that Ni atoms can be oxidized on $CeO_{1.95}(111)$ at low coverage while they remain mostly metallic on $CeO_{1.8}(111)$. The electronic perturbation of stoichiometric ceria on supported Ni nanoparticles is closely related to the activity and selectivity for catalyzing water-gas shift (WGS) reaction. In Chapter 4, it shows the results for the Ni growth on MgO(100) was studied at 300 and 100 K. Ni atoms grow 3D nanoparticles at 300 K, while they grow 2D islands and cover the whole surface area quickly at 100 K.

The heated discussion on Ni-based catalysts is not the only motivation for the studies presented here. In previous studies, Campbell and co-workers reported a strong linear correlation of the adhesion energies E_{adh} (in a unit of J/m^2) of metal nanoparticles on oxide surfaces with the oxophilicity of the metal.[35, 36] The oxophilicity is defined as $\left[\left(\Delta H_{sub,M} - \Delta H_{f,MO_X}\right)/N_A\right]/\Omega_M^{2/3}$, where $\Delta H_{sub,M}$ is the sublimation enthalpy of the bulk metal, $\Delta H_{f,MO_X}$ is the formation enthalpy of the most stable oxide of the metal (per metal atom), N_A is the Avogadro's number, and Ω_M is the volume per atom in the bulk metal.[35, 36] The $\Omega_M{}^{2/3}$ factor converts the oxophilicity from units of energy per metal atom to energy per unit area of metal surface, which is necessary for understanding adhesion energies, which are also energies per unit area on metal / oxide interface. Based on the adhesion energies measured with SCAC and particle shape measurements on clean $CeO_{1.95}(111)$ and MgO(100) surfaces, the adhesion energies of metals are found linearly correlated with the metals' oxophilicity, and the linear correlation for these two oxides have identical slope but different intercepts. The members of the Campbell group at the University of Washington have measured the adhesion energies of Pb, Ag, Au, Cu on $CeO_{1.95}(111)$ and MgO(100) surfaces using SCAC. Among these metals, Pb has the lowest oxophilicity (7.07 J/m^2), and Cu has the highest oxophilicity (16.19 J/m^2). The linear correlation matches the data well in this range for $CeO_{1.95}(111)$ and MgO(100). For comparison, the oxophilicity calculated for Ni is 22.72 J/m^2, which is much higher than any other metals studied before. This is another driving force for the studies about Ni presented here: to prove that the linear correlation between the metal adhesion energies and the oxophilicity can be extended to metals with higher oxophilicity. In Chapter 5, the adhesion energies of Ni on $CeO_{1.95}(111)$ and MgO(100) are calculated based on the chemical potential of Ni atoms in nanoparticles.[36] In previous studies, the adhesion energies are calculated with the integral heat of adsorption and the LEIS data using a simple thermodynamic cycle. A built-in assumption in this method is that the metal atoms form the same phase in the nanoparticles as the bulk metal. However, this assumption does not hold for Ni nanoparticles supported on some oxide surfaces. Using the method described above to calculate the adhesion energies, Ni has negative adhesion energies on $CeO_{1.95}(111)$ and MgO(100), which does not make physical sense. A previous study shows that when Ni is deposited on MgO(100) at 120 °C, the Ni nanoparticles formed with a diameter of 2.5 nm have a metastable hexagonal close-packed (hcp) phase to release the lattice mismatch (-16%). [37] The lattice mismatch between $CeO_{1.95}$(111) and Ni(111) is even bigger (-35%) [38]. Thus, it is possible that Ni atoms also form a metastable phase on $CeO_{1.95}$(111) to release the strain due to the lattice mismatch, and the method described above for calculating the adhesion energies also fails in this case. To calculate the adhesion energies of Ni on $CeO_{1.95}$(111) and MgO(100), we instead fit the data plot of the Ni chemical potential versus the Ni particle diameter. In previous studies, an equation was derived to describe the relationship between the metal chemical potential in metal nanoparticles and the metal particle diameter.[36] In Chapter 5, this equation is slightly improved by introducing a new term as the sublimation enthalpy of the metastable phase of Ni in the nanoparticles. By fitting the data plot of the Ni chemical potential versus the Ni particle diameter with this improved equation, the two fitting parameters are obtained: the adhesion energies of Ni on the oxide surfaces and the sublimation enthalpies of the metastable phase of Ni. The sublimation enthalpies are slightly lower than that of the most stable face-centered cubic (fcc) phase of bulk Ni. The obtained adhesion energies of Ni to MgO(100) and $CeO_{1.95}$(111) are well fit in the previous trend in adhesion energies of metal nanoparticles to oxide surfaces.

The interaction between the metal nanoparticles and the support materials does not tell a complete story of the heterogeneous catalysis. The support material can tune the electronic and structural properties of the metal nanoparticles. Finally, the reaction activity and selectivity are affected because the energies of the species (i.e., the intermediates and the transition states) in the reaction mechanism are changed.[1, 2] To find the optimized catalyst on which all the species in the reaction have the “just right” energies, people first need to know how the reaction rate changes with the energies of species. A simple but practical rule about the question is the Sabatier principle.[39] The Sabatier principle states that the binding between the catalyst and the substrate should be neither too weak nor too strong. If the binding is too weak, the substrate cannot effectively bind to the catalyst, and the reaction will not happen. If the binding is too strong, the product will fail to dissociate from the catalyst. As the binding energy of the substrate to the catalyst increases, the reaction rate increases first and then decreases after it passes the optimal point. This rate versus binding energy curve is called the volcano curve. The application of the volcano curve in the real study of catalysis is complicated. Not only the substrate can affect the reaction rate. In fact, every species in the reaction mechanism has the potential to affect the reaction rate. Thus, the optimization of the catalyst needs to be conducted on several dimensions, and the volcano curve becomes the volcano plot in real studies.

To simplify the work for understanding the reaction mechanism and searching for better catalysts, a concept called the degree of rate control (DRC) is introduced. It was first raised to define the rate-determining step (RDS).[40] The rate-determining step assumption is known as a central concept in chemical kinetics. It simplifies complicated multistep reactions to a single step that dominates the kinetic behavior of the reaction. Despite its great success, a problem with the RDS assumption is that there is no strict and reliable definition for the RDS.[41] The definition of the degree of rate control is[42, 43]

$$X_i = \left(\frac{\partial \ln\left(r\right)}{\partial\left(-G_i^0 / RT\right)} \right)_{G_{j \neq i}^0} \tag{1.1}$$

where ln(*r)* is the logarithm of the net rate to the product of interest, G_i^0 is the standard-state Gibbs free energy of the transition state in Step *i*. By its definition, the DRC of Step i, X_i, is the relative increase in the net rate to the product of interest due to a (differential) decrease in the standard-state free energy for the transition state for Step *i* (divided by RT), while holding constant the standard-state free energy for all other transition states and all intermediates. If there is a single RDS in the reaction mechanism, such RDS has a DRC equal to 1, and all other steps have zero DRCs. If there are several steps exhibit rate control, these steps will have nonzero DRCs with a value between 0 and 1, and their DRCs sum up to 1.[43, 44] Since the DRC is defined based on the standard-state Gibbs free energies, its application is extended from the transition states to all other species in the reaction mechanism, including the reactants, the intermediates, the transition states, and the products.[42] Eq (1.1) can still be used to define this generalized DRC. Instead of the DRC of Step *i*, Eq 1.1 now defines the DRC of species *i*. The DRC of species *i* gives the relative increase in the net rate to the product of interest due to a (differential) decrease in the standard-state free energy for species *i* (divided by RT), while holding constant the standard-state free energy for all other species. Only a few species with nonzero DRCs exhibit rate control, so the DRC analysis can simplify complicated reaction mechanisms to a few rate-controlling species.

The DRC analysis is usually performed together with the microkinetic modeling. The DRC of species *i* is calculated by differentiating the standard-state Gibbs free energy of species *i* and finding the corresponding change in the net rate of the reaction from a full microkinetic modeling. Although it is defined mathematically, the DRC can also be related to some parameters that are accessible experimentally, which means people can measure DRC with well-designed experiments. It was reported that for a surface catalyzed reaction, the DRCs of the adsorbed intermediates are proportional to their fractional coverage, and the proportional factor is usually -2.[42, 43] In Chapter 6, a proof for this relationship between the DRCs of the adsorbates and their fractional coverages is given. The proportional factor comes from the number of sites that participate in the elementary steps. If there is a single RDS in the reaction mechanism, and there are two sites involved in this RDS, the proportional factor equals -2, and this is the most common case for surface catalyzed reactions. If there is a single RDS, and there is only one site involved, the proportional factor equals -1. If there are several steps exhibit rate control, the proportional factor equals a weighted average of the number of sites that participate in these steps using the DRCs of these steps as the weighting factor. This relationship allows people to obtain the DRCs of the adsorbed intermediates by measuring their fractional coverage, even without knowing the full reaction mechanism and establishing a microkinetic model.

An application of DRC is understanding and interpreting the kinetic isotope effect (KIE). If one or several atoms in the reactant are replaced with its isotope, the energies of the species in the reaction mechanism will change, and the overall rate of the reaction will also change. This phenomenon is called the kinetic isotope effect. KIE is a useful tool for studying reaction mechanisms. By measuring the KIE, people can determine if a step involving the atom that is replaced with its isotope is the RDS, or if two reaction paths share a common transition state.[45-48] However, it can lead to conceptual mistakes if people only consider the RDS when they interpret KIE. In Chapter 7, the DRC analysis is used to interpreting and predicting KIE. The KIE results from the energy change of species in the reaction mechanism upon isotope substitution, and only rate-controlling species with nonzero DRCs contribute to the KIE. An equation is derived to calculate the KIE as the rate ratio between the reactions before and after the atoms are substituted with their isotopes, using the DRCs of the species and their free energy change upon isotope substitution. These rate-controlling species are not necessarily in the RDS, so considering the RDS only can easily cause misunderstanding on the KIE.

For a single-step reaction, the KIE is usually attributed to the activation energy change due to isotope substitution. In Chapter 7, it has been proved that the DRC analysis can be used to calculate the KIE for a multistep reaction. Therefore, it is possible to relate the DRCs of species in a multistep reaction to its activation energy, which is usually called the apparent activation energy of the multistep reaction. The catalysts are used to accelerate reactions by reducing the activation energies of the reactions. The apparent activation energy E_{app} is a key parameter to describe how well a catalyst works. Despite its importance, the origin of E_{app} and its relationship with the reaction mechanism has not been strictly described before. In Chapter 8, an equation is derived, which describes a simple relationship between the apparent activation energy and the energy diagram of the reaction via DRC analysis. It is proved that E_{app} equals a weighted average of the standard-state enthalpies of the species in the reaction mechanism, using their DRCs as weighting factors, plus RT. The derived relation clearly defines the role of rate-controlling intermediates and rate-controlling transition states, quantifying exactly the extent to which their enthalpies contribute to the apparent activation energy.

Chapter 2. Experimental Methods

The single-crystal adsorption calorimetry (SCAC) experiments are performed in ultrahigh vacuum (UHV) chambers with a typical base pressure $<2\times10^{-10}$ Torr. The apparatus designed for measuring metal vapor adsorption and adhesion to metal oxide surfaces consists of three UHV chambers: a sample preparation chamber, a main chamber and a beam chamber. In the sample preparation chamber, the ultrathin oxide films are grown on the metal single-crystal samples. The main chamber has the SCAC heat detector, together with other surface characterization instruments, including X-ray photoelectron spectroscopy (XPS), He^+ low energy ion scattering spectroscopy (LEIS), and low-energy electron diffraction (LEED). An e-beam evaporator is placed in the beam chamber for melting metal pellets and generating metal vapor. The apparatus and the methods have been discussed in detail previously. [17] In this chapter I will briefly describe how the apparatus works for the systems of Ni/CeO_{2-x}(111) and Ni/MgO(100).

2.1 SAMPLE PREPARATION

The ultrathin metal oxide films are grown epitaxially on 2-μm-thin single crystal metal samples. The metal single crystals are supplied by Jacques Chevallier at Aarhus University in Denmark. Before the oxide film growth, the metal single crystals need to be cleaned by successive cycles of 1 kV Ar^+ sputtering and annealing. If there is carbon presented in XPS, the sample also needs to be annealed in 1×10^{-6} Torr O_2 at 1073 K for a few minutes. The single crystal is qualified for sample growth when there is no C or O presented in XPS, and the single crystal gives a sharp LEED pattern.

The CeO_{2-x}(111) thin films ($x = 0.05$ and 0.2) were grown on a clean Pt(111) single crystal surface as described previously[49] via reactive evaporation of Ce in an atmosphere of 1×10^{-6} Torr

O_2 at 873 K. The as-grown films were annealed in the same pressure of O_2 for another 5 min to ensure an ordered surface and minimize the density of O vacancies. This procedure results in a film of $CeO_{1.95}$(111). To obtain the partially reduced $CeO_{1.8}$(111) film, the O_2 pressure is reduced to 1×10^{-7} Torr, and the post annealing time is reduced to 30-90 s. The thickness of the CeO_{2-x}(111) film is determined to be ~4 nm by the attenuation of the Pt $4p_{3/2}$ XPS peak with the inelastic mean free path of Pt $4p_{3/2}$. This is thick enough to give a bulk-like behavior based on the adsorption energy of Ag vapor.[49] A sharp (1.4×1.4) LEED pattern was observed for the as-grown CeO_{2-x}(111) films, indicating the surface was well ordered and the epitaxial relationship with the underlying Pt was in agreement with prior reports.[50] The Ce oxidation states were characterized with XPS based on lineshape fitting of the Ce 3d peaks as described previously[51].

The MgO(100) thin films were grown on a 2-µm-thick Mo(100) single crystal sample with a similar procedure.[52] Briefly, Mg was first evaporated onto the Mo(100) sample in vacuum at 25 °C for 1 min and then in 1×10^{-6} Torr of O_2 background with the Mo(100) sample heated up to 300 °C. The as-grown film was annealed in 1×10^{-6} Torr of O_2 at 550 °C for another 2 min to ensure a minimum concentration of O vacancies and to order the surface of the film. The thickness of the MgO overlayer is ~4 nm estimated using the attenuation of Mo $3p_{3/2}$ peak in XPS measurement. The MgO(100) surface order was verified by the observed square (1×1) LEED pattern that is expected.[53] More details of the characterization of the films grown in this way are provided elsewhere.[52]

2.2 HEAT MEASUREMENT

Metal vapor adsorption calorimetry was performed as described previously.[17] The prepared single crystal sample with an oxide film is transferred from the sample preparation chamber to the main chamber, and placed into grooves on a fixed thermal reservoir. The reservoir is cooled with liquid N_2 to perform experiments at 100 K. A pyroelectric polyvinylidene fluoride (PVDF) ribbon is pressed against the backside of the 2-µm-thick metal single crystal as the heat detector. During the experiment, a well-defined 4.26 mm diameter beam of Ni atoms is generated from an e-beam evaporator, collimated though a series of apertures, chopped into 100 ms pulses, and finally dosed onto the sample. The heat release upon the adsorption of Ni atoms is detected by the PVDF ribbon. For each calorimetry run, the heat detector's response is calibrated by pulses from a HeNe laser (632.8 nm) with known power. To subtract the signal of the thermal radiation from the hot metal source, the sample is blocked by a BaF_2 window that only allows a known fraction of radiation to penetrate. To measure the transmission coefficient of the BaF_2 window, the HeNe laser is shot on the sample with and without the BaF_2 window, and two signals are generated. The ratio of these two signals gives the transmission coefficient (~90%), assuming it is the same for the laser and the evaporator infrared radiation. The signal measured associated with the radiation is corrected with the BaF_2 transmission and subtracted from the total heat signal, to leave only the part that is due to Ni vapor adsorption. As we always do in SCAC, this heat is corrected for the difference in the metal vapor's internal energy (2RT in a directed beam) between the metal vapor source temperature (~2000 K) and the surface temperature (100 or 300 K), so that the heats reported below are equal to the negative of the standard enthalpy of Ni adsorption at the surface temperature.

The flux of Ni atoms is measured with an on-axis and an off-axis quartz crystal microbalance (QCM). The off-axis QCM facing directly to the e-beam evaporator monitors the flux throughout the whole experiment. The on-axis QCM is placed at the sample position only before and after the adsorption calorimetry. The beginning and ending fluxes measured by the on-axis QCM are used to scale the off-axis QCM fluxes so that it provides the Ni flux at the sample position for all times during the calorimetry.

The sticking probability of each pulse is measured simultaneously with its heat using a modified King and Well's method.[54] The quadrupole mass spectrometer (QMS) is located at the angle of 35° from the surface normal. It detects the reflected fraction of Ni atoms during the heat measurement. A heated W flag is placed in the sample position after these measurements to record the QMS signals associated with zero sticking (100% reflected). The ratio of the reflected QMS signals and the zero sticking QMS signals determines the sticking probabilities in each pulse. Combining the flux and the sticking probability, we calculated the amount of Ni atoms that stick to the sample in each pulse. The differential heat of adsorption versus the cumulative coverage of Ni is thus available. The Ni coverages are reported here in monolayers (ML), where 1 ML is defined as the areal density of coordinatively-unsaturated O atoms on the ideal bulk-terminated oxide surface. For $CeO_{2-x}(111)$ 1 ML is 7.89×10^{18} atoms per m^2, and for MgO(100) 1 ML is 1.12×10^{19} atoms per m^2.

2.3 GROWTH MORPHOLOGY

The growth morphology of adsorbed Ni on MgO(100) was determined using He^+ low energy ion scattering (LEIS) with an incident angle of 45° from normal and a scattering angle of 135°, and an incident ion energy of 1000 eV. Using the Ni/MgO(100) system as an example, gaseous Ni is deposited onto the oxide films at 300 and 100 K in discrete amounts. The Ni and Mg signals in He^+ LEIS are monitored after each Ni dose. The integrated Ni signals are normalized to the signal from a thick Ni overlayer (>10 nm average thickness). The Mg signals are normalized to those for a clean MgO(100) surface. The circular atomic-beam spot of metal deposition on the sample consists of an umbra of 4.00 mm in diameter and a penumbra of 4.52 mm in diameter, and the effective beam diameter is 4.26 mm.[17] Since the detected area of the LEIS energy analyzer is ~30% wider than this diameter,[52] the Mg signals from this out-of-spot area (i.e., ~30% of the Mg signal for a clean MgO(100) surface, or the residual Mg signal after 10-nm-thick Ni is deposited) is subtracted from each measured Mg LEIS signal. The normalized LEIS signals give the fraction of surface area that is covered by Ni nanoparticles.[55] The plots of the normalized LEIS signals versus the Ni coverage indicate different growth morphology.

Chapter 3. Ni Nanoparticles on $CeO_{2-x}(111)$: Energetics, Electron Transfer and Structure by Ni Adsorption Calorimetry, Spectroscopies and DFT

This chapter has been published as:
Z. Mao, P. G. Lustemberg, M. V. Ganduglia-Pirovano, C. T. Campbell, *ACS Catalysis*, 2020, 10, 5101-5114.

Chapter Abstract

The morphology, interfacial bonding energetics and charge transfer of Ni clusters and nanoparticles on slightly-reduced $CeO_{2-x}(111)$ surfaces at 100 to 300 K have been studied using single crystal adsorption calorimetry (SCAC), low-energy ion scattering spectroscopy (LEIS), X-ray photoelectron spectroscopy (XPS), low energy electron diffraction (LEED) and density functional theory (DFT). The initial heat of adsorption of Ni vapor decreased with the extent of pre-reduction (x) of the $CeO_{2-x}(111)$, showing that stoichiometric ceria adsorbs Ni more strongly than oxygen vacancies. On $CeO_{1.95}(111)$ at 300 K, the heat dropped quickly with coverage in the first 0.1 ML, attributed to nucleation of Ni clusters on stoichiometric steps, followed by the Ni particles spreading onto less favorable terrace sites. At 100 K, the clusters nucleate on terraces due to slower diffusion. Adsorbed Ni monomers are in the +2 oxidation state, and they bind by ~45 kJ/mol more strongly to step sites than terraces. The measured heat of adsorption versus average particle size on terraces is favorably compared to DFT calculations. The Ce 3d XPS lineshape showed an increase in Ce^{3+}/Ce^{4+} ratio with Ni coverage, providing the number of electrons donated to the ceria per Ni atom. The charge transferred per Ni is initially large but strongly decreases with increasing cluster size for both experiments and DFT, and shows large differences between clusters at steps versus terraces. This charge is localized on the interfacial Ni and Ce atoms in their atomic

layers closest to the interface. This knowledge is crucial to understanding the nature of the active sites on the surface of Ni-CeO_2 catalysts for which metal-oxide interactions play a very important role in the activation of O–H and C–H bonds. The changes in these interactions with Ni particle size (metal loading) and the extent of reduction of the ceria help to explain how previously reported catalytic activity and selectivity change with these same structural details.

3.1 INTRODUCTION

Nickel supported on CeO_2 is an important catalyst material with promise in a wide variety of applications,[25, 26, 29, 30, 33, 56-67] perhaps most importantly in the direct conversion of methane to methanol.[14] Ceria is a widely-used support material for late transition metal catalysts, [68-70] and is well known to enhance the stability of supported metals to resist deactivation by sintering.[16, 68, 69, 71-73] The (111) face of CeO_2 is the most studied and well-understood among the low-index faces of ceria in terms of structure and reactivity. Thus the interaction of Ni with the CeO_2(111) surface is of fundamental interest in catalysis. Recent works have shown that Ni-ceria interactions are crucial to achieving high catalytic performance.[6,10-12,14] In particular, it has been found that oxidized Ni species (Ni^{2+}) at the Ni-ceria interface that result from the transfer of two 4*s* electrons from Ni to the empty 4*f* band of ceria, generating two Ce^{3+} ions, activate O–H and C–H bonds at room temperature. Moreover, the metal loading has a drastic effect on the catalytic properties. For example, as the coverage of Ni increases and 3D nanoparticles form, the dissociation of O–H bonds is hindered on the Ni atoms that are not in direct contact with the ceria support,[6] and the ability of the system to dissociate methane is also hindered due to the formation of NiC_x on the surface. [11] Because the strong electronic perturbations in chemisorbed Ni species on ceria, which produce dramatic changes in their chemical properties, are extremely sensitive to the coverage of Ni on the ceria substrate, it is crucial to understand how the structure, heat of adsorption, and the amount of Ni→ ceria charge transfer changes with Ni coverage.

Here we study the morphology and interfacial energetics of vapor-deposited Ni on slightly-reduced CeO_2(111) surfaces using metal vapor adsorption calorimetry, surface analysis techniques and density functional theory. The results reveal that Ni grows as 3-dimensional particles and clarify electronic details of the Ni - CeO_2 interactions. The results show that the heat of Ni adsorption and the number of electrons donated to the ceria per Ni atom change strongly as the size of the Ni clusters grows and with the extent of reduction of the ceria support, and that the Ni clusters bind more weakly to (111) terrace sites than to step edges.

These results help explain the unique properties of ceria as a support for Ni nanoparticle catalysts.

3.2 COMPUTATIONAL METHODS

All electronic structure calculations were carried out using the spin-polarized DFT approach as implemented in the Vienna ab initio simulation package (VASP) {vasp site, http://www.vasp.at; version vasp.5.3.5}[74, 75] Ce (4f, 5s, 5p, 5d, 6s), O (2s, 2p), and Ni (3p,3d,4s) electrons were explicitly treated as valence states within the projector augmented wave (PAW) method[76] with a plane-wave cutoff energy of 415 eV, whereas the remaining electrons were considered as part of the atomic core. Total energies and forces were calculated with a precision of 10^{-6} eV and 10^{-2} eV/Å for electronic and force convergence, respectively, within the DFT+U approach by Dudarev et al.[77] ($U_{eff} = U - J = 4.5$ eV for the Ce 4*f* electrons) with the generalized gradient approximation (GGA) proposed by Perdew, Burke, and Ernzerhof (PBE).[78] We note that questions regarding the best value for the U parameter are still under debate.[79-81] Nonetheless, most DFT+U studies of reduced ceria-based systems agree that U values in the range of 4.5–6.0 eV with GGA are suitable for the description of the localization of charge driving the $Ce^{4+} \rightarrow Ce^{3+}$ reduction. However, one should bear in mind that there is in general no unique U that gives a reasonable account of all systems' properties.[82-84] Long-range dispersion corrections were also considered, employing the so-called DFT-D3 approach.[85, 86]

3.3 RESULTS

3.3.1 *Ni Sticking Probability on CeO_{2-x}(111)*

The sticking probability was measured using the signal for non-sticking Ni gas atoms in each pulse detected with the transient QMS signal for Ni gas, normalized to the signal for the reference zero-sticking pulse from a hot W flag, where no permanent sticking occurs. For all three systems we studied ($CeO_{1.95}$(111) at 300 K, $CeO_{1.8}$(111) at 300 K, $CeO_{1.95}$(111) at 100 K), the sticking probability started at ~97% and increased to unity within the first 0.5 ML.

3.3.2 *Ni Growth Morphology on CeO_{2-x}(111)*

Gaseous Ni was deposited onto CeO_{2-x}(111) films at 300 and 100 K in discrete amounts. The Ni and Ce signals in He^+ LEIS were monitored after each such Ni dose. The integrated Ni signals were normalized to the signal from a thick Ni overlayer (>10 nm average thickness). The Ce signals were normalized to those for a clean CeO_{2-x}(111) surface taken at the beginning of each experiment. The normalized Ni LEIS signal gives the fraction of surface covered and shadowed by Ni nanoparticles, and the normalized Ce signals give the fraction of surface which is not masked by Ni. The normalized Ni and Ce LEIS signal data are plotted versus Ni coverage in Figure 3.1 and compared with two typical growth models. The straight dashed lines correspond to the normalized LEIS signal that would be expected if Ni grew in a layer-by-layer mode. They do not fit well with the measured LEIS data. The solid curved lines correspond to 3-dimensional (3D) growth mode assuming the Ni grows as 3D particles with the shape of flat disks with a constant aspect ratio (height / diameter) of 0.25 on $CeO_{1.95}$(111) and 0.20 on $CeO_{1.8}$(111), as suggested by STM studies.[32] In the flat-disk model, we assume that the Ni particles all have this same shape at all coverages and the same size at any given coverage, and the particle number density *n* does not change with metal coverage (i.e., the saturation number density of nuclei is reached by the first dose, as is generally the case for such systems[87]). This model is applied only up to the coverage where ~35% of the surface is covered by particles, since particles overlap with each other at higher area fraction. Previous work showed that, if the particles grow as hemispherical caps, the total surface area masked by particles in the LEIS signals for the incident and detection angles used here is 1.207 times the metal/support interfacial area, due to a shadowing effect.[55] This ratio, calculated in the same way, is changed to 1.318 for $CeO_{1.95}(111)$ and 1.255 for $CeO_{1.8}(111)$ based on their flat-disk aspect ratios (height/diameter = 0.25 and 0.20, respectively). With these assumptions, the particle number density *n* is the only fitting parameter in the equation, and it is determined from the best fitting line in Figure 3.1.

Following this approach, the flat-disk model gives a good fit to the LEIS data as shown in Figure 3.1, and the best-fit particle number densities on $CeO_{2-x}(111)$ at 300 and 100 K are shown. The extent of reduction of the ceria has only a minor effect on the Ni particle density. At 300 K, it was 3.6×10^{12} particles/cm^2 on $CeO_{1.95}(111)$, and 4.5×10^{12} particles/cm^2 on $CeO_{1.8}(111)$. A similar small increase in the particle density with extent of reduction was reported based on STM images.[32] Comparing the growth of Ni on $CeO_{1.95}(111)$ at 300 and 100 K, a huge temperature effect was observed. The Ni particle density on $CeO_{1.95}(111)$ was 1.3×10^{13} particles/cm^2 at 100 K, about 4-fold higher than at 300 K.

3.3.3 *Heat of Adsorption of Ni on $CeO_{2-x}(111)$*

The heat of adsorption of Ni gas atoms on $CeO_{2-x}(111)$ for x = 0.05 and 0.2 at 300 K and for x = 0.05 at 100 K are plotted in Figure 3.2 as a function of Ni coverage. At 300 K on

$CeO_{1.95}$(111), Ni has an initial heat of adsorption of 345 kJ/mol, and it decreases rapidly to 323 kJ/mol by 0.2 ML. The heat then increases, slowly approaching the sublimation heat of bulk Ni at 430 kJ/mol by 9 ML. This type of reverse in slope with coverage has been seen before and attributed to the adsorption of metal adatoms to stronger-binding defects (step edges) at the lowest coverage that become saturated as coverage increases.[51] Thus, the initial heat of 345 kJ/mol on $CeO_{1.95}$(111) is attributed to Ni adsorption at step edges. The minimum heat occurs at 0.1-0.2 ML Ni, which is consistent with the step-site density of ~5% of the total sites, given that some Ni atoms will bind to other Ni atoms in clusters rather than directly at step sites as the step sites approach saturation by Ni atoms.   On $CeO_{1.8}$(111), where the degree of reduction is larger and there are many more O vacancies, the initial heat at 300 K is 65 kJ/mol lower than for $CeO_{1.95}$(111) (280 vs 345 kJ/mol), and the heat remains lower up to ~0.2 ML. This clearly shows that Ni atoms do *not* prefer oxygen vacancies on CeO_2(111), the opposite as we observed for Ag and Au adsorption,[49, 88] but the same as for Cu.[51] This is consistent with the fact that Cu and Ni are much more oxophilic than Ag and Au, so they prefer to bind to the surface O atoms. The stronger binding of Au and Ag atoms to oxygen vacancies than that to stoichiometric terrace sites was also predicted by DFT calculations[89-94] and confirmed experimentally[95-98] in previous literature, though the decoration of oxygen vacancies by Au atoms has been challenged by recent STM experiments.[94] On $CeO_{1.8}$(111), there is no minimum in the heat of Ni adsorption versus coverage of the type seen on $CeO_{1.95}$(111) here. We attribute this to the preferential loss of the step-edge oxygen atoms (by far the least stable type of lattice O[99]) upon reduction, so that the step edges on $CeO_{1.8}$(111) no longer have enough O atoms to make more stable sites for Ni than stoichiometric terrace sites.

At 100 K, the heat of Ni adsorption on $CeO_{1.95}(111)$ is initially 45 kJ/mol lower than that at 300 K, and remains lower until 2 ML. There is also no minimum in heat versus coverage of the type seen at 300 K. We attribute this to the lack of mobility of the metal adatoms at 100 K so that they cannot diffuse to the stronger-binding step sites as they do at 300 K, and thus remain on terrace sites and nucleate particles there instead.

Dividing the Ni particle number density from the flat-disk model fit to Figure 3.1 (particles/cm^2) by the Ni coverage (atoms/cm^2), gives the average number of Ni atoms per particle at each coverage. Assuming these particles have the same density as bulk Ni(s), gives the volume per particle. Combining this volume with the disk shape (aspect ratio stated above) also gives the average Ni particle (flat disk) diameter at each coverage. Using this approach, the heat-versus-coverage data in Figure 3.2 have been replotted as Ni heat of adsorption vs the average Ni particle (flat-disk) diameter, as shown in Figure 3.3a.

Figure 3.3a shows the heat of Ni adsorption versus particle diameter on $CeO_{1.95}(111)$ at 300 K and 100 K and $CeO_{1.8}(111)$ at 300 K. At 300 K, the heat of Ni adsorption on Ni nanoparticles smaller than 1.5 nm in diameter supported on $CeO_{1.95}(111)$ is higher than that on Ni nanoparticles supported on $CeO_{1.8}(111)$, indicating that Ni does not bind more strongly to oxygen vacancies on this surface. Above 1.5 nm diameter, the extent of reduction of CeO_{2-x} does not show a significant influence on the heat of Ni adsorption onto Ni nanoparticles. The plot for $CeO_{1.95}(111)$ at 100 K stops at 1.5 nm diameter because the fractional surface area masked by Ni nanoparticles reaches ~35% here, and the flat-disk model used to fit the LEIS data is no longer appropriate at higher coverages. The heat of Ni adsorption on $CeO_{1.95}(111)$ at 100 K for a given particle diameter below 1.3 nm is lower than the value for $CeO_{1.95}(111)$ at 300 K. At 0.6 nm diameter, the difference is ~40 kJ/mol. We attribute this difference to the nucleation of Ni particles at step edges, where they bind more strongly than on $CeO_2(111)$ terraces (by ~40 kJ per mole of Ni atoms at the smallest sizes measured). Due to the much slower diffusion of Ni atoms at 100 K, they are not able to nucleate particles at step edges, but at 300 K they can. When the particle diameter exceeds ~1.3 to 1.5 nm, the heat of Ni adsorption under all three conditions (i.e., $CeO_{1.95}(111)$ at 300 K, $CeO_{1.8}(111)$ at 300 K, $CeO_{1.95}(111)$ at 100 K) only show small differences between each other. Apparently, the new Ni atoms that add to particles larger than ~1.4 nm predominantly bind to sites that are far enough from step edges that they feel little effect of the step sites. Because of the much larger particle number density at 100 K than at 300 K, this particle size (> 1.4 nm) is not reached until a 4-fold higher coverage at 100 K. This size difference explains why the heats of adsorption in Fig. 2 at 100 K remain below those at 300 K until very high coverage.

As reported previously,[15] we can convert the differential heats of Ni adsorption measured here to the chemical potential of Ni atoms by assuming that the entropic contribution to the free energy is negligible compared to the huge enthalpic differences measured here. The difference between the chemical potential of Ni atoms in nanoparticles with a given diameter D and the chemical potential of Ni atoms in bulk Ni metal (set as the zero reference of chemical potential) equals the sublimation heat of bulk Ni minus the heat of Ni adsorption onto Ni nanoparticles with diameter D.[15] The data in Figure 3.3a have been replotted in Figure 3.3b as the chemical potential of Ni atoms in Ni nanoparticles versus the average particle diameter. As seen, the chemical potential generally decreases with increasing particle size, as has been reported for many related systems, and is largely related to the increasing number of metal-metal bonds per atom with increasing size.[15, 51, 88, 100] The chemical potential initially increases with increasing particle size for $CeO_{1.95}(111)$ at 300 K, due to the initial population of more stable sites at step edges, which saturate quickly as coverage increases.

It appears from Figure 3.3 that Ni particles do not nucleate at step edges on the $CeO_{1.8}(111)$ surface even at 300 K, or that step edges do not bind Ni significantly more strongly than terraces on this heavily reduced ceria surface, especially since O vacancies prefer to form at step edges, as noted above.

3.3.4 *Charge Transfer from Ni to $CeO_{2-x}(111)$ during Deposition*

The change of Ce oxidation state in the $CeO_{2-x}(111)$ surface during Ni deposition was monitored by monitoring the change in the Ce 3d XPS peak lineshape. The percentage of Ce^{3+} in the Ce 3d XPS probe depth (~1 nm) was determined from lineshape fitting of the XPS Ce 3d peak as described previously.[51, 101] The Ce^{3+} percentage is plotted with respect to Ni coverage in Figure 3.4. The Ce^{3+} percentage increases rapidly with the Ni coverage up to 2 ML for $CeO_{1.95}(111)$ at 300 and 100 K. Above 2 ML, the Ce^{3+} percentage does not change much with the Ni coverage, remaining very near the high-coverage (10 ML) limit of 22% at 300 K and 19% at 100 K. For $CeO_{1.8}(111)$, the Ce^{3+} percentage also increases in the first 2 ML, but only from 41% to 46%, and again stays fairly constant with coverage above 2 ML.

To quantify the extent of charge transfer per Ni atom to the film, we assume that the Ce atoms in the $CeO_{2-x}(111)$ film are reduced by the electrons donated from the Ni atoms by the percentage plotted in Figure 3.4, but only down to the XPS probe depth of 1.0 nm, with no reduction below that. (Using the TPP-2M equation[102] to calculate, the electron inelastic mean free path in CeO_2 for Ce 3d XPS peak is 1.24 nm. Since the XPS data was taken with the energy analyzer at 45° to the normal angle of the sample, 70% of the XPS signal of Ce 3d peak comes from the first 1.0-nm-thick layer of ceria in the sample.) Using the number of Ce atoms per unit area in this probe depth (2.5 × 10^{15} Ce atoms per cm^2), the data point in Figure 3.4 at each Ni coverage can then be converted to the average number of electrons donated per Ni atom, as done previously for Cu on this same surface.[51] If we further assume that Ni can only be in the form of neutral Ni or Ni^{2+}, this average number of electrons donated per Ni atom can be converted to the fraction of total Ni that is oxidized to Ni^{2+}. Figure 3.5a shows the resulting number of electrons donated per Ni atom and fraction of Ni^{2+}, calculated based on data in Figure 3.4, plotted versus Ni coverage. These both decrease rapidly with coverage, and are much smaller values on the more reduced ceria.

We observed that the Ni $2p_{3/2}$ XPS peak's binding energy (BE) at low Ni coverages had large contributions in the region expected for Ni^{2+}. This was studied in more detail by Carrasco et al.[33] , as shown in Figure 3.5b, where their Ni $2p_{3/2}$ BE for Ni on $CeO_2(111)$ at 300 K is plotted as a function of Ni coverage. For a coverage of 0.15 ML of Ni, they reported a shift of ~2 eV with respect to the reported value for metallic Ni, which indicates the formation of Ni^{2+}.[103] Zhou et al.[104] also observed with XPS that when ~0.5 ML Ni (which is ~1.2 ML in the definition of this paper) is deposited onto the fully oxidized $CeO_2(111)$ at 300 K, about 25% of the total Ni is oxidized to Ni^{2+}.

For the convenience of comparison to DFT calculations, the number of electrons donated per Ni atom and the fraction of Ni^{2+} are also replotted as a function of the average number of Ni atoms per Ni nanoparticle in Figure 3.6. Here, one clearly sees that the fraction of Ni^{2+} is larger for a given particle size when grown at 300 K (where they nucleate at steps and have a higher heat of adsorption) than at 100 K where they nucleate at terraces and are less stable. Thus, step edges seem to be important in making the Ni^{2+} species stable. Alternatively, the temperature could have a direct effect in that the process to make Ni^{2+} might have some activation barrier that is not reached at 100 K.

3.3.5 *DFT Models*

The $Ni_n/CeO_2(111)$ (n=1-7, 9, 13, 19, 24, 26, 29 and 32) surfaces were modeled with DFT by supercells with (3×3) surface periodicity, see Figure 3.7, with calculated ceria bulk equilibrium lattice constant (CeO_2: 5.485 Å, DFT+U). A CeO_2 slab of six atomics layers, i.e., two O-Ce-O trilayers, separated by at least 13 Å-thick vacuum layer, was used as model of the ceria support. Monkhorst-Pack[105] grids with (2×2×1) k-point sampling were used. All atoms in the three bottom atomic layers were fixed at their optimized bulk-truncated positions during geometry optimization, whereas the rest of the atoms were allowed to fully relax. The structures of the ceria-supported Ni_1, Ni_2, Ni_4.flat, and Ni_4.pyr aggregates (Figure 3.7) correspond to the ones previously reported,[30, 61, 64, 66] for which the locations of the Ce^{3+} ions, resulting from the metal-support interaction, were optimized. For the other Ni aggregates considered, some different adsorption sites were explored, but different Ce^{3+} configurations were not. Note that for Ni_n ($n > 19$), the (3×3) surface unit cell is not large enough to isolate the Ni_n aggregates, and the models correspond to continuous rows of supported Ni atoms, i.e., infinitely long 1D islands (i.e., stripes or wires) of Ni that are several Ni atoms wide. Selected calculations were performed for some $Ni_n/CeO_2(111)$ systems with (4×4), (2×2) and (1×1) surface periodicity and (1×1×1), (3×3×1), and (6×6×1) k-point sampling, respectively, in order to evaluate possible variations in the number of electrons transferred from the Ni_n aggregates to the ceria support as a function of Ni loading.

Reduced extended $CeO_{2-x}(111)$ surfaces were modeled with different concentrations of oxygen vacancies (Θ_{Ovac}=1/4, 1/2, and 3/4; Θ_{Ovac} = Nv/N, where Nv and N are the number of surface plus subsurface vacancies in the reduced overlayer and the total number of oxygen atoms in a single non-reduced oxygen atomic layer of the same cell, respectively) using a slab of nine atomic layers with (2×2) periodicity, as employed in previous work.[61] Furthermore, one and two layers of Ce_2O_3 on $CeO_2(111)$ as well as the fully reduced (A-type) $Ce_2O_3(0001)$ surface (Ce_2O_3: a_0/c_0 = 3.92/6.18 Å and internal parameters u_{Ce}/u_O = 0.2471/0.6448, ferromagnetic state, DFT+U) were also modeled; only the interaction of Ni_1 species on the reduced supports were considered, and this was done without accounting for long-range dispersion corrections.

The oxidation state of a given Ce ion (Ce^{4+} or Ce^{3+}) was determined by considering its local magnetic moment (the difference between up and down spins on the ion), which can be estimated by integrating the site- and angular momentum-projected spin-resolved density of states over spheres with radii chosen as the Wigner−Seitz radii of the PAW potentials. The magnetic moment of the Ce^{4+} ($4f^0$) and Ce^{3+} ($4f^1$) ions is 0 and ~1 μ_B, respectively, because the occupation of the Ce *f* states is 0 and ~1, respectively. As for the oxidation state of the Ni atoms in the supported clusters, using the Bader analysis method,[106] we obtained that only those Ni atoms in direct bonds to the ceria support are partially oxidized, and thus, the average oxidation state of these atoms is calculated as the total number of electrons transferred to the ceria support divided by the number of Ni atoms with direct bonds to the support (Figure 3.7).

The integral heat of adsorption of Ni gas atoms forming Ni_n clusters on the $CeO_2(111)$ support was calculated at 0 K as $E_{ads} = -1/n\ [E(Ni_n/CeO_2) - E(CeO_2) - n{*}E(Ni_{atom})]$ where $E(Ni_n/CeO_2)$ and $E(CeO_2)$ are the total energies of the $Ni_n/CeO_2(111)$ and $CeO_2(111)$ surfaces, and $E(Ni_{atom})$ is that of a gas-phase Ni^0 atom in the d^9s^1 configuration, calculated with a (12×11×16)

Å^3 periodic cell and the Γ-point. The lattice parameter of bulk fcc Ni was optimized (Ni_{bulk}: 3.48 Å, DFT+D3), using a Monkhorst-Pack grid with (15×15×15) k-point sampling of the Brillouin zone, and the heat (enthalpy) of sublimation of bulk Ni (bulk cohesive energy) was calculated to be $\Delta H_{sub,Ni}^{calc}$ = 518 kJ/mol. These are in good agreement with prior results.[107, 108]

We modeled stoichiometric <110>-type steps by adding a continuous stripe (or wire) of CeO_2 that was three atomic layers thick and covered 3/5 of the surface on top of a six-layer-thick (5×3) $CeO_2(111)$ slab (like described above) and (1×2×1) k-point sampling. This is similar to methods that have been used preciously to model steps of $CeO_2(111)$ using DFT.[99, 109] Reduced <110>-type steps with varying fractions of missing step-edge oxygen atoms ($\Theta_{Ovac,step}$=1/3, 2/3, and 1) were also modeled. This added "CeO_2 wire" had stoichiometry Ce_9O_{18} per (5×3) unit cell when not reduced, decreasing to Ce_9O_{15} for the most fully reduced step edge. The adsorption of Ni_1 species on these stoichiometric and reduced step edges were studied. The locations of the Ce^{3+} ions, resulting from the removal of the step-edge oxygen atoms and from the Ni-ceria interactions, were not optimized in detail when modelling step sites.

3.3.6 *Ni monomers on CeO_2 and $CeO_{2-x}(111)$ terraces: DFT results*

On $CeO_2(111)$, an isolated Ni_1 species was found to adsorb on a hollow site coordinated to three surface oxygen atoms with E_{ads} = 374 kJ/mol, in line with previous studies (Figure 3.7).[30, 61] As a result of strong metal-support interactions between Ni_1 and CeO_2, two electrons from Ni are transferred to the support, generating two Ce^{3+} ions, and the Ni atom becomes oxidized to Ni^{2+} (d^8). This is qualitatively consistent with the experimental observations in Figure 3.5, although the extent of charge transfer is not as large experimentally. This is probably related to the fact that the experimental surface is not stoichiometric CeO_2, but instead is already partially reduced to $CeO_{1.95}$, and the extent of charge transfer decreases with the degree of reduction (see above). For Cu adsorption on $CeO_{2-x}(111)$, we also found that such small amounts of pre-reduction (2.5%) greatly decreased the extent of charge transfer at the lowest Cu coverages compared to stoichiometric CeO_2.[51]

Figure 3.8a shows the calculated heat of adsorption of a nickel atom on reduced $CeO_{2-x}(111)$ surfaces. The two excess electrons resulting from the creation of a (neutral) oxygen vacancy have been reported to be localized at cation sites in the outermost plane of cations, but not adjacent to the vacancies, driving the $Ce^{4+} \rightarrow Ce^{3+}$ reduction; and, the energetically most stable near-surface oxygen vacancy structures for a broad range of vacancy concentrations all have their vacancies at subsurface oxygen sites.[110-113] As the degree of near-surface reduction increases, the adsorption energy of the Ni atom decreases and at the same time, Ni adatoms recover their metallic character ($Ni^{2+} \rightarrow Ni^{1+} \rightarrow Ni^{0}$). In other words, as the concentration of Ce^{3+} ions increases, it gradually becomes more and more difficult for Ni to transfer electrons to the already reduced support, as observed experimentally (Figure 3.6). The results in Figure 3.8 also help explain the experimental observations that the binding of Ni at low coverage is stronger on a ceria surface which is less reduced (cf. Figure 3.2 and Figure 3.3a). This suggests that the ability of ceria to stabilize oxidized nickel species (Ni^{2+}) on the CeO_2 surface, by re-localizing electrons on localized *f*-states (Ce^{3+}), is a key factor in determining the Ni heat of adsorption.

3.3.7 *Ni monomers at $CeO_2(111)$ and $CeO_{2-x}(111)$ step sites: DFT results*

Comparison of the heats of adsorption of Ni monomers on the flat stoichiometric $CeO_2(111)$ terraces (374 kJ/mol, Figure 3.7) and at stoichiometric <110> step edges (Figure 3.8c) shows that the step edge binds Ni_1 more strongly by 95 kJ/mol (Figure 3.8d). In both sites, the Ni binds as Ni_1^{2+}. These calculations thus predict that decoration of the stoichiometric step with Ni species will occur before adsorption on the terraces. The heat of adsorption of three Ni_1 species (Figure 3.8e), which corresponds to the maximum possible coverage of monodispersed Ni_1 species at the step edge, is almost the same as a single Ni_1, still also ~90 kJ/mol per Ni atom more strongly bound to the step edge than isolated Ni_1 species on the flat terrace. This is consistent with the observed minimum in the heat of Ni adsorption versus coverage on the $CeO_{1.95}(111)$ surface at 300 K (Figure 3.2), which we attributed to the existence of stronger-binding defect (step-edge) sites that are occupied first, i.e., at low Ni coverage.

However, on the more reduced $CeO_{1.8}(111)$ surface, no minimum in the calorimetric heat of Ni adsorption versus coverage has been observed, and the measured heat is always lower than on the nearly stoichiometric surface (Figure 3.3a). This is consistent with the calculated heat of adsorption of Ni at the step as a function of the step-edge oxygen vacancy fraction ($\Theta_{Ovac,step}$, Figure 3.8b), which shows that as the number of available step-edge oxygen atoms decreases, step sites eventually become less stable than terrace sites when all the step-edge oxygen atoms are removed.

We also calculated the average step-edge oxygen vacancy formation energy as a function of the step-edge O vacancy fraction ($\Theta_{Ovac,step}$) and found that oxygen atoms at the step are always easier to remove than those at the terrace. The average defect formation energy was 169, 207 and 219 kJ/mol for $\Theta_{Ovac,step}$=1/3, 2/3, and 1, respectively, and 265 kJ/mol at a terrace site, calculated using the model in Figure 3.8c without optimizing the location of the excess charge. This validates our claim above (based on prior literature) that the O vacancies are mainly at the step edges, which also suggests that on the more reduced $CeO_{1.8}(111)$ surface studied experimentally here, there may be no O atoms on the step edges.

3.3.8 *Ni clusters on stoichiometric $CeO_2(111)$ terraces: Heat of adsorption and charge transfer by DFT*

The formation of Ni_2 dimeric structures was considered, as studied in previous work.[66] In the case of two Ni atoms at neighboring hollow sites separated by 3.56 Å (Figure 3.7), each Ni atom transfers two electrons to the ceria support, generating four Ce^{3+} ions and two Ni^{2+} species. The adsorption energy of such a Ni pair is E_{ads}= 355 kJ/mol (per Ni atom, relative to Ni gas). Therefore, bringing two Ni^{2+} species closer but without forming a Ni-Ni bond destabilizes the system by 38 kJ/mol [$2\times Eads(Ni_2)$ $-2\times Eads(Ni_1)$], which implies a repulsive interaction of 38 kJ/mol between the positively charged Ni^{2+} atoms at this separation. We addressed whether a Ni_2 dimeric structure forming a Ni–Ni bond ($Ni_{2.}$b) is energetically preferred over two well-separated Ni_1^{2+} species by adsorbing such a $Ni_{2.b}$ species which have an optimized Ni–Ni bond length of 2.20 Å (cf. Figure 3.7). This results in one Ce^{3+} ion, and thus two partially oxidized $Ni^{0.5+}$ atoms. The adsorption energy of the $Ni_{2.}$b dimer is only E_{ads}= 329 kJ/mol, i.e., the system is 90 kJ/mol *less* stable than two isolated Ni_1^{2+} species. Even though the Ni atoms in the $Ni_{2.b}$ dimer have a low charge, it is still too high to allow intrinsic Ni-Ni bonding that exceeds the $Ni^{0.5+}$-$Ni^{0.5+}$ charge repulsion. This repulsive interaction of the two ceria-supported $Ni^{0.5+}$ species of 90 kJ/mol for the $Ni_{2.}b/CeO_2(111)$ system (cf. Figure 3.7) is 68 kJ/mol lower than the simple Coulomb repulsion of two +0.5 point charges at the same separation (2.20 Å) in vacuum (158 kJ/mol). The difference reflects some type of attractive bonding between the two Ni cations that partially overcomes the Coulomb repulsion.

In the case of a Ni_3 cluster, the Ni atoms form a flat triangle with three nearly equal Ni–Ni bonds of length 2.31-2.32 Å (Figure 3.7), two Ce^{3+} ions are formed, and therefore each of the three Ni atoms has a charge of +0.67. The adsorption energy of the Ni_3 trimer is E_{ads}= 382 kJ/mol; hence, compared to three isolated Ni_1^{2+} species, the Ni_3 cluster is 24 kJ/mol more stable (or 8 kJ/mol per Ni atom).

As for Ni_4, both three dimensional clusters with pyramidal shape (Ni_4.3D) and bi-dimensional flat rhombohedral-shaped (Ni_4.2D) clusters were considered, as studied previously.[30] The stability of these clusters is comparable, namely, E_{ads}= 389 and 386 kJ/mol for Ni_4.3D and Ni_4.2D, respectively (Figure 3.7). These Ni_4 species also reduce the ceria support upon adsorption, with the formation of two Ce^{3+} ions. In the Ni_4.3D case, these two electrons are transferred from the three Ni atoms forming the pyramid base, which are partially oxidized, $3\times Ni^{0.66+}$, whereas the top Ni atom remains as Ni^0. In the Ni_4.flat, all four Ni atoms in direct contact with the support are oxidized, $4\times Ni^{0.5+}$. As with the Ni atoms in the Ni_3 cluster, those in the Ni_4 clusters do not repel each other. For instance, the Ni_4.2D structure ($4\times Ni^{0.5+}$) is more stable by 228 kJ/mol [$4\times E_{ads}(Ni_4.2D)$ - $4\times E_{ads}(Ni_2.b)$] than two isolated Ni_2.b dimers ($2\times Ni^{0.5+}$ each). Even if the Ni atoms in the Ni_4.2D and Ni_2.b structures have a similar charge (+0.5), the larger number of Ni–Ni bonds in the Ni_4.flat cluster, with one bond length of 2.26 Å and four average bond lengths of 2.31 Å, is what optimally stabilizes the structure.

As the number of Ni atoms in the nanoparticles increases beyond three, the formation of 3D structures is preferred over flat ones (cf. Figure 3.7), in agreement with the experimental observation that Ni grows as 3D particles. For instance, the energy gained by adding one Ni atom to the flat Ni_4.2D cluster [$5\times Eads(Ni_5) - 4\times Eads(Ni_4.2D)$] is by 10 kJ/mol larger if a Ni_5.3D structure is formed (436 kJ/mol) (Figure 3.7), as compared to a 2D Ni_5 aggregate (426 kJ/mol).

The configuration of the Ni_5, Ni_6 and Ni_7 nanoparticles corresponds to 3D structures with 4, 5 and 6 Ni atoms, respectively, in contact with the ceria support, with $2\times Ce^{3+}$ ions for the Ni_5, Ni_6 structures and $3\times Ce^{3+}$ ions for the Ni_7 one. As for the case of Ni_4, electrons are transferred only from the Ni atoms in direct contact with atoms of the ceria support, and these are partially oxidized ($4\times Ni^{0.5+}$, $5\times Ni^{0.4+}$ and $6\times Ni^{0.5+}$ for the Ni_5, Ni_6 and Ni_7 nanoparticles, respectively), whereas the Ni atoms on top (not in direct contact to the ceria) remain as Ni^0. Also, for the Ni_9 ($3\times Ce^{3+}$), Ni_{13} ($5\times Ce^{3+}$) and Ni_{19} ($5\times Ce^{3+}$) aggregates, only the six, nine and fifteen Ni atoms, respectively, in direct contact with the oxide support are partially oxidized ($6\times Ni^{0.50+}$, $9\times Ni^{0.56+}$ and $5\times Ni^{0.34+}$, respectively), whereas the Ni atoms on top of the oxidized nickel retain their metallic character (Ni^0). Finally, the continuous stripes of Ni that we considered (i.e., Ni_{24}, Ni_{26}, Ni_{29} and Ni_{32}) donate 4 electrons for Ni_{24} and Ni_{32} and 5 electrons for Ni_{26} and Ni_{29} to the support ($5\times Ce^{3+}$). In the Ni_{24}, Ni_{26}, Ni_{29} and Ni_{32} stripes, also only the atoms in direct contact with the ceria support are partially oxidized (cf. Figure 3.7).

In summary, the DFT results produce firm computational evidence that for low Ni loadings on the $CeO_2(111)$ surface, for which a large dispersion of small Ni nanoparticles is observed,[1,64] the ceria support induces strong electronic perturbations in chemisorbed Ni species which are directly at the Ni-ceria interface, whereas there is a rapid weakening of the Ni-ceria interactions with increasing Ni loading, for which 3D nanoparticles form.[1,64]

3.4 DISCUSSION

Figure 3.9 compares the calculated integral heat of adsorption for the thermodynamically stable $Ni_n/CeO_2(111)$ systems with those obtained experimentally (cf. Figure 3.2), where the calculated points have been shifted by –88 kJ/mol $[\Delta\mathrm{H}^{\mathrm{calc}}_{\mathrm{sub,Ni}}\left(518\,\frac{\mathrm{kJ}}{\mathrm{mol}}\right) - \Delta\mathrm{H}^{\mathrm{exp}}_{\mathrm{sub.Ni}}(430\,\frac{\mathrm{kJ}}{\mathrm{mol}})]$. This correction corresponds to the 88 kJ/mol difference between the calculated bulk cohesive energy (sublimation energy) of bulk Ni(solid) with the PBE exchange-correlation functional with long-range dispersion corrections (DFT-D3), as compared to the experimental value.

The experimentally determined heats of adsorption are larger than the DFT ones for 1 and 3 atom clusters by 15 and 10 kJ/mol, respectively, after this 88 kJ/mol correction in Figure 3.9). This may be due to the fact that the cluster sizes could have been underestimated in the first two pulses in the heat measurements of Figure 3.2, Figure 3.3, and Figure 3.9. Although the LEIS measurements of Figure 3.1 are consistent with a constant number density of Ni clusters, independent of coverage, those measurements did not extend down to such low coverages as the heat measurements, so it is possible that in the first two heat points, the Ni clusters had not yet reached their saturation density, as we assumed here in estimating cluster sizes. For higher Ni loading, the DFT heats plotted in Figure 3.9 are larger than the experimental ones. This is actually to be expected based on the wire-like nature of the Ni aggregates modelled by DFT, which have more Ni–Ni bonds per Ni atom than in the corresponding isolated clusters studied experimentally.

The comparison and the discussion above reveal that, due to the strong Ni-ceria support interaction and its large charge transfer, at least three Ni atoms are required to make Ni clusters stable. Only then can the intrinsic Ni-Ni bond energies help win out over repulsive interactions between partially charged Ni atoms at the Ni-ceria interface.

Figure 3.10a shows the number of electrons transferred per Ni atom versus cluster size as calculated by DFT. The extent of charge transfer per Ni atom clearly decreases rapidly with cluster size, but for a given size we found it to be generally independent of the size of the unit cell, as discussed below. Figure 3.10b compares this number of electrons transferred per Ni atom versus particle size as calculated with the experimental results reported in Figure 3.5a and Figure 3.6.

As seen in Figure 3.10b, the charge transferred per Ni atom decreases strongly with particle size in all three curves. However, it decreases much more rapidly in the DFT calculations than in the closest corresponding experiment (i.e., $CeO_{1.95}(111)$ at 100 K, where the particles are at terrace sites like in the DFT). The transferred charge in the experiments also decreases with size much more rapidly at 100 K than at 300 K, so that the charge transferred per Ni atom on $CeO_{1.95}(111)$ is 3- to 4-fold larger for the same particle size at 300 K than at 100 K. This may be related to the fact that the clusters are at step edges at 300 K but on terraces at 100 K, although this is surprising since the 2.5% O vacancies in this $CeO_{1.95}(111)$ surface concentrate at step edges, and O vacancies clearly decrease the extent of charge transfer (see above). However, step edges may have other electronic or structural characteristics that enhance charge transfer in spite of these extra O vacancies. For example, charge-transfer-induced lattice strain is probably relieved more easily near steps. (Earlier DFT calculations have shown that such charge transferred to $CeO_2(111)$ and the corresponding conversion of Ce^{4+} to Ce^{3+} leads to lattice expansion parallel to the surface.[114]) Given that the DFT calculations are at 0 K, the three curves in Figure 3.10b separate by temperature, with greater charger transfer at higher temperature. Temperature seems unlikely to be the intrinsic reason for this, since the only reasonable explanation would be some activation energy associated with charge transfer of a type that we have never seen reported.

For the same particle size in Figure 3.10b, the total Ni coverages are quite different for the three curves for $CeO_2(111)$ and $CeO_{1.95}(111)$, since the Ni clusters are much closer together in the DFT models than in the experiments at 100 K, and they are closer together in the experiments at 100 K than at 300 K. It is possible that there are strong dipole-dipole repulsions between clusters, since the clusters carry so much charge and have their counter charge in the outermost ceria plane at the metal-ceria interface according to the DFT results. These repulsions get stronger as the distance between parallel dipoles decreases, and are therefore well known to lead to depolarization of adsorbate-substrate bonds as their coverage increases.[115] So these different coverages would affect charge transfer in the way seen here: higher coverages lead to less charge transfer for the same cluster size. The data for these curves in Figure 3.10b are replotted versus coverage in Figure 3.11. When plotted in this way, all three data sets converge into a single curve, which lends support to the proposal that the differences in Figure 3.10b are largely associated with this effect of coverage (cluster separation) on dipole-dipole repulsions between clusters. We tested this effect directly with DFT by changing the unit cell size for the same cluster size and shape. For one Ni atom with (4×4), (3×3), (2×2) periodicity, DFT shows that two electrons are transferred to the ceria support (Ni^{2+}), whereas for the (1×1) unit cell, only 2/3 of electron is transferred ($Ni^{0.66+}$). However, for both the Ni_3 and Ni_4.3D clusters with (3×3) and (2×2) periodicity, two electrons are transferred independent of the size of the unit cell ($3\times Ni^{0.67+}$). This can be seen as the pairs of DFT points in Figure 3.11 with nearly the same charge transfer but quite different coverages (cf. Ni_5.3D and Ni_{13} with about 0.4 electrons donated per Ni atom but corresponding to 0.56 and 1.45 ML). This gives rise to the greatest deviations from the single curve fit through these data in Figure 3.11. Since these DFT calculations do not show a direct effect of coverage on charge transfer, we cannot be sure that the nice correlation with coverage in Figure 3.11 that seems to bring all three data sets into pretty close agreement is really due to the direct effect of coverage (i.e., cluster separation). It may be that the largest unit cell size in the DFT calculations is still not large enough to see this effect, since the cluster density used in the DFT models is much higher than in the experiments. An alternative explanation is that the charge transfer in the 300 K experiments is greater for the same cluster size than in the 100 K experiments due to the fact that the clusters are at step edges at 300 K but on terraces at 100 K (see above).

The experimental charge transfer at 300 K in Figure 3.11 is quite large. For example, for particles with 278 atoms, ~1/3 electron is transferred per Ni atom, so that the particle has a charge of +93. Since the aspect ratio of the particle is 0.25, about 1/3 of the Ni atoms are on the interface. Therefore, the measured total charge transfer will be realized if each Ni atom at the Ni-CeO_2 interface transfers one electron to the ceria. Apparently there is not too much Coulombic repulsion, because of attractions to the negative charge on the ceria (i.e., Ce^{3+} ions) at the interface, as indicated by the DFT calculations. The high strength of this interfacial bonding decreases the chemical potential of the Ni atoms in a way that can be directly related to the superior sinter resistance of these materials via well know rate equations.[116, 117]

The results above clearly show that the electronic character of the Ni atoms changes with Ni particle thickness and size, and with the location of the Ni atoms within the 3D particles (i.e., whether in the interfacial layer or in layers further away from the CeO_2 support), and with the extent of reduction of the CeO_2 support. We next show how these changes can be related to some of the unique catalytic properties of Ni/CeO_2 materials that have been reported, and how these vary with the structural properties of these materials at the atomic scale.

First, let us consider highly dispersed Ni on CeO_2 with few oxygen vacancies, where all the Ni atoms are either isolated monomers or small 2D clusters. We show above that these Ni atoms are highly cationic. It has been recently shown[29, 33, 61, 62] that well-dispersed, small Ni nanoparticles on a non-reduced ceria support, with all the Ni atoms being interfacial, promote the activation of both O–H and C–H bonds at room temperature, with lower activation barriers than for extended metallic Ni surfaces. Most importantly, this type of material can perform direct catalytic conversion of methane to methanol at low temperature (450 K), using a mixture of oxygen and water as the oxidant, with ~30% selectivity.[64] This we attribute to the highly cationic character of the surface Ni atoms. These same types of structural features were also reported to be most active for catalyzing the water-gas shift (WGS) reaction ($CO+ H_2O \rightarrow CO_2+H_2$), where higher Ni loadings (larger Ni particles) were shown to be less active.[33, 56]

For larger Ni nanoparticles, we find that *neutral* Ni atoms are above the oxidized interfacial Ni atoms and thus are exposed to gas-phase reactants. The calculated O–H bond cleavage activation energy at these neutral Ni atoms is higher than at the Ni monomers and few-atom Ni clusters discussed above, and not very different from that on Ni(111).[33] Hence, the Ni atoms at the rim of these larger nanoparticles are the only effective sites for O–H bond cleavage. These larger particles with both neutral Ni atoms and cationic Ni at the particle perimeters appear to be the most active for converting $CO+H_2O$ into methane.[1] In fact, the selectivity of Ni/CeO_2(111) model catalysts was reported to depend strongly on Ni loading. Specifically, low-loaded systems catalyze the production of CO_2+H_2, whereas high-loaded systems catalyze the production of CH_4. The Ni loading also has a strong effect on the rate at which the system exposed to CH_4 deactivates: during dry reforming of methane on high-loaded systems, coke forms and deactivates the catalyst.[61]

The nature of the ceria support is also important. As discussed above, the binding of Ni nanoparticles on CeO_2 surfaces becomes increasingly weak as the degree of reduction of the ceria surface increases; and, the amount of charge transferred from the Ni to the CeO_2, for the same small Ni particle size, also decreases strongly with the extent of reduction. Therefore, if operating conditions are changed for low-loaded Ni/CeO_2 catalysts in such a way that the CeO_2 gets more reduced, this will markedly reduce the charge on the Ni atoms. This is the case during methane dry reforming with CO_2 over low-loaded Ni/CeO_2 catalysts at 650 K.[29, 61, 62] The C–H cleavage barrier remains low even though, as we show above, the charge transfer from Ni to ceria is decreased due to ceria reduction, but now the C–O bond cleavage barrier in CO_2 also becomes low,[10] due to the presence of surface oxygen vacancies.

3.5 CONCLUSIONS

Ni atoms adsorb on slightly reduced ceria $CeO_{2-x}(111)$ and form three-dimensional nanoparticles at 300 and 100 K, which increase in size with increasing Ni loading. The extent of reduction of ceria has a minor effect on the Ni particle number density at 300 K, while decreasing temperature from 300 to 100 K results in 3-fold higher Ni particle number density on $CeO_{1.95}(111)$. The heat of Ni adsorption onto $CeO_{1.95}(111)$ at 300 K starts from 345 kJ/mol (attributed to step edges), decreases within the first 0.2 ML to 323 kJ/mol (as step edge sites saturate), and increases afterward (due to growing particle size) until the bulk heat of Ni sublimation is reached by 9 ML. On $CeO_{1.8}(111)$ at 300 K, this initial drop in heat of adsorption was not observed, attributed to weaker Ni binding to step edges when full of O vacancies. The heat of adsorption is generally lower on the more reduced ceria surface (by up to 65 kJ/mol initially at 300 K), again suggesting that the oxophilic Ni atoms do not prefer O vacancies. DFT calculations support this. On $CeO_{1.95}(111)$ at 100 K, Ni atoms adsorb mainly on terraces due to slow Ni adatom diffusion, with an initial heat of adsorption that is 45 kJ/mol lower than that at 300 K where Ni atoms mainly adsorb on step edges. This highlights Ni's strong preference for step edges over terraces. Upon adsorption, Ni atoms donate electrons to the support to generate Ce^{3+}. DFT calculations show that this charge is localized on the interfacial Ni and Ce atoms in their atomic layers closest to the interface. As the coverage and particle size grow, the average number of electrons donated per Ni atom decreases in both experiments and DFT calculations. For the same size, Ni particles exhibit less charge transfer to $CeO_{1.95}(111)$ at 100 K (when on terraces) than at 300 K (when at step edges). The charge transfer from Ni particles is much less on $CeO_{1.8}(111)$ compared to $CeO_{1.95}(111)$ at both temperatures.

Ni-CeO_2 interactions that produce strong electronic perturbations in the Ni nanoparticles result in important changes in their chemical and catalytic properties, as discussed for the examples of both O–H and C–H bond cleavage. Manipulating these interactions by, for example, controlling the degree of reduction of the support, as well as particle size and metal loading, can lead to improved catalytic activity and/or selectivity. Our findings help explain some of the outstanding catalytic properties of Ni/CeO_2 materials and how they depend upon their atomic-level structural details. This may aid in the rational design of catalysts that involve O–H and C–H bond dissociation.

3.6 FIGURES

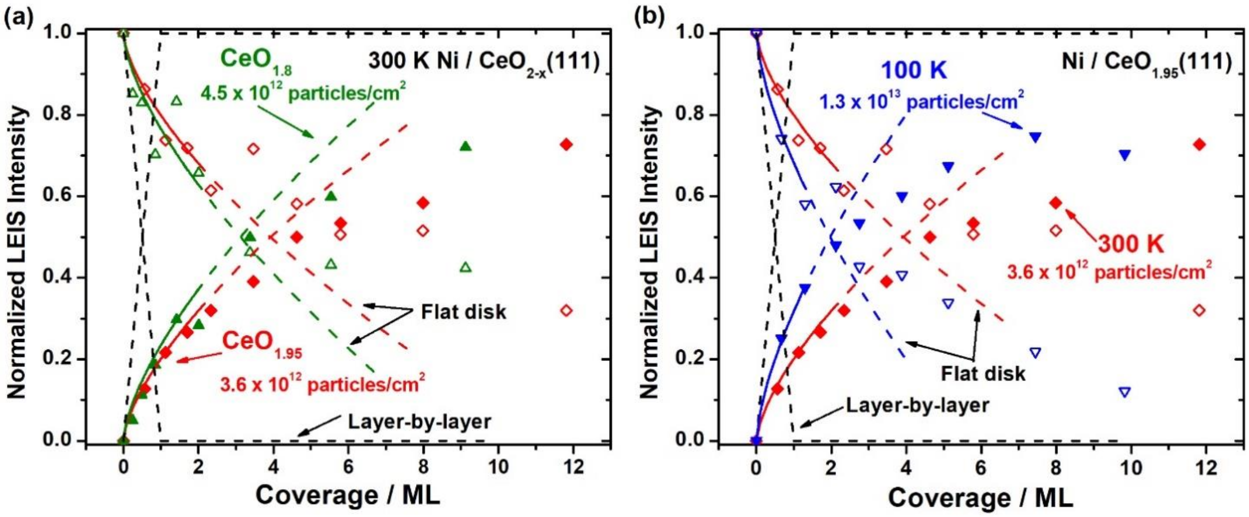

Figure 3.1 (a) Integrated Ni (closed symbols) and Ce (open symbols) LEIS signal intensities (normalized to thick multilayer Ni and clean CeO$_{2-x}$(111), respectively) as a function of Ni coverage after deposition onto (a) CeO$_{1.95}$(111) (red diamonds) and CeO$_{1.8}$(111) (green triangles) at 300 K (b) CeO$_{1.95}$(111) at 300 K (red diamonds) and 100 K (blue triangles). The black dashed lines correspond to the normalized LEIS signal that would be observed if Ni grew in a layer-by-layer fashion, while the colored solid lines correspond to Ni growing as flat disks with a fixed aspect ratio (0.25 on CeO$_{1.95}$ and 0.20 on CeO$_{1.8}$) and a fixed particle density of 3.6×10^{12} particles/cm^2 (red), 4.5×10^{12} particles/cm^2 (green) and 1.3×10^{13} particles/cm^2 (blue). This model is only reasonable up to ~35% of the surface is covered, since particles will soon start to overlap with each other at higher coverage. The colored dashed lines after that are only a guide to the eye.

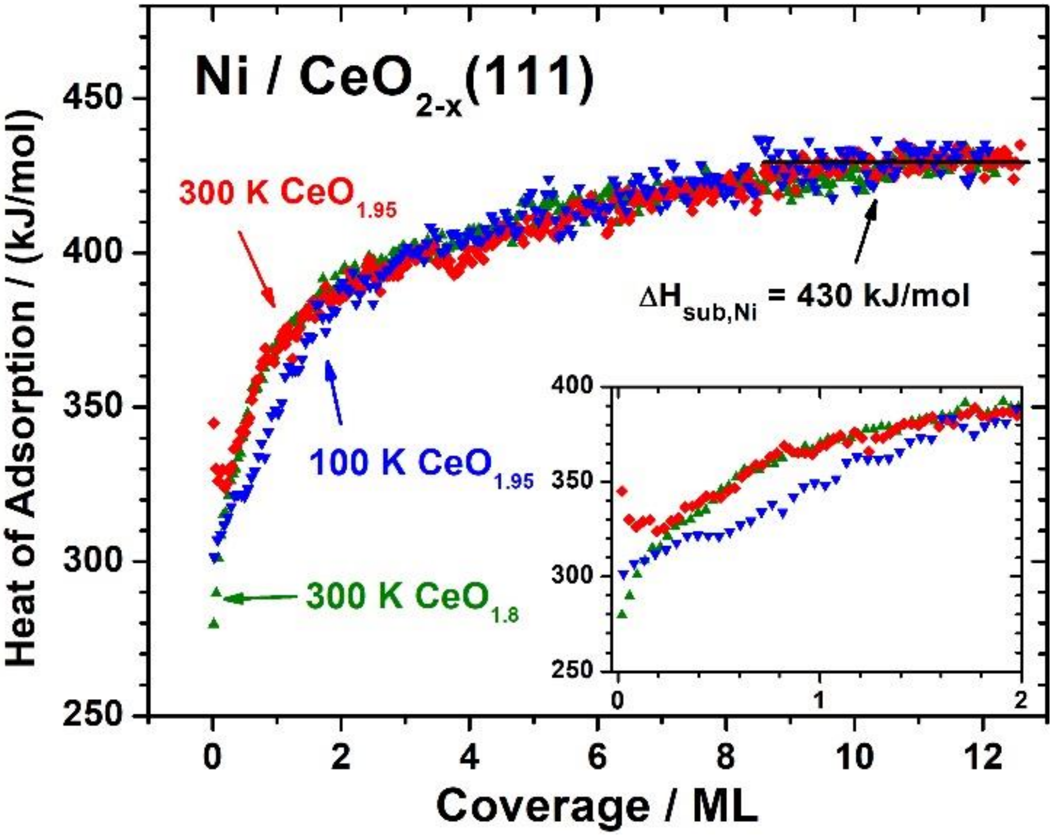

Figure 3.2 Differential heat of Ni atom adsorption on CeO1.95(111) at 300 K (red diamonds), CeO1.8(111) at 300 K (green triangles) and CeO1.95(111) at 100 K (blue triangles), as a function of Ni coverage. 1 ML is defined as 7.89×1018/m2 which is the areal density of coordinatively-unsaturated O atoms on the ideal bulk-terminated CeO2(111) surface.

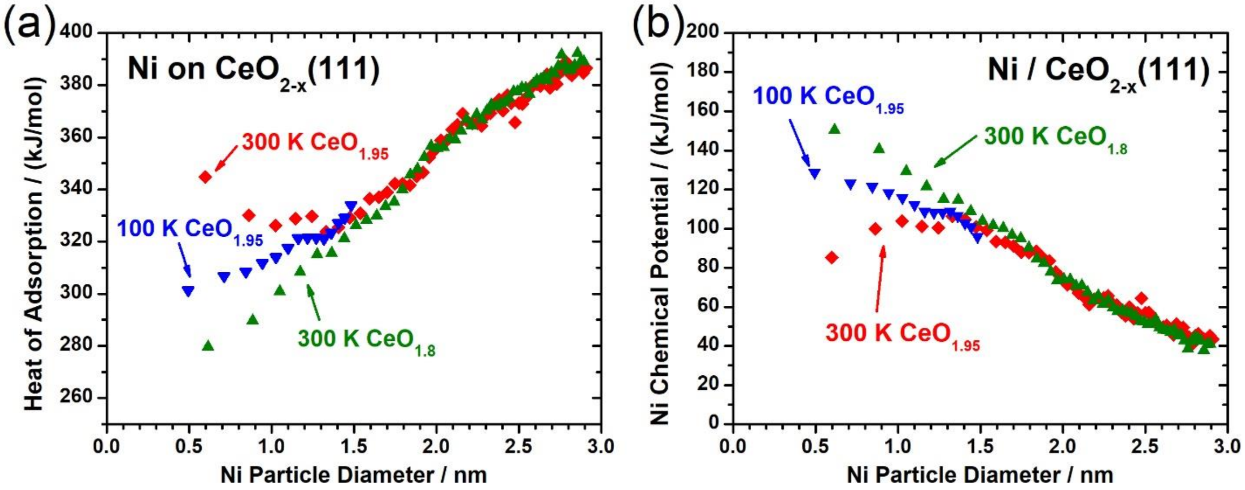

Figure 3.3 (a) Differential heat of Ni adsorption on $CeO_{2-x}(111)$ at 300 and 100 K as a function of Ni average particle (flat-disk) diameter to which Ni atoms add. (b) Chemical potential of Ni atoms in Ni particles versus the average Ni particle diameter on $CeO_{2-x}(111)$ at 300 and 100 K. Red diamonds, green triangles and blue triangles correspond to $CeO_{1.95}$ at 300 K, $CeO_{1.8}$ at 300 K, and $CeO_{1.95}$ at 100 K respectively.

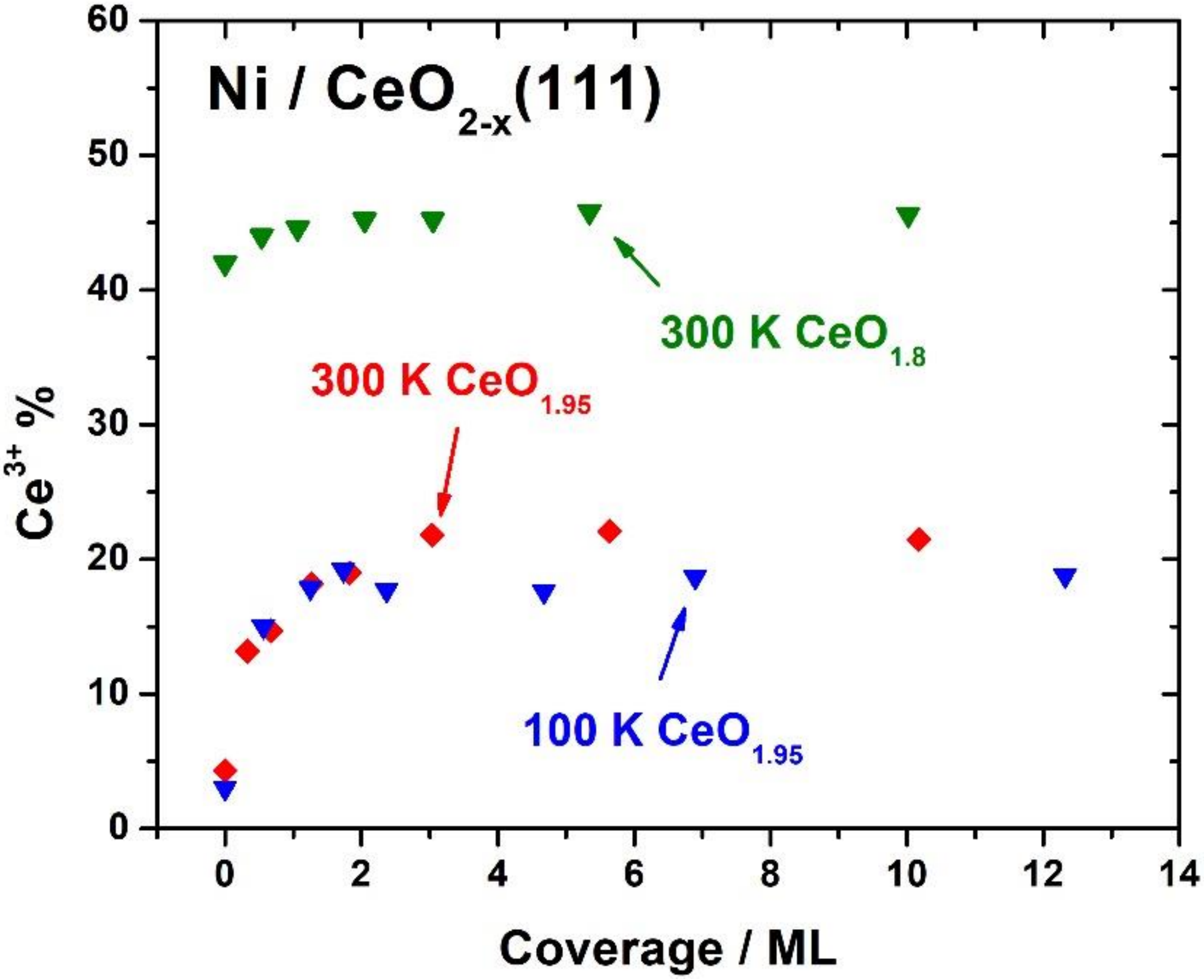

Figure 3.4 Percentage of Ce^{3+} (with the rest as Ce^{4+}) in the XPS probe depth versus Ni coverage based on lineshape fitting of the XPS Ce 3d peak measured during Ni deposition on CeO$_{1.95}$(111) at 300 K (red), CeO$_{1.8}$(111) at 300 K (green) and CeO$_{1.95}$(111) at 100 K (blue).

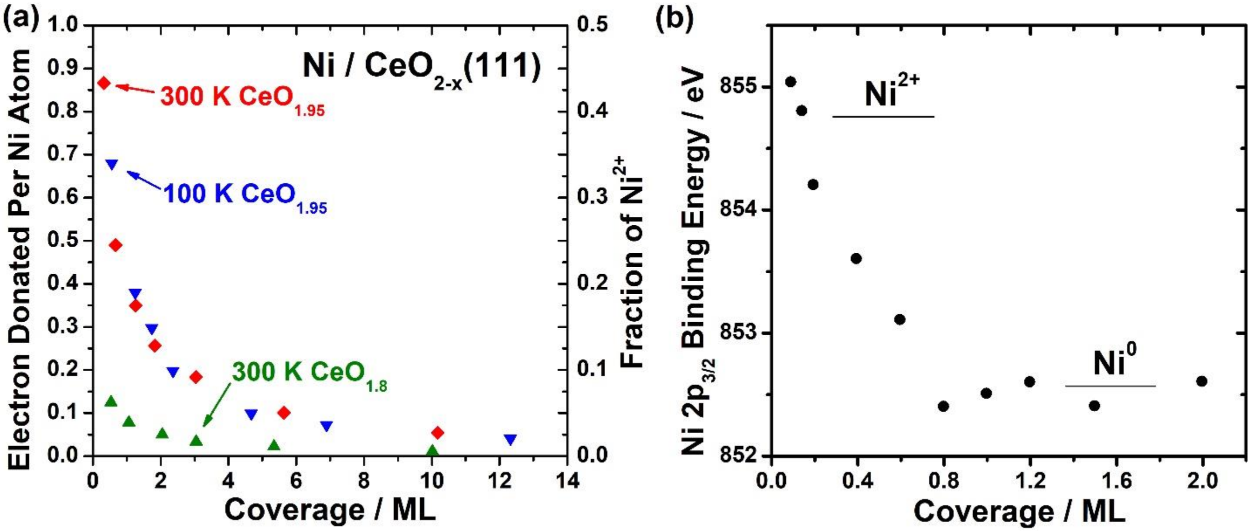

Figure 3.5 (a) Average number of electrons donated to ceria per Ni atom and corresponding fraction of total Ni that is oxidized (assuming it is Ni^{2+}) plotted as a function of Ni coverage; (b) Variation of the Ni $2p_{3/2}$ XPS binding energy as a function of Ni coverage on $CeO_2(111)$ at 300 K as was reported in the Supplementary Information of ref.[33]

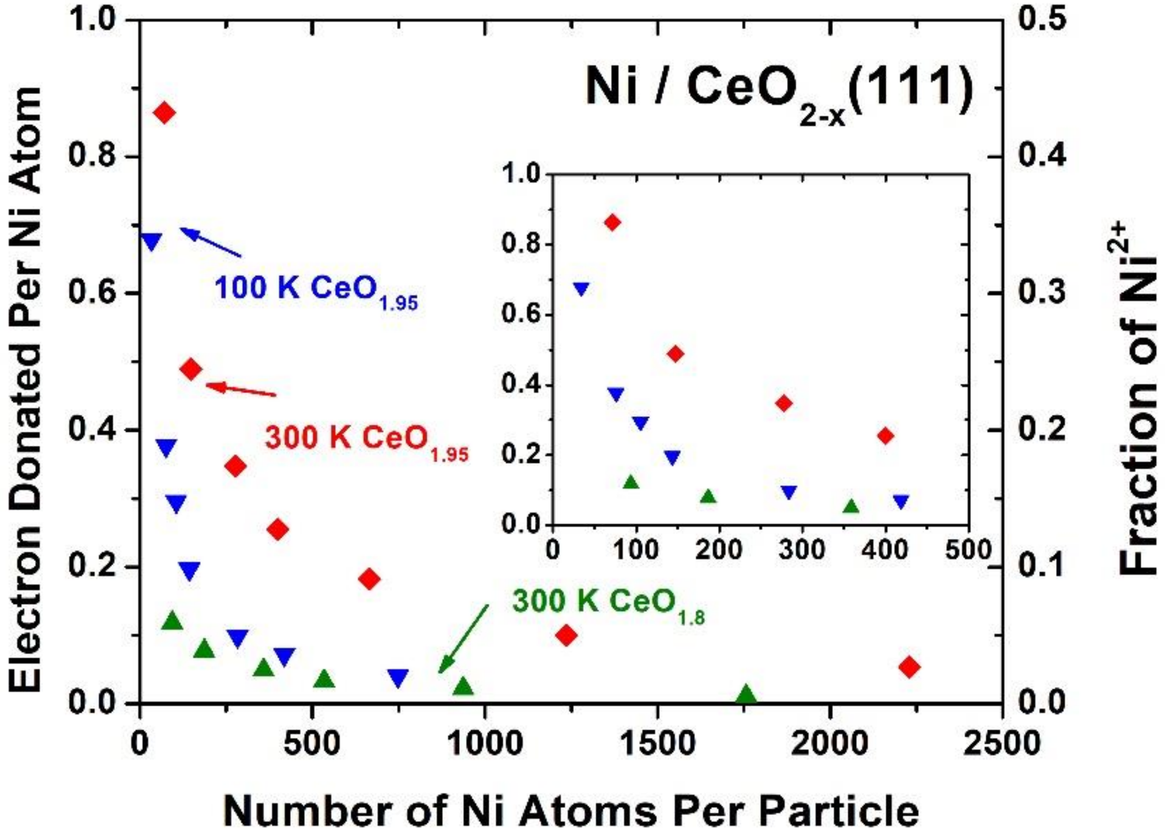

Figure 3.6 Average number of electrons donated to ceria per Ni atom and corresponding fraction of total Ni that is oxidized (assuming it is Ni^{2+}) from Figure 3.5a replotted as a function of number of Ni atoms per particle.

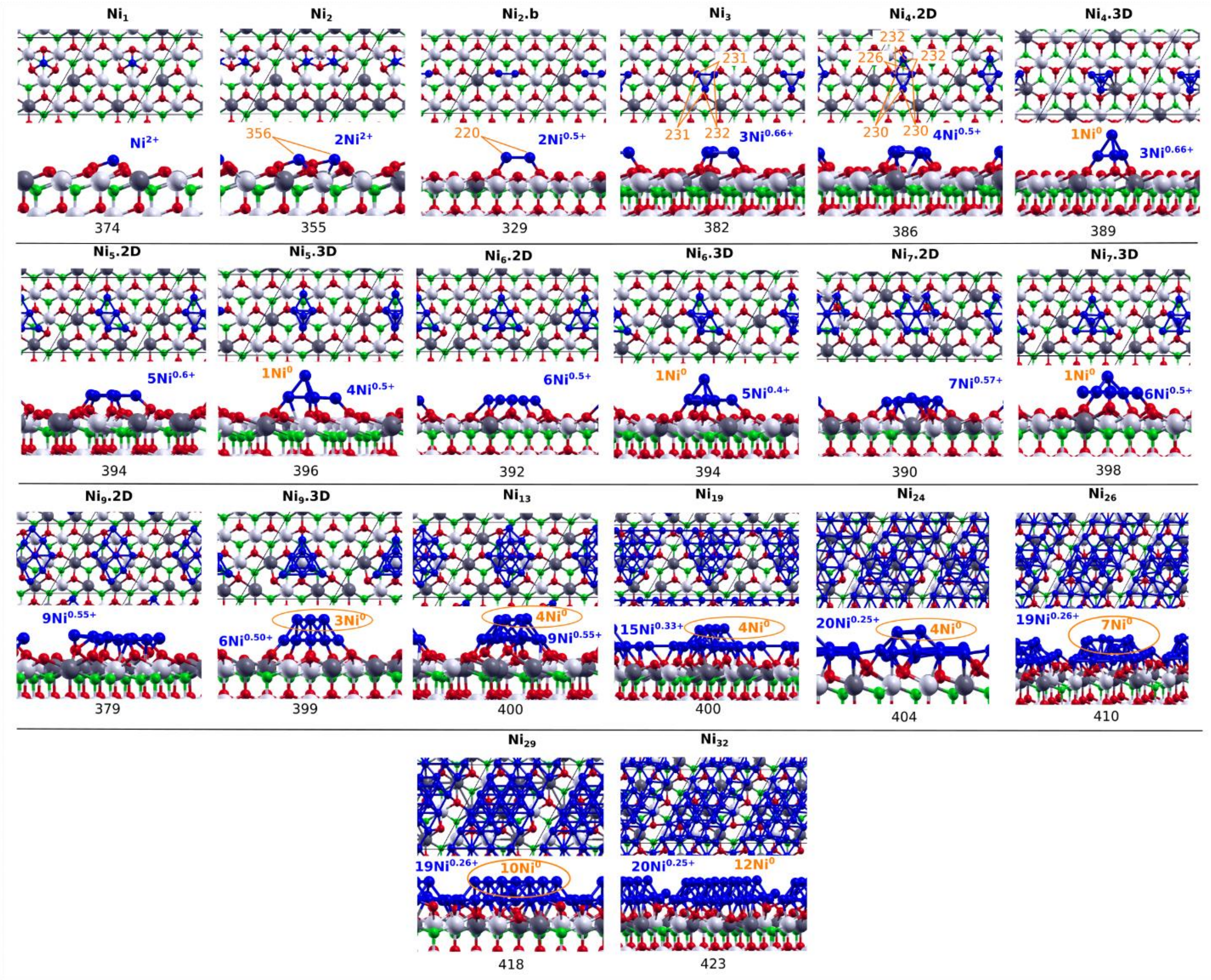

Figure 3.7 Models of $Ni_n/CeO_2(111)$ (n=1-7, 9, 13, 19, 24, 26, 29 and 32). Surface/subsurface oxygen atoms in the outermost O–Ce–O trilayer are depicted in red/green, Ce^{4+} in white, and Ce^{3+} in gray. Values of the integral heat of adsorption of Ni_n species are listed below each structure, in kJ/mol per Ni atom (relative to Ni gas). Optimized Ni-Ni bond lengths in pm for Ni_2, Ni_3 and Ni_4.2D are indicated in orange.

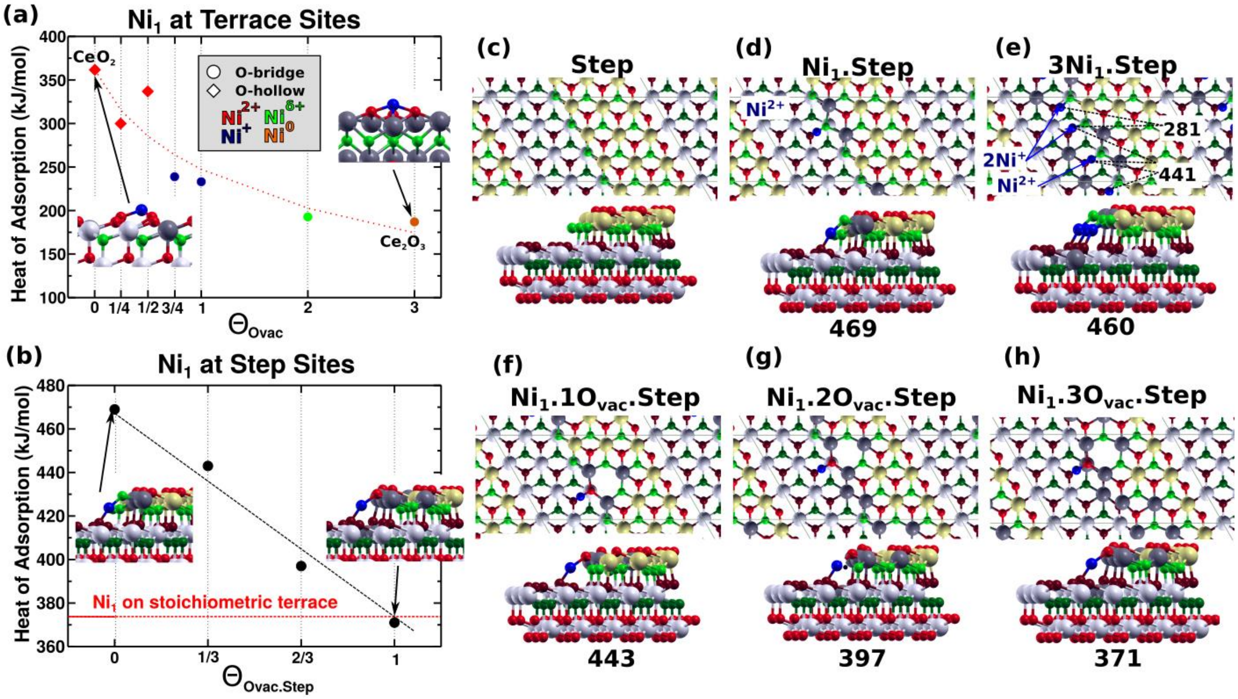

Figure 3.8 (a) Calculated heat of adsorption of a single Ni atom on the $CeO_2(111)$ surface, $CeO_{2-x}(111)$ with different concentrations of subsurface oxygen vacancies (Θ=1/4, 1/2, and 3/4, see text). Also shown are results for 1 and 2 layers of Ce_2O_3 on $CeO_2(111)$ and a slab of pure $Ce_2O_3(0001)$, plotted at $\Theta_{Ovac,step}$= 1, 2 and 3, respectively. The Ni oxidation state is color coded as shown ($0 < \delta < 1$), and the adsorption site corresponds to the most stable one. Note that the slab model and method used in these calculations slightly differ from those used to obtain the values reported in Figure 3.7 (see text), explaining the difference of 11 kJ/mol in the heat of adsorption of a single Ni atom on the $CeO_2(111)$ surface. (b) Calculated heat of adsorption of Ni monomer at a <110>-type step as a function of the step-edge O vacancy fraction ($\Theta_{Ovac,step}$= 0, 1/3, 2/3, and 1). The red dotted line corresponds to the heat of adsorption of one Ni atom on the stoichiometric terrace (374 kJ/mol, Figure 3.7). Atomic structures of the (c) stoichiometric <110>-type steps with (d) one and (e) three Ni atoms and of the (f)-(h) reduced steps with one Ni atom. Values of the heat of adsorption of Ni species are listed below each structure, in kJ/mol per Ni atom (relative to Ni_1 gas).

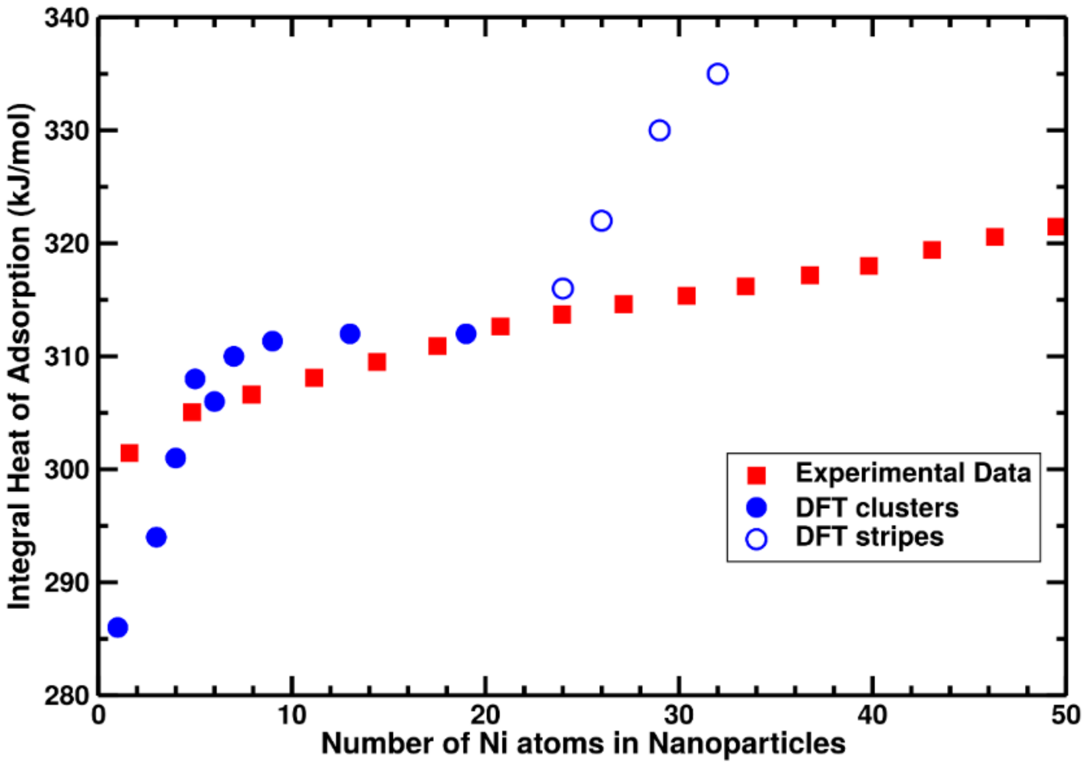

Figure 3.9 Integral heat of adsorption as function of the number of Ni atoms in the Ni_n aggregates. Experimental data for adsorption at 100 K (where terrace sites are predominantly populated) (red squares), calculated DFT data (blue filled and empty circles). For $n > 19$, the Ni_n aggregates in DFT correspond to continuous Ni stripes or wires (blue empty circles). The DFT points were shifted by 88 kJ/mol to smaller values (see text).

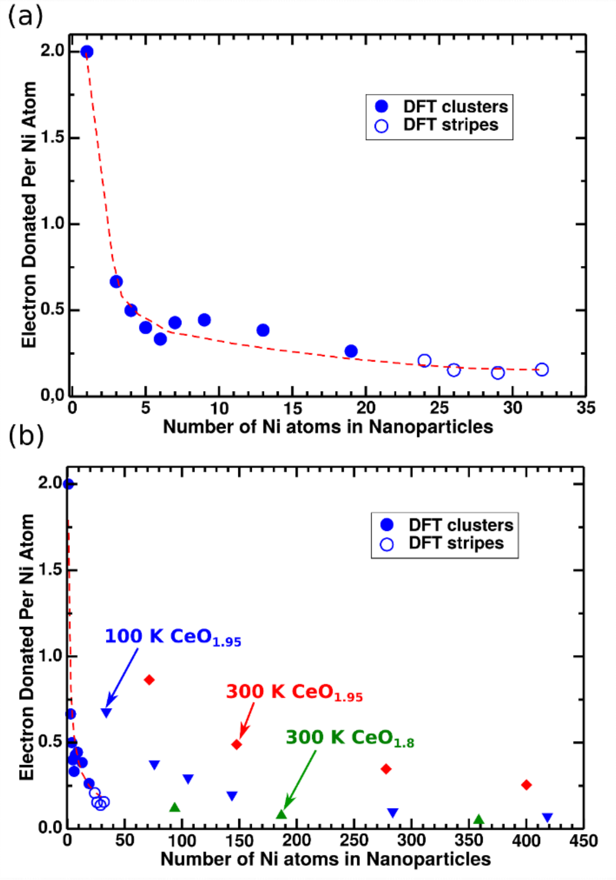

Figure 3.10 (a) Calculated number of electrons donated per Ni atom as a function of the number of Ni atoms in the nanoparticle. (b) DFT data from part (a) replotted over a larger range for comparison to the experimental data from Figure 3.6.

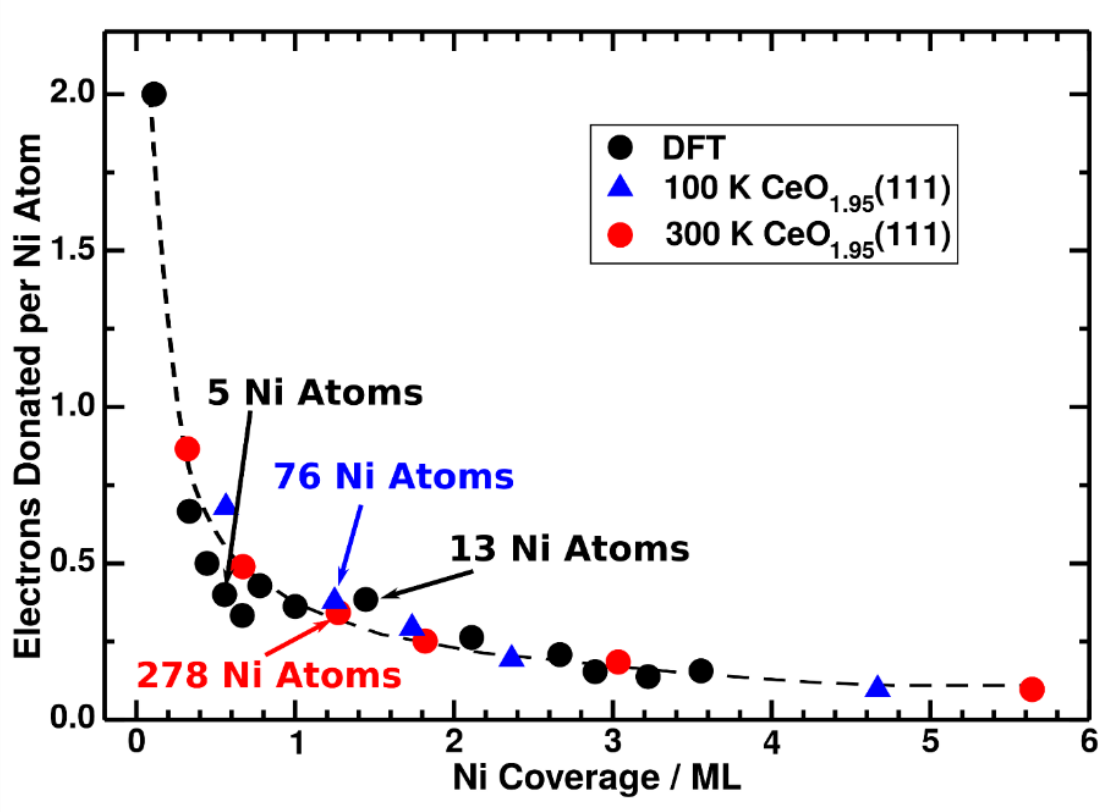

Figure 3.11 Number of electrons donated per Ni atom versus total Ni coverage, as calculated by DFT for $CeO_2(111)$ and as measured for $CeO_{1.95}(111)$ at 100 and 300 K. The numbers of atoms in the nanoparticles are also indicated for the points closest to 1.3 ML. The curve fit is just to guide the eye.

Chapter 4. Energetics and Structure of Ni Atoms and Nanoparticles on MgO(100)

This chapter contains unpublished results.

Chapter Abstract

The growth morphology and interfacial energetics of vapor deposited Ni on the MgO(100) surface at 300 and 100 K have been studied using single crystal adsorption calorimetry (SCAC), He^+ low-energy ion scattering spectroscopy (LEIS), X-ray photoelectron spectroscopy (XPS), and low-energy electron diffraction (LEED). At 300 K, the Ni atoms grow as three-dimensional nanoparticles with a saturation number density of 5×10^{16} particles/m^2. The differential heat of adsorption at 300 K increases rapidly with coverage, from 276 (initially) to 311 kJ/mol by 0.4 ML. Thereafter, it slowly increases asymptotically to the sublimation enthalpy of bulk Ni (430 kJ/ml) by 9 ML. The Ni $2p_{3/2}$ XPS peak binding energy at 300 K is initially (i.e., at 0.16 ML) 1.4 eV higher than that for bulk Ni(solid), but it decreases to that value at high coverage. At 100 K, the Ni atoms form single adatoms and then 0.17 nm thick 2D islands at low coverage with fewer Ni-Ni bonds compared to the Ni nanoparticles formed at 300 K. Thus, the initial heat (i.e., for the first ~0.03 ML) is 148 kJ/mol at 100 K, 128 kJ/mol lower than at 300 K, and remains lower for the 2D islands. With increasing coverage at 100 K, the tiny 2D Ni islands grow in size to cover nearly the entire surface before thickening. The XPS Ni $2p_{3/2}$ peak binding energy for 0.21 ML Ni on MgO(100) at 100 K is 2.2 eV higher than that for bulk Ni(solid), suggesting charge transfer from Ni to MgO(100) and formation of Ni^{2+} at very low coverage.

4.1 INTRODUCTION

Late transition metal nanoparticles anchored on support materials with a high surface area form a major fraction of the heterogeneous catalysts used in modern industry. They have been used for decades in clean energy, bulk chemical production, and environmental technologies. Within this kind of material, the interaction between the metal nanoparticles and the support materials is crucial to their behavior for catalyzing reactions. By changing the metal-support interaction, one can tune the binding energies of key intermediates and transition states in the reaction, and thus modify the catalyst's efficiency and selectivity.[1, 2] Also, strong interaction between the metal nanoparticles and the support materials helps maintain the size of the particles and keep them from sintering.[36, 73, 118] Thus, basic understanding and quantitative measurements of the interactions between metal nanoparticles and support materials are essential for designing better catalysts. Here we report calorimetric measurements of the strength of bonding of vapor-deposited Ni atoms and growing Ni nanoparticles to the MgO(100) surface, which is the most stable facet of MgO, and interpret these based on geometric and electron structural information provided by surface spectroscopies, and prior literature.

Catalysts consisting of Ni supported on MgO are important in a several reactions. Dry reforming (DRM) of methane is an important industrial reaction. It converts CO_2 and CH_4 to syngas ($CO+H_2$), which is a preferable feed for liquid fuel production, such as Fischer-Tropsch synthesis.[119, 120] Supported Ni nanoparticle catalysts are promising for catalyzing DRM for their high activity and selectivity, as well as their low cost.[119, 121-126] However, Ni nanoparticles quickly deactivate under reaction conditions due to sintering and carbon deposition.[3] The typical strategy for keeping Ni nanoparticles active is anchoring the Ni nanoparticles to selected oxide supports.[6-8, 10, 34, 127-134] Among all the oxides, MgO is one of the best supports for Ni catalysts in DRM applications due to their sinter resistance and reduced coking.[45, 119, 123, 131-133, 135] Nickel nanoparticles on MgO are also promising catalysts for steam reforming of ethanol, a reaction of interest in biomass conversion.[132, 136-138] Nickel nanoparticles supported on or partially embedded in MgO are thought to have strong metal-support interactions, due to their sinter resistance.[119, 131-133, 135] This ability to maintain small particles is also important for preventing coking, since coke formation requires large metal ensembles.[139]

Because of its importance in heterogeneous catalysis and other applications, and because the MgO(100) surface is one of the best understood of all oxide surfaces, the interactions of Ni with MgO(100) surfaces have been studied widely both by experiments[37, 140-144] and theory.[145-154] Studies have been performed on model systems consisting of Ni clusters/nanoparticles supported on MgO(100) surface to understand the growth of Ni on MgO and their interactions.[37, 142-144, 150-154] The binding energies of Ni atoms and Ni clusters on MgO(100) have been calculated using density-functional theory (DFT).[145, 151-153] However, no experimental measurements have been reported previously.

In this paper, we report the bonding energetics of Ni adatoms and Ni nanoparticles to MgO(100) model oxide supports using single crystal adsorption calorimetry (SCAC). SCAC measures the heat of adsorption of incoming gaseous Ni atoms when they adsorb on MgO(100), so it directly gives the binding strength between the Ni nanoparticles and the MgO(100) surface. The structure and electronic properties of the adsorbed Ni and the growing Ni nanoparticles is also monitored using He^+ low-energy ion scattering spectroscopy (LEIS) and X-ray photoelectron spectroscopy (XPS). The results show that the growth of Ni on MgO(100) has a very strong dependence on temperature. At 300 K, Ni forms three-dimensional nanoparticles, which have a strong adhesion energy to the MgO(100) surface due to Ni’s oxophilicity. At 100 K, Ni adsorbs mostly as single atoms and single-layer islands at low coverage, and there is a strong electron transfer from Ni to MgO(100). These results help in understanding the interaction between Ni and MgO(100) and its role in the reactions catalyzed by MgO-supported Ni catalysts.

4.2 RESULTS

4.2.1 *Ni Growth Morphology on MgO(100)*

The growth mode was characterized by monitoring the integrated LEIS signal from Mg in the substrate and Ni in the overlayer. The normalized Ni and Mg LEIS signal data are plotted versus Ni coverage in Figure 4.1a. One monolayer (ML) is defined as 1.12×10^{19} Ni atoms per m^2, which is the areal density of coordinatively-unsaturated O atoms on the ideal bulk-terminated MgO(100) surface. The integrated Ni signals were normalized to the signal from a thick Ni overlayer (>10 nm average thickness). The circular atomic-beam spot of metal deposition on the sample consists of an umbra of 4.00 mm in diameter and a penumbra of 4.52 mm in diameter, and the effective beam diameter is 4.26 mm.[17] Since the detected area of the LEIS energy analyzer is ~30% wider than this diameter, the Ni signal in LEIS at 100 K continues to grow slowly with Ni coverage (ultimately by ~10%) above the Ni coverage required to cover the area of the Ni beam's umbra completely with Ni at 100 K (i.e., by 6 ML). Similarly, the Mg signal at 100 K retains ~30% of its initial value at 6 ML. For these reasons, we used only 90% of the integrated Ni LEIS signal from a 10-nm-thick Ni overlayer as the reference for Ni signal normalization here. Similarly, the residual Mg signal at 6 ML coverage and 100 K was subtracted from the Mg signal at all coverages and both temperatures (after normalizing to the Mg signal for the clean MgO(100) surface taken at the beginning of each experiment). The resulting normalized Ni LEIS signal in

Figure 4.1a gives the fraction of surface covered and shadowed by Ni nanoparticles, and the normalized Mg signal gives the fraction of the MgO surface which is not masked by Ni.

The average thickness of the Ni islands on the surface is easily calculated from these data in Figure 4.1a, by simply converting the total number of Ni atoms per m^2 to the total volume of Ni per m^2, assuming the adsorbed Ni has the same density as bulk Ni(solid). The average island thickness (t) is thus calculated as: $t = \theta \times n_{ML} \times M_{Ni} /(N_A \times \rho_{Ni} \times A)$, where θ is the total Ni coverage (in ML), n_{ML} is the Ni atom number density that defines one monolayer (1.12×10^{19} atoms/m^2), M_{Ni} is the molar mass of Ni (58.69 g/mol), N_A is Avogadro's number, ρ_{Ni} is the density of Ni (8.9 g/cm^2), and A is the fraction of covered surface area that was obtained from the LEIS data.

The normalized Ni and Mg LEIS signals in Figure 4.1 are compared with three typical growth models. The black dashed lines correspond to the normalized LEIS signals that would be expected if Ni grew in a layer-by-layer mode with the layer packing density equal to the O number density on MgO(100). It does not fit well with the data taken at 300 K. The red lines correspond to a 3-dimensional (3D) growth mode assuming the Ni grows as 3D particles at 300 K with the shape of hemispherical caps, as suggested by STM studies of this same system.[144] In modelling this growth mode, we assume that the Ni particles all have the same hemispherical shape and particle size at any given coverage, and that the particle number density does not change with metal coverage. It is common for particles to grow with a constant number density after the first few percent of a ML,[87, 155, 156] as proven in classical nucleation and growth kinetics, where this is referred to as the "saturation number density" which is reached after a brief nucleation stage.[87] As shown previously,[55] when the particles grow as hemispherical caps, the total surface area masked by the particles in LEIS is 1.207 times the metal/support interfacial area since the energy analyzer detects ions normal to the sample and the He^+ ion beam is incident 45° from the surface normal.

Within these assumptions, the particle number density is the only fitting parameter in modelling the LEIS signals versus coverage.[55] The best fit to the data taken at 300 K gives a particle number density of 5.0×10^{16} particles / m^2, as shown by the red solid lines in Figure 4.1. Note that this fitting curve is only valid up to the coverage where ~35% of the surface is covered by the particles and their shadow), since particles might overlap with each other at higher coverage. Up to this coverage, we can divide the Ni coverage (in atoms per m^2) by this particle number density (in particles per m^2) to estimate the average number of Ni atoms per particle. Assuming these particles have the same density as bulk Ni(solid) allows us to convert this number per particle to the volume per particle and, from this volume, to the hemispherical-cap diameter at each coverage. This average Ni particle diameter at 300 K is plotted versus coverage in Figure 4.1b. For a nanoparticle with a shape of hemispherical cap, its diameter equals 3 times its average thickness, which is easy to see in Figure 4.1b.

At 100 K, the normalized Ni signal increases rapidly with coverage in Figure 4.1a to ~100%, and the normalized Mg signal decreases to near 0% by 2 ML. The average Ni thickness in Figure 4.1b stays nearly constant at ~0.17 nm for the first ~1.4 ML, and then increases linearly with coverage. As shown by the blue solid line, this is just what would be expected if the Ni grows in a layer-by-layer fashion, with a layer thickness of 0.17 nm and a full-layer packing density that is ~40% higher than the ML definition here (i.e., $1.4 \times 1.12 \times 10^{19}$ atoms per $m^2 = 1.6 \times 10^{19}$ atoms per m^2). This packing density is not unexpected, since it is nearly midway between the closest-packed Ni density in the (111) plane of Ni and the packing density expected if one Ni atom adsorbed on every O site of MgO(100) (i.e., 26% less than the Ni(111) packing density and 40% larger than the ML packing density). Also, this packing density corresponds to a layer completion coverage that is 40% larger than the ML packing density, totally consistent with the observed change in slope of the thickness data in Figure 4.1b at ~1.4 ML. We note that the LEIS data are not sensitive to the Ni film's morphology after completion of this first layer. (That is, the film could get rough at higher coverages, for example forming 3D particles on top of this first, flat layer.)

The LEIS data at 100 K show that the first Ni layer grows as a 2D film until it covers nearly 100 % of the surface at 1.4 ML, with a constant thickness on 0.17 nm above 0.4 ML. As we show next, the heat of Ni adsorption increases by ~200 kJ/mol in this first layer, and by ~50 kJ/mol in this 0.4-1.4 ML coverage range where the Ni thickness is constant at 0.17 nm. We will attribute this to the formation first of isolated Ni adatoms, followed by nucleation of clusters which then grow into tiny 2D islands (of 0.17 nm thickness). These 2D islands then grow in size until they cover nearly 100 % of the surface.

4.2.2 *Differential Heat of Adsorption and Sticking Probability*

The differential heat of adsorption of Ni gas atoms on MgO(100) at 300 and 100 K are presented in Figure 4.2a as a function of Ni coverage. At 300 K, the heat of adsorption starts initially from 276 kJ/mol, and it increases rapidly reaching 335 kJ/mol by 0.4 ML, which is still 95 kJ/mol below the sublimation enthalpy of bulk Ni of 430 kJ/mol.[157] The heat slowly increases thereafter and levels off at the sublimation enthalpy of bulk Ni by 9 ML. At 100 K, the heat of adsorption is initially 128 kJ/mol lower than that at 300 K, and it remains noticeably lower until about 6 ML. From 1.5 ML to 5 ML, the heat at 300 and 100 K only differ by ~10 kJ/mol. The lower initial heat and slower heat increase with coverage at 100 K in Figure 4.2a (compared to 300 K) are attributed to the fact that Ni grows as 2D islands up to ~1.4 ML. The limited diffusion of Ni adatoms at 100 K prevents them from forming the more stable 3D particles that can grow at

300 K, but instead grow as 2D islands until they cover nearly 100% of the surface, and then thicken into a 3D film.

Using the average particle diameter versus coverage at 300 K from Figure 4.1b allows us to replot the heat data at 300 K in Figure 4.2a as heat versus average particle diameter, as shown in Figure 4.3. The increase in heat with coverage and particle size seen here at 300 K is common for late transition metal on catalyst support-type oxides,[51, 52, 88, 100] and has been reported for Ni on $CeO_{2-x}(111)$.[158] It is always associated with the corresponding increase in particle size with coverage, and the associated increase in the number of metal-metal bonds that form upon metal atom adsorption, and the fact that downward bonds of the metal atoms to the oxide below (which form when the particles are tiny) is weaker than the downward metal-metal bonds which form when metal atoms add on top of existing metal particles.[156] That same explanation is valid here, as further quantified below.

Figure 4.2b shows the sticking probability of Ni on the MgO(100) thin film as a function of Ni coverage at 300 and 100 K. The result at 300 K shows that the sticking probability starts low (0.79). It then rises asymptotically with increasing Ni coverage to 1.00 above 8 ML. At 100 K, the initial sticking probability is 0.82 for the first pulse of Ni dosage, and it rises rapidly to 0.97 by 0.5 ML. It then increases slowly to 1.00 by 3 ML. This significant difference in sticking probability between the growth at 300 and 100 K can be explained based on their different growth morphology. At 300 K, the Ni atoms grow as 3D nanoparticles and they cover the MgO surface area slowly, as suggested by the LEIS results. However, at 100 K the Ni atoms grow following a layer-by-layer model, where the surface area is covered quickly as the coverage of Ni grows. For the same Ni coverage, the incident Ni atoms are more likely to be captured at the edges of Ni islands as they diffuse across the surface before they desorb when a higher fraction of the surface area is covered by Ni. This explains why the sticking probability increases much faster with coverage at 100 K compared to 300 K. In Figure 4.4, the sticking probabilities are replotted versus the fraction of surface area covered by Ni (as measured by LEIS). The Ni coverage was converted to the fraction of covered surface area using the model fits to the LEIS results shown in Figure 4.1. The large difference in sticking probability between 300 and 100 K in Figure 4.2b is much less significant when plotted as in Figure 4.4, which supports that the different fraction of surface area covered by Ni is the main reason for the large temperature effect in Figure 4.2b. For the same fraction of covered surface area, the sticking probability at 300 K is still slightly lower than that at 100 K. This is attributed to the increasing desorption rate of the diffusing Ni adatoms with increasing temperature (or more properly, the increase in desorption rate relative to diffusion rate, since diffusion generally has a much lower activation energy than desorption).

4.2.3 *Charge Transfer from Ni to MgO(100) during Deposition*

The Ni $2p_{3/2}$ peak and the Mg 2p peak in XPS were monitored during Ni deposition. Their binding energies (BEs) are plotted versus the Ni coverage in Figure 4.5. At 300 K, the Ni $2p_{3/2}$ BE after the first dose with 0.16 ML of Ni atoms is 853.2 eV. As the Ni coverage grows, the Ni $2p_{3/2}$ BE gradually decreases. When 10-nm-thick Ni was deposited onto the sample, the Ni $2p_{3/2}$ peak BE was 851.8 eV, which is consistent with the BE reported for metallic Ni.[103] For comparison, the Mg 2p BE does not change much with the Ni coverage. It stays stable at 50.2 eV and a variation smaller than 0.03 eV. At 100 K, the Ni $2p_{3/2}$ BE after 10-nm-thick Ni deposition is 851.9 eV. The Mg 2p BE stays constant at ~50.0 eV as the Ni coverage increases. These results are identical to what was observed at 300 K. However, the binding energy of the Ni $2p_{3/2}$ peak measured after the first dose with 0.21 ML Ni atoms is 854.1 eV. This corresponds to a shift of 2.2 eV of the Ni $2p_{3/2}$

peak to higher binding energy with respect to the position of metallic Ni, which indicates the formation of Ni^{2+} cations at the lowest coverage studies.[103] As suggested by the LEIS results, at 100 K Ni follows a layer-by-layer growth model on MgO(100). This large BE shift at low coverages suggest that the Ni deposited on MgO(100) exists mainly as small clusters or even single atoms. Combining with the XPS Ni $2p_{3/2}$ peak binding energies shown above, it shows that there is a significant charge transfer from Ni atoms to the MgO(100) support which oxidizes Ni atoms to Ni^{2+} cations when Ni exists as single atoms or few-atom clusters. For the same coverage but at 300 K, Ni forms nanoparticles with bigger size compared to that at 100 K, and the extent of charge transfer from Ni to the MgO support is much less than at 100 K when the Ni clusters are strictly 2D and much smaller in number of Ni atoms.

4.3 UNIQUE BEHAVIOR OF NI ADSORPTION ON MGO(100) AT 100 K

At 100 K, the Ni adsorption on MgO(100) shows a unique behavior. In the early stage of its growth, Ni grows following a layer-by-layer model. To our knowledge, this was not observed for any late transition metal on oxide system studied previously. It is frequently observed in metal film growth that the first layer nearly completes before the second layer starts to fill, but that usually happens because the metal atoms bind more strongly to the underlying material than to themselves. For example, that often happens when late transition metals are deposited onto the surfaces of earlier transition metals.[115] The situation for Ni/MgO here is quite different, since the heat data (and the tendency to form 3D particles at 300 K) show clearly that Ni bonds more weakly to MgO(100) than to Ni(solid). Nevertheless, 2D growth can continue throughout most of the first layer due to kinetics if the most stable site for a new Ni monolayer is not on top of an existing 2D island but instead at the edge of such islands. This could easily occur if the difference in downward bond energy of Ni to the Ni layer below versus Ni to MgO(100) below is more than compensated by the extra lateral bonding that this Ni monomer has to its 2 or 3 nearest-neighbor Ni atoms when it sits at the edge of a 2D Ni island. A similar situation has been reported previously for Cu on the O-terminated ZnO(000-1) surface.[159]

The question arises: What is the structure of this first Ni layer grown at 100 K? As noted above, this layer is 0.17 nm thick and has a full-layer packing density that is nearly midway between the closest-packed Ni density in the (111) plane of Ni and the packing density expected if one Ni atom adsorbed on every O site of MgO(100). In a previous paper, DFT calculation shows the optimized structure of the first two monolayers of Ni grown on MgO(100), where the first layer of Ni atoms sit on the O atoms with small displacements, and the second layer of Ni atoms align with the Mg atoms also with small displacements.[37] This bilayer structure has a coverage of 2.00 ML, since we define 1 ML as the number density of O atoms on MgO(100) and the Mg atoms have the same number density as O on MgO(100). Attributing the first Ni layer to this 2.0 ML bilayer structure is inconsistent with the break in slope of the LEIS first-layer thickness at ~1.4 ML. We cannot speculate further on its structure. We only know that its packing density is 1.6×10^{19} atoms per m^2, corresponding to an effective thickness of 0.17 nm assuming it has the same 3D density as normal fcc Ni(solid).

In general, the average adsorption energies of metals on oxide surfaces in the first monolayer have positive correlation with the metals' sublimation enthalpies, because the sublimation enthalpies hold the major contribution to the energies for forming metal nanoparticles from gaseous metal atoms.[156] However, Ni has an extreme low initial heat of adsorption of 148 kJ/mol on MgO(100) at 100 K, but its sublimation enthalpy is high (430 kJ/mol). For comparison, Au has a sublimation enthalpy of 363 kJ/mol, and its initial heat of adsorption is 217 kJ/mol on

MgO(100) at 100 K.[52] We attribute this low heat of adsorption at low coverage to the unique growth morphology of Ni on MgO(100) at 100 K. Using DFT calculations, people showed that Ni atoms bind O much stronger than Mg on MgO(100) surface.[152, 154, 160] Combining with the LEIS experiments, we suggest that Ni atoms adsorb on O atoms first at low coverage at 100 K. Since the diffusion length of Ni adatoms is limited at low temperature as mentioned above, a big fraction of Ni at low coverage should exist as isolated single atoms sitting on the O atoms with nearly no Ni-Ni bonding interactions. Even if the Ni atoms sit next to each other, the interaction should still be weak, since the distance between neighbor O atoms on MgO(100) (2.98 Å) is 0.5 Å longer than the Ni-Ni distance in bulk Ni (2.49 Å). Thus, the initial heat of adsorption at 100 K, 148 kJ/mol, represents the binding strength between Ni single atoms and lattice O on MgO(100). This is in agreement with previous DFT calculation that gives a binding energy of 1.453 eV (140 kJ/mol).[152] At 300 K, Ni grows as 3D nanoparticles. Even for the first pulse of deposition, each Ni nanoparticles contains 7 Ni atoms on average. Thus, the binding energy between the Ni atoms makes the initial heat of adsorption at 300 K much higher than that at 100 K.

The heat of Ni adsorption at 100 K increases very strongly (by ~200 kJ/mol) with coverage in the first layer (i.e., from ~150 kJ/mol at 0.03 ML to ~350 kJ/mol at 1.4 ML). We attribute this to an increase in the number of Ni-Ni bonds as the size of 2D Ni single-layer islands grows. The heat of sublimation of bulk Ni(solid) is 430 kJ/mol. In a pairwise bond-additivity model, this corresponds to six nearest-neighbor Ni-Ni bond energies, each at 430/6 = 71.7 kJ/mol. Since a Ni atom in the middle of a 2D island is expected to have ~6 nearest neighbors, with each sharing one Ni-Ni bond, each Ni atom in a huge 2D Ni island should have 3×71.7 = 215 kJ/mol, very close to the increase of ~200 kJ/mol observed in this first quasi-close-packed Ni layer.

4.4 CONCLUSIONS

The LEIS experiments showed that Ni grows as 3D nanoparticles on MgO(100) at 300 K with a particle number density of 5.0×10^{16} particles/m^2. At 100 K, Ni forms Ni single atoms on lattice O sites of MgO(100) at low coverage, then forms tiny 2D Ni islands with an average thickness of 0.17 nm (40% thicker than a Ni single layer with a packing density equals the number density of O on MgO(100)). The Ni atoms follow this 2D growth mode until the surface is covered completely at 1.4 ML, and the incoming Ni atoms then grow on this complete Ni overlayer. Since the Ni atoms cover the surface much faster at 100 K, the sticking probability at 100 K remains higher than that at 300 K until the sticking probability at 300 K also reaches unity by 8 ML. At 300 K, the heat of Ni vapor adsorption to make Ni particles containing 7 atoms on MgO(100) is 276 kJ/mol, and it increases rapidly reaching 335 kJ/mol by 0.4 ML. The heat slowly increases thereafter and levels off at the sublimation enthalpy of bulk Ni by 9 ML. At 100 K, the initial heat of adsorption is 128 kJ/mol lower than that at 300 K, which directly represents the binding energy between Ni single atoms and O on MgO(100). The binding energy of Ni $2p_{3/2}$ XPS peak for 0.16 ML Ni on MgO at 300 K is 1.4 eV higher than that for bulk Ni(solid). As the coverage increases, the Ni $2p_{3/2}$ peak binding energy decreases until the binding energy for bulk Ni is reached at high coverage. At 100 K, 0.21 ML of Ni on MgO(100) has its $2p_{3/2}$ XPS peak's binding energy higher than that for bulk Ni by 2.2 eV, which suggests electron transfer from Ni to MgO substrate and the formation of Ni^{2+}.

4.5 FIGURES

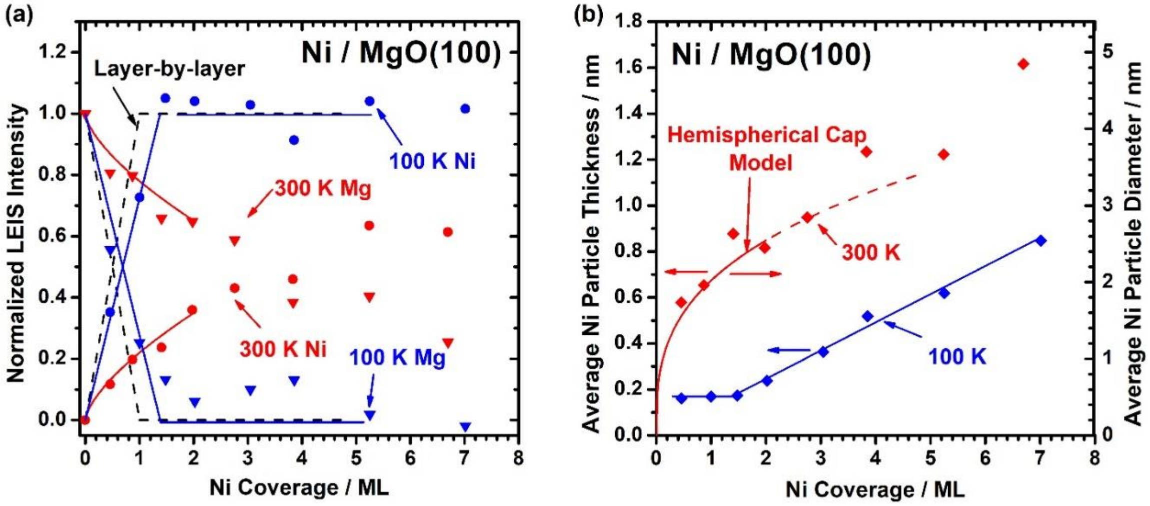

Figure 4.1 (a) Integrated Ni (circle) and Mg (triangle) LEIS signal intensities (normalized to a thick, multilayer Ni film and clean MgO(100), respectively) as a function of Ni coverage after Ni deposition onto MgO(100) at 300 K (red) and 100 K (blue). The black dashed lines correspond to the normalized LEIS signal that would be observed if Ni grew in a layer-by-layer fashion, while the red solid lines fit to the low-coverage data at 300 K correspond to Ni growing as hemispherical caps with a fixed particle density of 5.0×10^{16}/m^2. This model is only reasonable up to ~35% of the surface is covered, since particles may start to overlap with each other at higher coverage, so we only show the fitting curve up to 2 ML. The blue solid lines show the fit of the low-coverage data at 100 K to a layer-by-layer model where the layer packing density is 1.6×10^{19} atom / m^2. (b) Average Ni particle thickness versus Ni coverage calculated from the Ni LEIS data points of panel (a). The blue curve here shows the fit of the 100 K data to the layer-by-layer model described in the text, where the layer packing density is 1.6×10^{19} atom / m^2, corresponding to a layer thickness of 0.17 nm. The red curve corresponds to the hemispherical cap model with a particle number density of 5.0×10^{16} /m^2, which gave the best fit to the data obtained at 300 K up to 2 ML in (a). The right Y-axis shows the average diameter of hemispherical caps that corresponds to this thickness for the Ni nanoparticles grown at 300 K.

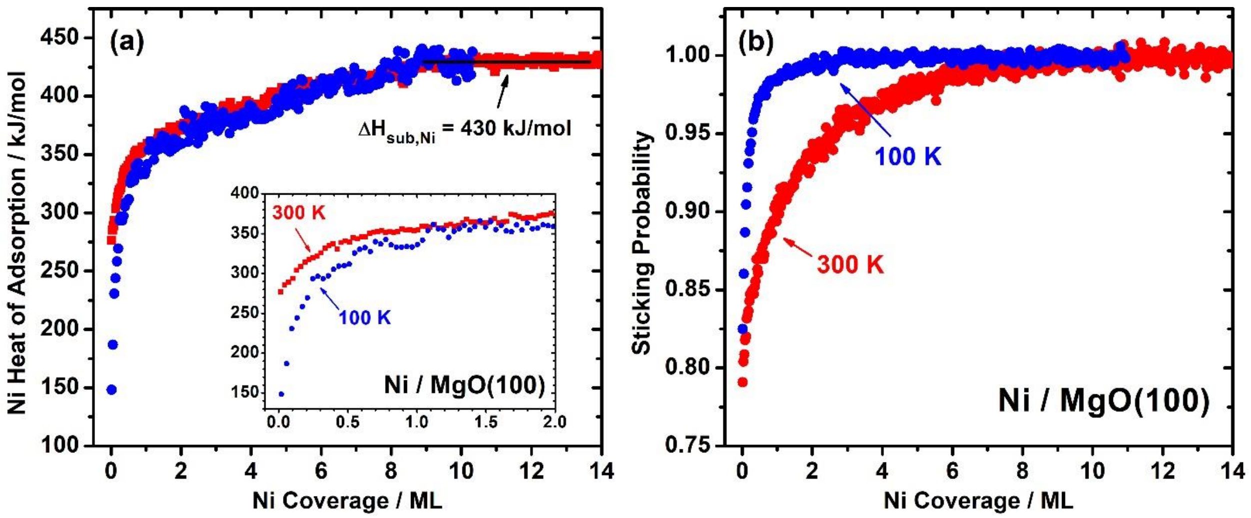

Figure 4.2 (a) Differential heat of Ni atom adsorption on MgO(100) as a function of Ni coverage at 300 K (red) and 100 K (blue). The inset shows an enlargement of the heat in the low coverage range. (b) Sticking probability of Ni gas atoms onto MgO(100) as a function of Ni coverage at 300 K (red) and 100 K (blue).

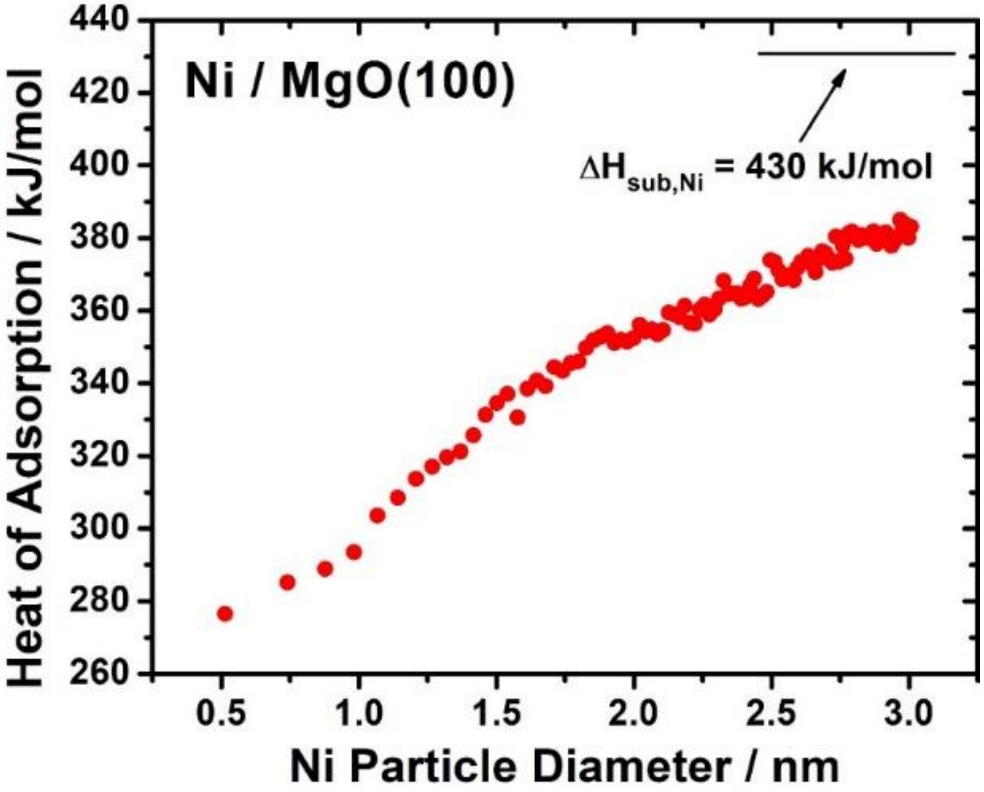

Figure 4.3 Differential heat of Ni adsorption on MgO(100) at 300 K as a function of the average effective Ni particle (hemispherical) diameter to which Ni atoms add.

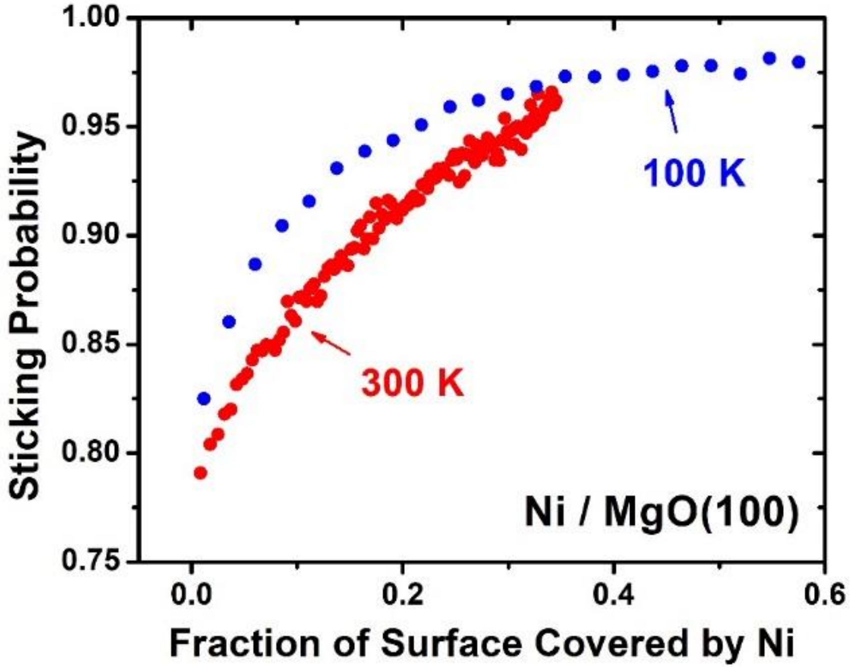

Figure 4.4 The sticking probability of Ni atoms onto MgO(100) at 300 K (red) and 100 K (blue) plotted versus the fraction of MgO(100) surface that is covered with Ni. For 300 K, the fraction of Ni-covered surface at each coverage is calculated using the particle density and size given by the best-fit curve to the LEIS signal shown in Figure 4.2. For 100 K, the fraction of Ni-covered surface at each coverage is calculated assuming the Ni atoms follow the layer-by-layer growth mode, shown to fit well the LEIS data in Figure 4.2.

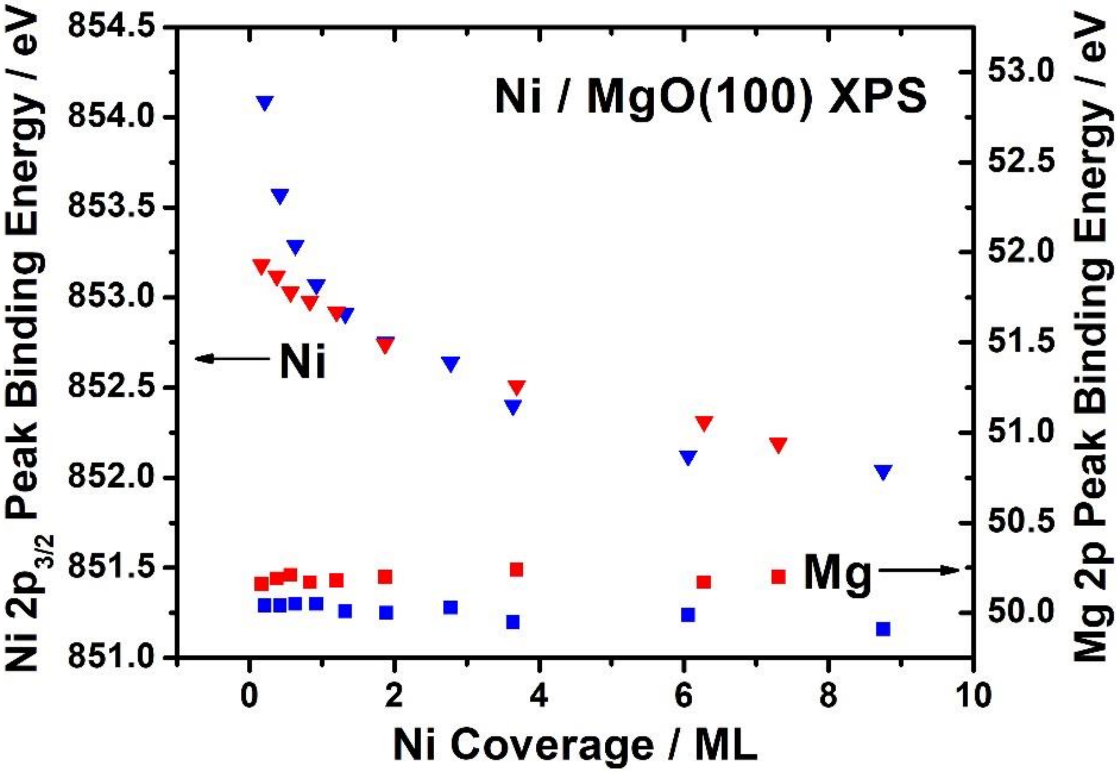

Figure 4.5 Variation of the Ni $2p_{3/2}$ (triangles) and the Mg 2p (squares) XPS binding energies as a function of Ni coverage on MgO(100) at 300 K (red) and 100 K (blue).

Chapter 5. Chemical Potential of Ni Atoms in Supported Nanoparticles

This chapter contains unpublished results.

Chapter Abstract

The chemical potential of metal atoms in supported nanoparticles with diameter D relative to the bulk metal, $\mu(D)-\mu(\infty)$, can be described with an equation $\left(3\gamma_M - E_{adh}\right)\left(1+D_0/D\right)\left(2V_M/D\right)$. This equation quantitatively shows that when the particle diameter D decrease, the chemical potential of metal atoms in the particle increases, and when the adhesion energy of the metal to the support material increases, the chemical potential of metal atoms in the particle decreases. The adhesion energy of the metal to the support material is the most important parameter in this equation. Applying this equation to the recent single crystal adsorption calorimetry (SCAC) results of Ni on MgO(100) and $CeO_{1.95}$(111), the adhesion energies of Ni to MgO(100) and $CeO_{1.95}$(111) are calculated by fitting the plots of the chemical potential of Ni versus the particle diameter. The calculated adhesion energy of Ni is 3.05 J/m^2 to MgO(100) and 4.39 J/m^2 to $CeO_{1.95}$(111). The adhesion energies of Ni to MgO(100) and $CeO_{1.95}$(111) agree with a previous trend that the adhesion energies of metals to a given oxide support material correlates with their oxophilicity. Plotting the adhesion energies of metals to MgO(100) and $CeO_{1.95}$(111) versus $\left[\left(\Delta H_{\mathrm{sub,M}} - \Delta H_{\mathrm{f,MO_x}}\right)/N_A\right]/\Omega_M{}^{2/3}$, ($\Delta H_{\mathrm{sub,M}}$ is the sublimation enthalpy of the metal, $\Delta H_{\mathrm{f,MO_x}}$ is the formation enthalpy of the metal's most stable oxide, N_A is Avogadro's number, Ω_M is the volume per metal atom) the data points are well fit with two straight lines with the same slope. The addition of the Ni data validates the predictive power of this trend in a wider range.

5.1 INTRODUCTION

In heterogeneous catalysis, metal nanoparticles are finely dispersed on support materials with high surface areas. Noble metals are usually inert as bulk metals. However, when these metals are downsized to nanoparticles that is smaller than 7 nm in diameter, they become highly active for catalyzing reactions. [118, 161-170] For example, bulk Au has inert chemical properties, but nanosized Au particles can catalyze CO oxidation reaction even at a temperature far below 0°C. [171] It has been shown that the size of the metal nanoparticles is one of the key parameters that determines the performance of the heterogeneous catalysts. [13, 172] In most cases, metal nanoparticles are more active than bulk metals, and the activities of the metal nanoparticles for catalyzing reactions usually increase with decreasing particle size. As the particle size decreases, more metal atoms are exposed as coordinatively-unsaturated atoms, and such atoms are often recognized as active sites in heterogeneous catalysis. [173-175] Also, the variety of such active sites is narrowed for smaller metal nanoparticles, which increases the selectivity of the catalyzed reactions. [176, 177] Although the basic principle of the size effect in heterogeneous catalysis seems obvious, it is worth exploring how the performance of the catalysts correlates with the size of the nanoparticles quantitively.

The chemical potential of the metal atoms in the metal nanoparticles provides a helpful descriptor for the size effect in heterogeneous catalysis.[36] In many examples, the binding energies of small molecules to the metal vary with the chemical potential of the metal atoms.[15, 35, 73] The small molecules bind strongly to the metal atoms with structures of high chemical potential, which are usually tiny nanoparticles. For metal atoms with structures of low chemical potential, which are usually large particles or bulk metal, the small molecules bind weakly. A quantitative interpretation of the correlation between the binding energies of small molecules and the chemical potential of the metal atoms is given recently by Mpourmpakis and coworkers.[178] They show that the DFT-calculated binding energies of small molecules and molecular fragments to the metal atoms correlates linearly with the DFT-calculated local cohesive energies of the metal atoms. The local cohesive energy is defined as the energy required to move the metal atom participating directly in the binding interaction away from the system. It has the same magnitude as the heat of adsorption of such metal atoms on the nanoparticles. Since the chemical potential of the metal atoms relative to the bulk metal can be calculated as the difference between the sublimation enthalpy of the bulk metal and the heat of adsorption of the metal atom,[15] the local cohesive energies of the metal atoms equal the sublimation enthalpy of the bulk metal minus the chemical potential (relative to the bulk metal) of the metal atoms. Thus, the binding energies of the small molecules to the metal atoms correlate linearly with the chemical potential of the metal atoms. The chemical potential of the metal atoms also affects the rate of sintering. For Ostwald ripening, the rate equation of the sintering kinetics includes a factor of the chemical potential of the metal atoms in nanoparticles as the driving force of sintering.[116, 117] In other kinetic models for sintering, the chemical potential of metal atoms also appears directly in the rate equations.[117]

The chemical potential of the metal atoms in nanoparticles is a powerful descriptor for catalytic performance, whether with regard to the catalyst's chemical reactivity or its long-term resistance to deactivation by sintering.[36] Thus, a predictive model for estimating the chemical potential of metal atoms in nanoparticles with different sizes can enhance the understanding for the size effect in heterogeneous catalysis. In this chapter an equation for predicting the chemical potential of the metal atoms in nanoparticles with given diameters is introduced. The key parameter in this predictive equation is the adhesion energies between the metals and the support materials. This equation can also be used in an opposite way to extract the adhesion energies for Ni/$CeO_{1.95}$(111) and Ni/MgO(100) systems. The adhesion energies between the metals and the oxide surfaces were calculated using the integrated heat of adsorption measured in SCAC experiments.[179] However, this method does not work for Ni because Ni forms metastable phases on oxide surfaces to reduce lattice mismatch.[37] Instead, the plots of the Ni chemical potential versus the diameter of the Ni nanoparticles are fitted with the predictive equation for metal chemical potential, and the adhesion energies are obtained as the fitting parameters. The adhesion energies of Ni on $CeO_{1.95}(111)$ an MgO(100) fit well with a trend in adhesion energies of metal nanoparticles supported on oxide surfaces, where the adhesion energies of the metals on a given oxide surfaces correlates linearly with the metals' oxophilicity.

5.2 CHEMICAL POTENTIAL VERSUS PARTICLE SIZE

The chemical potential of the metal atoms in nanoparticles correlates with the particle size. A simple example is the Gibbs-Thomson effect which states that small particles with high curvatures exhibit higher vapor pressure compared to bulk materials.[180] This phenomenon is explained that the chemical potential of the atoms in a particle with a small size and a high curvature is higher than that in the bulk. For metal particles, a commonly used approach for estimating the size dependence of particle energy has been to use the Gibbs-Thomson relation which states that the chemical potential (partial molar free energy) of a metal atom in a particle of radius R, $\mu(R)$, differs from that in the bulk metal [$\mu(\infty)$] by[116]

$$\mu(R) - \mu(\infty) = 2\gamma_M V_M / R \tag{5.1}$$

where γ_M is the surface free energy of the metal, and V_M is the bulk metal's molar volume. Eq 5.1 describes the situation of a free-standing spherical metal particles. It shows that for such metal particles, the positive surface energy of the metal makes the metal atoms in the particles have higher chemical potential than that in the bulk metal. As the radius of the particle decreases, the chemical potential of the metal atoms in the particles increases.

The Gibbs-Thomson relation explains that metal atoms are more active in nanoparticles since they have higher chemical potential compared to the bulk metals. However, the metal nanoparticles used as catalysts are dispersed on the support materials. The interaction between the metal nanoparticles and the support materials can stabilize the metal nanoparticles, but this support effect is missing in the Gibbs-Thomson relation. A new equation was derived to address the support effect by including the adhesion energies between the metals and the support materials. This equation is[36]

$$\mu(D)-\mu(\infty)=\left(3\gamma_M-E_{adh}\right)\left(1+D_0/D\right)\left(2V_M/D\right). \tag{5.2}$$

$\mu(D)$ is the chemical potential of a metal atom in a particle with diameter D. E_{adh} is the adhesion energy between the metal and the support material, with a unit of J/m^2. The factor $(1+D_0/D)$ is an empirical correction that models the increase in γ_M and E_{adh} (above their bulk values for the large diameter limit) with decreasing particle size. With D_0 = 1.5 nm, this predictive equation has been shown to fit the chemical potential versus particle diameter plot well for five metal-on-oxide systems studied before with SCAC: Cu/CeO$_{1.95}$(111), Ag/CeO$_{1.95}$(111), Au/CeO$_{1.95}$(111), Ag/Fe$_3$O$_4$(111), and Ag/MgO(100).[36] Thus, D_0 will still be 1.5 nm in the following sections. Eq (5.2) gives a simple but practical explanation for the size effect and the support effect of supported metal nanoparticles. As the particle diameter decreases, the chemical potential of metal atoms increases, which means the metal atoms in smaller particles are more reactive. For particles with the same size, the chemical potential of metal atoms decreases with increasing adhesion energy of the metal to the support material. It suggests that the metal atoms are less active when the support has a strong interaction with the metal nanoparticles, while they are more stable against sintering.

5.3 EXTRACT THE ADHESION ENERGY FROM THE PLOT OF CHEMICAL POTENTIAL VERSUS PARTICLE DIAMETER

In much of our previous work,[51, 52, 88, 179, 181-183] the adhesion energies of metal nanoparticles on the support materials were calculated with a thermodynamic cycle where the formation of large supported metal nanoparticles from metal vapor is divided into two steps.[179] In the first step, the metal atoms in the gas phase form free metal nanoparticles in vacuum with the same size and shape as they are on the support material. The energy change of this step can be calculated with the sublimation enthalpy and the surface free energy of the bulk metal (times the surface area of the free-standing particles). In the second step, the metal nanoparticles formed in the first step are attached to the support material. The energy change in this step equals the product of the adhesion energy (in a unit of $\mathrm{J/m^2}$) and the total interfacial area between the metal nanoparticles and the support material. The overall energy change of these two steps, which is the formation energy of the supported metal nanoparticles from metal atoms in the gas phase, equals the integral heat of adsorption, which can be obtained by integrating the differential heat of adsorption measured in the SCAC experiments. This thermodynamic cycle shows that the adhesion energy E_{adh} can be calculated using:[179]

$$n \times \sum_{n} \Delta H_{\mathrm{adsorption}} = -n \times \Delta H_{\mathrm{sublimation}} + A \times \left[\left(1 + f\right) \gamma_M - E_{\mathrm{adh}} \right] \tag{5.3}$$

where γ_M is the surface free energy of the bulk metal, f is the surface roughness factor of the nanoparticle (for a hemispherical cap $f = 2$), $\sum_{n} \Delta H_{\mathrm{adsorption}}$ is the integral (average) molar heat of adsorption up to the coverage of interest, n is the number of metal atoms in moles at that coverage, A is the interfacial area between the metal nanoparticles and the support material at that coverage obtained from the LEIS data, and $\Delta H_{\text{sublimation}}$ is the sublimation enthalpy of the bulk metal. Eq (5.3) has been used to calculate the adhesion energies for several metal/oxide systems.[51, 52, 88, 182, 183] However, using Eq (5.3) to calculate the adhesion energy between Ni and MgO(100) with the LEIS growth mode results and the measured differential heat of adsorption up to 2.0 ML (corresponding to Ni nanoparticles with diameter of 2.6 nm) at 300 K gives $E_{adh} = -4.47$ J/m^2. This negative adhesion energy is physically impossible, and it comes from the failure of one assumption for Eq (5.3). In the first step of the designed thermodynamic cycle above, the sublimation enthalpy of bulk metal is used to calculate the formation energy of metal nanoparticles in vacuum. A built-in assumption for this step is that the metal nanoparticles are in the most stable phase of the bulk metal where the sublimation enthalpy reported in the literature was measured. However, it was reported that when Ni was deposited onto MgO(100) at 120 °C, Ni forms an unnatural hexagonal close-packed (hcp) phase with an unusually large crystallographic *c/a* ratio (~6% larger than ideal hcp) in the early stage of the growth with an average particle size of ~2.5 nm in diameter,[37] while the sublimation enthalpy of Ni (430 kJ/mol) is reported for the normal (most stable) face-centered cubic (fcc) phase of bulk Ni(solid).[157] Thus, the sublimation enthalpy of Ni in this metastable hcp phase is expected to be considerably smaller than the literature value for the bullk sublimation enthalpy of Ni (430 kJ/mol), as confirmed below. If this metastable phase is made in the experiments of Figure 4.2 at 300 K for coverage below 2 ML as expected, then using 430 kJ/mol for $\Delta H_{\text{sublimation}}$ in Eq (5.3) will not provide a good estimation of the adhesion energy in this Ni/MgO(100) system. We show below a much better way to estimate this.

The chemical potential of metal atoms in supported nanoparticles of a given average diameter, when defined relative to the bulk metal reference set to zero chemical potential, can be calculated by subtracting the differential heat of Ni adsorption measured for this particle diameter (shown in Figure 4.3 here) from the sublimation enthalpy of the bulk metal (430 kJ/mol for Ni).[15] The resulting chemical potential of Ni atoms in the Ni nanoparticles is plotted versus average particle diameter in Figure 5.1.

We have previously shown that the chemical potential of late transition metals in supported hemispherical nanoparticles of diameter D relative to that for the bulk metal (large particle size limit) can be well approximated by the Eq (5.2). Whenever we have used Eq (5.2) in the past, the metal atoms in the nanoparticles formed the same phase as the most stable phase of the bulk metal, which is used as the zero reference for the chemical potential. However, for this Ni/MgO(100) system, the metal nanoparticles in the size range of Figure 5.1 are forming instead a metastable phase, according to the literature mentioned above.[37] To compensate for the energy difference between the most stable (fcc) phase of bulk Ni and the metastable phase of Ni nanoparticles, we add an extra term $\left(\Delta H_{\text{sublimation}} - \Delta H^{*}_{\text{sublimation}}\right)$ to Eq (5.2), so that:

$$\mu(D) = \left[\left(3\gamma_{\text{v/m}} - E_{\text{adh}}\right)\left(1 + D_0/D\right)\right]\left(2V_{\text{m}}/D\right) + \left(\Delta H_{\text{sublimation}} - \Delta H^{*}_{\text{sublimation}}\right), \qquad (5.4)$$

where $\Delta H^{*}_{\text{sublimation}}$ is the sublimation enthalpy of the metastable phase, and $\Delta H_{\text{sublimation}}$ is the heat of sublimation of the most stable bulk (fcc) phase (430 kJ/mol for Ni). The two remaining variables, E_{adh} and $\Delta H^{*}_{\text{sublimation}}$, are the fitting parameters of interest. Eq (5.4) fits the data points in Figure 5.1 well with the best-fit parameters E_{adh} = 3.05 J/m^2 and $\Delta H^{*}_{\text{sublimation}} = 405$ kJ/mol, except for a few points when the particles are below 1 nm in diameter. Below 1 nm, these particles might assume a different shape or structure than the hemispherical cap assumed in Eq (5.4). Note that the LEIS measurements in Figure 4.1 that were well fit with the hemispherical cap shape were all at larger particle sizes than 1 nm. This shape change might explain this observation in Figure 5.1

that for particles smaller than 1 nm, where the metal atoms are more stable (lower chemical potential) than predicted for hemispherical shape.

There is a large lattice mismatch of -16% between Ni(100) and MgO(100), and the reduction of misfit strain energy is believed to be the driving force that dictates the formation of the metastable hcp phase.[37] The lattice mismatch between Ni(111) and $CeO_{1.95}(111)$ is even bigger (-35%). It is possible that Ni also forms a metastable phase on $CeO_{1.95}(111)$ to reduce lattice mismatch, and Eq (5.3) cannot be used to calculate E_{adh} for Ni on $CeO_{1.95}(111)$. Here we use Eq (5.4) with a minor correction to calculate E_{adh} for Ni on $CeO_{1.95}(111)$.

Eq (5.4) applies to metal nanoparticles with a shape of hemispherical cap. However, STM studies showed that Ni nanoparticles supported on $CeO_{1.95}(111)$ have a shape of flat disk with an aspect ratio (height/diameter) of 0.25.[32] Eq (5.4) is corrected to address this shape difference, and the derivation follows the same approach used previously.[35] The new equation is

$$\mu\left(D\right)=\left(3\gamma_M-E_{adh}\right)\left(1-D_0/D\right)\left(8V_M/3D\right)+\left(\Delta H_{\text{sublimation}}-\Delta H^*_{\text{sublimation}}\right). \tag{5.5}$$

Eq (5.5) is used to fit the data points corresponding to $CeO_{1.95}(111)$ in Figure 3.3, and the result is shown in Figure 5.2. The fitting of Eq (5.5) to the data in Figure 5.2 gives E_{adh} = 4.39 J/m^2 and $\Delta H^*_{sublimation} = 404\ \text{kJ/mol}$. Importantly, this best-fit value for the metastable phase is within 1 kJ/mol of the best-fit value found on MgO(100) (above), which lends credence to our approach here. The data points with diameter below 1 nm show significant deviation from the fitting curve, as explained in the Ni/MgO(100) system. The deviation for the data at 300 K particularly big. The small Ni nanoparticles grow at 300 K nucleate at step edges first, where the Ni atoms have strong bonding with the step edges, and the Ni nanoparticles are stabilized better than that on terrace sites at 100 K. This factor is not addressed in the model of Eq (5.5).

$\Delta H^{*}_{\text{sublimation}}$ provides an estimate of the sublimation enthalpy of the metastable phase of Ni in the nanoparticles, and its value is close for $CeO_{1.95}(111)$ (404 kJ/mol) and MgO(100) (405 kJ/mol). The metastable phase of Ni on MgO(100) is 25 kJ/mol less stable than the fcc phase, and on $CeO_{1.95}(111)$ the difference is 26 kJ/mol. From the last point of the chemical potential plot, as we deposit more Ni onto the oxide surfaces, the Ni nanoparticles will grow bigger and overlap. As seen in Figure 3.2 and Figure 4.2, the heat increases slowly from 2 ML to 8 ML, and the chemical potential decreases. We attribute this slow increase in heat of adsorption to a gradual phase transition from the metastable phase to most stable fcc phase, as suggested by a previous study.[37]

5.4 CORRELATE THE ADHESION ENERGY WITH THE METAL'S OXOPHILICITY

The adhesion energy of Ni is 3.05 J/m^2 on MgO(100) and 4.39 J/m^2 on $CeO_{1.95}(111)$. These adhesion energies are larger than any other metals that we have measured previously. On MgO(100), the adhesion energies of the other metals are 0.3 J/m^2 for Ag,[179] 0.3 J/m^2 for Au,[52] and 1.92 J/m^2 for Cu.[183] On $CeO_{1.95}(111)$, the adhesion energies of the other metals are 2.3 J/m^2 for Ag,[49] 2.53 J/m^2 for Au,[88] and 3.52 J/m^2 for Cu.[51] This was actually predicted by the trend in adhesion energies of metal nanoparticles on oxide surfaces we summarized before. In ref [35] the adhesion energy of metals to a given oxide surface is plotted versus $\left[\left(\Delta H_{\text{sub,M}} - \Delta H_{\text{f,MO}_\text{x}}\right)/N_A\right]/\Omega_M^{2/3}$, where $\left[\left(\Delta H_{\text{sub,M}} - \Delta H_{\text{f,MO}_\text{x}}\right)/N_A\right]/\Omega_M^{2/3}$ is used as a measure of the oxophilicity of the metal's element. Here $\Delta H_{\text{sub,M}}$ is the sublimation enthalpy of metal M, $\Delta H_{\text{f,MO}_\text{x}}$ is the formation enthalpy of the most stable oxide of the metal (per mole of metal atoms), N_A is Avogadro's number, and Ω_M is the volume per atom in the bulk solid metal. $\left[\left(\Delta H_{\text{sub,M}} - \Delta H_{\text{f,MO}_\text{x}}\right)/N_A\right]$ gives the enthalpy change of forming the metal's most stable oxide from one gaseous metal atom and $O_2(g)$, which directly reflects the strength of the chemical bonding between the metal atom and the oxygen atom. This enthalpy change is normalized with the surface area per metal atom, which is approximately $\Omega_M^{2/3}$. $\left[\left(\Delta H_{\mathrm{sub,M}} - \Delta H_{\mathrm{f,MO_x}}\right)/N_A\right]/\Omega_M^{2/3}$ has a unit of J/m^2, which is the same as E_{adh}. The plot shows that the correlation of E_{adh} with $\left[\left(\Delta H_{\mathrm{sub,M}} - \Delta H_{\mathrm{f,MO_x}}\right)/N_A\right]/\Omega_M^{2/3}$ is positive and essentially linear for MgO(100) and $CeO_{1.95}$(111).[35] For MgO(100) and $CeO_{1.95}$(111), the data are fitted well by two straight lines with the same slope (0.147±0.001) but a huge difference in the intercept (~2 J/m^2).[35] This correlation emphasizes that the dominant contribution to the bonding at the metal/oxide interface is from the bonds of the metal atoms to the oxygen anions on the oxide surfaces. Janik and Mallouk's group also showed similar relations where the binding energies for single metal atoms and M_4 metal clusters on niobium oxide and silica correlate linearly with $\left(\Delta H_{\mathrm{sub,M}} - \Delta H_{\mathrm{f,MO_x}}\right)$[184], and the DFT-calculated binding energies of single metal atoms correlate linearly with $\Delta H_{\mathrm{f,MO_x}}$[185].

Among the metal elements whose adhesion energies on MgO(100) and $CeO_{1.95}$(111) have been included in ref [35], Cu has the highest oxophilicity, which is 15.9 J/m^2 by definition as shown above. Now the adhesion energies of Ni can be added to the plot, and the new plot is seen in Figure 5.3. The oxophilicity of Ni is 22.7 J/m^2, and the data points of Ni is located farthest to the right side of the plot. However, the trend adhesion energy still holds for Ni. The trend predicts that Ni/MgO(100) adhesion energy should be 2.53 J/m^2, and the value obtained in experiment is 3.05 J/m^2. The error is -0.52 J/m^2 and the relative error is -17%. For $CeO_{1.95}$(111) the predicted adhesion energy is 4.43 J/m^2. The experimental result is 4.39 J/m^2, with a relative error of only 4%. After including the data of Ni, the effective range of the trend in the adhesion energy is almost doubled.

5.5 CONCLUSION

The chemical potential of metal atoms in nanoparticles are described with Eq (5.2). It shows how the chemical potential of metal atoms increases with the decreasing particle size, and decreases with the increasing metal/oxide adhesion energy. Eq (5.2), with some minor corrections to address the formation of metastable phase of Ni and the flat-disk shape of Ni nanoparticles on $CeO_{1.95}(111)$, is used to calculate the adhesion energies of Ni to MgO(100) and $CeO_{1.95}(111)$ surfaces. Ni atoms form a metastable phase on MgO(100) due to a large lattice mismatch when they grow as nanoparticles with a diameter <2.5 nm. This metastable phase has a sublimation enthalpy 25 kJ/mol lower than that of the stable fcc Ni. The adhesion energy of Ni to MgO(100) is 3.05 J/m^2. Using the same method, the sublimation enthalpy of the metastable Ni phase on $CeO_{1.95}(111)$ is calculated to be 24 kJ/mol lower than that of the stable fcc Ni, which is very close to the number for MgO(100). The calculated adhesion energy of Ni to $CeO_{1.95}(111)$ is 4.39 J/m^2. As predicted by the trend in adhesion energies of metal nanoparticles on oxide surfaces, Ni has higher adhesion energy to MgO(100) and $CeO_{1.95}(111)$ compared to other metals whose adhesion energies have been measured with SCAC. Based on the experimental adhesion energies of different metals to MgO(100) and $CeO_{1.95}(111)$, the adhesion energies of metal correlate linearly with their oxophilicity measured as $\left[\left(\Delta H_{\mathrm{sub,M}} - \Delta H_{\mathrm{f,MO_x}}\right) / N_A\right] / \Omega_M{}^{2/3}$. The adhesion energy of Ni to MgO(100) and $CeO_{1.95}(111)$ obtained recently also fits well in this trend. Since Ni has a much higher oxophilicity than any other metal included in the trend before, the new result of Ni's adhesion energy validates the power of the trend in a wider range, and proves that it has true predictive ability.

5.6 FIGURES

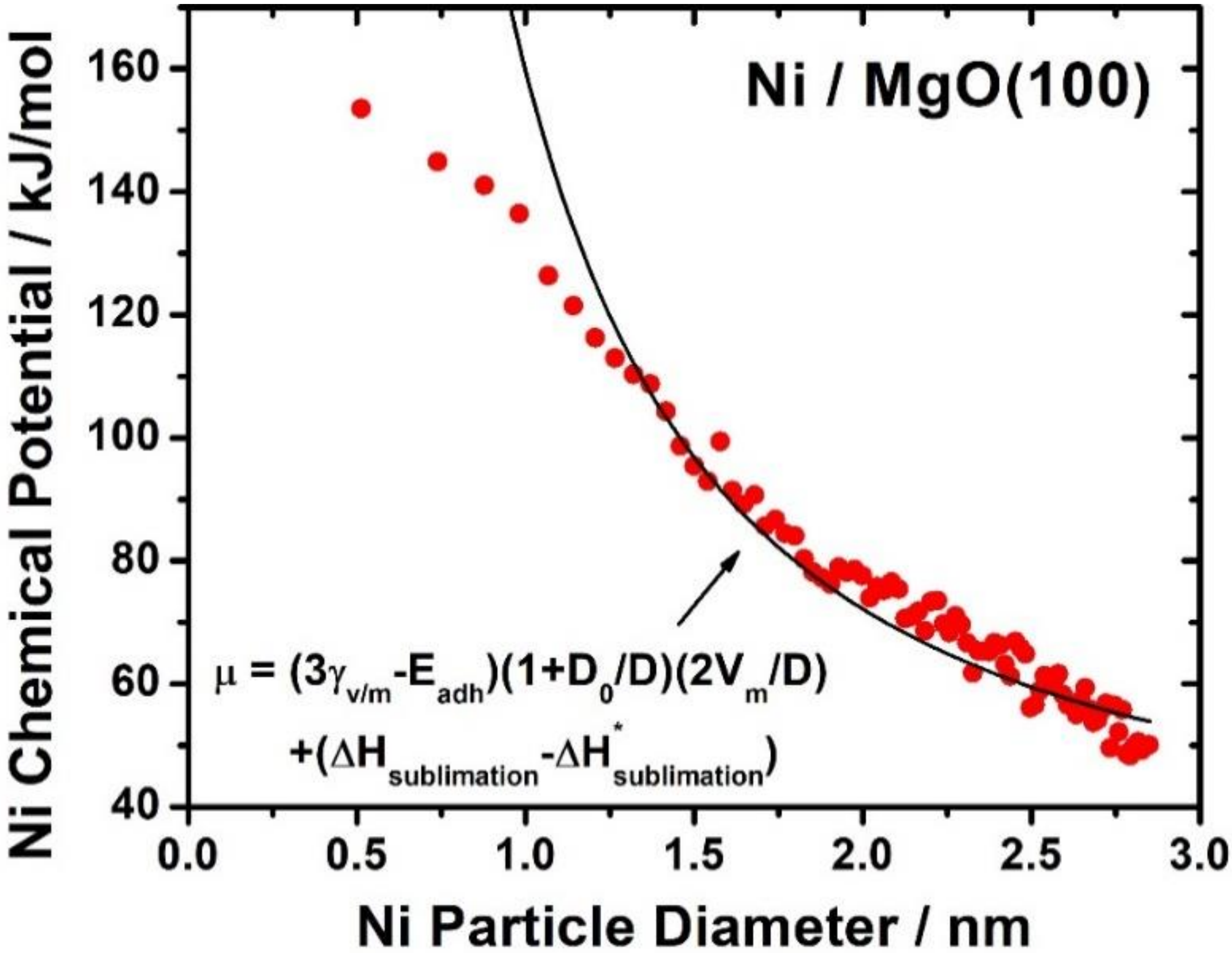

Figure 5.1 Chemical potential of Ni atoms in Ni particles (relative to bulk Ni(solid)) versus the average effective Ni particle diameter on MgO(100) at 300 K. The black line is the fitting curve of Eq (5.4), with the best-fit parameters: E_{adh} = 3.05 J/m^2 and $\Delta H^*_{sublimation} = 405$ kJ/mol.

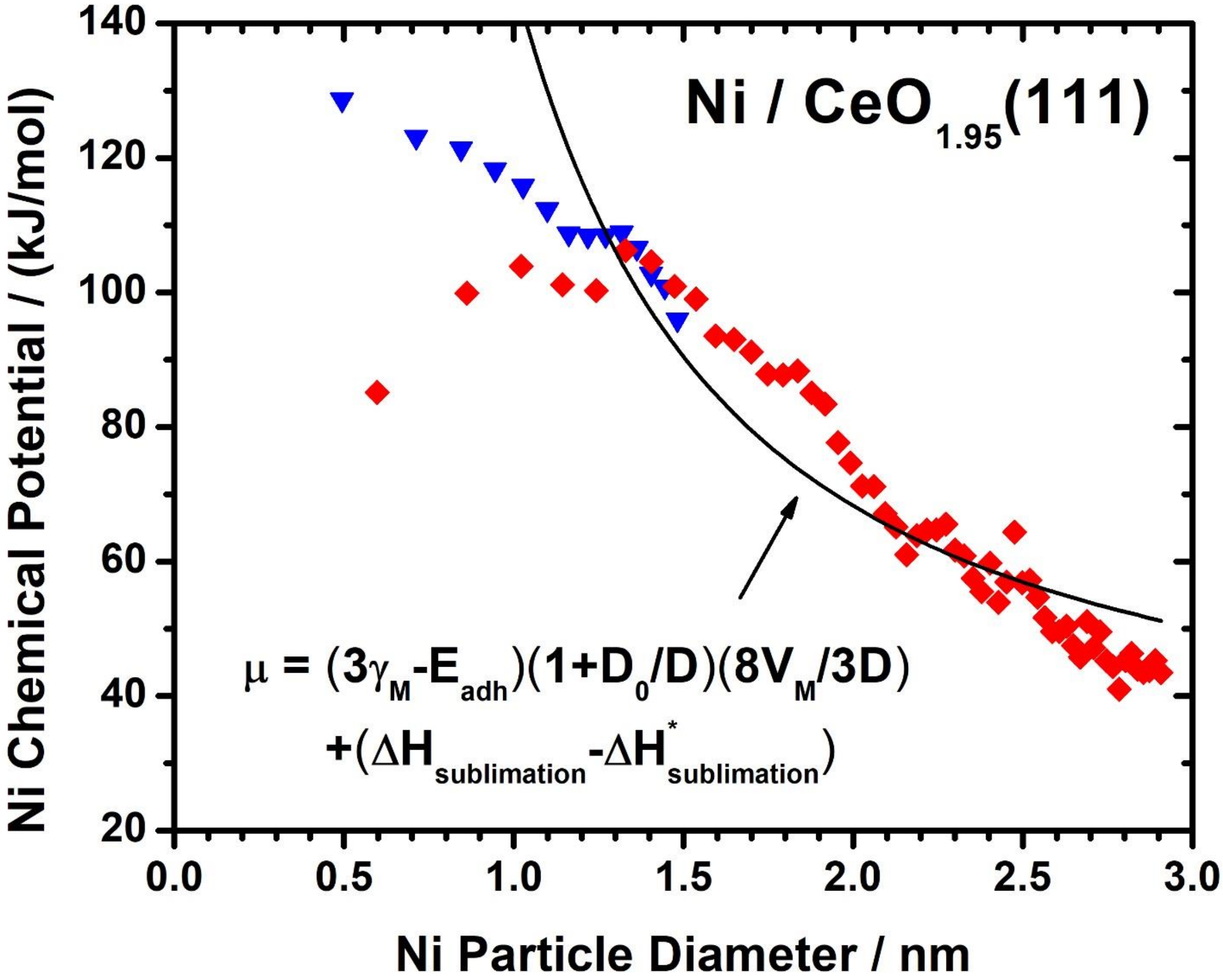

Figure 5.2 Chemical potential of Ni atoms in Ni particles (relative to bulk Ni(solid)) versus the average effective Ni particle diameter on CeO$_{1.95}$(111) at 300 and 100 K. The red points correspond to 300 K, and the blue points correspond to 100 K. The black line is the fitting curve of Eq (5.5), with the best-fit parameters: E_{adh} = 4.39 J/m^2 and $\Delta H^*_{sublimation} = 404$ kJ/mol.

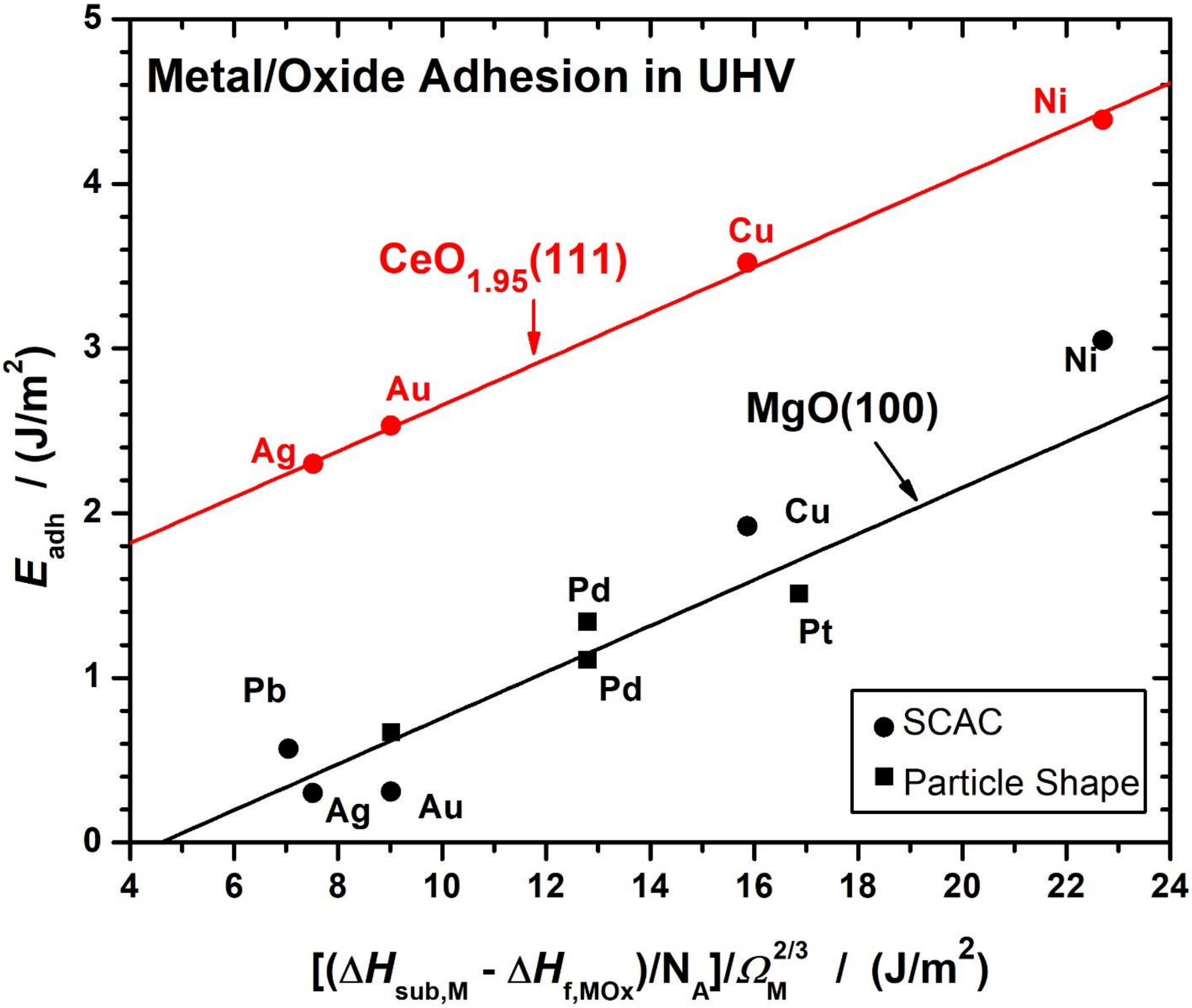

Figure 5.3 Experimental adhesion energies of different metals (as continuous films or for the largest nanoparticles studied) to MgO(100) and CeO$_{2\text{-x}}$(111) surfaces versus $\left[\left(\Delta H_{\text{sub,M}}-\Delta H_{\text{f,MO}_\text{x}}\right)/N_A\right]/\Omega_M{}^{2/3}$, which is measure of the oxophilicity of the metal element, per unit surface area. These measurements were all down in UHV on clean oxide surfaces, using either SCAC or particle-shape measurements by electron microscopy or grazing-incidence X-ray scattering. Adapted with permission from ref [35].

Chapter 6. The Degree of Rate Control of Catalyst-Bound Intermediates in Catalytic Reaction Mechanisms: Relationship to Site Coverage

This chapter has been published as:
Z. Mao, C. T. Campbell, *Journal of Catalysis*, 2020, 381, 53-62.

Chapter Abstract

The degree of rate control (DRC) quantifies how much the energy of each species in a reaction mechanism (e.g., catalyst-bound intermediates and transition states) affects the net reaction rate. It thus plays an important role in understanding catalyst activity and selectivity, and in guiding efforts to find better catalysts. We show here that at steady-state reaction conditions, the degree of rate control for any catalyst-bound intermediate *n* (X_n) is proportional to its fractional population of catalyst sites (θ_n):

$$X_n = -\sigma \times \theta_n \ ,$$

where the proportionality constant σ is given by:

$$\sigma = \sum_i X_i \times n_i \ .$$

Here, X_i is the DRC of the transition state in step *i*, n_i is the number of catalyst sites of the same type required for the elementary step *i*, and the sum is over all transition states (or elementary steps) *i*. Since only a few transition states typically have non-negligible DRCs, this simple sum (or weighted average of elementary-step site requirements) includes only a few terms (and only one term when there is a single rate-determining step). We also show that the DRC of reactants and catalyst depends upon the choice of zero-energy reference, but simplify to zero when using their standard states as the zero-energy reference.

6.1 INTRODUCTION

The generalized degree of rate control (DRC) is a mathematical approach used to identify rate-controlling species in multistep reaction mechanisms.[42, 43] It quantifies the extent by which a small decrease in the standard-state free energy of a species in the reaction pathway affects the reaction rate, which is of clear value in understanding how different catalysts might change the rate and selectivity. It has found many important applications in catalysis research,[1, 43, 186-189] including use for computational catalyst screening.[1, 190] The definition of the generalized DRC is:[42]

$$X_i = \left(\frac{\partial (\ln r)}{\partial \left(-G_i^0 / RT \right)} \right)_{G_{j \neq i}} , \tag{6.1}$$

where r is the net steady-state reaction rate (per catalyst site) towards the product of interest (or for the consumption of one reactant), G_i^0 is the standard-state Gibbs free energy of species *i* (i.e., a catalyst-bound intermediate or transition state). The derivative is taken holding constant the standard-state Gibbs free energies of all other species.

In the following treatment, we will define these G_i^0 free energies relative to the standard-state Gibbs free energy of the stoichiometrically-combined reactants (plus the catalyst with no bound intermediate) as the zero-energy reference. (Maintaining element-balance with every step in the mechanism simplifies picturing this zero-energy reference in a reaction-energy diagram and analyzing DRCs.) However, we only do this as a matter of convenience, and one can also take other states as the zero-energy reference. Indeed, we show in the section on Reference States below that when using quantum mechanical methods (such as density functional theory, i.e., DFT) to estimate the energies of species, it is often more convenient to choose the zero-energy reference differently, and even then the reference state typically varies between heterogeneous and homogeneous catalysis.

Since the term -G_i^0/RT will be used frequently in the following sections, it will be replaced with a dimensionless variable (reduced free energy) g_i:

$$g_i = -G_i^0 / RT \quad , \tag{6.2}$$

so that Eq (6.1) can be rewritten as

$$X_i = \left(\frac{\partial (\ln r)}{\partial g_i} \right)_{g_{j \neq i}} .$$

There are some similar measures of the sensitivity of the rate to the values of rate constants.[44, 188] Those apply to elementary steps, so that the contributions of the individual species in each step (e.g., the initial state intermediate, the transition state and the final state) are coupled together. We focus here instead on the generalized DRC, because it relates directly to the free energies of individual species and has a more direct connection to the reaction energy diagram. There are only a few species with non-negligible DRCs even in the most complex reaction mechanisms. Thus, the generalized DRC greatly simplifies analysis of the connection between reaction rate and species' energetics. This benefit increases as the complexity of the mechanism grows.[43] Since it was raised in 2009, the generalized DRC has shown its power in catalysis research. Wolcott et al. introduced a method for computational catalyst screening based on the generalized DRC.[1] Mao et al.[191] proved that the apparent activation energy of a multistep reaction equals the weighted average of the standard-state enthalpies of all the species in the reaction mechanism (relative to the reactants), each weighted by its generalized DRC, plus RT. Thus, knowing the values of the DRCs for the species in a reaction mechanism can be quite helpful. The DRC values not only quantify the extent to which different elementary steps control the rate, but also the extent to which the energy of each catalyst-bound intermediate and transition state affects the rate. They are very important in interpreting reaction kinetics, in understanding apparent activation energies, and in predicting better catalyst materials. Here, we show that the DRC for any catalyst-bound reaction intermediate n (X_n) is proportional to its fractional population of catalyst sites (θ_n):

$$X_n = -\sigma \times \theta_n \ , \tag{6.3}$$

where the proportionality constant σ is a weighted average of elementary-step site requirements, i.e.:

$$\sigma = \sum_i X_i \times n_i \tag{6.4}$$

The weighting factor X_i here is the DRC of the transition state in step i, n_i is the number of catalyst sites of the same type required for the elementary step i, and the sum is taken over all transition states (or elementary steps) i. It is well known that in typical complex reaction mechanisms, even ones with many elementary steps, there are only a few transition states that have non-negligible DRCs.[42, 43] Therefore this simple sum typically includes only a few terms. It has only one term when there is a single rate-determining step.

We defined n_i in Eq (6.4) as the number of catalyst sites *of the same type* required for the elementary step i. This takes into consideration that a catalyst might have two different types of sites that bind different reactant gases but are both required in some rate-controlling step(s). An example of this type is treated in Reaction 3 below. This could occur in many real situations. For example, if a rate-controlling reaction occurs at the periphery of an oxide-supported metal nanoparticle, it might be a bond-forming reaction between one adsorbate bound to a site on the metal surface and another adsorbate bound to a nearby site on the oxide surface, or a bond-breaking reaction where the two product fragments bind to different types of sites (metal versus oxide sites).

We note that Eqs (6.3) and (6.4) relate the DRCs of adsorbates to the fraction of catalyst sites they occupy (θ_n) at the reaction conditions of interest. The fraction of free sites (θ_*) is 1 minus the sum of θ_n for all adsorbates. However, free sites themselves do not have a degree of rate control (since they are part of the zero-energy reference in Eq (6.1)). This can be seen from the definition of DRC in Eq (6.1), where the derivative is taken with respect to -G_i^0/RT, where "G_i^0 is the standard-state Gibbs free energy of species *i* (i.e., a catalyst-bound intermediate or transition state) relative to the standard-state Gibbs free energy of the stoichiometrically-combined reactants (plus the adsorbate-free catalysts surface) as the zero-energy reference. Thus, it is impossible to determine the DRC for the free surface sites, since they are included in the reference-state energy that cannot be changed in calculating DRCs. However, this is only true because we chose the reactants and catalyst (with no bound intermediates) as a convenient zero-energy reference state here. This changes when using other reference states, as shown below in the section on Reference States.

Some attractive mathematical properties of DRCs have already been reported. The DRCs of transition states are usually positive (or zero), and the DRCs of intermediates are usually negative (or zero).[42] For the DRCs of transition states, if there is a single rate-determining step (RDS), the transition state in the RDS has a DRC of 1, leaving the DRCs of other transition states near zero unless the reaction has branching. If several transition states show rate-control, their DRCs sum up to 1.[43, 44] In a sequential fluid-phase reaction with no catalyst, the steady-state rate (for given steady-state reactant concentration(s)) is determined by the energy difference between the reactants and the transition state of the RDS.[192, 193] We can offer further justification for this as follows. Within transition state theory (TST), one calculates the rate by assuming that the reactants of the RDS are in equilibrium with its transition state. If all the steps before this RDS are in equilibrium, then the initial-step's reactants are also in equilibrium with the transition state for the RDS. Thus, one need not even consider the intervening intermediates to calculate the steady-state rate for given steady-state reactant concentration(s). One can simply calculate the rate assuming there is single step that converts initial reactants to the transition state for the RDS, applying TST as if it were a single elementary step since they are in equilibrium. Thus, the intermediates do not exhibit significant rate-control (their DRCs are close to zero).

In a catalyzed reaction, the story is quite different because there is often a limited amount of active reaction sites. By investigating several catalytic reactions involving adsorbed intermediates, Campbell and coworkers already discovered that the DRCs of the adsorbates are usually proportional to their fractional coverages,[42, 43] with a proportionality constant almost always been observed to be a positive integer that applies to all the surface-bound intermediates along the reaction pathway to a given product, and it is often 2 in microkinetic models. Knowing how to predict this proportionality constant $-\sigma$ between coverage and DRC of adsorbates using Eq (6.4) should allow experimental estimation of DRCs of adsorbates, because their coverages can be measured by a variety of methods. Alternately, measuring the experimental proportionality between rate and adsorbate coverage would allow experimental determination of the value of σ, which would give experimental information about the number of sites required in the rate controlling step(s) through Eq (6.4).

In the following sections of this paper, we analyze many different classes of catalytic reaction mechanisms, in both heterogeneous and homogeneous catalysis, elucidate the origin of this proportional relation, and show that the proportionality constant is given by the DRC-weighted average of elementary-step site requirements as given by Eq (6.4) above. We first analyze six different reaction mechanisms where analytical rate expressions can be derived at steady state, and for several of these we also analyze multiple limiting cases where the rate laws simplify. All these rate laws give DRCs in agreement with Eqs (6.3) and (6.4). We next perform case studies of two more complex mechanisms where analytical rate expressions have not be determined, but where we have calculated the steady-state rates at various reaction conditions using a computer, based on the reaction energetics taken from the literature (which were calculated using density functional theory). In all these cases, the DRCs are in agreement with Eqs (6.3) and (6.4).

6.2 REACTION 1. A TYPICAL LANGMUIR-HINSHELWOOD MECHANISM

To validate Eqs (6.3) and (6.4), we first consider a Langmuir-Hinshelwood (L-H) reaction mechanism with four elementary steps and competitive adsorption. There is a single RDS (Step 3) and all other steps are quasi-equilibrated:

$$\begin{array}{lll} 1. & A+*\rightarrow A* & (\textit{fast to equilibrium}) \\ 2. & B+*\rightarrow B* & (\textit{fast to equilibrium}) \\ 3. & A*+B*\rightarrow C*+* & (RDS) \\ 4. & C*\rightarrow C+* & (\textit{fast to equilibrium}) \end{array}$$

Since Step 3 is the only RDS, the coverage of C* should be very low compared to A* and B* at low conversion limit. Campbell[42] proved that if the surface is nearly saturated with A* and step 3 is so exothermic that it is essentially irreversible, the DRC of A* is -2 and Eq (6.3) is true with σ = 2, just as expected based on Eq (6.4). Here we give a general proof that $\sigma = 2$ for this L-H mechanism in the more general case where both A* and B* can occupy any fractions of surface sites.

Using the Langmuir adsorption model for adsorption, the fractional coverages of A* and B* are given by:

$$\theta_{A*} = \frac{K_1 p_A}{1 + K_1 p_A + K_2 p_B} \quad \text{and} \tag{6.5}$$

$$\theta_{B*} = \frac{K_2 p_B}{1 + K_1 p_A + K_2 p_B} \ , \tag{6.6}$$

where p_X is the partial pressure of X and K_i is the equilibrium constant of Step *i*. (We do all the derivations here and below assuming gas-phase catalysis and using partial pressures *p* as a convenient way to express concentrations. However, we emphasize that the resulting equations would apply equally well to liquid-phase heterogeneous catalysis, where the partial pressures would simply be replaced with concentrations (or activities)). For the quasi-equilibrated adsorption steps, the equilibrium constants K_i can be expressed as $K_i = \exp(-G^0_{X*} / RT)$, where G^0_{X*} is the standard-state Gibbs free energy of the adsorbate X* formed in Step *i*. Since Step 3 is an irreversible step, the rate of the reaction per catalyst site can be written as:

$$r = k_3 \theta_{A*} \theta_{B*} = k_3 \frac{K_1 K_2 p_A p_B}{\left(1 + K_1 p_A + K_2 p_B\right)^2} \ , \tag{6.7}$$

where k_3 is the forward rate constant of Step 3. It can be expressed as k_3 = $\left(k_B T / h\right) \exp\left[-\left(G^0_{TS3} - G^0_{A*} - G^0_{B*}\right) / RT\right]$ using transition state theory, where G^0_{TS3} is the standard-state Gibbs free energy of transition state in Step 3 (TS3). If all rate constants and equilibrium constants in Eq (6.7) are expressed as functions of Gibbs free energies, Eq (6.7) becomes:

$$\begin{aligned} r &= \frac{k_B T}{h} \exp(g_{TS3} - g_{A*} - g_{B*}) \frac{\exp(g_{A*} + g_{B*}) p_A p_B}{\left[1 + \exp(g_{A*}) p_A + \exp(g_{B*}) p_B\right]^2} \\ &= \frac{k_B T}{h} \frac{\exp(g_{TS3}) p_A p_B}{\left[1 + \exp(g_{A*}) p_A + \exp(g_{B*}) p_B\right]^2} \end{aligned} \tag{6.8}$$

Plugging Eq (6.8) into Eq (6.1) gives the DRCs of TS3 and of intermediates A* and B*:

$$X_3 = \frac{\partial\left(\ln r\right)}{\partial\left(g_{TS3}\right)} = 1 \tag{6.9}$$

$$X_{A^*} = \frac{\partial(\ln r)}{\partial(g_{A^*})} = -2 \times \frac{\exp(g_{A^*})\, p_A}{1+\exp(g_{A^*})\, p_A + \exp(g_{B^*})\, p_B} = -2\theta_{A^*} \tag{6.10}$$

$$X_{B^*} = \frac{\partial(\ln r)}{\partial(g_{B^*})} = -2 \times \frac{\exp(g_{B^*})\, p_B}{1+\exp(g_{A^*})\, p_A + \exp(g_{B^*})\, p_B} = -2\theta_{B^*} \tag{6.11}$$

Eq (6.9) shows that TS3 has DRC = 1. Comparing Eqs (6.10) and (6.11) to Eq (6.3) shows that the proportionality constant σ equals 2 for both A* and B*. The "-2" comes from the square in the denominator of the rate in Eq (6.8) (usually called the adsorption or site blocking term[194]), which becomes a factor -2 after taking the logarithm. It also equals the number of reaction sites required in the RDS times -1. The DRCs are 0 for all the other transition states and intermediates. These results are all consistent with Eqs (6.3) and (6.4).

6.3 REACTION 2. A SIMPLE ELEY-RIDEAL MECHANISM

We next consider a three-step reaction following the Eley-Rideal (E-R) mechanism:

1. $A+* \rightarrow A*$ $(\textit{fast to equilibium})$
2. $A*+B \rightarrow C*$ (RDS)
3. $\mathrm{C}* \rightarrow C+*$ $(\textit{fast to equilibium})$

The coverage, the reaction rate per catalyst site and the DRCs can be calculated in the same way as shown in the L-H mechanism, giving:

$$\theta_{A^*} = \frac{K_{ads,A^*} p_A}{1+K_{ads,A^*} p_A} = \frac{\exp(g_{A^*}) p_A}{1+\exp(g_{A^*}) p_A} \tag{6.12}$$

$$\begin{aligned} r &= k_2 \theta_{A^*} p_B = \frac{k_B T}{h} \exp(g_{TS2} - g_{A^*}) \theta_{A^*} p_B \\ &= \frac{k_B T}{h} \exp(g_{TS2} - g_{A^*}) \frac{\exp(g_{A^*}) p_A p_B}{1+\exp(g_{A^*}) p_A} \\ &= \frac{k_B T}{h} \frac{\exp(g_{TS2}) p_A p_B}{1+\exp(g_{A^*}) p_A} \end{aligned} \tag{6.13}$$

$$X_2 = \frac{\partial(\ln r)}{\partial(g_{TS2})} = 1 \tag{6.14}$$

$$X_{A*} = \frac{\partial(\ln r)}{\partial(g_{A*})} = -\frac{\exp(g_{A*})\,p_A}{1+\exp(g_{A*})\,p_A} = -\theta_{A*} \tag{6.15}$$

The DRCs are 0 for all the other transition states and intermediates. In this case, the DRC of the transition state in the RDS (TS2) is still 1. The main difference between the E-R mechanism and the L-H mechanism studied above is, gas B does not adsorb on the surface and only one surface site participates in the RDS. The denominator in Eq (6.13) is no longer squared as it was in Eq (6.8), and so σ decreases from 2 to 1. These results are all consistent with the predictions of Eqs (6.3) and (6.4).

6.4 REACTION 3. A LANGMUIR-HINSHELWOOD MECHANISM WITH TWO TYPES OF SITES

The third model reaction mechanism we consider is an extension of the L-H mechanism above, where the two adsorbates A* and B* adsorb on different types of surface sites, i.e., non-competitive adsorption. When A and B are in equilibrium with their own different sets of surface sites, their fractional coverages are given by:

$$\theta_{A*} = \frac{K_{ads,A*}\,p_A}{1+K_{ads,A*}\,p_A} = \frac{\exp(g_{A*})\,p_A}{1+\exp(g_{A*})\,p_A} \text{ , and} \tag{6.16}$$

$$\theta_{B*} = \frac{K_{ads,B*}\,p_B}{1+K_{ads,B*}\,p_B} = \frac{\exp(g_{B*})\,p_B}{1+\exp(g_{B*})\,p_B} \text{ .} \tag{6.17}$$

Then the rate per catalyst site and DRCs can be calculated as:

$$\begin{aligned} r &= \frac{k_B T}{h} \exp(g_{TS3} - g_{A*} - g_{B*}) \frac{\exp(g_{A*}) p_A \exp(g_{B*}) p_B}{\left[1+\exp(g_{A*}) p_A\right]\left[1+\exp(g_{B*}) p_B\right]} \\ &= \frac{k_B T}{h} \frac{\exp(g_{TS3}) p_A p_B}{\left[1+\exp(g_{A*}) p_A\right]\left[1+\exp(g_{B*}) p_B\right]} \end{aligned} \tag{6.18}$$

$$X_3 = \frac{\partial(\ln r)}{\partial(g_{TS3})} = 1 \tag{6.19}$$

$$X_{A*} = \frac{\partial(\ln r)}{\partial(g_{A*})} = -\frac{\exp(g_{A*}) p_A}{1+\exp(g_{A*}) p_A} = -\theta_{A*} \tag{6.20}$$

$$X_{B*} = \frac{\partial(\ln r)}{\partial(g_{B*})} = -\frac{\exp(g_{B*}) p_B}{1+\exp(g_{B*}) p_B} = -\theta_{B*} \ . \tag{6.21}$$

The DRCs are 0 for all other transition states and intermediates. Eqs (6.20) and (6.21) show that Eq (6.3) still holds in this case. The ratio σ is 1 instead of 2 for both A* and B* despite the fact that there are two surface sites participate in the RDS. These results are all consistent with Eqs (6.3) and (6.4).

Gathering together the results of these three model reaction mechanism studies, we can conclude that the simple proportional relation between the DRCs of adsorbates in a surface reaction and their fractional coverage as expressed in Eq (6.3) is true in all these limiting cases. The proportionality constant σ is given accurately by Eq (6.4) in all cases. It comes from the denominator in the rate equation that arises from the coverage expressions for the adsorbates involved in the RDS. It equals the number of surface sites *of the same type* that participate in the RDS. If the adsorbates occupy different types of surface sites, the ratio σ of an adsorbate X* equals the number of that specific type of sites on which X* adsorbs in the RDS.

6.5 REACTION 4. A REACTION WITH TWO RATE-CONTROLLING STEPS

Although these three model reactions cover many of the cases in real surface reactions when there is a single RDS, we would still like to explore more complicated reaction mechanisms with more than a single RDS, so that these conclusions regarding ratio σ (i.e., Eq (6.4)) can be understood and used in a more general way. Starting from the L-H mechanism (**Reaction 1** above), let us add another step just after Step 3. In the new reaction, we assume that both Step 3 and Step 4 have non-negligible DRCs. These two steps are labeled as RCS 1 and RCS 2 (RCS = rate-controlling step).

1. $A+*\rightarrow A*$ $(\textit{fast to equilibium})$
2. $\mathrm{B}+*\rightarrow B*$ $(\textit{fast to equilibium})$
3. $\mathrm{A}*+B*\rightarrow C*+*$ $(RCS\ 1)$
4 $C*\rightarrow D*$ $\left(RCS\ 2\right)$
5. $\mathrm{D}*\rightarrow D+*$ $(\textit{fast to equilibium})$

Assuming B* is the most abundant species (θ_{B*} ~ 1) and applying the steady-state approximation to Steps 3 and 4, we can equate the net rate of production of C* to its net rate of consumption, and rearrange to solve for the coverage of C*, as:

$$
\begin{aligned}
r &= k_3\theta_{A*}\theta_{B*} - k_{-3}\theta_{C*}\theta_{*} = k_3\frac{K_{ads,A*}p_A}{K_{ads,B*}p_B} - k_{-3}\theta_{C*}\frac{1}{K_{ads,B*}p_B} = k_4\theta_{C*} \\
\theta_{C*} &= \frac{k_3K_{ads,A*}p_A}{k_{-3}+k_4K_{ads,B*}p_B}
\end{aligned}
\tag{6.22}
$$

The rate expression for the production of the final product D per catalyst site is then:

$$\begin{aligned} r &= k_4\theta_{C*} = \frac{k_3 k_4 K_{ads,A*} p_A}{k_{-3} + k_4 K_{ads,B*} p_B} \\ &= \frac{k_B T}{h} \frac{\exp(g_{TS3} - g_{A*} - g_{B*})\exp(g_{TS4} - g_{C*})\exp(g_{A*}) p_A}{\exp(g_{TS3} - g_{C*}) + \exp(g_{TS4} - g_{C*})\exp(g_{B*}) p_B} \\ &= \frac{k_B T}{h} \frac{\exp(g_{TS3} - g_{A*} - g_{B*} + g_{TS4} - g_{C*} + g_{A*}) p_A}{\exp(g_{TS3} - g_{C*}) + \exp(g_{TS4} - g_{C*} + g_{B*}) p_B} \\ &= \frac{k_B T}{h} \frac{\exp(g_{TS3} - g_{B*}) p_A}{\exp(g_{TS3} - g_{TS4}) + \exp(g_{B*}) p_B} \end{aligned} \tag{6.23}$$

The DRCs of the two RCS transition states are given by

$$X_3 = \frac{\partial(\ln r)}{\partial(g_{TS3})} = \frac{\exp(g_{B*}) p_B}{\exp(g_{B*}) p_B + \exp(g_{TS3} - g_{TS4})} \tag{6.24}$$

$$X_3 = \frac{\partial(\ln r)}{\partial(g_{TS4})} = \frac{\exp(g_{TS3} - g_{TS4})}{\exp(g_{B*}) p_B + \exp(g_{TS3} - g_{TS4})} \tag{6.25}$$

The sum of X_3 and X_4 is 1, which has been proven before for series reactions.[44] The DRC of the most abundant adsorbed species B* can also be calculated and expressed in terms of X_3 and X_4

$$\begin{aligned} X_{B*} &= \frac{\partial(\ln r)}{\partial(g_{B*})} = -1 - \frac{\exp(g_{B*}) p_B}{\exp(g_{B*}) p_B + \exp(g_{TS3} - g_{TS4})} \\ &= -(X_3 + X_4) - X_3 = -(2X_3 + X_4)\theta_{B*} \end{aligned} \tag{6.26}$$

The DRCs are 0 for all the other transition states and intermediates. Eq (6.26) shows that if there is more than one RCS, and the numbers of sites of the same type involved in these RCSs are not equal, the ratio σ in Eq (6.3) will no longer be an integer. It instead equals the average of the site numbers required for all the RCSs (2 and 1 in this example), each weighted with the DRCs of their transition states. This is the rule already expressed as in Eq (6.4) above.

If G^0_{TS3} is significantly higher than G^0_{TS4}, then Step 3 will be the single RDS and this case reduces to the first L-H model reaction we studied above, where $\sigma = 2$. Conversely, if G^0_{TS4} is much higher, then Step 4 will be the single RDS and σ reduces to 1. If both Step 3 and Step 4 need two sites of the same type, σ would always be $2X_3+2X_4 = 2$. These results are all consistent with Eq (6.4).

6.6 REACTION 5. A BRANCHED REACTION MECHANISM GIVING TWO POSSIBLE PRODUCTS

We next show that Eq (6.4)is valid for a much more complex mechanism, a branched reaction starting from common reactants to two different products, D and E:

1. $A+* \rightarrow A*$ $(\textit{fast to equilibium})$
2. $\mathrm{B+*} \rightarrow B*$ $(\textit{fast to equilibium})$
3. $\mathrm{A*+}B* \rightarrow C*+*$ $(RCS\ 1)$
4. $C* \rightarrow D*$ $\left(RCS\ 2\mathrm{A}\right)$
5. $C* \rightarrow E*$ $\left(RCS\ 2B\right)$
6. $\mathrm{D*} \rightarrow D+*$ $(\textit{fast to equilibium})$
7. $E* \rightarrow E+*$ $(\textit{fast to equilibium})$

There are now three different rates to consider in DRC evaluations: a rate of reactant consumption and two rates of product generation. Step 3 is a rate-controlling step before the branching at Steps 4 and 5. Assuming B* nearly saturates the surface (θ_{B*} ~ 1), a method like used in the previous model reaction above can be applied. Applying the steady-state approximation to Steps 3, 4 and 5, the coverage of C* is given by equating the net rate of production of C* to its net rate of consumption, and rearranging:

$$\begin{aligned} r &= k_3\theta_{A*}\theta_{B*} - k_{-3}\theta_{C*}\theta_* = \left(k_4 + k_5\right)\theta_{C*} \\ \theta_{C*} &= \frac{k_3 K_{ads,A*} p_A}{k_{-3} + \left(k_4 + k_5\right) K_{ads,B*} p_B} \end{aligned} \qquad (6.27)$$

The rate of production of D per site can be written as

$$\begin{aligned} r_D &= k_4\theta_{C*} = \frac{k_3 k_4 K_{ads,A*} p_A}{k_{-3} + \left(k_4 + k_5\right) K_{ads,B*} p_B} \\ &= \frac{k_B T}{h} \frac{\exp\left(g_{TS3} - g_{A*} - g_{B*}\right) \exp\left(g_{TS4} - g_{C*}\right) \exp\left(g_{A*}\right) p_A}{\exp\left(g_{TS3} - g_{C*}\right) + \left[\exp\left(g_{TS4} - g_{C*}\right) + \exp\left(g_{TS5} - g_{C*}\right)\right] \exp\left(g_{B*}\right) p_B} \\ &= \frac{k_B T}{h} \frac{\exp\left(g_{TS3} - g_{B*}\right) \exp\left(g_{TS4}\right) p_A}{\exp\left(g_{TS3}\right) + \left[\exp\left(g_{TS4}\right) + \exp\left(g_{TS5}\right)\right] \exp\left(g_{B*}\right) p_B} \end{aligned} \tag{6.28}$$

Similarly, the rates of production of E and consumption of A (or B) are given by

$$r_E = \frac{k_B T}{h} \frac{\exp\left(g_{TS3} - g_{B*}\right) \exp\left(g_{TS5}\right) p_A}{\exp\left(g_{TS3}\right) + \left[\exp\left(g_{TS4}\right) + \exp\left(g_{TS5}\right)\right] \exp\left(g_{B*}\right) p_B} \tag{6.29}$$

$$r_A = \frac{k_B T}{h} \frac{\exp\left(g_{TS3} - g_{B*}\right) \left[\exp\left(g_{TS4}\right) + \exp\left(g_{TS5}\right)\right] p_A}{\exp\left(g_{TS3}\right) + \left[\exp\left(g_{TS4}\right) + \exp\left(g_{TS5}\right)\right] \exp\left(g_{B*}\right) p_B} \tag{6.30}$$

Extra attention should be paid to the calculation of DRCs here because there are three types of rates: the rate to product D r_D, the rate to product E r_E and the overall reactant consumption rate r_A. For example, the DRC of the transition state in Step 3 for the rate to D (r_D) is

$$\begin{aligned} X_{TS3,D} &= \frac{\partial\left(\ln r_D\right)}{\partial\left(g_{TS3}\right)} = 1 - \frac{\exp\left(g_{TS3}\right)}{\exp\left(g_{TS3}\right) + \left[\exp\left(g_{TS4}\right) + \exp\left(g_{TS5}\right)\right] \exp\left(g_{B*}\right) p_B} \\ &= \frac{\left[\exp\left(g_{TS4}\right) + \exp\left(g_{TS5}\right)\right] \exp\left(g_{B*}\right) p_B}{\exp\left(g_{TS3}\right) + \left[\exp\left(g_{TS4}\right) + \exp\left(g_{TS5}\right)\right] \exp\left(g_{B*}\right) p_B} \end{aligned} \tag{6.31}$$

Similarly,

$$\begin{aligned} X_{TS3,E} &= \frac{\partial\left(\ln r_E\right)}{\partial\left(g_{TS3}\right)} = 1 - \frac{\exp\left(g_{TS3}\right)}{\exp\left(g_{TS3}\right) + \left[\exp\left(g_{TS4}\right) + \exp\left(g_{TS5}\right)\right] \exp\left(g_{B*}\right) p_B} \\ &= \frac{\left[\exp\left(g_{TS4}\right) + \exp\left(g_{TS5}\right)\right] \exp\left(g_{B*}\right) p_B}{\exp\left(g_{TS3}\right) + \left[\exp\left(g_{TS4}\right) + \exp\left(g_{TS5}\right)\right] \exp\left(g_{B*}\right) p_B} \end{aligned} \tag{6.32}$$

$$\begin{aligned} X_{TS4,D} &= \frac{\partial\left(\ln r_D\right)}{\partial\left(g_{TS4}\right)} = 1 - \frac{\exp\left(g_{TS4}\right) \exp\left(g_{B*}\right) p_B}{\exp\left(g_{TS3}\right) + \left[\exp\left(g_{TS4}\right) + \exp\left(g_{TS5}\right)\right] \exp\left(g_{B*}\right) p_B} \\ &= \frac{\exp\left(g_{TS3}\right) + \exp\left(g_{TS5}\right) \exp\left(g_{B*}\right) p_B}{\exp\left(g_{TS3}\right) + \left[\exp\left(g_{TS4}\right) + \exp\left(g_{TS5}\right)\right] \exp\left(g_{B*}\right) p_B} \end{aligned} \tag{6.33}$$

$$X_{TS4,E} = \frac{\partial\left(\ln r_E\right)}{\partial\left(g_{TS4}\right)} = \frac{-\exp\left(g_{TS4}\right)\exp\left(g_{B*}\right)p_B}{\exp\left(g_{TS3}\right)+\left[\exp\left(g_{TS4}\right)+\exp\left(g_{TS5}\right)\right]\exp\left(g_{B*}\right)p_B} \tag{6.34}$$

$$X_{TS5,D} = \frac{\partial\left(\ln r_D\right)}{\partial\left(g_{TS5}\right)} = \frac{-\exp\left(g_{TS5}\right)\exp\left(g_{B*}\right)p_B}{\exp\left(g_{TS3}\right)+\left[\exp\left(g_{TS4}\right)+\exp\left(g_{TS5}\right)\right]\exp\left(g_{B*}\right)p_B} \tag{6.35}$$

$$\begin{aligned} X_{TS5,E} &= \frac{\partial\left(\ln r_E\right)}{\partial\left(g_{TS5}\right)} = 1-\frac{\exp\left(g_{TS5}\right)\exp\left(g_{B*}\right)p_B}{\exp\left(g_{TS3}\right)+\left[\exp\left(g_{TS4}\right)+\exp\left(g_{TS5}\right)\right]\exp\left(g_{B*}\right)p_B} \\ &= \frac{\exp\left(g_{TS3}\right)+\exp\left(g_{TS4}\right)\exp\left(g_{B*}\right)p_B}{\exp\left(g_{TS3}\right)+\left[\exp\left(g_{TS4}\right)+\exp\left(g_{TS5}\right)\right]\exp\left(g_{B*}\right)p_B} \end{aligned} \tag{6.36}$$

$$\begin{aligned} X_{TS3,A} &= \frac{\partial\left(\ln r_A\right)}{\partial\left(g_{TS3}\right)} = 1-\frac{\exp\left(g_{TS3}\right)}{\exp\left(g_{TS3}\right)+\left[\exp\left(g_{TS4}\right)+\exp\left(g_{TS5}\right)\right]\exp\left(g_{B*}\right)p_B} \\ &= \frac{\left[\exp\left(g_{TS4}\right)+\exp\left(g_{TS5}\right)\right]\exp\left(g_{B*}\right)p_B}{\exp\left(g_{TS3}\right)+\left[\exp\left(g_{TS4}\right)+\exp\left(g_{TS5}\right)\right]\exp\left(g_{B*}\right)p_B} \end{aligned} \tag{6.37}$$

$$\begin{aligned} X_{TS4,A} &= \frac{\partial\left(\ln r_A\right)}{\partial\left(g_{TS4}\right)} \\ &= \frac{\exp\left(g_{TS4}\right)}{\exp\left(g_{TS4}\right)+\exp\left(g_{TS5}\right)} - \frac{\exp\left(g_{TS4}\right)\exp\left(g_{B*}\right)p_B}{\exp\left(g_{TS3}\right)+\left[\exp\left(g_{TS4}\right)+\exp\left(g_{TS5}\right)\right]\exp\left(g_{B*}\right)p_B} \end{aligned} \tag{6.38}$$

$$\begin{aligned} X_{TS5,A} &= \frac{\partial\left(\ln r_A\right)}{\partial\left(g_{TS5}\right)} \\ &= \frac{\exp\left(g_{TS5}\right)}{\exp\left(g_{TS4}\right)+\exp\left(g_{TS5}\right)} - \frac{\exp\left(g_{TS5}\right)\exp\left(g_{B*}\right)p_B}{\exp\left(g_{TS3}\right)+\left[\exp\left(g_{TS4}\right)+\exp\left(g_{TS5}\right)\right]\exp\left(g_{B*}\right)p_B} \end{aligned} \tag{6.39}$$

$$\begin{aligned} X_{B*,D} &= \frac{\partial\left(\ln r_D\right)}{\partial\left(g_{B*}\right)} = -1-\frac{\left[\exp\left(g_{TS4}\right)+\exp\left(g_{TS5}\right)\right]\exp\left(g_{B*}\right)p_B}{\exp\left(g_{TS3}\right)+\left[\exp\left(g_{TS4}\right)+\exp\left(g_{TS5}\right)\right]\exp\left(g_{B*}\right)p_B} \\ &= \frac{-\exp\left(g_{TS3}\right)-2\left[\exp\left(g_{TS4}\right)+\exp\left(g_{TS5}\right)\right]\exp\left(g_{B*}\right)p_B}{\exp\left(g_{TS3}\right)+\left[\exp\left(g_{TS4}\right)+\exp\left(g_{TS5}\right)\right]\exp\left(g_{B*}\right)p_B} \\ &= X_{B*,E} = X_{B*,A} \end{aligned} \tag{6.40}$$

To check if the above relation between DRCs and coverages (Eqs (6.3) and (6.4)) still holds in this branched reaction, the DRCs calculated above are compared to Eqs (6.3) and (6.4). It is important to note that Eqs (6.3) and (6.4) apply independently to all three rates here (i.e., to the rates of reactant consumption, D production or E production), but it can only be applied to one of these rates at a time. For example, if we consider the DRC for intermediate B* in the rate to product D, then Eq (6.4) gives:

$$
\begin{aligned}
\sigma &= \sum_i X_{i,D} \times n_i = 2\times X_{TS3,D} + 1\times X_{TS4,D} + 1\times X_{TS5,D} \\
&= \frac{2\times\left[\exp\left(g_{TS4}\right)+\exp\left(g_{TS5}\right)\right]\exp\left(g_{B^*}\right)p_B}{\exp\left(g_{TS3}\right)+\left[\exp\left(g_{TS4}\right)+\exp\left(g_{TS5}\right)\right]\exp\left(g_{B^*}\right)p_B} \\
&\quad +\frac{\exp\left(g_{TS3}\right)+\exp\left(g_{TS5}\right)\exp\left(g_{B^*}\right)p_B}{\exp\left(g_{TS3}\right)+\left[\exp\left(g_{TS4}\right)+\exp\left(g_{TS5}\right)\right]\exp\left(g_{B^*}\right)p_B} \\
&\quad +\frac{-\exp\left(g_{TS5}\right)\exp\left(g_{B^*}\right)p_B}{\exp\left(g_{TS3}\right)+\left[\exp\left(g_{TS4}\right)+\exp\left(g_{TS5}\right)\right]\exp\left(g_{B^*}\right)p_B} \\
&= \frac{\exp\left(g_{TS3}\right)+2\times\left[\exp\left(g_{TS4}\right)+\exp\left(g_{TS5}\right)\right]\exp\left(g_{B^*}\right)p_B}{\exp\left(g_{TS3}\right)+\left[\exp\left(g_{TS4}\right)+\exp\left(g_{TS5}\right)\right]\exp\left(g_{B^*}\right)p_B} \\
&= -X_{B^*,D} = -X_{B^*,D}/\theta_{B^*} = \sigma
\end{aligned}
\tag{6.41}
$$

The last line above is seen to follow from the line above it by comparison to Eq (6.40) for the DRC of B* in the rate to D, and by remembering that the coverage of B* is nearly 1. The same result can also be achieved if DRCs corresponding to the rates to produce E or consume reactant A are plugged into Eq (6.4), which means in this branched reaction mechanism the DRC-coverage relation described by Eqs (6.3) and (6.4) is valid, but must be applied independently to each type of rate.

These equations above are rather complex. We next discuss their results under two extreme conditions which simplify the equations and their interpretation. First, if the energy barrier in Step 3 is much higher than those in Step 4 and 5, the term $\exp(g_{TS3})$ is negligible compared to $\exp(g_{TS4})$ and $\exp(g_{TS5})$. In this case, $X_{TS3,D}$, $X_{TS3,E}$ and $X_{TS3,A}$ all simplify to 1, while $X_{TS4,A}$ and $X_{TS5,A}$ reduce to 0. This means that Step 3 has complete control on the overall throughput (rate of reactant consumption). However, the transition states in Step 4 and 5 still can determine how the overall throughput is divided into the two branches. Eqs (6.33)-(6.36) reduce under this condition to:

$$X_{TS4,D} = \frac{\exp\left(g_{TS5}\right)}{\exp\left(g_{TS4}\right) + \exp\left(g_{TS5}\right)} \tag{6.42}$$

$$X_{TS4,E} = \frac{-\exp\left(g_{TS4}\right)}{\exp\left(g_{TS4}\right) + \exp\left(g_{TS5}\right)} \tag{6.43}$$

$$X_{TS5,D} = \frac{-\exp\left(g_{TS5}\right)}{\exp\left(g_{TS4}\right) + \exp\left(g_{TS5}\right)} \tag{6.44}$$

$$X_{TS5,E} = \frac{\exp\left(g_{TS4}\right)}{\exp\left(g_{TS4}\right) + \exp\left(g_{TS5}\right)} \; . \tag{6.45}$$

Eqs (6.42)-(6.45) show that these DRCs control the selectivity of the reaction. The DRCs of Step 4 and 5 to the same product have the same absolute value with different sign, and they both require one site, so they cancel each other in Eq (6.4). The ratio σ for B* to either product is therefore dominated by Step 3 and equals 2.

If the energy barrier in Step 3 is enough lower than those in Step 4 and 5, the terms $\exp(g_{TS4})$ and $\exp(g_{TS5})$ are negligible compared to $\exp(g_{TS3})$. Thus $X_{TS3,D}$, $X_{TS3,E}$ and $X_{TS3,A}$ all reduce to 0; $X_{TS4,D}$ and $X_{TS5,E}$ reduce to 1; while $X_{TS4,E}$ and $X_{TS5,D}$ reduce to 0. In this case, Step 3 has a low energy barrier and the transition state in Step 3 exhibits no rate-control. The transition states in Step 4 and 5 have complete rate-control on the rate of product formation in its own branch, but they have no rate-control on the other branch. The DRCs of transition states in the rate of reactant consumption still add up to 1, with fractional contributions from the two branches based on the relative height of the transition states in Step 4 versus 5. Eqs (6.38) and (6.39) simplify in this case to Eqs (6.46) and (6.47):

$$X_{TS4,A} = \frac{\exp\left(g_{TS4}\right)}{\exp\left(g_{TS4}\right) + \exp\left(g_{TS5}\right)} \tag{6.46}$$

$$X_{TS5,A} = \frac{\exp\left(g_{TS5}\right)}{\exp\left(g_{TS4}\right) + \exp\left(g_{TS5}\right)} \tag{6.47}$$

The ratio σ calculated with Eq (6.4) (which is the same for all intermediates) equals 1, no matter which rate's DRC you use in Eq (6.4) (i.e., that corresponding to rate of D production, E production or A consumption). This result is reasonable because the steps that exhibit rate-control only require one surface site.

All of the results for this complex mechanism are consistent with Eqs (6.3) and (6.4).

6.7 USING DIFFERENT ZERO-ENERGY REFERENCE STATES

In the sections above, we used the standard-state Gibbs free energy of the stoichiometrically-combined reactants (plus the intermediate-free catalyst) as a convenient zero-energy reference state. However, when using quantum mechanical methods (such as DFT) to estimate reaction energetics, it is often more convenient to use absolute energies for the species *i*, where the zero-energy reference is, for example, isolated atoms or the free electrons plus nuclei. In Reaction 6 below, we use this type of zero-energy reference for an example in homogeneous catalysis. We also used this in the example of Michaelis−Menten kinetics for enzyme-catalyzed reactions treated in ref.,[191] but failed to explicitly state that there. The DRCs of intermediates and transitions remain unchanged with choice of reference state, as shown below. However, an important result of using such an absolute zero-energy reference is that the DRCs of reactants and free catalyst are no longer zero, as shown below. In heterogeneous catalysis studied using DFT with periodic boundary conditions, such an absolute-energy reference is often used for the reactants and products, but the energy of the adsorbate-free catalyst slab is subtracted from that of the catalyst-bound absorbates, so that the energy of the adsorbate-free catalyst slab is part of the zero-energy reference state, and its DRC is therefore 0. The choice of reference state does not affect the numbers in Eq (6.4), but it does change the terms is calculating apparent activation energies (E_{app}) using the equation we derived recently,[191] which is:

$$E_{app} = RT + \sum_i X_i H_i^0 \quad . \tag{6.48}$$

Here, the second term is the sum of the standard-state enthalpies of all species *i* that appear in the reaction pathway, including all intermediates and transition states (and reactants and catalyst sites), each weighted by its DRC (which is zero for reactants and catalyst sites when using them as the zero-energy reference). Since H_i^0 is the enthalpy of species *i*, its value depends on the choice of reference state. As we show next, the change in DRC value for reactants and catalyst sites from zero (with reactants and catalyst as the reference state) to non-zero (with an absolute energy reference state) is exactly compensated by Eq (6.48), so that the same E_{app} results, provided that one includes also the reactants and catalyst sites in the sum over *i* in Eq (6.48).

We take Reaction 1 and its rate expression (Eq (6.7)) above as an example to show how this works. To simplify this, we assume the surface is nearly saturated with A*, in which case Eq (6.7) reduces to:[42]

$$r = \frac{k_B T}{h} \exp\left(g_{TS3} - 2g_{A*}\right) \frac{p_B}{p_A} \tag{6.49}$$

From Eq (6.49) it is easy to calculate that TS3 has a DRC of 1, A* has a DRC of -2 and B* has a DRC of 0. The relation between the absolute (standard-state) free energies of these species and their free energies using the reactants (plus the intermediate-free catalysts) as the zero-energy reference can be expressed as:

$$g_{TS3} = g'_{TS3} - g'_A - g'_B - 2g'_* \tag{6.50}$$

$$g_{A*} = g'_{A*} - g'_{A} - g'_{*} \tag{6.51}$$

where g'_i is the reduced *absolute* free energy of species *i* and g_i is its reduced free energy relative to that of the reactants plus catalyst. Plugging Eqs (6.50) and (6.51) into Eq (6.49) gives:

$$r = \frac{k_B T}{h} \exp\left(g'_{TS3} - 2g'_{A*} + g'_{A} - g'_{B}\right) \frac{p_B}{p_A} \tag{6.52}$$

From Eq (6.52) we can calculate that $X_3 = 1$, $X_{A*} = -2$, $X_A = 1$ and $X_B = -1$. Note that the reactants (A and B) now have non-zero DRCs that are equal to the negative of their reaction orders. However, the DRCs of transition states and intermediates remain unchanged with this change of reference state. One can prove this for the general case as follows:

$$\left(\frac{\partial \ln r}{\partial g_{TS3}}\right) = \left(\frac{\partial \ln r}{\partial g'_{TS3}}\right)\left(\frac{\partial g'_{TS3}}{\partial g_{TS3}}\right) = \left(\frac{\partial \ln r}{\partial g'_{TS3}}\right) \tag{6.53}$$

$$\left(\frac{\partial \ln r}{\partial g_{A*}}\right) = \left(\frac{\partial \ln r}{\partial g'_{A*}}\right)\left(\frac{\partial g'_{A*}}{\partial g_{A*}}\right) = \left(\frac{\partial \ln r}{\partial g'_{A*}}\right) \tag{6.54}$$

Although using the absolute energies gives non-zero DRCs to reactants (and often to free catalyst sites), it does not affect the value of E_{app} calculated with Eq (6.48). If the stoichiometrically-combined reactants (plus the intermediate-free catalysts) is used as zero-energy reference, the E_{app} calculation with Eq (6.48) can be written as:

$$\begin{aligned} E_{app} &= RT + X_3 H^0_{TS3} + X_{A*} H^0_{A*} \\ &= RT + H^0_{TS3} - 2H^0_{A*} \\ &= RT + \left(H'_{TS3} - H'_{A} - H'_{B} - 2H'_{*}\right) - 2\left(H'_{A*} - H'_{A} - H'_{*}\right) \\ &= RT + H'_{TS3} - 2H'_{A*} - H'_{B} + H'_{A} \end{aligned} \tag{6.55}$$

If the absolute energies are used as a reference, Eq (6.48) should be written instead to also include reactants and free catalyst sites in its sum, giving:

$$\begin{aligned} E_{app} &= RT + X_3 H'_{TS3} + X_{A*} H'_{A*} + X_A H'_A + X_B H'_B + X_* H'_* \\ &= RT + H'_{TS3} - 2H'_{A*} - H'_B + H'_A \end{aligned} \tag{6.56}$$

Note that Eq (6.55) and Eq (6.56) give the same value for E_{app}.

6.8 REACTION 6. ENZYME-CATALYZED REACTION FOLLOWING MICHAELIS-MENTON KINETICS

The relationship between the fractional coverage of rate-determining intermediates and their DRCs described above can be easily applied to homogeneous and enzyme catalysis, with some minor adjustments. In homogeneous catalysis, an absolute energy reference is often used, so we will use that here. Here an enzyme-catalyzed reaction following the Michaelis-Menton (M-M) mechanism[195] is used as an example.

In the M-M mechanism, a typical enzyme-catalyzed reaction consists of two steps:

1. $E + S \rightleftharpoons ES$
2. $ES \rightarrow E + P$

Step 1 is a reversible binding process between the substrate (S) and the enzyme (E), and ES is the enzyme-substrate complex. Step 2 is the formation and release of the product (P). Appling steady-state approximation to ES gives the rate equation:[195]

$$r = \frac{k_2 [E]_0}{1 + K_M / [S]_0} \tag{6.57}$$

$$K_M = \frac{k_{-1} + k_2}{k_1} \tag{6.58}$$

where r is the rate per unit volume, $[E]_0$ is the initial concentration of the enzyme, $[S]_0$ is the initial concentration of the substrate (treated here more exactly as its unitless activity), and K_M is the Michaelis constant. If the rate constants and the equilibrium constants are expressed in terms of g_is, the rate (per catalyst site) from Eq (6.57) can be rewritten as:

$$r/[E]_0 = \frac{k_B T}{h} \frac{\exp(g'_{TS2} - g'_{ES})}{1 + \exp(g'_E + g'_S - g'_{ES})\left[1 + \exp(g'_{TS2} - g'_{TS1})\right]/[S]_0} \tag{6.59}$$

Here we have used an absolute energy reference, so that g_E and g_S are non-zero. The DRC of intermediate ES and transition states can be calculated by plugging Eq (6.59) into Eq (6.1):

$$X_{ES} = \frac{\partial(\ln r)}{\partial g'_{ES}} = -1 + \frac{1 + \exp(g'_{TS2} - g'_{TS1})}{1 + \exp(g'_{TS2} - g'_{TS1}) + \exp(g'_{ES} - g'_E - g'_S)[S]_0} \tag{6.60}$$

$$X_{TS1} = \frac{\partial(\ln r)}{\partial g'_{TS1}} = \frac{\exp(g'_{TS2} - g'_{TS1})}{1 + \exp(g'_{TS2} - g'_{TS1}) + \exp(g'_{ES} - g'_E - g'_S)[S]_0} \tag{6.61}$$

$$X_{TS2} = \frac{\partial(\ln r)}{\partial g'_{TS2}} = 1 - \frac{\exp(g'_{TS2} - g'_{TS1})}{1 + \exp(g'_{TS2} - g'_{TS1}) + \exp(g'_{ES} - g'_E - g'_S)[S]_0} = 1 - X_{TS1} \tag{6.62}$$

Frequently, the energy of the transition state for Step 2 is much higher than that for Step 1, so $\exp(g'_{TS2} - g'_{TS1}) \ll 1$, In this case, X_{TS1} reduces to 0, and X_{TS2} reduces to 1. When the enzyme is also present at low level compared to the substrate, the initial concentration of S approximately equals its equilibrium concentration. Also note that the term $\exp(g'_{ES} - g'_E - g'_S)$ equals the equilibrium constant of Step 1. In this case,

$$\exp(g'_{ES} - g'_E - g'_S)[S]_0 = K_1[S]_0 = \frac{[ES]}{[E][S]}[S]_0 \approx \frac{[ES]}{[E]} \tag{6.63}$$

Plugging Eq (6.63) back to Eq (6.60) gives:

$$X_{ES}=-1+\frac{1}{1+[ES]/[E]}=-1+\frac{[E]}{[E]+[ES]}=-\frac{[ES]}{[E]_0} \tag{6.64}$$

Eq (6.64) suggests that the DRC of intermediate ES equals the fraction of enzyme occupied by the substrate times -1. $[ES]/[E]_0$ is the fractional coverage of catalyst sites by S, θ_S, in this enzyme-catalyzed reaction. Comparing Eq (6.64) with Eq (6.3) gives $\sigma = 1$. It is consistent with the result derived from surface-catalyzed reactions because the enzyme here is as a single-site catalyst, so only 1 site is required in any rate-controlling steps. These results are all consistent with Eqs (6.3) and (6.4).

We previously discussed three special cases of this M-M mechanism:[191]

1. When $[S]_0 >> K_M$, the initial steady-state turnover-frequency (TOF, or overall rate per catalyst site) expression is:[191]

$$TOF = r/[E]_0 = k_2[E]_0/[E]_0 = \frac{k_BT}{h}\exp\left(g'_{TS2}-g'_{ES}\right)$$

In this case, the DRC of ES is -1, consistent with Eq (6.4)and the fact that essentially all the enzyme sites are bound as ES ($\theta_S = 1$).

2. When $[S]_0 << K_M$ and $k_{-1}<<k_2$,[191]

$$TOF = r/[E]_0 = \frac{k_BT}{h}\exp\left(g'_{TS1}-g'_{E}-g'_{S}\right)[S]_0$$

In this case, the DRC of ES is 0, consistent with Eq (6.4) and the fact that essentially none of the enzyme sites are bound as ES ($\theta_S = 0$). Note that both reactant (S) and free catalyst (E) have DRCs of -1 in this energy reference. Eq (6.48) give that $E_{app} = RT+H^0_{TS1}-H^0_E-H^0_S$ in this absolute-energy reference system.

3. When $[S]_0 << K_M$ and $k_{-1}>>k_2$,[191]

$$TOF = r/[E]_0 = \frac{k_B T}{h}\exp\left(g'_{TS2} - g'_E - g'_S\right)[S]_0$$

In this case, TS2 has DRC = 1 . Again both E and S have DRC = -1. Eq (6.48) gives $E_{app} = RT+H^0_{TS2}-H^0_E-H^0_S$.

We note that we used this absolute energy reference in our previous paper[191] discussing these three special cases of M-M kinetics without properly clarifying that we were doing so.

6.9 CASE STUDIES THAT FURTHER VALIDATE EQ (6.4) COMBINED WITH EQ (6.3)

To further validate Eq (6.4) (plus Eq (6.3)) for calculating the DRCs of adsorbed intermediates, we will next apply it to several more complex reaction mechanisms and their associated microkinetic models that have been published in the literature, and compare the resulting DRCs for adsorbates computationally obtained using Eq (6.4) with those obtained by full computational analysis of the microkinetic model and calculations of DRCs via Eq (6.1) (by taking numerical derivatives of the rates).

6.9.1 *Case Study I. Carbonyl Reaction Mechanism for the Water-Gas Shift Reaction*

We first consider the water-gas shift reaction over Cu(111) via the carboxyl mechanism studied by Dumesic's group[193] to validate Eqs (6.3) and (6.4) above. The elementary steps are listed below,

1. $CO + * \rightarrow CO*$
2. $H_2O + * \rightarrow H_2O*$
3. $H_2O* + * \rightarrow H* + OH*$
4. $CO* + OH* \rightarrow cCOOH* + *$
5. $cCOOH* \rightarrow tCOOH*$
6. $tCOOH* + * \rightarrow CO_2* + H*$
7. $CO_2* \rightarrow CO_2 + *$
8. $2H* \rightarrow H_2 + 2*$

All the rate constants and equilibrium constants are obtained from Dumesic's paper,[193] and the microkinetic modeling was carried out under the same conditions they used: P_{CO}, P_{H2O}, P_{H2} and P_{CO2} = 0.07, 0.21, 0.38 and 0.085 atm, respectively, and temperature = 523 K.

The coverages and DRCs we calculated from numerical solutions of the rate are the same as Dumesic's published results.[193] The transition state in Step 6 (TS6) has a DRC of 1 while the DRCs of all other transition states are close to zero, which indicates that Step 6 is essentially the rate-determining step in the mechanism. CO* is the most abundant adsorbate whose fractional coverage is 0.932. Its DRC is -1.865. The ratio σ is 1.865/0.932 = 2.001. It is in great agreement with our derivation above since there are two surface sites that participate in the only RDS. To further test the applicability of Eq (6.4), we increased the activation energy of Step 5 (from its initial value of 0.48 eV used above), so that Step 5 gains some DRC and finally become the RDS when its activation energy is increased enough. The DRCs of Step 5 and 6 changing with the activation energy of Step 5 are shown in Figure 6.1.

As the activation energy of Step 5 increases, the DRC of the transition state in Step 6 (TS6) decreases and TS5 gradually takes over as the rate-determining transition state. Meanwhile CO* is still the most abundant adsorbate and the fractional coverage of CO* stays 0.932 in this range where the activation energy of Step 5 varies. Using Eqs (6.3) and (6.4), the DRC of CO* can be predicted, and the prediction is compared with that obtained by computational differentiation of the rates calculated using the full microkinetic model in Figure 6.2.

This shows that Eqs (6.3) and (6.4) are valid and give highly accurate predictions of the DRCs of adsorbates based on their fractional coverages in real reaction mechanisms, even where two steps exhibit large degrees of rate-control at the same time.

6.9.2 *Case Study II. Selective Ethylene Oxidation over Silver*

In collaboration with Per Stoltze's group at Aalborg University and N.C. Schiødt at Haldor Topsøe, Campbell performed a study of selective epoxidation of ethylene with O_2 over metallic Ag catalysts, and it shows the power of DRC analysis in analyzing complicated branched reactions.[196] In this case study, we will revisit this reaction with both full microkinetic modelling and DRC analysis.

This reaction includes 17 elementary steps as shown below,

1. $O_2(g) + * \rightleftharpoons O_2^*$
2. $O_2^* + * \rightleftharpoons 2O*$
3. $O_2(g) + 2O^* \rightleftharpoons 2O/O^*$
4. $C_2H_4(g) + O^* \rightleftharpoons C_2H_4/O^*$
5. $C_2H_4/O^* + O/O^* \rightleftharpoons CH_2CH_2O/O^* + O^*$
6. $C_2H_4O(g) + O^* \rightleftharpoons C_2H_4O/O^*$
7. $CH_2CH_2O/O^* \rightleftharpoons C_2H_4O/O^*$
8. $CH_2CH_2O/O^* \rightleftharpoons CH_3CHO/O^*$
9. $CH_3CHO/O^* \rightleftharpoons CH_3CHO(g) + O^*$
10. $CH_3CHO/O^* + 6O^* \rightleftharpoons 2CO_2^* + 4OH^* + *$
11. $C_2H_4(g) \rightleftharpoons C_2H_4^*$
12. $C_2H_4/O^* + O^* \rightleftharpoons CH_2CHOH/O^* + *$
13. $CH_2CHOH/O^* + O^* \rightleftharpoons CH_2CHO/O^* + OH^*$
14. $CH_2CHO/O^* + 5O^* \rightleftharpoons 2CO_2^* + 3OH^* + *$
15. $2OH^* \rightleftharpoons H_2O^* + O^*$
16. $CO_2^* \rightleftharpoons CO_2(g) + *$
17. $H_2O^* \rightleftharpoons H_2O(g) + *$

The microkinetic modeling is carried out with $P_{O_2} = P_{C_2H_4} = 100$ kPa at 500 K in the limit of low conversion using the parameters listed in ref.[196] There are three potential products: ethylene epoxide (C_2H_4O), CO_2 (plus water) and CH_3CHO. At steady state with the given reaction conditions, the production rate of CH_3CHO is significantly smaller than the other two products, so we will focus on the rate to the other two products and ignore CH_3CHO in the following analysis. In Table 6.1, the DRCs of the transition states in each step corresponding to the rate of C_2H_4 consumption (r4, rate of Step 4), the rate of C_2H_4O production (r6) and the rate of CO_2 production (r16) are listed. These are similar to those in ref.[196] The sum of these DRCs and the predicted σ values using Eq (6.4) are also listed in Table 6.1. For the transition states, their DRCs for each corresponding rate add up to 1.0. In Table 6.2, the DRCs of adsorbed intermediates corresponding to the same three rates and their fractional coverages are listed, along with their ratio σ calculated with Eq (6.3). (Intermediates whose fractional coverages are below 0.01 are not listed.) The prediction of the ratio of their DRCs to coverages, σ, calculated using Eq (6.4) (shown in Table 6.1) is in excellent agreement with that obtained from applying Eq (6.3) to the actual DRCs and coverages (in Table 6.2) calculated based on the rates and coverages resulting from the computational analysis of the full microkinetic model. This strongly supports the general validity of Eqs (6.3) and (6.4).

6.10 SITE-BLOCKING POISONS

In the examples above, we have not considered the presence of a "poison" species in the reactant fluid that does not contribute to the reaction but can poison sites on the catalyst, often also called a "spectator" species. One can include this poison and its elementary reactions in the rate equation solution, so the adsorbed species produced by this poison (and the transition states to and from this adsorbed poison) can have non-zero DRCs. To calculate these, one must include the standard state of the fluid poison in the zero-energy reference state along with the reactants.

For example, Eqs (6.3) and (6.4) are still correct if such a catalyst-bound species is generated from fluid reactants. In this case, the poison can be considered as a catalyst-bound intermediate produced in a side reaction in a branched reaction of the type already discussed above.

To extend to cases where there is a poison species generated from some new fluid-phase species that is mixed in with the normal reactants, let us consider the simple L-H mechansim (Reaction 1 above) as an example. An extra step is simply added to this mechanism:

$$P + * \rightleftharpoons P*$$

which indicates that a poison species P is mixed with the reactants and it can block the catalyst sites. It adds an extra term in the denominators of Eqs (6.5)-(6.7) and an extra term $\exp\left(g_{P*}\right) p_P$

in the denominator of Eq (6.8). The coverage of A*, B*, P* and the rate equation with this poison is now

$$\theta_{A*} = \frac{\exp(g_{A*})p_A}{1+\exp(g_{A*})p_A+\exp(g_{B*})p_B+\exp(g_{P*})p_P}$$
$$\theta_{B*} = \frac{\exp(g_{B*})p_B}{1+\exp(g_{A*})p_A+\exp(g_{B*})p_B+\exp(g_{P*})p_P}$$
$$\theta_{P*} = \frac{\exp(g_{P*})p_P}{1+\exp(g_{A*})p_A+\exp(g_{B*})p_B+\exp(g_{P*})p_P}$$
$$r = \frac{k_B T}{h}\frac{\exp(g_{TS3})p_A p_B}{\left[1+\exp(g_{A*})p_A+\exp(g_{B*})p_B+\exp(g_{P*})p_P\right]^2}$$

Plugging the new rate equation into Eq (6.1) gives the DRC of A*, B* and P*

$$X_{A*} = -\frac{2\exp(g_{A*})p_A}{1+\exp(g_{A*})p_A+\exp(g_{B*})p_B+\exp(g_{P*})p_P} = -2\theta_{A*}$$
$$X_{B*} = -\frac{2\exp(g_{B*})p_B}{1+\exp(g_{A*})p_A+\exp(g_{B*})p_B+\exp(g_{P*})p_P} = -2\theta_{B*}$$
$$X_{P*} = -\frac{2\exp(g_{P*})p_P}{1+\exp(g_{A*})p_A+\exp(g_{B*})p_B+\exp(g_{P*})p_P} = -2\theta_{P*}$$

It shows that Eqs (6.3) and (6.4) are still valid with poison species. It is easy to give similar proof for many other model reactions with poisons present.

6.11 CONCLUSIONS

Under steady-state reaction conditions, the degree of rate control for any catalyst-bound intermediate is proportional to its fractional population of catalyst sites, as in Eq (6.3), with a proportionality constant σ that is the DRC-weighted average of the site requirements for all the elementary steps as given by the sum in Eq (6.4). This sum typically includes only a few terms (only one when there is a single rate-determining step), since only a few transition states have non-negligible DRCs.

6.12 FIGURES

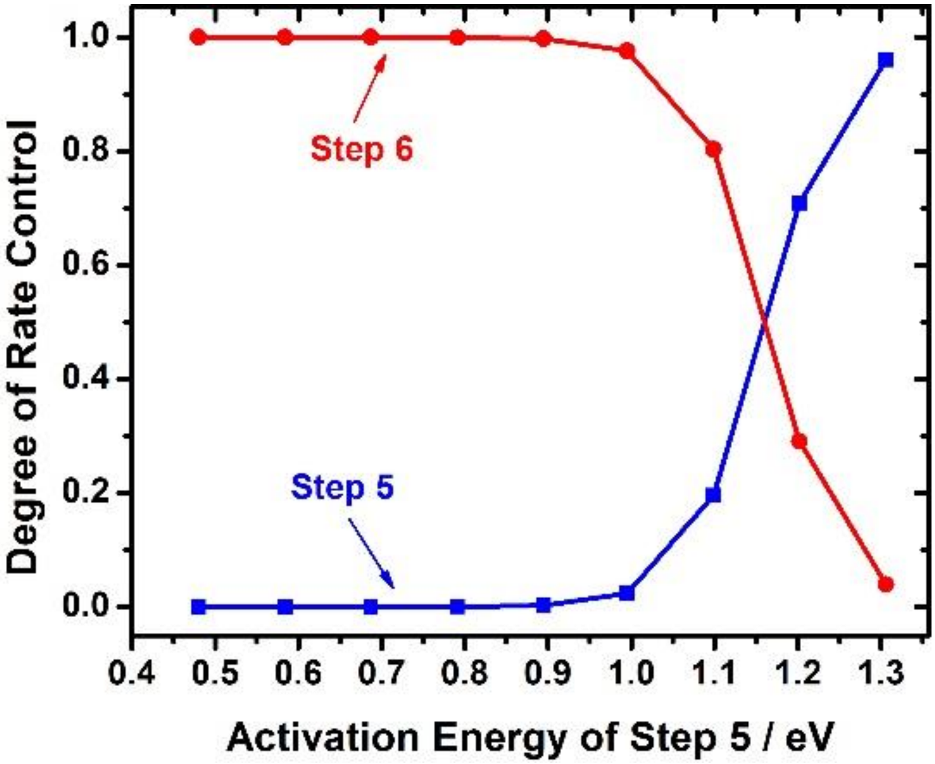

Figure 6.1 The effect of increasing the activation energy for Step 5 on the degrees of rate control of the transition states for the rate-controlling steps (blue, Step 5; red, Step 6) for the rate of water-gas shift over Cu(111) via the carboxyl mechanism, under the given conditions (P_{CO}=0.07 atm, P_{H2O}=0.21 atm, P_{H2}=0.38 atm and P_{CO2}=0.085 atm, T=523 K). The DRCs of all other 6 transition states are close to zero, so they are not shown here.

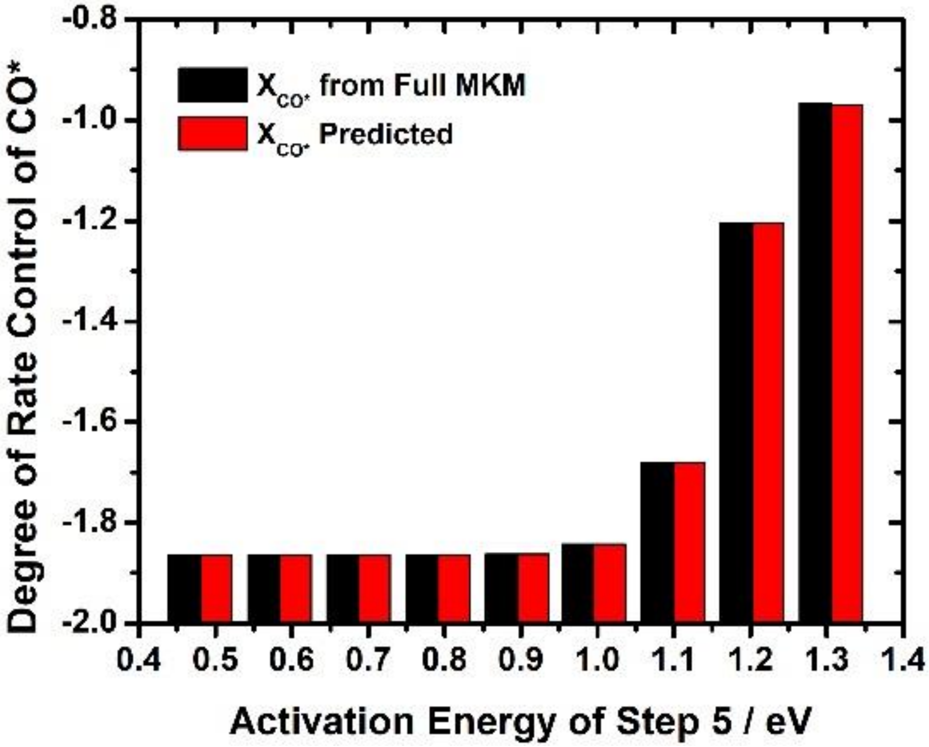

Figure 6.2 Comparison of predicted degrees of rate control of adsorbed CO with the full microkinetic analysis. Black, predicted using Eqs 3 and 4; red, full microkinetic model (MKM) analysis.

6.13 TABLES

Table 6.1 DRCs of transition states for the three net rates in ethylene oxidation over Ag. DRCs of the transition states and the ratios σ (appropriate for any adsorbate) predicted using these in Eq 4, for selective ethylene oxidation, with separate columns corresponding to DRCs for three different rates: the rate of C_2H_4 consumption, the rate of C_2H_4O production and the rate of CO_2 production. The reaction condition is $P_{O2} = P_{C2H4}$ =100 kPa at 500 K in the limit of low conversion.

Step	DRC_{C2H4}	DRC_{C2H4O}	DRC_{CO2}
1	0.001	0.001	0.001
2	0.490	0.471	0.514
3	0.002	0.002	0.001
4	0.000	0.000	0.000
5	0.380	0.439	0.312
6	0.000	0.000	0.000
7	0.321	0.754	-0.174
8	-0.295	-0.729	0.200
9	0.000	0.000	0.000
10	0.000	0.000	0.000
11	0.000	0.000	0.000
12	0.000	0.000	0.000
13	-0.021	-0.061	0.024
14	0.000	0.000	0.000
15	0.123	0.123	0.123
16	0.000	0.000	0.000
17	0.000	0.000	0.000
Sum	1.000	1.000	1.000
Predicted σ	1.972	1.972	1.975

Table 6.2 Coverages and DRCs of adsorbed intermediates for the three net rates in ethylene oxidation over Ag, and their ratio σ calculated with Eq (6.3). Coverages and DRCs of the adsorbed intermediates and their corresponding ratios σ calculated using Eq (6.3) for species with coverage higher than 0.01, with columns corresponding to the rate of C_2H_4 consumption, the rate of C_2H_4O production and the rate of CO_2 production. The reaction conditions are the same as in Table 6.1.

Species	**Coverage**	**C_2H_4**		**C_2H_4O**		**CO_2**	
		DRC	σ	**DRC**	σ	**DRC**	σ
O*	0.074	-0.147	-1.972	-0.147	-1.972	-0.147	-1.974
O/O*	0.095	-0.188	-1.972	-0.188	-1.972	-0.188	-1.974
C_2H_4/O*	0.183	-0.361	-1.972	-0.361	-1.972	-0.362	-1.974
CH_2CH_2O/O*	0.013	-0.026	-1.971	-0.026	-1.971	-0.026	-1.974
C_2H_4*	0.159	-0.314	-1.972	-0.314	-1.972	-0.314	-1.974
OH*	0.124	-0.245	-1.972	-0.245	-1.972	-0.246	-1.974

Chapter 7. Kinetic Isotope Effects: Interpretation and Prediction Using Degrees of Rate Control

This chapter has been published as:
Z. Mao, C. T. Campbell, *ACS Catalysis*, 2020, 10, 4181-4192.

Chapter Abstract

Kinetic isotope effects (KIEs) have been used for decades in catalysis research as a tool for clarifying reaction mechanisms. Significant primary kinetic isotope effects have usually been interpreted as being a result of isotope substitution at a site of bond breaking (or forming) in the rate-determining step in the reaction mechanism. However, quantitative analysis of the magnitude of the KIE in complex multistep reaction mechanisms is seldom reported. We prove here that the logarithm of the rate ratio for two isotopes is the weighted average over all species in the mechanism of their standard-state free energy difference between the two isotopes, divided by RT. The weighting factor is the degree of rate control (DRC) for that species (e.g., transition state, intermediate, reactant) when the rate is measured separately for each isotope. It is instead the degree of selectivity ratio control (DSRC) when the KIE is measured as the product selectivity in a parallel competition between two isotopes within the same reactant molecule. Since only a few species have non-zero DRCs (or DSRCs) for most reactions, only these few contribute to this weighted average and the KIE. We show that this provides a simple way to interpret and quantitatively predict kinetic isotope effects that is powerful in the insights it provides, allowing one to evaluate directly which species contribute most to the KIE. By applying it to H/D KIEs in several example mechanisms, we further show that the traditional way of interpreting KIEs that focuses only on the rate-determining step can easily lead to misunderstanding of KIE and the reaction mechanism. This highlights the importance to consider the effect of isotope substitution

on the energies of *all* species with large DRCs (i.e, those whose energies are kinetically relevant). This method also offers opportunities for quantitative validation of mechanism-based microkinetic models.

7.1 INTRODUCTION

The measurement of kinetic isotope effects (KIE) has been a major tool for investigating reaction mechanisms for decades. It provides important information about which bond is broken or formed in each step of the reaction, since the strongest isotope effects are associated with the breaking/forming of bonds involving the isotopically-substituted atoms.[45-48] Comparison between experimental and theoretical KIE values are often used to support or reject proposed mechanistic pathways.[47, 197] In complex reaction networks where several reaction pathways occur simultaneously, KIE measurements can also give clues about whether two reaction pathways share a common transition state (TS).[45, 198] Here, we introduce a simple method for analyzing kinetic isotope effects that provides deep insight into the reaction mechanism's energy diagram and its quantitative connection to the KIE. This also provides a quantitative tool for testing microkinetic models using KIE measurements.

The degree of rate control (DRC) is a powerful concept for understanding complex reaction mechanisms and the species whose energies most sensitively affect the net reaction rate.[42, 43] The DRC for species *i* (an intermediate or a transition state) is defined as

$$X_i = \left[\frac{\partial(\ln r)}{\partial\left(-G_i^0/RT\right)} \right]_{G_{j\neq i}^0} \tag{7.1}$$

where *r* is the net reaction rate (the rate of consumption of some reactant or the rate of production of some product) and G_i^0 is the standard-state Gibbs free energy of species *i*. The partial derivative is taken holding constant the standard-state Gibbs free energies of all other species. The concept of DRC was raised initially as a quantitative approach to identify the rate-determining step (RDS), but its application has been shown to be more than that. Mao et al.[191] proved that the apparent activation energy of a multistep reaction equals the weighted average of the standard-state enthalpies of all the species in the reaction mechanism, each weighted by its generalized DRC, plus RT. Combining the DRC with the linear scaling correlation, Wolcott et al.[1] developed a method for computational catalyst screening. Based on a similar approach, Avenesian and Christopher[186] introduced the scaled degree of rate control (S-DoRC) that mathematically couples well-known linear scaling relations with DRC analysis.

Here we show that DRC analysis provides a quantitative way to interpret and even predict kinetic isotope effects (KIEs) in complex mechanisms. This analysis reveals some important shortcomings of common methods previously used to interpret KIEs. For example, it is very common to interpret KIEs based entirely on analysis of the rate-determining step.[197-201] We show here that this can lead to large errors, and show that one must instead consider the effects of isotope substitution not only on the rate-determining step, but instead on all species with large DRCs (i.e., all species whose energies are kinetically relevant).

7.2 THEORY

For a given temperature (*T)* and at steady-state concentrations of reactants and products, the net steady-state rate (r) of a reaction is a function of the standard-state Gibbs free energies, G_i^0 , (divided by *RT*) of the species in the reaction mechanism (all reactants, intermediates, transition states and products), since all the equilibrium constants and rate constants for all the elementary steps can be calculated from them (within Transition State Theory). The total differential of (ln r) can then be written as:

$$d\left(\ln r\right)=\sum_{i=species}\left(\frac{\partial\left(\ln r\right)}{\partial\left(-G_i^0/RT\right)}\right)_{G_{j\neq i}^0}d\left(-G_i^0/RT\right)=\sum_{i=species}X_i d\left(-G_i^0/RT\right) \tag{7.2}$$

Integrating Eq (7.2) over a range of interest from some initial state with one set of G_i^0s to a final state with different G_i^0s gives the change in steady-state rate due to some change in any G_i^0s:

$$\int_{initial}^{final}\ln r=\ln\left(\frac{r_{final}}{r_{initial}}\right)=\sum_{i=species}\left(\int_{initial}^{final}X_i d\left(-G_i^0/RT\right)\right) \tag{7.3}$$

where $r_{initial}$ denotes the steady-state rate of the initial state, and r_{final} denotes that of the final state. Assuming X_i remains constant over a narrow range of interest from initial to final state, this simplifies to:[1]

$$\ln\left(\frac{r_{final}}{r_{initial}}\right)=\sum_{i=species}X_i\left(-\frac{G_{i,final}^0-G_{i,initial}^0}{RT}\right) \tag{7.4}$$

Taking the exponent of both sides yields:

$$\frac{r_{final}}{r_{initial}}=e^{\sum\limits_{i=species}-X_i\left(\frac{G_{i,final}^0-G_{i,initial}^0}{RT}\right)} \tag{7.5}$$

Eq (7.5) provides a simple way to predict the steady-state rate change if a small change of standard-state Gibbs free energy is applied to each species *i*, from $G_{i,initial}^0$ to $G_{i,final}^0$. Since most species have DRCs near zero,[42, 43] only a few species with significant DRCs exhibit rate-control and contribute to the right side of Eqs (7.4) and (7.5). Eq (7.5) has been used previously to estimate the rate of a new catalyst material relative to a reference catalyst material with similar but different properties, so that changing the catalyst changes the G_i^0 values without affecting the X_i (or DRC) values by too much.[1] It was shown to be fast and reasonably accurate for estimating rates within a similar class of materials, with errors that only arise from the change in DRC values with material. Here we will apply Eq (7.5) instead to predict the effect on the rate of a simple change in isotope of a reactant, where DRCs are expected to remain constant under many conditions.

If the reaction with isotope-substituted reactants is considered as the final system, and the reaction with normal reactants is considered as the initial system, Eqs (7.3) to (7.5) can be used to predict the kinetic isotope effect or isotope rate ratio. In this case, the integral in Eq (7.3) is over the range of free energies (G_i^0s) that occur upon isotope substitution, so that $G_{i,initial}^0$ and $G_{i,final}^0$ in Eq (7.5) correspond to the values for the H and D isotopes, respectively. For example, when some (or all) hydrogen atoms in one reactant (or several reactants) are replaced with deuterium, the KIE due to this isotope substitution is given by Eq (7.5) (after inverting both sides) as:

$$KIE = \frac{r_H}{r_D} = e^{\sum_{i=species} -X_i\left(\frac{G_{i,H}^0 - G_{i,D}^0}{RT}\right)} = \prod_{i=species} \exp\left[-X_i\left(\frac{G_{i,H}^0 - G_{i,D}^0}{RT}\right)\right] \qquad (7.6)$$

where r_H is the rate with normal reactants, r_D is the rate with deuterated reactants, X_i are the DRC values (which were assumed in this derivation to be the same for D and H), and $G_{i,H}^0$ and $G_{i,D}^0$ are the standard-state Gibbs free energies of species i which result in the proposed mechanism from normal and deuterated reactants, respectively, with the specified locations of isotope substitution. Even though the sum (or product) in Eq (7.6) looks complicated since it is over all species in the mechanism (reactants, intermediates, transition states and products), in practice only a few species have non-zero DRCs and contribute to this sum, while most species have DRCs close to zero and drop out of the sum. It has been shown before that most intermediates and transition states have negligible DRCs.[42] Also, the DRCs of products are zero when the rates are measured at low conversion. Thus, Eq (7.6) provides very direct insight into which species in the reaction mechanism influence the KIE value. *Eq (7.6) is the main result of this paper. It shows that the logarithm of the rate ratio for two isotopes is the weighted average over all species in the* *mechanism of their standard-state free energy difference between the two isotopes, divided by RT, where the weighting factor is the DRC for that species.* This is similar to our recent proof that the apparent activation energy of a complex mechanism equals a weighted average of the standard-state enthalpies (relative to reactants) of all the species, each weighted by its DRC.[191] We validate Eq (7.6) further below, and extend it to a different type of KIE measurement with Eq (7.19) below. Note that the product symbol in the right-most part of Eq (7.6) shows that each species in the mechanism contributes its own factor to the KIE. The contribution factor depends on the free energy difference between isotopes times the DRC for the species. For species with DRC close to zero (which is the case for most species), the factor equals 1.

In deriving Eq (7.6), we assumed that the DRCs of all species are the same for both isotopes. We show below that they are indeed usually very similar, but in some cases, the DRCs do change significantly with the isotope, and Eq (7.6) will have a significant quantitative error. Even in that case. Eq (7.6) does give important insights into the mechanistic reasons for the KIE.

Note that the energies of reactants can also change with isotope substitution. It is easier to include (and understand) the effect of reactant energies on the KIE via Eq (7.6) by using the "absolute zero-energy reference" method for calculating the DRC values, which results in non-zero DRCs for reactants. (Our meaning of "absolute zero-energy reference" method has been defined previously.[202]) We use that method exclusively below. (See ref. [202] for a discussion of the effect of energy reference states on the DRC values of reactants.)

We reiterate that since there are usually only a few species i that have non-zero X_i values, there are only a few terms in the sum of Eq (7.6). This makes it easy to see which species in the mechanism contribute to the KIE. We show below that this insight also allows one to uncover serious errors in methods that have been commonly used to interpret KIEs in the past. Since the difference $G_{i,H}^0 - G_{i,D}^0$ is often dominated by the difference in ZPEs (as shown below), which is easy to predict, Eq (7.6) makes it relatively easy to predict KIEs.

The free energy change upon isotope substitution can be further written as a sum of the contributions from zero-point energy (ZPE), heat capacity and entropy differences:

$$G_{i,D}^0 - G_{i,H}^0 = \left(ZPE_{i,D} - ZPE_{i,H}\right) + \left(\Delta U_{Cp,D} - \Delta U_{Cp,H}\right) - T\left(S_{i,D}^0 - S_{i,H}^0\right) \tag{7.7}$$

The first term, $ZPE_{i,D} - ZPE_{i,H}$, is the difference in enthalpy of species *i* at 0 K due to isotope substitution. The second term is the contribution from the change in enthalpy with temperature (which is usually expressed as the integral of $C_p dT$ from 0 K to the reaction temperature) due to the difference in heat capacities between the two isotopes. The last term is due to the contribution from their standard-state entropies (S^0). In most analyses, the kinetic isotope effect is attributed mainly to the zero-point energy difference due to isotope substitution, and the contributions from heat capacity and entropy differences are ignored.[203, 204] Also, it has become rather common in heterogeneous catalysis studies to neglect the heat capacity term here but include the entropy term.[47, 197, 198] We will discuss below how much each of these terms contribute to the overall KIE of several multistep reactions.

We next present a number of case studies where we look at specific reaction mechanisms where full microkinetic models have been reported in the literature, and test the validity of Eq (7.6) for predicting H/D KIEs at different reaction conditions. It generally is highly accurate and simple to perform (compared to the KIE calculated by solving the full microkinetic model for both isotopes), and provides deep insight into the proper interpretation of KIEs. It can be inaccurate, however, under conditions where the DRCs change strongly with isotope, which occurs only when two species *i* with large DRCs have quite different energy changes upon isotope substitution.

In some cases, the KIE is evaluated by measuring the H/D selectivity ratio of a branching reaction in a single reaction event, where both isotopes are included in the reactants.[205-208] In this type of measurement, r_H/r_D equals the ratio of rates to the product with H versus D isotopic label, i.e., their selectivity ratio. In Case Study IV, we derive an equation (Eq (7.19) below) analogous to Eq (7.6) for calculating the KIE in such measurements.

The results below prove the importance of going beyond the rate-determining step if one wants to understand KIEs, and that Eq (7.6) (or Eq (7.19) below) provides a simple way to interpret and even predict KIEs. These equations, when coupled with KIE measurements, will provide a powerful tool for testing the accuracy of the energies of the most kinetically-relevant species in microkinetic models, and for improving such models.

7.3 CASE STUDY I: A SIMPLE SURFACE REACTION FOLLOWING THE LANGMUIR-HINSHELWOOD MECHANISM

We first consider a typical Langmuir-Hinshelwood (L-H) mechanism with four elementary steps, a single rate-determining step (Step 3), and all other steps being fast to equilibrate:

$$1.\, A + * \leftrightharpoons A^* \qquad \text{(fast to equilibrium)}$$

$$2.\, B + * \leftrightharpoons B^* \qquad \text{(fast to equilibrium)}$$

$$3.\, A^* + B^* \rightarrow C^* + * \qquad (\text{rate} - \text{determining step})$$

$$4.\, C^* \leftrightharpoons C + * \qquad \text{(fast to equilibrium)}$$

To simplify the equations, we further assume that the RDS, Step 3 is essentially irreversible (i.e., highly exothermic) and A* is the most abundant adsorbate and it almost saturates the surface. At steady-state, application of the most-abundant surface intermediate approximation and RDS approximation showed that the rate of the reaction can be written under these conditions as:[42]

$$r = k_3 \frac{K_{ads,B^*}}{K_{ads,A^*}} \frac{p_B}{p_A} \tag{7.8}$$

where k_3 is the forward rate constant of Step 3, K_{ads,X^*} is the equilibrium constant of adsorption of gas X, and p_X is the partial pressure (or activity) of gas X. When all the rate constants and equilibrium constants are expressed in terms of the standard-state Gibbs free energies, Eq (7.8) can be written as:

$$\begin{aligned} r &= \frac{k_B T}{h} \exp\left(-\frac{G^0_{TS3} - G^0_{A^*} - G^0_{B^*}}{RT} \right) \exp\left(-\frac{\left(G^0_{B^*} - G^0_B\right) - \left(G^0_{A^*} - G^0_A\right)}{RT} \right) \frac{p_B}{p_A} \\ &= \frac{k_B T}{h} \exp\left(-\frac{G^0_{TS3} - 2G^0_{A^*} - G^0_B + G^0_A}{RT} \right) \frac{p_B}{p_A} \end{aligned} \tag{7.9}$$

where G^0_A is the standard-state Gibbs free energy of A in gas phase, and $G^0_{A^*}$ is the standard-state Gibbs free energy of A* minus that for the clean surface (and the same for B and B*). It is easy to see from Eq (7.9) that the transition state of Step 3 (TS3) has a DRC of 1, and A* has a DRC of -2, A has a DRC of 1, B has a DRC of -1, and all other DRCs are 0. If r_H is the rate with normal reactants and r_D is the rate with D-substituted reactants, the ratio of KIE can be calculated by taking the ratio of H and D rates, each from Eq (7.9). This direct calculation gives:

$$\begin{aligned} \frac{r_H}{r_D} &= \exp\left[\left(-\frac{G^0_{TS3,H} - 2G^0_{A^*,H} - G^0_{B,H} + G^0_{A,H}}{RT} \right) - \left(-\frac{G^0_{TS3,D} - 2G^0_{A^*,D} - G^0_{B,D} + G^0_{A,D}}{RT} \right) \right] \\ &= \exp\left[-\frac{\left(G^0_{TS3,H} - G^0_{TS3,D}\right) - 2\left(G^0_{A^*,H} - G^0_{A^*,D}\right) - \left(G^0_{B,H} - G^0_{B,D}\right) + \left(G^0_{A,H} - G^0_{A,D}\right)}{RT} \right] \\ &= \exp\left[-\sum_i X_i \times \frac{G^0_{i,H} - G^0_{i,D}}{RT} \right] \end{aligned} \tag{7.10}$$

As can be seen from the last line above, Eq (7.10) gives the same value of KIE as would be calculated using only Eq (7.6) and the DRCs given above.

Note that one estimates the wrong KIE for this mechanism if one focuses only on the rate-determining step, Step 3. The change in the rate constant of Step 3, k_3, due to D isotope substitution can be written as:

$$\begin{aligned}\frac{k_{3,H}}{k_{3,D}} &= \exp\left[-\frac{\left(G^0_{TS3,H}-G^0_{A^*,H}-G^0_{B^*,H}\right)-\left(G^0_{TS3,D}-G^0_{A^*,D}-G^0_{B^*,D}\right)}{RT}\right] \\ &= \exp\left[-\frac{\left(G^0_{TS3,H}-G^0_{TS3,D}\right)-\left(G^0_{A^*,H}-G^0_{A^*,D}\right)-\left(G^0_{B^*,H}-G^0_{B^*,D}\right)}{RT}\right]\end{aligned}. \tag{7.11}$$

Comparing Eq (7.11) with Eq (7.10) shows that the contribution of the energy change due to D substitution from the transition state in the rate-determining step, TS3, is correctly addressed in Eq (7.11), where only the rate constant of Step 3 in considered. However, the contributions from the catalyst-bound intermediates, A* and B*, and the contributions from the reactants, A and B, do not enter the calculation of KIE by Eq (7.11) with the correct weight factors, which should be their DRCs, as shown by Eq (7.10). This gives rise to a difference in the free energy terms between Eq (7.10) and Eq (7.11), which equals: $\left[\left(G^0_{A,H}-G^0_{A^*,H}\right)-\left(G^0_{A,D}-G^0_{A^*,D}\right)\right]+\left[\left(G^0_{B^*,H}-G^0_{B,H}\right)-\left(G^0_{B^*,D}-G^0_{B,D}\right)\right]$. This is just the changes in the adsorption free energies of A* and B* upon D substitution summed together. For many molecularly adsorbed species, their free energies of adsorption will not depend much upon the isotope. However, if a bond to a H atom within the molecule is considerably weakened upon adsorption (for example, in making a three-center bond to a metal atom on the catalyst), then there can be a large isotope effect on the adsorption energy, and this can contribute greatly to the KIE. Also, this simple L-H mechanism considers *only* molecular adsorption as the equilibrated steps before the rate-determining step. However, real L-H mechanisms often involve equilibrated dissociative adsorption steps, or equilibrated steps where H is abstracted from or added to an adsorbate, and the isotope effect on these reactions' free energies can be very large (see below). To generalize, the isotope effect on the equilibrated steps is not included if the KIE is calculated considering only the rate-determining step. Thus, the KIE on the rate constant for a single step, even if it is the rate-determining step, is often not nearly enough to represent the overall KIE of a multistep reaction. For example, in the Discussion section we will show that calculating the KIE by considering the rate-determining step only over-estimates the KIE by a factor of 1.8 for an example DFT-based microkinetic model of the CO_2 hydrogenation reaction catalyzed by the Cu(211) surface.

7.4 CASE STUDY II: MICHAELIS-MENTEN MECHANISM FOR ENZYME CATALYZED REACTIONS

Here we analyze a simple enzyme-catalyzed reaction that follows the Michaelis-Menten (M-M) mechanistic model using Eq (7.6). The M-M mechanism can also be applied to other homogeneous or heterogeneous catalyzed reactions, but here we only consider an enzyme-catalyzed reaction as an example, and the method we show here also works for other reactions that follow the M-M mechanism.

The reaction consists of two steps:

$$1. E + S \leftrightharpoons ES$$

$$2. ES \rightarrow E + P$$

Step 1 is a reversible binding process between the substrate (S) and the enzyme (E), and ES is the enzyme-substrate complex. Step 2 is the formation and release of the product (P). Applying the steady-state approximation to the enzyme-substrate complex ES concentration [ES], the rate equation is:[195]

$$r = \frac{k_2[E]_0}{1 + K_M/[S]} \tag{7.12}$$

$$K_M = \frac{k_{-1} + k_2}{k_1} \tag{7.13}$$

where $[E]_0$ is the initial concentration of the enzyme, [S] is the concentration of the substrate, and K_M is the Michaelis constant. If we consider a typical situation where the enzyme is present at very low concentration compared to the substrate, and at steady state almost all enzymes exist as ES, Eq (7.12) reduces to:[191]

$$r = k_2[E]_0 = \frac{k_B T}{h} \exp\left(-\frac{G^0_{TS2} - G^0_{ES}}{RT} \right)[E]_0 \tag{7.14}$$

In this case, the transition state of Step 2 (TS2) has a DRC of 1, ES has a DRC of -1, and the rate is only determined by the rate constant of Step 2 and the initial concentration of the enzyme. If some H atoms in the reactants are replaced with D, the KIE will be:

$$\begin{aligned} \frac{r_H}{r_D} &= \exp\left[\left(-\frac{G^0_{TS2,H} - G^0_{ES,H}}{RT} \right) - \left(-\frac{G^0_{TS2,D} - G^0_{ES,D}}{RT} \right) \right] \\ &= \exp\left[-\frac{\left(G^0_{TS2,H} - G^0_{TS2,D}\right) - \left(G^0_{ES,H} - G^0_{ES,D}\right)}{RT} \right] \\ &= \exp\left[-\frac{X_{TS2}\left(G^0_{TS2,H} - G^0_{TS2,D}\right) + X_{ES}\left(G^0_{ES,H} - G^0_{ES,D}\right)}{RT} \right] \end{aligned} \tag{7.15}$$

Note Eq (7.15) gives the same value as predicted by Eq (7.6).

7.5 CASE STUDY III: CO_2 HYDROGENATION OVER CU(211) AND ZN-PROMOTED CU(211)

In this section, the kinetic isotope effects of methanol synthesis through CO_2 hydrogenation over Cu(211) and Zn-promoted Cu(211) model catalysts are investigated to verify the accuracy of Eq (7.6) in real reaction mechanisms, and under what class of conditions its accuracy is lacking. The reaction is:

$$3\mathrm{H_2} + \mathrm{CO_2} \rightarrow \mathrm{H_2O} + \mathrm{CH_3OH}.$$

We analyze here the KIE for replacing H_2 with D_2 in a previously reported mechanism consisting of 8 elementary steps[191] with full microkinetic modeling and this DRC method (Eq (7.6)). This mechanism and the energies of all species in these steps are taken from the DFT calculations reported by Studt et al.[198, 209] The standard-state Gibbs free energy change upon D isotope substitution for H in all species was also reported for all species on this Zn-promoted Cu model catalyst and they are summarized in Table 6.1.[209] We assume here that the change in free energy of each species upon replacing H with D is the same on Cu(211) as on the Zn-promoted Cu, which is equivalent to assuming that the adsorbates and adsorbed transition states have very similar normal mode vibrational frequencies on both surfaces. Since in this paper the value of the energetic change used in Eq (7.6) and in full microkinetic modeling is the same, this assumption may be wrong but it does not affect the comparison we wish to make here, which is only the accuracy of results from Eq (7.6) compared to full microkinetic modeling for such complex mechanisms. Indeed, it does not even matter for this comparison whether the mechanism and DFT energetics for the H isotope are correct or not, and we make no attempt here to evaluate their accuracy.

Figure 7.1 shows the standard-state Gibbs free energy diagram on Cu(211) and Zn-promoted Cu(211) surfaces at 480 K for both normal reactants and deuterated reactants.

Microkinetic modeling and DRC calculations were carried out using CATMAP, a Python-based catalytic microkinetic modeling package.[210] The net rates, coverages, and DRCs at steady state were calculated under the following steady-state conditions at the low-conversion limit: 30 bar total, $H_2(D_2)$:CO_2 = 3:1, 480 K.

Throughout this paper, we calculate the DRCs using an absolute zero-energy reference (i.e, the isolated nuclei and electrons). (See ref. [202] for a discussion of how the zero-energy reference can affect the DRCs.) The calculated DRCs of all species (including reactants, intermediates and transition states) and the intermediate coverages on Cu(211) with normal and deuterated reactants are listed in Table 7.2 for the reaction conditions given there. The DRCs do not change much from the normal H isotope to the fully deuterated reaction system. The DRC of H_2 has the largest relative change, from -0.56 to -0.51. There is only one transition state, H-HCOOH, with a non-negligible DRC, and it is close to 1 for both isotopes. This means that this step (i.e., the third hydrogenation step) is the rate-determining step, whether the reactants are deuterated or not. Adsorbed formate (HCOO*) is the most abundant surface intermediate. It almost saturates the surface and thus has a large DRC close to -2, leaving the DRCs of all the other adsorbates close to zero. The proportionality factor of -2 that relates its fractional coverage to its DRC is as expected based on their general relationship presented elsewhere.[202] The DRC of CO_2 changes from 0.86 for H to 0.97 for D, but since its free energy is the same for H and D, it does not contribute to the KIE according to Eq (7.6).

Solving the full microkinetic model to get rates on Cu(211) at the conditions of Table 7.2 for both H and D gives an inverse KIE of r_H/r_D = 0.45. The KIE predicted using Eq (7.6) considering species with DRC values (for the H isotopes in Table 7.2) greater than 0.1 (H_2, CO_2, HCOO*, H-HCOOH) is:

$$\begin{aligned}\frac{r_H}{r_D} &= e^{\sum_{i=species} -X_i\left(\frac{G_{i,H}-G_{i,D}}{RT}\right)} = \prod_{i=species} \exp\left[-X_i\left(\frac{G_{i,H}-G_{i,D}}{RT}\right)\right] \\ &= \exp\left[-(-0.56)\times\frac{5.50\text{ kJ/mol}}{RT}\right]\times\exp\left[-(+0.86)\times\frac{0\text{ kJ/mol}}{RT}\right] \\ &\quad\times\exp\left[-(-1.86)\times\frac{9.46\text{ kJ/mol}}{RT}\right]\times\exp\left[-(+1.00)\times\frac{24.38\text{ kJ/mol}}{RT}\right] \\ &= (2.16)(1)(82)(1/450) = 0.40\end{aligned} \tag{7.16}$$

Using instead the DRC values for the deuterated species from Table 7.2, Eq (7.6) gives r_H/r_D = 0.51. Whether the DRCs of normal or deuterated species are used in this calculation, the results from Eq (7.6) are in good agreement with the value of 0.45 from full microkinetic modeling (i.e., within 11 and 13%). Most importantly, Eq (7.6) provides a method to calculate the contribution from each species to the KIE, and this reveals that the small KIE here is due to a fortuitous cancellation of large isotope effects on the free energies of the key species that determine the KIE (i.e., those with large DRCs). As shown in Eq (7.16), the isotope effect on the free energy of the H-HCOOH transition state is very large (24.38 kJ/mol, since it has 3 H atoms), and this, when multiplied by its DCR (1) would decrease the H rate compared to D by a factor of 450 if taken alone. However, the isotope effect on the free energy of the adsorbed formate HCOO* is also large (9.46 kJ/mol), and it, multiplied by its DRC (-1.85) would enhance the H rate compared to D by a factor of 82 if taken alone. There is also a small contribution from the free energy of the H_2 reactant (5.50 kJ/mol) that, when multiplied by its DRC (-0.56), would enhance the H rate compared to D by a factor of 2.16. The overall KIE (0.40) is the product of the contributions from all these rate-controlling species.

Inverse KIEs like this prediction (0.40) or the prediction of the full microkinetic model solution (0.45) were also reported from experimental rate measurements at these same pressures but slightly higher temperature (523 K) for Cu supported on SiO_2 and on MgO (KIE = r_H/r_D = 0.63

and 0.75, respectively).[198] At 5-fold lower pressures, the experimental KIE for Cu on SiO_2 increases slowly with increasing temperature,[211] so those KIEs would probably be lower than 0.63 and 0.75 at 480 K, giving even better agreement with the predictions of this DFT-based model. Note that any possible remaining disagreement of experiments with the result of the full microkinetic model (0.45) must be due to DFT-based errors in the microkinetic model.

The situation is more complicated when the reaction is carried out on Zn-promoted Cu(211) surface. The DRCs of species and intermediate coverages on Zn-promoted Cu(211) surface with normal and deuterated reactants are listed in Table 7.3. The full microkinetic modeling shows that the reaction on Zn-promoted Cu(211) exhibits a normal KIE of $r_H/r_D = 1.78$. HCOO* remains the most abundant adsorbates with a coverage of 1.00, and its DRC is -1.99. Unlike the reaction on the Cu(211) surface, more than one transition state exhibits rate-control on the Zn-promoted Cu(211) surface. With the normal H_2 reactant, there are four transition states with significant DRC values: H-CH_2O(0.14), H-HCOOH(0.50), H-OH(0.14), HCOO-H(0.22). The transition state of the third hydrogenation step, H-HCOOH, has the greatest DRC. With D_2, these four transition states still have DRCs greater than 0.1 and the DRCs of all other transition states are still close to zero. However, their DRCs change significantly from that with H_2 to: H-CH_2O(0.11), H-HCOOH(0.15), H-OH(0.12), HCOO-H(0.62). With D_2, the transition state of the second hydrogenation step, HCOO-H, now has the greatest DRC. This is consistent with ref [198], which states that the rate-determining step changes from the third hydrogenation to the second hydrogenation due to deuterium substitution. While this is not commonly considered, this result makes it clear that the most rate-controlling step can indeed change upon isotope substitution in some cases.

As shown in Table 7.3, the assumption that DRCs do not change upon isotope substitution *does not hold in this case*. Thus, using Eq (7.6) to predict the KIE results in a big error in this case.

Considering only species with DRCs greater than 0.1 (i.e., H_2, CO_2, HCOO*, H-CH_2CO, H-HCOOH, H-OH, HCOO-H), Eq (7.6) gives a KIE r_H/r_D of 1.14 (using DRCs of normal reaction) and 2.65 (using DRCs of deuterated reaction). These two values are in error by -36% and +49% compared to the KIE from solving the full microkinetic model for both isotopes ($r_H/r_D = 1.78$). Nevertheless, Eq (7.6) still has considerable value, since it clearly reveals the species whose H/D energy difference gives rise to the KIE: H_2, HCOO*, H-CH_2CO, H-HCOOH, H-OH and HCOO-H. This has important value in identifying the physical origin of the KIE.

The KIE value $r_H/r_D = 1.78$ calculated by solving for the rates using the full microkinetic model is not close to the experimental KIE of 0.57 measured at these conditions.[198] The difference may be due to errors in the DFT-based energies for the species with large DRCs (which would affect their DRC values more than their isotopic energy differences), or some problem with the mechanism or DFT-based model for the active site. These inaccuracies in the microkinetic model, which were not previously reported to our knowledge, do not detract from the value of using it as we have here, to test the strengths and limitations of Eq (7.6) for predicting KIEs within any given microkinetic model. Note also that Eq (7.6) and full microkinetic modeling give normal KIEs ($r_H/r_D > 1$) for this reaction, while the experimental data shows an inverse KIE ($r_H/r_D < 1$). Despite the inaccuracies of Eq (7.6) in this case, it is still accurate enough to identify that there is a rather large and qualitative difference between experiment and the predictions of this DFT-based model.

7.6 CASE STUDY IV. KINETIC ISOTOPE EFFECTS MEASURED FROM BRANCHING SELECTIVITY: INTRODUCING THE DEGREE OF SELECTIVITY RATIO CONTROL (DSRC)

In the derivation and case studies above, we only show the cases where two separate rates are measured for two reactions, one with normal reactants and one with isotope-substituted reactants. The relative ratio of these independently determined reaction rates (i.e., r_H/r_D) gives the reported KIE. However, in some cases the KIE has also been evaluated by measuring the H/D selectivity ratio of a branching reaction in a single reaction event, where both isotopes are included in the reactants.[205-208] A simplified model reaction of this type discussed by Simmons and Hartwig[208] is shown in Figure 7.2.

In this type of measurement, the KIE (i.e., r_H/r_D) equals the ratio of rates to the product via C-H bond cleavage versus C-D bond cleavage, i.e., their selectivity ratio (SR). For example, Sibbald et al. observed a intramolecular isotope effect with SR = 4 in the reaction of 1,3,5-trideuterobenzene with another reactant which reacts at either the C-H bond or the C-D bond in the benzene ring.[205] An extension of the DRC called the degree of selectivity control (DSC) offers an approach for analysis of such KIE experiments that is analogous to the methods in the sections above. The DSC for species *i* is defined as:[43]

$$DSC_i = \left(\frac{\partial \ln S}{\partial \left(-G_i^0 / RT \right)} \right)_{G_{j\neq i}^0} = \left(\frac{\partial \ln \left(r_P / r_R \right)}{\partial \left(-G_i^0 / RT \right)} \right)_{G_{j\neq i}^0} = X_{i,P} - X_{i,R} \tag{7.17}$$

where the selectivity S is defined as the ratio of the rate to the desired product, r_P, versus the rate of consumption of the most valuable reactant, r_R, and $X_{i,P}$ and $X_{i,R}$ refer to the DRCs of i in those two rates. The DSC quantifies how much the selectivity increases per unit decrease in the standard-state Gibbs free energy of species i. Here we introduce an extension of DSC which we will call the *degree of selectivity ratio control* (DSRC) for the interpretation of kinetic isotope effects on selectivities in branching reactions, where the reaction shown in Figure 7.2 is just one example. Instead of targeting the selectivity ($S = r_P/r_R$), the DSRC targets the H/D isotope selectivity ratio ($SR = r_H/r_D$):

$$DSRC_i = \left(\frac{\partial \ln\left(r_H / r_D \right)}{\partial\left(-G_i^0 / RT \right)} \right)_{G_{j \neq i}} = \left(\frac{\partial \ln\left(r_H \right)}{\partial\left(-G_i^0 / RT \right)} \right)_{G_{j \neq i}} - \left(\frac{\partial \ln\left(r_D \right)}{\partial\left(-G_i^0 / RT \right)} \right)_{G_{j \neq i}} = X_{i,H} - X_{i,D} \ ,$$

(7.18)

where $X_{i,H}$ is the DRC of species *i* for the rate of the branch via C-H bond cleavage to make the product with the D isotope label (we call this branch “Branch H” below), and $X_{i,D}$ is the DRC of species *i* for the rate of the branch via C-D bond cleavage to make the product with the H isotope label (we call this branch “Branch D” below). The DSRC quantifies the extent to which a change in the energy of species *i* affects the selectivity ratio (or branching ratio) of a branched reaction. It equals the difference between the DRCs of species *i* for the rates to different products (e,g., the product with C-H bond cleavage and the product with C-D bond cleavage).

Following the same approach as in Eqs (7.2)-(7.6) above, we derived an equation using DSRCs that can be used to calculate the KIE for cases like this where the KIE (r_H/r_D) equals the H/D selectivity ratio, as shown in the Supporting Information. As in deriving Eq (7.6), we again assumed that the DSRC of the species *i* in Branch D does not depend on the relative height of its energy in the two branches, $G_{i(D)}^0 - G_{i(H)}^0$. This gave:

$$\ln(KIE) = \ln\left(\frac{r_H}{r_D} \right) = \sum_{i=\text{species in Branch D}} -DSRC_{i(D)} \left(\frac{G_{i(D)}^0 - G_{i(H)}^0}{RT} \right) \tag{7.19}$$

Eq (7.19) provides a simple approach to interpret the deuterium kinetic isotope effect when measured as a selectivity ratio. The summation in Eq (7.19) is over all species in the reaction mechanism in Branch D, but only a few species have non-zero DSRCs and exhibit free energy difference between different branches.

We next show how this DSRC analysis of Eq (7.19) works in a quantitative way for the general reaction mechanism shown in Figure 7.2a, for the three extreme cases described in ref [208]. This reaction involves an intramolecular competition between functionalization at a C-H bond versus a C-D bond in a single reactant, which possesses a directing group (DG) that is positioned between the C-H and C-D bonds on a benzene ring. The KIE is calculated from the relative amount of the products formed from the functionalization at the C-H bond versus the C-D bond. Figure 7.2b shows a representative Gibbs free energy diagram of this reaction. The overall reaction involves three elementary steps, the reactant A, the intermediates B and C, and the product P, which can have 1 D atom or none. The transition states are named as TS1, TS2 and TS3 for the three steps. Step 2 is the step involving the cleavage of C-H or C-D bond, and it is where the branching occurs. The species in the branch where the C-H bond is broken ("Branch H") are specified with an "H" in the bracket, and the species in the other branch ("Branch D") are specified with a "D" in the bracket.

Limiting Case #1

In the first limiting case described in ref.[208], Step 2 is the single RDS, the C-H or C-D bond cleavage is irreversible, and Step 1 is fast to equilibrium. In this case, the net rates of the two branches equal the forward rate of Step 2 in these two branches, respectively. Thus, the kinetic isotope effect measured as the selectivity ratio can be written as $r_H/r_D = \left(k_{2,H}\left[B\right]\right)/\left(k_{2,D}\left[B\right]\right)$, where $k_{2,H}$ is the forward rate constant of Step 2 in Branch H, $k_{2,D}$ is the forward rate constant of Step 2 in Branch D, and [B] is the concentration (or activity) of B. Taking the logarithm of both sides of this, and expressing the rate constants with the Gibbs free energies of species gives:

$$\ln\left(\frac{r_H}{r_D}\right)=\ln\left(\frac{k_{2,H}[B]}{k_{2,D}[B]}\right)=\ln\left(\frac{\exp\left[-\left(G^0_{TS2(H)}-G^0_B\right)/RT\right]}{\exp\left[-\left(G^0_{TS2(D)}-G^0_B\right)/RT\right]}\right)=\frac{G^0_{TS2(D)}-G^0_{TS2(H)}}{RT} \tag{7.20}$$

Eq (7.20) has the same form as the equation of the Curtin-Hammett principle.[212, 213] It shows that the product selectivity in this limiting case is determined by the free energy difference between the selectivity-determining transition states, TS2(H) and TS2(D). Combining Eqs (7.20) and (7.18) gives that only the transition state in Step 2 in Branch D (TS2(D)) has a DSRC of -1 and all other species in Branch D have zero DSRCs. Plugging these DSRCs for Branch D into Eq (7.19) gives:

$$\begin{aligned}\ln\left(\frac{r_H}{r_D}\right)&=\sum_{i=\text{species in Branch D}}-DSRC_{i(D)}\left(\frac{G^0_{i(D)}-G^0_{i(H)}}{RT}\right)\\&=0-DSRC_{TS2(D)}\times\left(\frac{G^0_{TS2(D)}-G^0_{TS2(H)}}{RT}\right)=\frac{G^0_{TS2(D)}-G^0_{TS2(H)}}{RT}\end{aligned} \tag{7.21}$$

This is the same result for the KIE as Eq (7.20), showing that Eq (7.19) is correct here.

These same DSRC values can also be obtained by using results from an equivalent branching mechanism we treated in ref. [202], where the branching starts from an irreversible RDS. We proved there that (see Eqs 33-36 in ref [202]):

$$X_{TS2(D),P(D)}=1 \quad \text{and} \tag{7.22}$$

$$X_{TS2(D),P(H)}=0 \ , \tag{7.23}$$

where $X_{TS2(D),P(D)}$ is the DRC for TS2(D) in the rate to make the product of the Branch D, P(D), and $X_{TS2(D),P(H)}$ is the DRC for TS2(D) in the rate to make the product of Branch H, P(H). All other species in Branch D have DRCs close to zero, so their DSRCs are also negligible. Plugging Eqs (7.22) and (7.23) back into Eq (7.18) gives:

$$DSRC_{TS2(D)} = X_{TS2(D),P(H)} - X_{TS2(D),P(D)} = -1 \ , \tag{7.24}$$

which is the same value for $DSRC_{TS2(D)}$ as from the above analysis of Eq (7.20).

Eq (7.21) shows that if the C-H or C-D bond cleavage is an irreversible RDS, a significant KIE should be observed, since $G^0_{TS2(D)} - G^0_{TS2(H)}$ is not close to zero.

Limiting Case #2

Let us consider the second limiting case described in ref.[208], where C-H and C-D bond cleavage are irreversible but Step 1 is now the RDS instead. Since C-H and C-D bond cleavage are still irreversible, the net rates in Branch H and Branch D equal the forward rate of Step 2 in each branch. Thus, Eq (7.20) still holds and $DSRC_{TS2(D)}$ is still -1. Similarly, the value of $DSRC_{TS2(D)}$ can also be calculated from ref [202] where we proved:

$$X_{TS2(D),P(D)} = \frac{\exp(-G^0_{TS2(H)} / RT)}{\exp(-G^0_{TS2(H)} / RT) + \exp(-G^0_{TS2(D)} / RT)} \tag{7.25}$$

$$X_{TS2(D),P(H)} = \frac{-\exp(-G^0_{TS2(D)} / RT)}{\exp(-G^0_{TS2(H)} / RT) + \exp(-G^0_{TS2(D)} / RT)} \tag{7.26}$$

and all other species after the branching have DRCs near zero (and therefore DSRCs near zero). Note that $X_{TS2(D),P(D)}$ and $X_{TS2(D),P(H)}$ are determined by the relative height of TS2(H) and TS2(D) in the energy diagram, but $DSRC_{TS2(D)} = X_{TS2(D),P(H)} - X_{TS2(D),P(D)} = -1$ is independent with the energy of TS2(H) and TS2(D). Plugging the value of $DSRC_{TS2(D)}$ into Eq (7.19) still gives the same value of r_H/r_D as Eq (7.20).

Gathering together the results of these first two limiting cases, we can conclude that for such a reaction as shown in Figure 7.2, a significant KIE should be observed whenever irreversible C-H and C-D bond cleavage occur in the RDS or in a step after the RDS. The KIE ratio is the same for these two cases, and it is determined by the Gibbs free energy difference between the transition state for C-H bond cleavage and the transition state for C-D bond cleavage, as shown by Eq (7.20) . These results are consistent with the analysis reported previously.[208] The KIE is usually attributed to the isotope effect on the ZPE difference between the transition state and the reactants of the rate-determining step, wherein the initial state of that step has more contribution since the isotope effect on the ZPE is bigger in the initial state compared to the transition state. However, in these first two limiting cases we discuss here, where Step 2 is irreversible and determines the selectivity, Step 2 in the two branches share a common initial state B. The free energy of the initial state (B) is therefore the same for both Branches H and D, and so state B exhibits no effect on the relative rates of the two branches. Thus, the KIE is determined only by the energy difference between the transition states, TS2(H) and TS2(D).

Limiting Case #3

Finally, let us consider the case from ref. #21[208], where Step 3 is now the RDS and intermediate C is equilibrated with intermediate B (i.e., Step 2 is fast to equilibrium). It can be proven (see SI) that:

$$DSRC_{TS3(D)} = -1 \tag{7.27}$$

and that the DSRCs of all other species are zero. The KIE then can be calculated with Eq (7.19) to be:

$$\begin{aligned}\ln\frac{r_H}{r_D} &= -DSRC_{TS3(D)}\times\left(\frac{G^0_{TS3(D)}-G^0_{TS3(H)}}{RT}\right)\\ &= \frac{G^0_{TS3(D)}-G^0_{TS3(H)}}{RT}\end{aligned} \tag{7.28}$$

In Branch H, there is a C-D bond present in intermediate C(H) and in TS3(H), and in Branch D there is a C-H bond present in intermediate C(D) and TS3(D). The energy difference between C(H) versus C(D) and between TS3(H) versus TS3(D) mainly comes from the energy difference between the C-H bond and the C-D bond. Thus, the forward rate constants of Step 3 in the two branches should be close. However, a significant KIE would still be observed based on Eq (7.28). This is because the steady-state concentrations of intermediate C in these two branches are not the same, due to the difference between the equilibrium constants (free energies of intermediates C(H) and C(D)) of Step 2 in these two branches. This KIE can be directly calculated from the ratio of the rates of step 3, which differ only because of this difference in equilibrium constants, giving:

$$\ln(KIE) = \ln\left(\frac{k_{3,H}K_{2,H}\left[B\right]}{k_{3,D}K_{2,D}\left[B\right]}\right) \approx \frac{G^0_{C(D)}-G^0_{C(H)}}{RT} \tag{7.29}$$

(Note that [B] is the same in both branches here.) The KIE value given by Eq (7.29) is very close to the value predicted by Eq (7.28), again confirming the validity of Eq (7.28). This result is also consistent with the analysis reported previously.[208]

An alternative explanation for Eq (7.28) is the Curtin-Hammett principle. The Curtin-Hammett principle states that, in a reaction that has a pair of equilibrated intermediates, where each goes irreversibly to a product, the product selectivity is determined by the free energy difference between the two rate-limiting transition states.[212, 213] In limiting case #3, TS3(H) and TS3(D) are the transition states in the rate-determining step, and the intermediates C(H) and C(D) are in equilibrium. Although the branch starts at Step 2 where a C-H or C-D bond cleavage occurs, Eq (7.28) gives that the selectivity ratio is controlled by the relative free energy of the transition states in the rate-determining step, which is Step 3 here. Similar phenomenon was observed by Bures et al.,[214] where they proposed a mechanism for the conjugate addition of aldehydes to nitro-olefins whereby the relevant transition state for determining the product enantiomeric ratio is not in the stereogenic center-forming step.

7.7 DISCUSSION

7.7.1 *The Role of the Rate-Determining Step in the Kinetic Isotope Effect*

The measurement of kinetic isotope effects has been widely used as a powerful tool to determine reaction mechanisms, especially for answering which step is the rate-determining step (RDS).[45-48] It is usually assumed that when there is a cleavage of bond that directly involves the isotope-substituted atom, a significant primary kinetic isotope effect should be observed. However, as we showed above, considering only the rate-determining step in the calculation of KIE can result in serious quantitative errors because the intermediates in the initial state of the RDS may not be the rate-controlling species with non-zero DRC, and the rate-controlling intermediates are not necessarily in the RDS. This separation of rate-controlling intermediates from the RDS is already well known.[41, 42]

Let us again take the case study of CO_2 hydrogenation on Cu(211) as an example. The transition state, H-HCOOH, has a DRC close to one, leaving the DRCs of all other transition states near zero. Thus, under given condition (480 K, total pressure 30 bar with $H_2/CO_2 = 3:1$) the third hydrogenation step is the rate-determining step. The change in the forward rate constant of the third hydrogenation step due to isotope substitution can be calculated as:

$$\begin{aligned}\frac{k_H}{k_D} &= \exp\left(-\frac{\left(G^0_{H-HCOOH}-G^0_{D-DCOOD}\right)-\left(G^0_{HCOOH*}-G^0_{DCOOD*}\right)-\left(G^0_{H*}-G^0_{D*}\right)}{RT}\right)\\ &= \exp\left(\frac{\left[24.38-19.01-4.62\right]\text{kJ/mol}}{\left(8.314\times 480/1000\right)\text{kJ/mol}}\right)\\ &= \exp\left(\frac{\left(-0.75\right)\text{kJ/mol}}{\left(8.314\times 480/1000\right)\text{kJ/mol}}\right)\\ &= 0.83\end{aligned} \tag{7.30}$$

The KIE is k_H/k_D = 0.83. This is far from the ratio r_H/r_D = 0.45 from full microkinetic modeling and 0.40 from Eq (7.6), showing the error that can result when one focuses *only* on the RDS to estimate KIEs. The DRC values here are approximately $X_{CO_2} \approx 1$, $X_{H-HCOOH} \approx 1$, $X_{HCOO*} \approx -2$, and $X_{H_2} \approx -0.5$. Using these approximate values for the DRCs, the difference between Eq (7.30) and Eq (7.16) in the free energy terms can be written as:

$$\begin{aligned}&-0.5\left(G^0_{H_2}-G^0_{D_2}\right)-2\left(G^0_{HCOO*}-G^0_{DCOO*}\right)+\left(G^0_{HCOOH*}-G^0_{DCOOD*}\right)+\left(G^0_{H*}-G^0_{D*}\right)\\ =\ &\left[\left(G^0_{H*}-0.5G^0_{H_2}\right)-\left(G^0_{D*}-0.5G^0_{D_2}\right)\right]\\ &+\left[\left(G^0_{CO_2}+G^0_{H*}-G^0_{HCOO*}\right)-\left(G^0_{CO_2}+G^0_{D*}-G^0_{DCOO*}\right)\right]\\ &+\left[\left(G^0_{HCOOH*}-G^0_{H*}-G^0_{HCOO*}\right)-\left(G^0_{DCOOD*}-G^0_{D*}-G^0_{DCOO*}\right)\right]\end{aligned}$$

This includes the isotope effect on the equilibrated steps of $\mathrm{H_2} \leftrightharpoons 2\mathrm{H}^*$, $\mathrm{CO_2} + \mathrm{H}^* \leftrightharpoons \mathrm{HCOO}^*$ and $\mathrm{H}^* + \mathrm{HCOO}^* \leftrightharpoons \mathrm{HCOOH}^* + *$. The RDS-only method fails to include the isotope effects on these equilibrated steps in the calculation, just as we mentioned in the example of the L-H mechanism above.

7.7.2 *Reactions with Multiple Rate-Controlling Transition States*

When there are multiple transition states exhibit rate-control (i.e., with significant DRCs), the relative strength of their rate-control is very sensitive to tiny changes in their energies. Thus, under this condition, Eq (7.6) might not give an accurate prediction of the KIE since the assumption that the DRC remains constant in a range of interest no longer holds. The case study of CO_2 hydrogenation on Zn-promoted Cu(211) given above is an example of this situation. However, this is rarely be a problem in most applications. In the parameter space formed with the energies of species in a reaction, it shows broad regions where the DRC is dominated by a single transition state. The situation where multiple transition states exhibit rate-control only occurs in narrow boundaries between these regions.[1]

Even if Eq (7.6) does not work properly in some situations, it still gives insight for understanding KIEs. For example, in the case of CO_2 hydrogenation on Zn-promoted Cu(211), we showed that it is very helpful for labeling the rate-controlling species that in fact do determine the KIE.

7.7.3 *The Error in Using only ZPE Differences in Eq* (7.7)

We can also use these data to assess the error associated with calculating KIEs using only the ZPE differences in Eq (7.7) to estimate free energy differences. The KIE calculated from Eq (7.6) based only on the differences in ZPEs is $r_H/r_D = 0.62$ (corresponding to an activation energy change of 1.9 kJ/mol). The difference between the value calculated using ZPE only and the value calculated above using the full H/D free energy difference (which still neglected the heat capacity difference or ΔU_{C_p} term in Eq (7.7)) gives the contribution of entropy to the KIE. It can be calculated as 0.40/0.62 = 0.65, corresponding to an activation free energy change of 1.8 kJ/mol. This shows that the entropic contribution to the KIE value is nearly the same as the ZPE contribution for this reaction. So when the KIE based on ZPE differences alone is within a factor of 2 of unity (as it is here), it is questionable to neglect the entropy term in Eq (7.7). Since we do not have the heat capacities for any of the adsorbed species or transition states in Table 7.1 (since they were not reported in the references from which we extracted these DFT energetics), we cannot makes such a quantitative comparison to assess the error associated with neglected the heat capacity term in Eq (7.7). However, we did make this comparison for the gas-phase reactants (3 H_2 + CO_2) and products (CH_3OH + H_2O), all at 480 K as in Table 7.1. For H_2, the difference between isotopes for both the entropy and heat capacity contributions to Eq (7.7) are zero. For H_2O they are also small (-0.11 and +0.28 kJ/mol, respectively), but for methanol, the differences are rather large (-2.79 and +2.63 kJ/mol, respectively), so that the difference for the net reaction is also large (-2.90 and +2.91 kJ/mol, respectively). Clearly, none of the terms in Eq (7.7) should really be neglected, in spite of the fact that it has become common in heterogeneous catalysis to neglect the heat capacity term here, since entropy's contribution to the total free energy is usually much larger in magnitude than the integral of $C_p dT$.[47, 197, 198, 209] For example, the entropy contribution is larger by a factor of 3 to 5 for gas-phase H_2, water and methanol at 480 K. In spite of this, the differences in these two terms between H and D isotopes is very small, at least for the gas-phase molecules and net reaction above. This is very interesting. It means that the heat capacity term in Eq (7.7) is nearly cancelled by the entropy term, since they have the same magnitude but opposite signs. This suggests that it is more accurate to neglect *both* of these terms than just to neglect one or the other. This perhaps explains some of the successes of past KIE analyses that used only ZPE differences. This is a very tentative suggestion, since confirming it would require a much broader comparison of these terms for more species, including catalyst-bound intermediates, which is beyond the scope of this paper.

7.8 CONCLUSIONS

A method to interpret kinetic isotope effects (KIEs) using degree of rate control (DRC) analysis is presented. When the KIE is measured as the rate ratio for two isotopes in separate experiments, the logarithm of the rate ratio equals the weighted average over all species in the mechanism of their standard-state free energy differences between the two isotopes, divided by RT, where the weighting factor for each species is its DRC (Eq (7.6)). This method assumes that the DRCs do not change with isotope (which is sometimes not the case). It reveals that the KIE calculated from the isotope effect on the rate-determining step is not enough to represent the overall KIE of the whole catalytic cycle, since species in other steps often also exhibit large influences on the KIE (i.e., large DRCs). We also show that when the KIE is measured as the product selectivity in the competition between two isotopes in the same reactant, an extension of DRC called the degree of selectivity ratio control (DSRC) provides a similar equation (Eq (7.19)) whereby the weighting factor is now the DSRC. These equations aid in the mechanistic interpretation and quantitative analysis of KIEs.

7.9 SUPPLEMENTARY INFORMATION

7.9.1 *Proof of Eq (7.19)*

Here we show a proof for Eq (7.19) following a similar approach as shown in Eqs (7.2)-(7.6) in the Theory Section. Figure 7.3 schematically shows how this method works for a single elementary step.

Let us assume that there is an arbitrary reaction's free-energy diagram for the reaction mechanism of interest but with energies appropriate for specific isotope masses, M. The standard-state Gibbs free energies of species *i* in this reaction path (we will call it "Branch M" below) are varied from M = H to M = D between the free energies of species *i* in Branch H and Branch D (as defined in the main paper), as shown by the green lines in Figure 7.3. Using the rate in Branch H as a reference and keeping the standard-state Gibbs free energy of all species in Branch H constant, the DSRC of species in Branch M can be defined as

$$DSRC_{i(M)} = \left(\frac{\partial \ln\left(r_H / r_M \right)}{\partial \left(-G^0_{i(M)} \middle/ RT \right)} \right)_{G^0_{j \neq i}} \tag{7.31}$$

In Figure 7.3, only Branch H and Branch M exist in the reaction system for a chosen value of the M, so it is a competition between Branch H and M. The energies of species in Branch D are given by blue dashed lines in Figure 7.3 because they do not exist in the reaction system for the competition until M = D at the final state of the integral. Since the species in the main reaction path (e.g., B) have constant energies and the species in Branch H (e.g., TS2(H) and intermediate C(H)) are anchored as the reference branch, the energies of species in Branch M (e.g., TS2(M) and C(M)) are the only variables in the system, and the total differential of $\ln\left(r_H / r_M \right)$ can be written as:

$$d\ln\left(\frac{r_H}{r_M}\right)=\sum_{i=\text{species in Branch M}}\left(\frac{\partial\ln\left(r_H/r_M\right)}{\partial\left(-G^0_{i(M)}/RT\right)}\right)_{G^0_{j\neq i}}d\left(-\frac{G^0_{i(M)}}{RT}\right)=\sum_{i=\text{species in Branch M}}DSRC_{i(M)}d\left(-\frac{G^0_{i(M)}}{RT}\right)\tag{7.32}$$

Note that the summation in Eq (7.32) is over all species in Branch M. Taking integral on both sides of Eq (7.32) from some initial state to some final state gives:

$$\ln\left[\frac{\left(r_H/r_M\right)_{final}}{\left(r_H/r_M\right)_{initial}}\right]=\sum_{i=\text{species in Branch M}}\int_{M=initial}^{M=final}DSRC_{i(M)}d\left(-\frac{G^0_{i(M)}}{RT}\right)\tag{7.33}$$

As shown in Figure 7.3, the initial state of the integral is M = H and the energies of species *i* in Branch M equal the energies of species *i* in Branch H. In this initial state, the probabilities for intermediate B to take Branch H and Branch M are 50%, so $r_H/r_M = r_H/r_H = 1$. As the integral starts, the energies of species *i* in Branch M move towards the energies of species *i* in Branch D, and finally a final state is achieved where the energies of species in Branch M equal their energies in Branch D. This final state is the same as the real reaction mechanism shown in Figure 7.2b in the main paper, and $r_H/r_M = r_H/r_D$ is the value for KIE. Taking the initial and final state shown in Figure 7.3, Eq (7.33) can be rewritten as:

$$\ln\left[\frac{\left(r_H/r_D\right)}{\left(r_H/r_H\right)}\right]=\ln\left[\frac{r_H}{r_D}\right]=\sum_{i=\text{species in Branch M}}\int_{M=H}^{M=D}DSRC_{i(M)}d\left(-\frac{G^0_{i(M)}}{RT}\right)\tag{7.34}$$

Eq (7.34) gives a general equation for the evaluation of KIE defined as the selectivity ratio for a reaction mechanism shown in Figure 7.2 in the main paper. If we further assume, in the small range of interest from the initial state to the final state in the integral in Eq (7.34), the DSRC of species *i* can be treated as a constant, Eq (7.34) further simplifies to:

$$KIE=\ln\left[\frac{r_H}{r_D}\right]=\sum_{i=\text{species in Branch D}}\left[-DSRC_{i(D)}d\left(\frac{G^0_{i(D)}-G^0_{i(H)}}{RT}\right)\right]\tag{7.35}$$

Eq (7.35) is the same as Eq (7.19) in the main paper. Note that Eq (7.35) (i.e., Eq (7.19)) no longer relies on the arbitrary reaction's energy diagram Branch M. It is a summation over all species in Branch D and the DSRC used in the summation are for the species in Branch D.

To derive Eq (7.35) from Eq (7.34), we assumed that the DSRC of species *i* can be treated as a constant, independent of isotope M. This assumption is valid in most cases. For example, in the first case of Case Study IV in the main paper where Step 2 is the irreversible RDS, Eqs (7.22) and (7.23) still hold for Branch H and Branch M here, which can be written as:

$$X_{TS2(M),P(M)} = 1 \text{ and} \tag{7.36}$$

$$X_{TS2(M),P(H)} = 0 \ . \tag{7.37}$$

Note that the DRCs of the transition states TS2(M) for the two rates to generate P(M) and P(H) do not depend on $G^0_{TS2(M)}$. Thus, the DSRC of TS2(M) is truly a constant in the integral of Eq (7.34). In the second case of Case Study IV where Step 1 is the RDS and Step 2 is irreversible, Eqs (7.25) and (7.26) still hold for Branch H and Branch M here. They can be rewritten as:

$$X_{TS2(M),P(M)} = \frac{\exp(-G^0_{TS2(H)} / RT)}{\exp(-G^0_{TS2(H)} / RT) + \exp(-G^0_{TS2(M)} / RT)} \tag{7.38}$$

$$X_{TS2(M),P(H)} = \frac{-\exp(-G^0_{TS2(M)} / RT)}{\exp(-G^0_{TS2(H)} / RT) + \exp(-G^0_{TS2(M)} / RT)} \tag{7.39}$$

In this case the DRCs of the transition state TS2(M) for the two rates to the two products depend on $G^0_{TS2(M)}$, but the DSRC, which is the difference between these two DRCs, is constant: $DSRC_{TS2(M)} = X_{TS2(M),P(H)} - X_{TS2(M),P(M)} = -1$. Thus, it does not change in the integral of Eq (7.34).

7.9.2 *Proof of Eq (7.27)*

When Step 3 in Figure 7.2 is the single RDS and intermediate C is equilibrated with intermediate B, the rate of Branch H can be calculated as:

$$r_H = k_{3,H}\left[C\left(H\right)\right] = k_{3,H}K_{2,H}\left[B\right] \tag{7.40}$$

where $k_{3,H}$ is the forward rate constant of Step 3 in Branch H, $K_{2,H}$ is the equilibrium constant of Step 2 in Branch H, and [C(H)] is the concentration of intermediate C in the H branch. Similarly, the rate of Branch D can be calculated as:

$$r_D = k_{3,D}\left[C\left(D\right)\right] = k_{3,D}K_{2,D}\left[B\right] \tag{7.41}$$

where $k_{3,D}$ is the forward rate constant of Step 3 in Branch D, and $K_{2,D}$ is the equilibrium constant of Step 2 in Branch D. The ratio r_H/r_D then equals:

$$\begin{aligned}
&\frac{r_H}{r_D} = \frac{k_{3,H}K_{2,H}}{k_{3,D}K_{2,D}} \\
&= \frac{\exp\left[-\left(G^0_{TS3(H)} - G^0_{C(H)}\right)\big/RT\right]\exp\left[\left(G^0_{C(H)} - G^0_{B}\right)\big/RT\right]}{\exp\left[-\left(G^0_{TS3(D)} - G^0_{C(D)}\right)\big/RT\right]\exp\left[\left(G^0_{C(D)} - G^0_{B}\right)\big/RT\right]} \\
&= \frac{\exp\left[-\left(G^0_{TS3(H)}\right)\big/RT\right]}{\exp\left[-\left(G^0_{TS3(D)}\right)\big/RT\right]}
\end{aligned} \tag{7.42}$$

Taking the logarithm of both sides of Eq (7.42) above gives:

$$\ln\frac{r_H}{r_D} = \frac{G^0_{TS3(D)} - G^0_{TS3(H)}}{RT} \tag{7.43}$$

Then the DSRC of TS3(D) can be calculated as:

$$DSRC_{TS3(D)} = \left(\frac{\partial \ln\left(r_H/r_D\right)}{\partial\left(-G^0_{TS3(D)}\big/RT\right)}\right)_{G_{j\neq TS3(D)}} = -1 \tag{7.44}$$

This is the same as Eq (7.27) in the main text. One can also see from looking at Eq (7.43) that the DSRC is 0 for all of the other species in the mechanism (since they do not appear in Eq (7.43)).

7.10 Figures

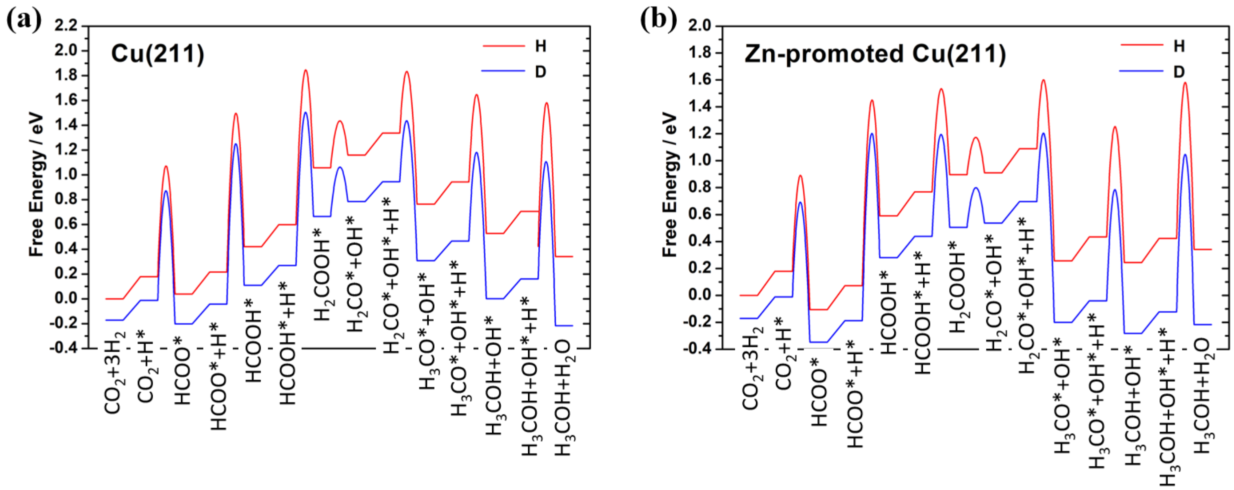

Figure 7.1 Standard-state Gibbs free energy diagram of CO_2 hydrogenation on (a) Cu(211) (b) Zn-promoted Cu(211) at 480 K, based on DFT results taken from Studt et al.[198, 209], with minor modifications. The red line and blue line correspond to reaction with normal reactants and deuterated reactants respectively. Note that H_2 has been omitted in the labels of many of the states, and it should be included in the necessary amount to achieve element balance for each step and species. The energy axis has been offset for all species by a constant amount (relative to the absolute zero-energy reference) so that the reactants have zero energy for the H isotope.

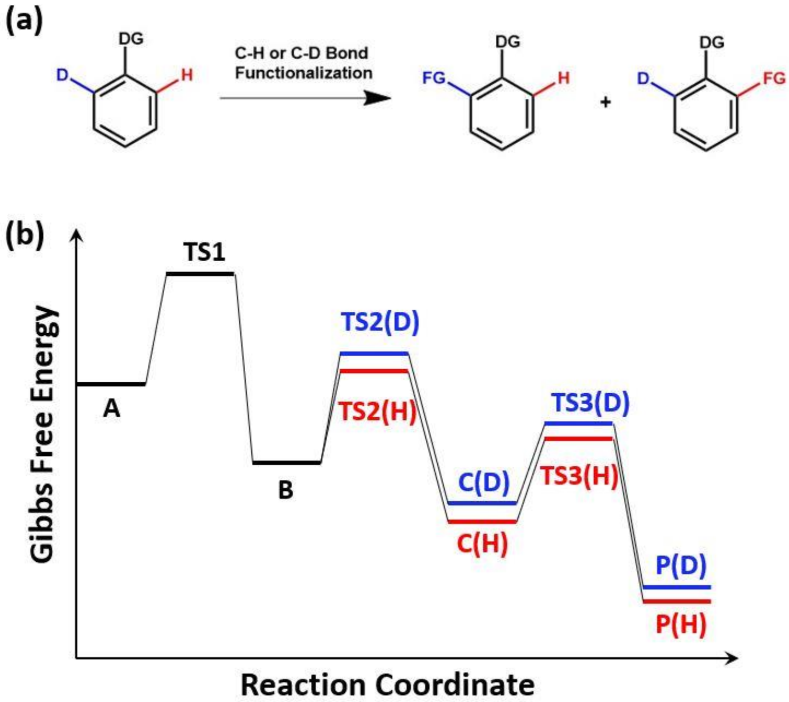

Figure 7.2 (a) A deuterium kinetic isotope effect experiment involving an intramolecular competition between functionalization (addition of a functional group, FG) at a C-H bond versus a C-D bond on a substituted benzene ring, of the type described previously, where DG refers to different directing groups on the benzene ring.[208] (b) A representative standard-state free energy diagram for such a reaction. The red line represents the reaction branch where the C-H bond breaks. The blue line represents the reaction branch where the C-D bond breaks.

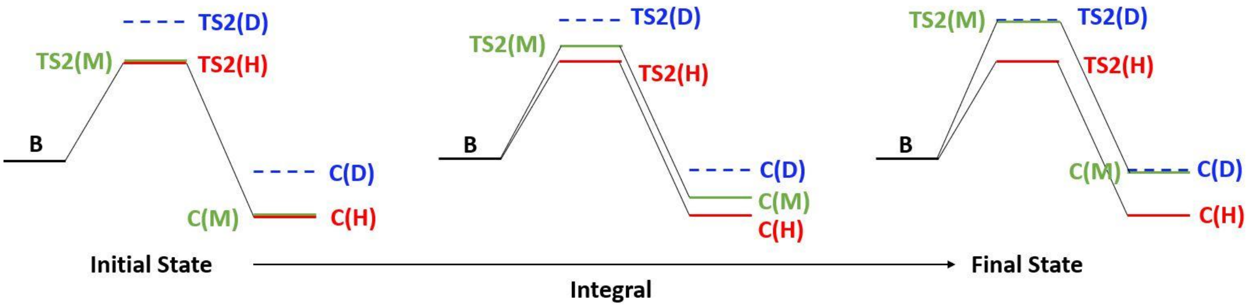

Figure 7.3 Schematic of the integral method we will use to derive Eq (7.19), using Step 2 in Figure 7.2 of the main paper as an example. The black solid lines denote the energies of species in the main reaction path, the red solid lines denote the energies of species in Branch H, the green solid lines denote the energies of species in Branch M (an imaginary isotope with standard-state free energies that will be varied continuously between those for H and D), and the blue dashed lines denote the energies of species in Branch D. In the initial state, the energies of species in Branch M equal their energies in Branch H. As the integral starts, the energies of species in Branch M start to move towards their energies in Branch D. In the final state, the energies of species in Branch M equal their energies in Branch D.

7.11 TABLES

Table 7.1 The standard-state Gibbs free energies of species in the CO_2 hydrogenation reaction at 480 K with normal H-isotope reactants on Cu(211) and Zn-promoted Cu(211) (“CuZn”), and the changes upon deuterium isotope substitution in their zero-point energies, standard-state entropies and standard-state Gibbs free energies on CuZn, from ref.[198, 209] We assume here that these three isotope differences are the same on Cu(211).

Species	G^0(H) on Cu	G^0(H) on CuZn	ZPE(H)-ZPE(D)	$T^{480K}[S^0(H)-S^0(D)]$	$G^0(H)-G^0(D)$
Reactants					
H_2	0.00	0.00	5.50	0.00	5.50
CO_2	0.00	0.00	0.00	0.00	0.00
Intermediates					
H_2COOH*	102.01	86.52	26.34	-3.21	29.56
H_2CO*	93.85	97.17	15.73	-2.12	17.85
HCOOH*	40.57	56.94	16.60	-2.41	19.01
HCOO*	3.71	-10.27	8.30	-1.16	9.46
H*	17.22	17.21	4.44	-0.18	4.62
OCH_3*	55.78	34.04	25.09	-3.52	28.61
OH*	17.97	-9.33	8.11	-1.84	9.95
Transition States					
H-COO	103.27	85.36	3.96	-1.73	5.68
H-CH_2O	156.38	158.98	19.88	-3.52	23.40
H-HCOOH	176.91	147.86	20.46	-3.92	24.38
H-OCH_3	139.87	129.95	27.50	-5.08	32.58
H-OH	124.68	119.59	9.94	-3.57	13.51
H_2CO-OH	138.33	113.17	23.84	-3.97	27.81
HCOO-H	144.18	138.40	10.42	-2.17	12.59

The Gibbs free energies of the H-isotope reactants have been subtracted from all free energies here to simplify energy comparisons. All values in this table are given in kJ/mol. In calculating $G^0(H)-G^0(D)$ here, we used Eq (7.7) but assumed that its second term (due to heat capacity differences between isotopes) is negligible, since that same assumption was made in the original DFT papers[198] from which we extracted these energies and entropies, and since that paper did not report the heat capacities needed to include this term.

Table 7.2 The degrees of rate control (X_i) of all reactants, intermediates and transition states of CO_2/H_2 hydrogenation on Cu(211) at 480 K with normal reactants and fully deuterated reactants. The coverages of adsorbates are also shown.

Species	H_2 Reactants		D_2 Reactants	
	Coverage	X_i	Coverage	X_i
Reactants				
H_2		-0.56		-0.51
CO_2		0.86		0.97
Intermediates				
H_2COOH*	0.00	0.00	0.00	0.00
H_2CO*	0.00	0.00	0.00	0.00
HCOOH*	0.00	0.00	0.00	0.00
HCOO*	0.93	-1.85	0.98	-1.97
H*	0.00	-0.01	0.00	0.00
OCH_3*	0.00	0.00	0.00	0.00
OH*	0.00	0.00	0.00	0.00
Transition States				
H-COO		0.00		0.00
H-CH_2O		0.00		0.00
H-HCOOH		1.00		0.99
H-OCH_3		0.00		0.00
H-OH		0.00		0.00
H_2CO-OH		0.00		0.00
HCOO-H		0.00		0.01

Reaction conditions: 480 K, P_{CO2} = 7.5 bar, P_{H2} = 22.5 bar, and in the limit of low conversion.

Table 7.3 The degrees of rate control of all reactants, intermediates and transition states of CO_2/H_2 hydrogenation on Zn -promoted Cu(211) at 480 K with normal H_2 reactant and with D_2. The coverages of adsorbates are also shown.

Species	H_2 Reactant		D_2 Reactants	
	Coverage	X_i	Coverage	X_i
Reactants				
H_2		-0.32		-0.13
CO_2		1.13		1.11
Intermediates				
H_2COOH^*	0.00	0.00	0.00	0.00
H_2CO^*	0.00	0.00	0.00	0.00
HCOOH*	0.00	0.00	0.00	0.00
HCOO*	1.00	-1.99	1.00	-1.99
H*	0.00	0.00	0.00	0.00
OCH_3^*	0.00	0.00	0.00	0.00
OH*	0.00	0.00	0.00	-0.01
Transition States				
H-COO		0.00		0.00
$H\text{-}CH_2O$		0.14		0.11
H-HCOOH		0.50		0.15
$H\text{-}OCH_3$		0.00		0.00
H-OH		0.14		0.12
$H_2CO\text{-}OH$		0.00		0.00
HCOO-H		0.22		0.62

Reaction conditions: 480 K, P_{CO2} = 7.5 bar, P_{H2} = 22.5 bar, and in the limit of low conversions.

Chapter 8. Apparent Activation Energies in Complex Reaction Mechanisms: A Simple Relationship via Degrees of Rate Control

This chapter has been published as:
Z. Mao, C. T. Campbell, *ACS Catalysis*, 2020, 9, 9465-9473.

Chapter Abstract

The apparent activation energy of chemical reactions has played a central role in the field of chemical kinetics and has served as an important tool for analyzing and understanding reaction rates, mechanistic details of complex reaction mechanisms, elementary-step energetics, catalytic activity and reaction selectivity. We derive here a general expression which shows that the apparent activation energy equals a weighted average of the standard-state enthalpies (relative to reactants) of all the species (intermediates, transition states and products) in the reaction mechanism, each weighted by its generalized degree of rate control (DRC). Since the DRC is zero for most of these species, even in very complex mechanisms, the weighted average includes only a few terms. This simplicity provides deep insight into the connection between the reaction energy diagram and the apparent activation energy. We prove both this and the quantitative validity of this equation by analysis of numerous reaction mechanisms. We also show the failures or weaknesses of previous equations for the apparent activation energy.

8.1 INTRODUCTION

Catalytic reactions play a huge role in the world's economy and are vital for clean energy and sustainability. Whether in homogeneous or heterogeneous catalysis, they always consist of several elementary steps. It is known that the observed reaction kinetics represents a composite of the contribution from each of these elementary steps. Analytical rate equations sometimes apply to multistep reaction mechanisms when the "rate-determining step" (RDS) assumption is valid. Efforts have been made to define the RDS, and the "degree of rate control" (DRC) is the most general. It is a rigorous mathematical approach to quantify to what extent the standard-state Gibbs free energy of a "species" in the reaction (i.e., a catalysts-bound intermediate or transition state) affects the rate of the overall reaction under a given condition.[42, 43] When there is a single RDS, its transition state has a DRC of 1 and the DRC of all other transition states is zero (unless branching pathways occur after this RDS, since the fast branching reaction that leads to the desired product can have a transition state with a DRC of ~1, while the fast branch that leads to undesired products can have a transition state with a DRC of ~-1, as in ethylene epoxidation over Ag[196]). The apparent activation energy (E_{app}) is an experimentally accessible value which has played a powerful role in understanding reaction kinetics and mechanisms. It is typically measured by fitting the temperature dependence of the reaction rate or rate constant to the Arrhenius law. Its value is often correlated with the intrinsic activity of catalysts, and is compared to the activation energies for elementary steps in the mechanism when trying to assess which step is rate determining.[189, 215-219] Of course, much more rigorous analyses are often performed, as described below. By comparing the E_{app} from experimental measurements and microkinetic modeling, one can test whether the reaction mechanism proposed is consistent with experiments, or the calculated energetics of the species are accurate.[197, 220] Despite the wide application and importance of the apparent activation energy, its microscopic origin is often unclear. We rigorously derive here a general expression for the apparent activation energy using DRC analysis that makes clear its microscopic origin within the reaction-energy diagram, even for the most complex reaction mechanisms, and prove its quantitative validity with many example mechanisms. *The apparent activation energy equals RT plus the weighted average of the enthalpies of all species in the mechanism (intermediates, transition states and products, relative to reactants), each multiplied by its DRC.* While it is derived with catalytic reactions in mind, it is applicable to any complex reaction mechanism where transition state theory is valid.

Unlike in a single-step reaction, it is often difficult to picture the apparent activation energy in an energy diagram of a multistep reaction, for example as the energy difference between some initial reactant and a transition state. The equation presented here makes a quantitative connection between the energies of such species and the apparent activation energy. A few previous approaches for bridging this gap between the microscopic energetics and the macroscopic apparent activation energy have been reported, as we discuss next.

Kozuch and Shaik[189,221-223] introduced the highly-cited Energy Span Model, which shows that the apparent activation energy of a catalytic cycle involving only a single catalyst site equals the energy difference between the TOF(turnover-frequency)-determining intermediate (TDI) and the TOF-determining transition state (TDTS), whenever there is a single RDS and a single TDI. The Energy Span Model has achieved success for analyzing chemical kinetics, especially in physical organic chemistry. However, it was not intended to apply to reactions where more than one catalyst site is involved in an elementary step (e.g., when two catalysts-bound intermediates form a bond, or when an intermediate dissociates to make two catalyst-bound intermediates), as is common in heterogeneous catalysis. We show below that it fails in such cases in terms of predicting apparent activation energies, and that the equation derived here has other advantages over this Energy Span Model.

Meskine et al.[188] derived an equation showing that E_{app} is a weighted average of the activation energies of all elementary steps (both forward and reverse steps) each multiplied by $DRC^{+/-}$, where $DRC^{+/-}$ is a new type of degree of rate control defined differently than the older DRC mentioned above and used exclusively below. This $DRC^{+/-}$ is not directly related to the reaction-energy diagram like the generalized DRC, and therefore also not as widely used. We show that the equation for E_{app} of Meskine et al. is consistent with the equation derived below (differing only by RT), but not nearly so easily interpretable with a reaction-energy diagram as the one derived below. Also, their equation for E_{app} generally has many more non-zero terms compared to the new equation presented below, so their equation is more difficult to implement and conceptualize.

In 2002, Parmon[192] proposed that, for a non-catalytic stepwise reaction wherein every step is first-order in each intermediate, the apparent activation energy equals the difference between the standard-state enthalpy of the rate-limiting transition state and that of the initial reagents plus RT. For a catalyzed reaction, we show below that the apparent activation energy is often different than predicted by this relation, due to the limited availability of free catalyst sites.

Motagamwala and Dumesic[193] used maximum rate analysis with DRC analysis to derive a general rate expression for sequential reaction schemes, including catalyzed reactions. It provides useful insights into the apparent activation energy, but does not offer the direct connection to the reaction-energy diagram like that provided by the equation we present below.

Jørgensen and Grönbeck[224] derived a connection between the apparent activation energy and DRC values that looks very similar to that derived by Meskine et al.[188], but actually differs substantially. We show below that their equation is often incorrect and suggest a specific error in their derivation that may have caused this.

Here, a simple but general mathematical expression for the apparent activation energy (E_{app}) in terms of the enthalpies of species in the reaction and their DRCs is derived and validated for numerous example mechanisms by comparisons to analytical rate expressions and numerically calculated rates. It proves that E_{app} equals RT plus the weighted average of enthalpies of all species (relative to reactants), each multiplied by its DRC. This weighting factor in our equation is the generalized DRC, which is clearly defined with respect to standard-state free energy variations of individual species, and can be pictured easily on a reaction-energy diagram.[42] This generalized DRC can be applied to both intermediates and transition states, so it possesses all the energetical information in the reaction scheme. The derived relation clearly defines the role of rate-controlling intermediates and rate-controlling transition states, quantifying exactly the extent to which their enthalpies contribute to the apparent activation energy. No prior work has been reported that accurately relates the apparent activation energy so directly with the energies of individual intermediates and transition states as derived below.

8.2 APPARENT ACTIVATION ENERGY DERIVATION

The (generalized) degree of rate control, DRC, for some species i (e.g., an intermediate or transition state of an elementary step) is defined as[42, 43]

$$X_i = \left(\frac{\partial(\ln r)}{\partial(-G_i^0 / RT)} \right)_{G_{j \neq i}} \tag{8.1}$$

where r is the net reaction's rate (the rate of consumption of some reactant or the rate of production of some product) and G_i^0 is the standard-state Gibbs free energy of species i relative to the standard-state Gibbs free energy of the stoichiometrically-combined reactants (plus the adsorbate-free catalysts surface) as the zero-energy reference. (An easy way to determine the G_i^0 for any one species in the mechanism on this relative energy scale is described in the Tutorial for CATMAP[210, 225] under "Formation Energy Approach.". Maintaining element balance (i.e., atom balance) with every step in the mechanism offers some conceptual simplification in making and analyzing energy diagrams and in picturing this zero-energy reference.) The partial derivative above is taken holding constant the standard-state Gibbs free energies of all other species. Since the term $-G_i^0/RT$ will be used frequently in the following sections, it will be replaced with the dimensionless variable g_i, defined as:

$$g_i = -G_i^0 / RT \quad . \tag{8.2}$$

The steady-state rate of a reaction is a function of the activities of reactants and products (c_i), the equilibrium constants and the rate constants for all the elementary steps in the mechanism. Below, we will assume ideal solutions and/or gas mixtures, such that the activity of each species is equal to its concentration. While the validity of the following derivation would be correct without this assumption about the meaning of c_i, it makes the derivation easier for the reader to follow. We note that there are many cases where such non-ideal behavior is very important to consider.[226] Since the equilibrium constants and the rate constants, according to transition state theory, can all be expressed in terms of the change of standard-state Gibbs free energies between different states in the reaction, the steady-state rate can then always be written as a product of two terms:

$$r = \frac{k_B T}{h} \times f(g_1, g_2, \ldots, g_N, c_1, c_2, \ldots, c_M) \tag{8.3}$$

The first term, k_BT/h is the frequency factor in transition state theory and has units of s^{-1}. The second term, f is a function of $-G_i^0/RT$ (or g_i) for all the species i (reactants, products, intermediates and transition states) in the mechanism and the concentrations of all reactants and products. Since all concentrations are assumed constant, *f* is a function of g_i only. This function *f* includes the concentration distributions of intermediates at steady state and the equilibrium relations between the transition states and their initial-state intermediates.

The apparent activation energy is defined as

$$E_{app} = -R\left[\frac{\partial(\ln r)}{\partial(1/T)}\right] = RT^2\frac{\partial(\ln r)}{\partial T} \tag{8.4}$$

It can be calculated by substituting Eq (8.3) into Eq (8.4) and applying the chain rule to the derivative:

$$\begin{aligned} E_{app} &= RT^2\frac{\partial(\ln r)}{\partial T} = RT^2\left\{\frac{\partial\ln(k_BT/h)}{\partial T} + \frac{\partial\ln f}{\partial T}\right\} \\ &= RT^2\left\{\frac{1}{T} + \sum_i \frac{\partial\ln f}{\partial g_i}\frac{\partial g_i}{\partial T}\right\} \end{aligned} \tag{8.5}$$

where the sum here runs over all intermediates and transition states in the reaction. The DRC of any species i can be calculated from its definition and Eq (8.3) as:

$$X_i = \frac{\partial(\ln r)}{\partial g_i} = \frac{\partial\left[\ln(k_BT/h) + (\ln f)\right]}{\partial g_i} = \frac{\partial(\ln f)}{\partial g_i} \tag{8.6}$$

Eq (8.5) can thus be rewritten by substituting X_i for $\partial(\ln f)/\partial g_i$ to give:

$$\begin{aligned} E_{app} &= RT^2\left\{\frac{1}{T} + \sum_i \frac{\partial\ln f}{\partial g_i}\frac{\partial g_i}{\partial T}\right\} \\ &= RT + RT^2\left\{\sum_i X_i \frac{\partial\left(-G_i^0 / RT\right)}{\partial T}\right\} \\ &= RT + RT^2\left\{\sum_i X_i\left(-T\frac{\partial G_i^0}{\partial T} + G_i^0\right) / RT^2\right\} \end{aligned} \tag{8.7}$$

We can write that G_i^0 as $G_i^0 = H_i^0 - TS_i^0$, with the standard-state enthalpy and entropy of i (H_i^0 and S_i^0, respectively) both defined relative to that of the reactants as the zero-energy reference state (see above). In the narrow temperature range of interest when measuring apparent activation energies, it is reasonable to assume that H_i^0 and S_i^0 do not change with temperature. The expression for apparent activation energy then simplifies to

$$\begin{aligned} E_{app} &= RT + RT^2 \left\{ \sum_i X_i \left(-T \frac{\partial G_i^0}{\partial T} + G_i^0 \right) / RT^2 \right\} \\ &= RT + \sum_i X_i \left[-T \times \left(-S_i^0 \right) + G_i^0 \right] \\ &= RT + \sum_i X_i H_i^0 \end{aligned} \tag{8.8}$$

The second term is the sum of the standard-state enthalpies of all species that appear in the reaction pathway, including all intermediates and transition states, each weighted by its DRC. *This bottom version of Eq (8.8) above is the key result of this paper. It states that the apparent activation energy equals the weighted average of the standard-state enthalpies of all the species (intermediates, transition states and products) in the reaction mechanism (relative to the reactants), each weighted by its DRC, plus RT.* The reactants (and adsorbate-free catalyst surface) are not included because their energies are always set to zero as the reference in Eq (8.1). The enthalpies of all other species appearing in Eq (8.8) are given relative to stoichiometric reactants (and adsorbate-free catalyst surface). If the conversion of the reaction is low and the system is far away from equilibrium, products can be ignored when applying Eq (8.8) because they have DRCs close to zero in this case. If the system is not far away from equilibrium and the equilibrium between products and some intermediates is not negligible, the products may have non-negligible DRCs and should be considered in Eq (8.8). In practice, usually only a few species have non-negligible DRCs.[42, 43] One only need to sum those species to get accurate results. Although the cases we discuss below get the DRC values from applying Eq (8.1) to the rates calculated by a full microkinetic model, there are also experimental ways to get estimate the DRCs. For example, researchers often experimentally determine the rate-determining step, which gives that the DRC = 1 for that step's transition state (and near zero for the other steps in any non-branched mechanism).[1] There are experimental ways to measure the fraction of catalyst sites bound by various intermediates, and their DRCs are proportional to this fraction bound.[1]

In applying Eq (8.8), it is useful to know that the DRCs of adsorbates *n* are proportional to their fractional coverages (θ_n), $X_n = - \sigma \theta_n$, where the proportionality constant σ is a positive integer that applies to all the surface-bound intermediates along the reaction pathway to a given product.[42, 43, 202]The fraction of free sites (θ_*) is 1 minus the sum of θ_n for all adsorbates, but free sites do not have a degree of rate control (since they are part of the zero-energy reference in Eq (8.1)) and do not enter into Eq (8.8).

The derivation above is similar to that used by Meskine et al.[188] in that it applies the chain rule like in Eq (8.5) here to take the appropriate derivative of the rate needed to get E_{app}. However, above we express the rate as a function of the standard-state free energies of all the species in the mechanism, whereas Meskine et al. express the rate as a function of the rate constants (forward and reverse) for all the elementary steps involved. Their equation for E_{app} therefore is quite different. It uses a different type of degree of rate control ($DRC^{+/-}$ instead of DRC), which becomes the weighting factor in their weighted average, which is an average over all the individual-step's *activation* energies rather than an average over all the individual species enthalpies as done here in Eq (8.8). The result is that Eq (8.8)is easier to implement, visualize and interpret, but it gives the same result (within RT) as the equation from Meskine et al., as shown below.

We next present a number of case studies of different reaction mechanisms which prove the validity of Eq (8.8) by comparing its prediction for E_{app} with that derived from analytical rate expressions or computational solutions to microkinetic models.

8.3 CASE STUDY I. A SIMPLE SURFACE REACTION FOLLOWING LANGMUIR-HINSHELWOOD MECHANISM

In this case study, the rate equations are very commonly encountered for gas-phase reactions catalyzed by a solid surfaces, but we want to emphasize that the equations are valid independent of whether the reaction is in gas or liquid phase and whether the catalyst is a solid surface or a homogeneous catalyst, with some very minor modifications mentioned below.

We first consider a simple but typical Langmuir-Hinshelwood (L-H) mechanism with competitive adsorption, four elementary steps, a single rate-determining step (Step 3) and all other steps being fast to equilibrate:

$$
\begin{array}{ll}
1.\ A+* \rightleftharpoons A* & (\textit{fast to equilibium}) \\
2.\ \mathrm{B}+* \rightleftharpoons B* & (\textit{fast to equilibium}) \\
3.\ \mathrm{A}*+B* \rightarrow C*+* & (RDS, \textit{irreversible}) \\
4.\ C* \rightleftharpoons C+* & (\textit{fast to equilibium})
\end{array}
$$

Here i represents some species in the fluid phase, * is free surface site, and i* is some intermediate species bound to a catalyst site. We further assume that step 3 is essentially irreversible (i.e., highly exothermic) and the surface is almost saturated with A*. The equilibrium constant for the formation of i* from fluid-phase reactant i, $K_{ads,i*}$ is simply

$$K_{ads,i*} = \exp(\frac{-G_{i*}^{0}}{RT}) = \exp(g_{i*}) \tag{8.9}$$

where G_{i*}^{0} is the standard-state Gibbs free energy of i* relative to the reactants. Using the Langmuir adsorption model, the site balance is given by Eq (8.10):

$$1 = \theta_{*} + \theta_{A*} + \theta_{B*} + \theta_{C*} = \theta_{*}\left(1 + K_{ads,A*}c_A + K_{ads,B*}c_B + K_{ads,C*}c_C\right) \tag{8.10}$$

where c_i is the concentration (or activity) of species i in the fluid phase. (Partial pressure could be used instead for gas phase species.) At steady state, application of the quasi-equilibrium approximation showed that the rate of the reaction can be written under these conditions as[42]

$$r = k_3 \frac{K_{ads,B*}}{K_{ads,A*}} \frac{c_B}{c_A} \tag{8.11}$$

where k_3 is the forward rate constant of Step 3. When all the rate constants and equilibrium constants are expressed in terms of standard-state Gibbs free energies, Eq (8.11) can be written as[43]

$$\begin{aligned} r &= \frac{k_B T}{h} \exp\left(g_{TS3} - 2g_{A*}\right) \frac{c_B}{c_A} \\ &= \frac{k_B T}{h} \exp\left(\frac{-G^0_{TS3} + 2G^0_{A*}}{RT} \right) \frac{c_B}{c_A} \\ &= \frac{k_B T}{h} \exp\left(\frac{S^0_{TS3} - 2S^0_{A*}}{R} \right) \exp\left(-\frac{H^0_{TS3} - 2H^0_{A*}}{RT} \right) \frac{c_B}{c_A} \end{aligned} \tag{8.12}$$

where g_{TS3} corresponds to the transition state in Step 3. Eq (8.12) fits well into Arrhenius form, with the apparent activation energy from the exponential term being $E_{app} = H^0_{TS3}-2H^0_{A*}$. Performing the partial derivatives of Eq (8.1) for the rate expression in Eq (8.12) gives that $X_{TS3} = 1$ and $X_{A*} = -2$. Plugging these DRCs into Eq (8.8) gives the same result except the RT term: $E_{app} = RT+H^0_{TS3} -2H^0_{A*}$. Strictly speaking, this additional RT is also included in E_{app} from Eq (8.12), since it results from the temperature dependence of the preexponential factor k_BT/h.

If the assumption that A* nearly saturates the surface does not hold, the analytical expression of the reaction rate is more complicated. Let us assume that the coverage of C* is negligibly low (as is generally the case for rate measurements at low conversions). Starting from the site balance in Eq (8.10), the fractional coverage of A* and B* are then:

$$\theta_{A*} = \frac{K_{ads,A*} c_A}{1 + K_{ads,A*} c_A + K_{ads,B*} c_B} = \frac{\exp(g_{A*}) c_A}{1 + \exp(g_{A*}) c_A + \exp(g_{B*}) c_B} \tag{8.13}$$

$$\theta_{B*} = \frac{K_{ads,B*}c_B}{1+K_{ads,A*}c_A + K_{ads,B*}c_B} = \frac{\exp(g_{B*})c_B}{1+\exp(g_{A*})c_A + \exp(g_{B*})c_B} \tag{8.14}$$

Applying the RDS assumption to Step 3 and transition state theory to this surface reaction, the final expression for the net rate r is:

$$\begin{aligned} r &= k_3\theta_{A*}\theta_{B*} = \frac{k_BT}{h}\exp(g_{TS3} - g_{A*} - g_{B*})\theta_{A*}\theta_{B*} \\ &= \frac{k_BT}{h}\exp(g_{TS3} - g_{A*} - g_{B*})\frac{\exp(g_{A*})c_A\exp(g_{B*})c_B}{\left[1+\exp(g_{A*})c_A + \exp(g_{B*})c_B\right]^2} \\ &= \frac{k_BT}{h}\frac{\exp(g_{TS3})c_Ac_B}{\left[1+\exp(g_{A*})c_A + \exp(g_{B*})c_B\right]^2} \end{aligned} \tag{8.15}$$

This rate equation does not explicitly fit in Arrhenius form. However, since the rate expression given by Eq (8.15) still has the same form as Eq (8.3), the derivation starting from Eq (8.3) to Eq (8.8) must still be correct for these more complicated conditions.

We show in the Supporting Information that this more complex expression for the rate gives the same (more complex) expression for E_{app} when calculate with Eq (8.8) above as that obtained using the alternate equation of Meskine et al.[188], except for the small difference of RT that appears in Eq (8.8) but not in their corresponding equation. Importantly, one can see in Eq (8.15) that there are only 3 species whose g_i values enter the rate expression (TS3, A* and B*), so there are only 3 species with non-zero DRCs and therefore only 3 terms needed in Eq (8.8) to calculate E_{app}. In contrast, the equation of Meskine et al. has 5 non-zero DRCs and thus 5 terms to evaluate to get E_{app}. The extent of this difference grows with the number of steps in the mechanism, so that this conceptual (and computational) simplification afforded by the new Eq (8.8) here over the method of Meskine et al. grows rapidly with mechanistic complexity.

8.4 CASE STUDY II. THE MICHAELIS-MENTEN MECHANISM FOR ENZYME CATALYZED REACTIONS

In enzyme catalyzed reactions, the enzyme is usually present at very low concentration compared to the substrate. The behavior of enzyme catalyzed reactions is similar to surface catalyzed reactions because both of them have limited amounts of active catalyst sites. Michaelis-Menten (M-M) mechanism is one of the best-known models for enzyme catalyzed reactions.[195] It consists of two steps:

$$\begin{aligned} &1.\ E+S \rightleftharpoons ES \\ &2.\ ES \rightarrow E+P \end{aligned}$$

Step 1 is a reversible binding process between the substrate (S) and the enzyme (E), and ES is the enzyme-substrate complex. Step 2 is the formation and release of the product (P). Applying the steady-state approximation to the enzyme-substrate complex ES concentration, [ES], the rate equation is:[195]

$$r = \frac{k_2[E]_0}{1+K_M/[S]_0} \tag{8.16}$$

$$K_M = \frac{k_{-1}+k_2}{k_1} \tag{8.17}$$

where $[E]_0$ is the initial concentration of the enzyme, $[S]_0$ is the initial concentration of the substrate, and K_M is the Michaelis constant.

When $[S]_0 >> K_M$, the rate expression reduces to:[195]

$$\begin{aligned} r &= k_2[E]_0 = \frac{k_BT}{h}\exp\left(g_{TS2}-g_{ES}\right)[E]_0 \\ &= \frac{k_BT}{h}\exp\left(\frac{S^0_{TS2}-S^0_{ES}}{R}\right)\exp\left(-\frac{H^0_{TS2}-H^0_{ES}}{RT}\right)[E]_0 \end{aligned} \tag{8.18}$$

In this case almost all the enzymes are bound to substrates, so the rate is only determined by the rate constant of Step 2 and the concentration of enzymes. Eq (8.18) fits well into the Arrhenius form, and it gives $E_{app} = RT+H^0_{TS2}-H^0_{ES}$. (Note that the RT here comes from the k_BT/h factor.) There are two species with non-zero DRCs: the transition state in Step 2 (TS2) has DRC = 1, and ES has DRC = -1. Plugging these DRCs into Eq (8.8) gives the same result: $E_{app} =RT+ H^0_{TS2}-H^0_{ES}$.

When $[S]_0 << K_M$ and $k_{-1}<<k_2$, Eq (8.16) reduces to:[195]

$$\begin{aligned} r &= \frac{k_2[E]_0[S]_0}{k_2/k_1} = k_1[E]_0[S]_0 = \frac{k_BT}{h}\exp\left(g_{TS1}-g_E-g_S\right)[E]_0[S]_0 \\ &= \frac{k_BT}{h}\exp\left(\frac{S^0_{TS1}-S^0_E-S^0_S}{R}\right)\exp\left(-\frac{H^0_{TS1}-H^0_E-H^0_S}{RT}\right)[E]_0[S]_0 \end{aligned} \tag{8.19}$$

The RDS is now Step 1. TS1 has DRC = 1, and both E and S have DRC = -1. Plugging the DRCs into Eq (8.8) gives $E_{app} = RT+H^0_{TS1}-H^0_E-H^0_S$, which is the same as given by the Arrhenius form of the rate law as written above in Eq (8.19).

When $[S]_0 << K_M$ and $k_{-1}>>k_2$, Eq (8.16) reduces to:[195]

$$\begin{aligned} r &= \frac{k_2[E]_0[S]_0}{k_{-1}/k_1} = \frac{k_BT}{h}\exp\left(g_{TS2}-g_{ES}-g_{TS1}+g_{ES}+g_{TS1}-g_E-g_S\right)[E]_0[S]_0 \\ &= \frac{k_BT}{h}\exp\left(\frac{S^0_{TS2}-S^0_E-S^0_S}{R}\right)\exp\left(-\frac{H^0_{TS2}-H^0_E-H^0_S}{RT}\right)[E]_0[S]_0 \end{aligned} \tag{8.20}$$

Now the three species with non-negligible DRCs, TS2, E and S, are not in the same step. TS2 has DRC = 1; E and S have DRC = -1. Eq (8.8) gives $E_{app} = RT+H^0_{TS2}-H^0_E-H^0_S$, and the Arrhenius form above gives the same.

In summary, Eq (8.8) gives the correct expression for E_{app} in all of these limiting cases of M-M kinetics.

8.5 CASE STUDY III. METHANOL SYNTHESIS THROUGH CO_2 HYDROGENATION ON CU(211)

The kinetics of methanol synthesis through CO_2 hydrogenation on Cu(211) model catalyst is investigated computationally in this section to verify how well the derived relation between DRCs, coverages and apparent activation energies match the results from full microkinetic modeling.

$$\mathrm{CO_2{+}3H_2 \rightarrow CH_3OH{+}H_2O}$$

We analyze here only a mechanism consisting of 8 elementary steps, using energies (and symbology) of all species in these steps taken from DFT calculations by Studt et al., as summarized in ref.,[209] where they used these DFT energetics to explain experimental rate measurements. Figure 3.1 shows the standard-state Gibbs free energy diagram of this reaction at 450 K. Microkinetic modeling and DRC calculations were carried out using CATMAP, a Python-based catalytic microkinetic modeling package.[210] The net rate, coverages, and DRCs at steady state were calculated under the following steady-state reaction conditions, in the limit of low conversion: 30 bar total, H_2/CO_2 = 3:1, 450 K.

The DRCs, coverages and enthalpies of intermediates and transition states relative to reactants are listed in Table 8.1. There is only one transition state, H-HCOOH, with a non-negligible DRC. It indicates that the third hydrogenation step is the RDS. There are two intermediates with coverages higher than 0.001, HCOO* and H*. HCOO* almost saturates the surface with a coverage of 0.984, and a DRC of -1.96.

The apparent activation energy is calculated first by modeling this reaction at 440, 450, 460 K and plotting ln(r) versus 1/T. The plot is shown in Figure 8.2a. The apparent activation energy determined from the slope of this Arrhenius plot is 220.06 kJ/mol. Using Eq (8.8), the apparent activation energy estimated with the DRCs and enthalpies of HCOO* and H-HCOOH is 220.79 kJ/mol, which is also in great agreement with the full microkinetic model:

$$\begin{aligned} E_{app} &= RT + \sum_i H_i X_i \\ &= 8.314 \times 450 / \left(1000 \text{ kJ/mol}\right) + \left[(-98.33) \times (-1.969) + 23.45 \times 0.999\right] \text{ kJ/mol} \\ &= 220.79 \text{ kJ/mol} \end{aligned}$$

The temperature was raised from 450 K to 570 K and the total pressure decreased from 30 to 25 bar, so that most of the sites became unoccupied, and the DRCs of intermediates changed significantly. The DRCs, coverages and enthalpies under this condition (still in the limit of low conversion) are listed in Table 8.2, and the corresponding Arrhenius plot of the rate at 560 to 580 K is shown in Figure 8.2b. An apparent activation energy of 63.64 kJ/mol is given. Adsorbed formate HCOO* is still the only abundant species, but the fractional coverage of HCOO* is now only 0.174 and its (negative) DRC also decreases in magnitude with its coverage down to -0.348. However, Eq (8.8) still works nearly perfectly in this case, giving an apparent activation energy E_{app} of 63.05 kJ/mol, with an error of only 0.59 kJ/mol.

8.6 CASE STUDY IV. METHANOL SYNTHESIS THROUGH CO_2 HYDROGENATION ON ZN-PROMOTED CU(211)

Studt et al.[209] also showed that the surface species in the CO_2 hydrogenation reaction on Zn-promoted Cu(211) model catalyst have different energies by DFT compared to those on pure Cu(211). Unlike this reaction on pure Cu(211), there is more than one transition state on Zn-promoted Cu(211) that exhibits rate-control based on the DRC calculation, and the relative strengths of their rate-control are sensitive to reaction conditions. The coverages, DRCs and enthalpies of species in this reaction are listed in Table 8.3 for a total pressure of 30 bar and a temperature of 503 K, again in the limit of low conversion. There are two surface transition states with a DRC larger than 0.1, HCOO-H and H-HCOOH, which means both the second and the third hydrogenation step are rate-controlling steps.

When Eq (8.8) is used for the apparent activation energy estimation, including only species with DRC larger than 0.01 (or smaller than -0.01) (i.e,, HCOOH*, HCOO*, H-H2CO, H-HCOOH, HCOO-H, H-OH), it gives the apparent activation energy to be 228.09 kJ/mol. The error is only 0.19 kJ/mol compared to the value given by the Arrhenius plot of the rates from the full microkinetic model's computational solutions, which is 228.28 kJ/mol (shown in Figure 8.2c).

8.7 DISCUSSION: COMPARISONS OF EQ (8.8) TO OTHER METHODS FOR ESTIMATING E_{APP}

We have provided above not only a rigorous derivation of Eq (8.8) but also proof that it gives the correct value for the apparent activation energy in all of the many case studies examined. We now summarize the weaknesses of previous attempts for predicting E_{app}.

8.7.1 *The Energy Span Model of Kozuch and Shaik*[189, 223, 227]

We first discuss only cases where there is a single RDS and a single rate-determining intermediate (i.e., "the most abundant reaction intermediate" or "the intermediate with the largest thermodynamic degree of rate control," by Kozuch and Shaik as the "TDI"), and when the rate-controlling transition state (i.e., the "TDTS") occurs after the rate-controlling intermediate in the mechanism. Under these conditions, the Energy Span Model proposes that E_{app} equals the difference in energies between these two states (plus RT, due to the k_BT/h factor).[189, 223, 227] Even though this model was developed for catalytic reactions involving only a single site, it has often been applied in reactions in heterogeneous catalysis where more than one site is involved. Therefore, it is worth considering whether this approximation can also be applied to the more general case studies and reactions explored above where Eq (8.8) is shown to be generally valid.

A problem with applying this Energy Span Model to reactions involving more than one catalyst site can be seen already from looking at the simplest situation in Case I above (the L-H mechanism), when the rate is given by Eq (8.12), from which it is obvious that $E_{app} = RT+H^0_{TS3}-2H^0_{A*}$. We noted above that Eq (8.8) also gives this same value. Since A* is "the most abundant reaction intermediate" and "the intermediate with the largest thermodynamic degree of rate control", A* should act as the TDI in the Energy Span Model, which would give $E_{app} = RT+H^0_{TS3}-H^0_{A*}$ based on the Energy Span Model. However, this is not the correct value. In papers which have applied the Energy Span Model in heterogeneous catalysis, the authors usually determined the TDI differently, by looking for the lowest-energy intermediate on an element-balanced reaction energy diagram.[228-234] If that type of element-balanced analysis were done for this simple mechanism, either B* or B would have to be added to A* to achieve element balance in defining the TDI. This type of element-balanced TDI would be either A*+B* or A*+B, giving either $E_{app} = RT+H^0_{TS3}-H^0_{A*}-H^0_{B*}$ or $E_{app} = RT+H^0_{TS3}-H^0_{A*}-H^0_{B}$ when applying the Energy Span Model to this simple mechanism. None of these are the correct value. This kind of mistake can be frequently seen in papers using the Energy Span Model in heterogeneous catalysis.[228-232, 234]

In the Energy Span Model, the apparent activation energy is directly calculated as the energy span between the TDI and the TDTS in cases where there is a single TDTS and a single TDI. However, if there is more than one TDTS or more than one TDI, as, for example, in the case of CO_2 hydrogenation on Zn-promoted Cu(211) above, the Energy Span Model does not provide a simple way to estimate the apparent activation energy like Eq (8.8) does.

Nevertheless, the Energy Span Model often does work for single-site catalysts, which probably explains its wide use in the homogeneous catalysis community. We show next, for example, that it works in all three of the limiting cases of M-M enzyme kinetics treated using Eq (8.8) above. Inspection of Eqs (8.18) to (8.20) for E_{app} of the M-M enzyme kinetics shows that they give the same result as the Energy Span Model. When $[S]_0 >> K_M$, the TDTS is TS2 and the TDI is ES. The Energy Span Model gives that $E_{app} = RT + H^0_{TS2} - H^0_{ES}$. When $[S]_0 << K_M$ and $k_{-1} << k_2$, the TDTS is TS1 and the TDI is E+S. The Energy Span Model gives that $E_{app} = RT + H^0_{TS1} - H^0_{E} - H^0_{S}$. When $[S]_0 << K_M$ and $k_{-1} >> k_2$, the TDTS is TS2 and the TDI is E+S. The Energy Span Model gives that $E_{app} = RT + H^0_{TS2} - H^0_{E} - H^0_{S}$. In all these three cases, E_{app} given by the analytical rate expression, the Energy Span Model and Eq (8.8) are the same.

8.7.2 *The Equation of Meskine et al.*[188]

As noted above, we prove in the SI that the equation of Meskine et al.[188] gives the same E_{app} expression for the more complex L-H rate expression in Case I, Eq (8.15), as we get from Eq (8.8). Because their derivation appears to us to be valid, we expect that it will generally give the same apparent activation energy as Eq (8.8) except the RT term. Its main problems are: (1) it is not as easily interpretable with a reaction-energy diagram as the new one derived here (Eq (8.8)), (2) the type of DRC used by Meskine et al. in their equation for E_{app} is not as easy to understand (nor as widely used) as the DRC type used here, (3) there are many more steps with non-zero DRCs, so their equation is much more difficult to implement and conceptualize than Eq (8.8).

8.7.3 *The Equation of Jørgensen and Grönbeck*[224]

The equation of Jørgensen and Grönbeck[224] says that the apparent activation energy is given by:

$$\begin{aligned} E_{app} = & \sum_{i\in vib} X_i \left(E_i + k_B T + T^2 \frac{\partial S_i}{\partial T} \right) + \sum_{j\in trans} X_j \left(E_j - \frac{k_B T}{2} + k_B T^2 \frac{\partial \ln P_j}{\partial T} \right) \\ & - k_B T^2 \sum_X \frac{\partial n_X}{\partial T} \ln p_X \end{aligned} \tag{8.21}$$

Note that the DRCs that appear here are the same type as we used above (and not the DRC$^{+/-}$ type used by Meskine et al.). However, they used <u>*only*</u> the DRCs for transition states (steps) in the summations in the above equation. We show below by comparison of the predictions of this equation to the case studies above that it is often incorrect. We believe the authors had a built-in mistake in their derivation of this equation above. Specifically, they apply the chain rule to get Eq 11 in their paper. This equation neglects the fact that rate also depends on some of the equilibrium constants for elementary steps, and not just rate constants, as seen even in many analytical rate expressions. Thus, it was incorrect for them to hold the equilibrium constants fixed (with the subscript K_i on the partial derivatives of the rate (r) with respect to rate constants $k_{i.}$). If they did not hold these constants, and if they had summed over all steps in both the forward and reverse directions, this would have been a correct equation. Indeed, in that case, their Eq 11 would have been very similar to the *correct* derivation using the chain rule by Meskine et al.[188]. Because they did not do that, Jørgensen and Grönbeck's equation above for E_{app} often fails. For example, if the most rate-controlling intermediate is not in the same step with the rate-controlling transition state, it fails.

In Case Study I, the L-H Mechanism, Jørgensen and Grönbeck's equation gives E_{app} = $RT+H^0_{TS2}-H^0_{A*}-H^0_{B*}$, whereas the correct value from Eq (8.12) (and Eq (8.8)) is E_{app} = $RT+H^0_{TS2}-2H^0_{A*}$

. In Case Study II, the M-M Mechanism, the equation of Jørgensen and Grönbeck gives the correct E_{app} for the first two limiting cases because the rate-determining transition state and the rate-determining intermediate are in the same step. However, it fails for the third, when $[S]_0 << K_M$ and $k_{-1}>>k_2$, where it gives $E_{app} = RT+ H^0_{TS2}-H^0_{ES}$, instead of the correct value from Eq (8.8): $E_{app} = RT+H^0_{TS2}-H^0_{E}-H^0_{S}$. Similarly, Jørgensen and Grönbeck's equation gives incorrect values for E_{app} for all of the examples treated above in Case Studies III and IV involving CO_2 Hydrogenation on both Cu(211) and Zn-Promoted Cu(211). For example, for Case Study III, it would give that E_{app} approximately equals to the activation energy for the RDS (i.e., $H^0_{H..HCOOH}-H^0_{H2COOH*}$) rather than the correct result that E_{app} is approximately $H^0_{H..HCOOH}-0.348\ H^0_{HCOO*}$.

8.7.4 *The Method of Choksi and Greeley*[235]

Choksi and Greeley[235] demonstrated, for specific reaction networks, that the apparent activation energy is the sum of activation energies of the elementary steps each weighted by the respective degrees of rate control of their transition states. This is essentially the same as the equation of Jørgensen and Grönbeck discussed above, and fails for the same reasons as outlined there.

8.7.5 *Parmon's Equation*

The equation of Parmon[192] states that E_{app} equals the difference between the standard-state enthalpy of the rate-limiting transition state and that of the initial reagents, plus RT. It was derived for *non-catalytic* stepwise reactions wherein every step is first-order in each intermediate. We therefore do not expect it to work for the catalytic reactions above. Indeed, it fails in most cases treated above, but works in a few (for example, Eqs (8.19) and (8.20)). For a catalyzed reaction, if the substrate is present only at very low concentration compared to the catalyst, the catalyst sites will only be slightly occupied at steady state. In this case, the number of available catalyst sites in no way limits the reaction, and the kinetic behavior of the reaction is more like a non-catalytic reaction. This is why Parmon's equation works in the two limiting cases described by Eqs (8.19) and (8.20). However, in most cases the catalyst sites are significantly occupied, so Parmon's equation seldom works for catalyzed reactions, nor was it intended for them.

8.8 CONCLUSIONS

The apparent activation energy for steady-state reactions, even for the most complex reaction mechanisms, has been proven here to equal the weighted average of the standard-state enthalpies of all the species in the reaction mechanism (intermediates, transition states and products) relative to reactants, each weighted by its DRC, plus RT. This relationship offers improvements over any previous equations used for estimating apparent activation energies. It is valid whenever transition state theory is valid for all forward and reverse steps. Since usually only a small number of species have non-negligible DRCs, this relationship makes it easy to understand the relationship between the reaction energy diagram and the apparent activation energy.

8.9 SUPPLEMENTARY INFORMATION

Starting from Eqs (8.13)-(8.15) in the main paper, the rate equation of L-H mechanism with competitive adsorption in terms of rate constants and equilibrium constants can be written as

$$\begin{aligned} r &= k_3\theta_{A*}\theta_{B*} \\ &= \frac{k_3K_{ads,A*}c_AK_{ads,B*}c_B}{\left(K_{ads,A*}c_A + K_{ads,B*}c_B + 1\right)^2} \\ &= \frac{k_3k_1k_2c_Ac_B \,/\, (k_{-1}k_{-2})}{\left(k_1c_A / k_{-1} + k_2c_B / k_{-2} + 1\right)^2} \\ &= \frac{k_3k_1k_2k_{-1}k_{-2}c_Ac_B}{\left(k_1k_{-2}c_A + k_2k_{-1}c_B + k_{-1}k_{-2}\right)^2} \end{aligned}$$

The degrees of rate control (referred to as DRC$^{+/-}$ in the main text) are defined by Eq 3 in the paper of Meskine et al.[188] as:

$$\begin{aligned} x_1^+ &= k_1\frac{\partial \ln r}{\partial k_1} = k_1\left[\frac{1}{k_1} - \frac{2k_{-2}c_A}{k_1k_{-2}c_A + k_2k_{-1}c_B + k_{-1}k_{-2}}\right] = \frac{k_2k_{-1}c_B + k_{-1}k_{-2} - k_1k_{-2}c_A}{k_1k_{-2}c_A + k_2k_{-1}c_B + k_{-1}k_{-2}} \\ x_1^- &= k_{-1}\frac{\partial \ln r}{\partial k_{-1}} = k_{-1}\left[\frac{1}{k_{-1}} - \frac{2\left(k_2c_B + k_{-2}\right)}{k_1k_{-2}c_A + k_2k_{-1}c_B + k_{-1}k_{-2}}\right] = \frac{-k_2k_{-1}c_B - k_{-1}k_{-2} + k_1k_{-2}c_A}{k_1k_{-2}c_A + k_2k_{-1}c_B + k_{-1}k_{-2}} \\ x_2^+ &= k_2\frac{\partial \ln r}{\partial k_2} = k_2\left[\frac{1}{k_2} - \frac{2k_{-1}c_B}{k_1k_{-2}c_A + k_2k_{-1}c_B + k_{-1}k_{-2}}\right] = \frac{-k_2k_{-1}c_B + k_{-1}k_{-2} + k_1k_{-2}c_A}{k_1k_{-2}c_A + k_2k_{-1}c_B + k_{-1}k_{-2}} \\ x_2^- &= k_{-2}\frac{\partial \ln r}{\partial k_{-2}} = k_{-2}\left[\frac{1}{k_{-2}} - \frac{2\left(k_1c_A + k_{-1}\right)}{k_1k_{-2}c_A + k_2k_{-1}c_B + k_{-1}k_{-2}}\right] = \frac{k_2k_{-1}c_B - k_{-1}k_{-2} - k_1k_{-2}c_A}{k_1k_{-2}c_A + k_2k_{-1}c_B + k_{-1}k_{-2}} \\ x_3^+ &= k_3\frac{\partial \ln r}{\partial k_3} = k_3 * \frac{1}{k_3} = 1 \end{aligned}$$

Expressing these DRC$^{+/-}$'s in terms of energies (g_i) gives:

$$\begin{aligned}
x_1^+ &= \frac{\exp(g_{B*})c_B + 1 - \exp(g_{A*})c_A}{\exp(g_{A*})c_A + \exp(g_{B*})c_B + 1}\\
x_1^- &= \frac{-\exp(g_{B*})c_B - 1 + \exp(g_{A*})c_A}{\exp(g_{A*})c_A + \exp(g_{B*})c_B + 1}\\
x_2^+ &= \frac{-\exp(g_{B*})c_B + 1 + \exp(g_{A*})c_A}{\exp(g_{A*})c_A + \exp(g_{B*})c_B + 1}\\
x_2^- &= \frac{\exp(g_{B*})c_B - 1 - \exp(g_{A*})c_A}{\exp(g_{A*})c_A + \exp(g_{B*})c_B + 1}\\
x_3^+ &= 1
\end{aligned}$$

The DRC$^{+/-}$'s of all other steps are zero. Then plugging these DRC$^{+/-}$'s into Eq 12 in their paper gives E$_{app}$:

$$\begin{aligned}
E_{app} &= x_1^+\left(E_{TS1} - E_A\right) + x_1^-\left(E_{TS1} - E_{A*}\right) + x_2^+\left(E_{TS2} - E_B\right) + x_2^-\left(E_{TS2} - E_{B*}\right) + x_3^+\left(E_{TS3} - E_{A*} - E_{B*}\right)\\
&= \frac{1}{\exp(g_{A*})c_A + \exp(g_{B*})c_B + 1}\left\{\begin{array}{l}\exp(g_{B*})c_B\left[\left(E_{TS1} - E_A\right) - \left(E_{TS1} - E_{A*}\right) - \left(E_{TS2} - E_B\right) + \left(E_{TS2} - E_{B*}\right)\right]\\ + \exp(g_{A*})c_A\left[-\left(E_{TS1} - E_A\right) + \left(E_{TS1} - E_{A*}\right) + \left(E_{TS2} - E_B\right) - \left(E_{TS2} - E_{B*}\right)\right]\\ + \left[\left(E_{TS1} - E_A\right) - \left(E_{TS1} - E_{A*}\right) + \left(E_{TS2} - E_B\right) - \left(E_{TS2} - E_{B*}\right)\right]\end{array}\right\}\\
&\quad + \left(E_{TS3} - E_{A*} - E_{B*}\right)\\
&= \frac{1}{\exp(g_{A*})c_A + \exp(g_{B*})c_B + 1}\left\{\exp(g_{B*})c_B\left[E_{A*} - E_{B*}\right] + \exp(g_{A*})c_A\left[-E_{A*} + E_{B*}\right] + \left[E_{A*} + E_{B*}\right]\right\}\\
&\quad + \left(E_{TS3} - E_{A*} - E_{B*}\right)\\
&= \frac{1}{\exp(g_{A*})c_A + \exp(g_{B*})c_B + 1}\left\{\exp(g_{B*})c_B\left[-2E_{B*}\right] + \exp(g_{A*})c_A\left[-2E_{A*}\right]\right\} + E_{TS3}
\end{aligned}$$

Starting over from Eq (8.15) in the main paper and calculating generalized DRCs defined by Eq (8.1) in the main paper gives:

$$\begin{aligned}
X_{A*} &= \frac{\partial \ln r}{\partial g_{A*}} = \frac{-2\exp\left(g_{A*}\right)c_A}{1 + \exp\left(g_{A*}\right)c_A + \exp\left(g_{B*}\right)c_B}\\
X_{B*} &= \frac{\partial \ln r}{\partial g_{B*}} = \frac{-2\exp\left(g_{B*}\right)c_B}{1 + \exp\left(g_{A*}\right)c_A + \exp\left(g_{B*}\right)c_B}\\
X_{TS3} &= \frac{\partial \ln r}{\partial g_{TS3}} = 1
\end{aligned}$$

Comparing the generalized DRCs with the final form of E$_{app}$ calculated with their equation, the expression of E$_{app}$ given by their equation can be rewritten as

$$E_{app} = X_{B*}E_B + X_{A*}E_{A*} + X_{TS3}E_{TS3}$$

which is the same result as Eq (8.8) in the main paper except for the RT term and the fact that this has energies where Eq (8.8) has enthalpies.

8.10 FIGURES

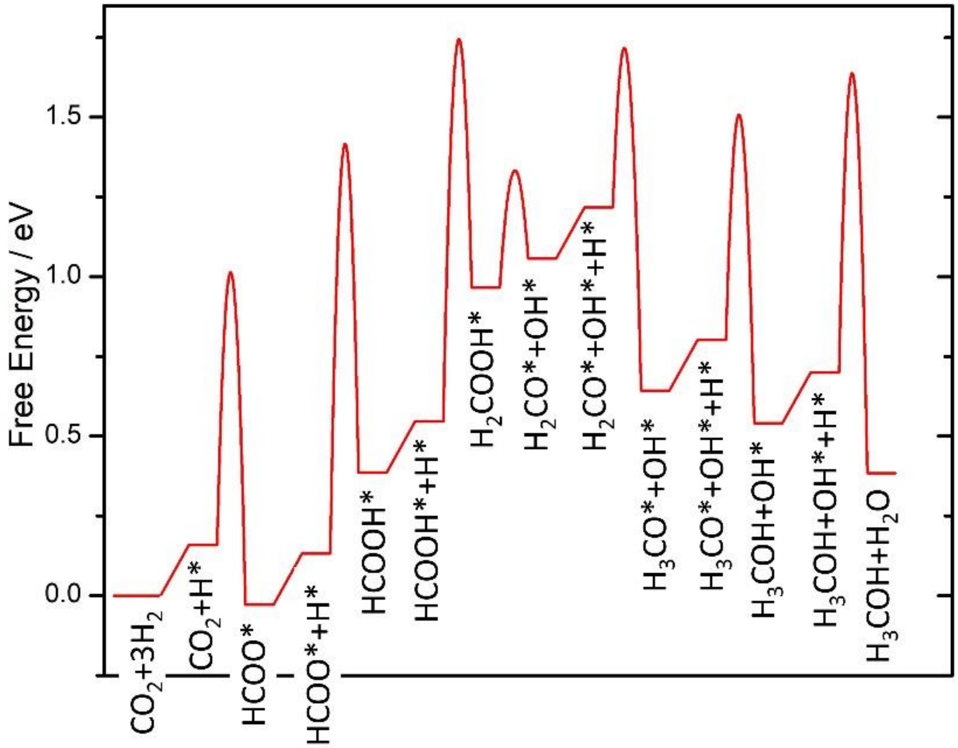

Figure 8.1 Standard-state Gibbs free energy diagram of CO_2 hydrogenation on Cu(211) at 450 K, based on DFT results taken from Studt et al.[209], with minor modifications. Note that H_2 has been omitted in the labels of many of the states, and should be included in the necessary amount to achieve element balance for each step and species.

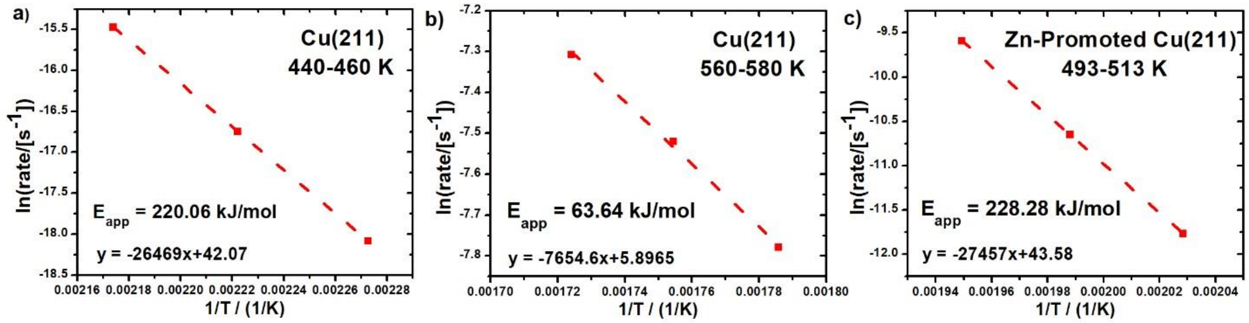

Figure 8.2 Arrhenius plots for determination of the apparent activation energy E_{app} of CO_2 hydrogenation on (a) Cu(211) at 30 bar from 440 to 460 K, (b) Cu(211) at 25 bar from 560 to 580 K, and (c) Zn-promoted Cu(211) at 30 bar from 493 to 513 K. For each plot, the two outer points are separated by only 10 K from the center point, so their slopes from the center point differ very little (and symmetrically) from the 3-point-average slope shown here (i.e., by 0.89 and -0.93 kJ/mol, 4.97 and -5.21 kJ/mol and 1.98 and -2.09 kJ/mol for a, b and c, respectively). This average slope is therefore an excellent approximation to the true differential slope at the center point, which provides the E_{app} of interest here.

8.11 TABLES

Table 8.1 The coverages, degrees for rate control and enthalpies of all intermediates and transition states of CO_2/H_2 hydrogenation on Cu(211) at 450 K.

Species	Coverage	X_i	H_i/(kJ/mol)
Intermediates			
H_2COOH^*	0.000	0.000	- 39.08
H_2CO^*	0.000	0.000	-17.18
HCOOH*	0.000	0.000	- 11.68
HCOO*	0.984	-1.969	-98.33
H*	0.001	-0.002	-11.87
OCH_3^*	0.000	0.000	-86.75
OH*	0.000	0.000	-27.99
*	0.015	–	–
Transition states			
H-COO	–	0.000	12.16
$H\text{-}H_2CO$	–	0.000	22.10
H-HCOOH	–	0.999	23.45
$H\text{-}OCH_3$	–	0.000	-18.91
H-OH	–	0.000	56.36
$H_2CO\text{-}OH$	–	0.000	-19.30
HCOO-H	–	0.001	18.14

Table 8.2 The coverages, degrees for rate control and enthalpies of all intermediates and transition states of CO_2/H_2 hydrogenation on Cu(211) at 570 K.

Species	Coverage	X_i	H_i/(kJ/mol)
Intermediates			
H_2COOH^*	0.000	0.000	- 39.08
H_2CO^*	0.000	0.000	-17.18
HCOOH*	0.002	-0.005	- 11.68
HCOO*	0.174	-0.348	-98.33
H*	0.003	-0.006	-11.87
OCH_3^*	0.000	0.000	-86.75
OH*	0.000	0.000	-27.99
*	0.821	–	–
Transition states			
H-COO	–	0.000	12.16
$H\text{-}H_2CO$	–	0.000	22.10
H-HCOOH	–	0.998	23.45
$H\text{-}OCH_3$	–	0.000	-18.91
H-OH	–	0.000	56.36
$H_2CO\text{-}OH$	–	0.000	-19.30
HCOO-H	–	0.001	18.14

Table 8.3 The coverages, degrees for rate control and enthalpies of all intermediates and transition states of CO_2/H_2 hydrogenation on Zn-promoted Cu(211) at 503 K.

Species	Coverage	X_i	H_i/(kJ/mol)
Intermediates			
H_2COOH^*	0.000	0.000	-54.52
H_2CO^*	0.000	0.000	-13.80
HCOOH*	0.024	-0.048	-39.37
HCOO*	0.966	-1.931	-112.33
H*	0.000	-0.001	-11.87
OCH_3^*	0.000	0.000	-108.47
OH*	0.002	-0.004	-55.29
*	0.008	–	–
Transition states			
H-COO	–	0.000	-5.79
$H\text{-}H_2CO$	–	0.076	24.80
H-HCOOH	–	0.632	-5.60
$H\text{-}OCH_3$	–	0.000	-28.76
H-OH	–	0.080	51.34
$H_2CO\text{-}OH$	–	0.000	-44.39
HCOO-H	–	0.212	12.45

Chapter 9. Conclusions and Future Outlook

This dissertation includes fundamental studies in heterogeneous catalysis with both experimental and theoretical approaches. It talks about two major questions: (1) how the properties of metal nanoparticles supported on oxide surfaces vary with the size of nanoparticles and the choice of oxide surfaces; (2) how to simplify the complex reaction mechanisms of surface catalyzed reactions and describe them with a few key factors.

Chapters 2-5 are about the first question. In Chapter 2, an apparatus designed for Single Crystal Adsorption Calorimetry (SCAC) and the procedure of SCAC experiment are introduced. The apparatus generates a focused metal molecular beam with an e-beam evaporator and deposits the gaseous metal onto the prepared metal oxide single crystal surface in pulses. The heat released up metal adsorption is detected and converted to the heat of adsorption of the metal on the given oxide surface as a function of the meta coverage. The growth morphology of the metal nanoparticles on the oxide surface is measured with He^+ LEIS, and the oxidation states of the elements in metal nanoparticles and oxide substrate are monitored with XPS.

In Chapter 3, Ni nanoparticles on reducible ceria $CeO_{2-x}(111)$ is studied with SCAC, XPS, LEIS and DFT. Ni atoms adsorb on slightly reduced ceria $CeO_{2-x}(111)$ and form three-dimensional nanoparticles at 300 and 100 K, which increase in size with increasing Ni loading. The extent of reduction of ceria has a minor effect on the Ni particle number density at 300 K, while decreasing temperature from 300 to 100 K results in 3-fold higher Ni particle number density on $CeO_{1.95}(111)$. The heat of Ni adsorption onto $CeO_{1.95}(111)$ at 300 K starts from 345 kJ/mol (attributed to step edges), decreases within the first 0.2 ML to 323 kJ/mol (as step edge sites saturate), and increases afterward (due to growing particle size) until the bulk heat of Ni sublimation is reached by 9 ML. On $CeO_{1.8}(111)$ at 300 K, this initial drop in heat of adsorption was not observed, attributed to weaker Ni binding to step edges when full of O vacancies. The heat of adsorption is generally lower on the more reduced ceria surface (by up to 65 kJ/mol initially at 300 K), again suggesting that the oxophilic Ni atoms do not prefer O vacancies. DFT calculations support this. On $CeO_{1.95}(111)$ at 100 K, Ni atoms adsorb mainly on terraces due to slow Ni adatom diffusion, with an initial heat of adsorption that is 45 kJ/mol lower than that at 300 K where Ni atoms mainly adsorb on step edges. This highlights Ni's strong preference for step edges over terraces. Upon adsorption, Ni atoms donate electrons to the support to generate Ce^{3+}. DFT calculations show that this charge is localized on the interfacial Ni and Ce atoms in their atomic layers closest to the interface. As the coverage and particle size grow, the average number of electrons donated per Ni atom decreases in both experiments and DFT calculations. For the same size, Ni particles exhibit less charge transfer to $CeO_{1.95}(111)$ at 100 K (when on terraces) than at 300 K (when at step edges). The charge transfer from Ni particles is much less on $CeO_{1.8}(111)$ compared to $CeO_{1.95}(111)$ at both temperatures.

In Chapter 4, Ni nanoparticles supported on MgO(100) is studied. The LEIS experiments showed that Ni grows as 3D nanoparticles on MgO(100) at 300 K with a particle number density of 5.0×10^{16} particles/m^2. At 100 K, Ni forms Ni single atoms on lattice O sites of MgO(100) at low coverage, then forms tiny 2D Ni islands with an average thickness of 0.17 nm (40% thicker than a Ni single layer with a packing density equals the number density of O on MgO(100)). The Ni atoms follow this 2D growth mode until the surface is covered completely at 1.4 ML, and the incoming Ni atoms then grow on this complete Ni overlayer. Since the Ni atoms cover the surface much faster at 100 K, the sticking probability at 100 K remains higher than that at 300 K until the sticking probability at 300 K also reaches unity by 8 ML. At 300 K, the heat of Ni vapor adsorption to make Ni particles containing 7 atoms on MgO(100) is 276 kJ/mol, and it increases rapidly reaching 335 kJ/mol by 0.4 ML. The heat slowly increases thereafter and levels off at the sublimation enthalpy of bulk Ni by 9 ML. At 100 K, the initial heat of adsorption is 128 kJ/mol lower than that at 300 K, which directly represents the binding energy between Ni single atoms and O on MgO(100). The binding energy of Ni $2p_{3/2}$ XPS peak for 0.16 ML Ni on MgO at 300 K is 1.4 eV higher than that for bulk Ni(solid). As the coverage increases, the Ni $2p_{3/2}$ peak binding energy decreases until the binding energy for bulk Ni is reached at high coverage. At 100 K, 0.21 ML of Ni on MgO(100) has its $2p_{3/2}$ XPS peak's binding energy higher than that for bulk Ni by 2.2 eV, which suggests electron transfer from Ni to MgO substrate and the formation of Ni^{2+}.

In Chapter 5, first an equation is introduced that describes the chemical potential of metal atoms in supported nanoparticles as a function of the particle diameter and the adhesion energy of metal to oxide surface. It quantitatively describes how the chemical potential of metal atoms in supported nanoparticles increases with decreasing particle size and decreasing adhesion energy of metal to oxide surface. Applying this equation to the chemical potential of Ni atoms in nanoparticles supported on MgO(100) and $CeO_{1.95}(111)$ gives the adhesion energy of Ni to MgO(100) (3.05 J/m^2) and $CeO_{1.95}(111)$ (4.39 J/m^2) surfaces. Ni has higher adhesion energy on these two oxide surfaces than the other metals that measured previously, due to its high oxophilicity. The adhesion energies of Ni to MgO(100) and $CeO_{1.95}(111)$ are well fit in a trend that the adhesion energy of metals to a given oxide correlate linearly with their oxophilicity.

Chapters 6-8 talks about the second question. Using degree of rate control (DRC) analysis, the complex reaction mechanisms can be simplified and only a few kinetically-relevant species with nonzero DRCs are focused. In Chapter 6, a relation between the DRCs of adsorbed species and their fractional population of catalyst sites is proven. Under steady-state reaction conditions, the DRC for any catalyst-bound intermediate is proportional to its fractional population of catalyst sites, with a proportional factor that is the DRC-weighted average of the site requirements for all the elementary steps.

In Chapter 7, a method to interpret kinetic isotope effects (KIEs) using degree of rate control (DRC) analysis is presented. When the KIE is measured as the rate ratio for two isotopes in separate experiments, the logarithm of the rate ratio equals the weighted average over all species in the mechanism of their standard-state free energy differences between the two isotopes, divided by RT, where the weighting factor for each species is its DRC. This method assumes that the DRCs do not change with isotope (which is sometimes not the case). It reveals that the KIE calculated from the isotope effect on the rate-determining step is not enough to represent the overall KIE of the whole catalytic cycle, since species in other steps often also exhibit large influences on the KIE (i.e., large DRCs). We also show that when the KIE is measured as the product selectivity in the competition between two isotopes in the same reactant, an extension of DRC called the degree of selectivity ratio control (DSRC) provides a similar equation whereby the weighting factor is now the DSRC. These equations aid in the mechanistic interpretation and quantitative analysis of KIEs.

In Chapter 8, the apparent activation energy for steady-state reactions, even for the most complex reaction mechanisms, is proven to equal the weighted average of the standard-state enthalpies of all the species in the reaction mechanism (intermediates, transition states and products) relative to reactants, each weighted by its DRC, plus RT. This relationship offers improvements over any previous equations used for estimating apparent activation energies. It is valid whenever transition state theory is valid for all forward and reverse steps. Since usually only a small number of species have non-negligible DRCs, this relationship makes it easy to understand the relationship between the reaction energy diagram and the apparent activation energy.

For the studies of supported metal nanoparticles, the correlation of the adhesion energies of metals to oxide surfaces with the metals' oxophilicity is clear, but only for the two oxides that have been studied intensively, MgO(100) and $CeO_{1.95}$(111). Another question left is how the adhesion energy of a given metal to the oxide surfaces varies with the choice of oxide. A new project has been finished last year to measure the adhesion energy of Ag to TiO_2(100) surface. The result agrees with another trend reported previously that the adhesion energies of metal nanoparticles to oxide surfaces correlate with the reduction enthalpy of the oxide (or the formation energy of O vacancies in the oxide). To further elucidate the correlation, the library of adhesion energy needs more data.

Beside oxide, carbon is another class of materials used to support metal nanoparticles. Studies about carbon support has also started last year in Campbell lab. The heat of adsorption of Ag onto the single-layer graphene grown on Ni(111) surface has been measured. The next step is switching the sample from the single-layer graphene to the multilayer graphite.

For the degree of rate control, the framework of the theory has been well established. The DRC analysis has been proved to be a powerful tool for catalysis research, and has been implemented in several computational package for microkinetic modeling such as CatMap. The next move is using this powerful tool in important catalyzed reactions, improving the understanding for complex reaction mechanisms, and helping the rational design of better catalysts.

BIBLIOGRAPHY

[1] Wolcott, C. A.; Medford, A. J.; Studt, F.; Campbell, C. T., Degree of Rate Control Approach to Computational Catalyst Screening. *J. Catal.* **2015,** *330*, 197-207.

[2] Xu, Y.; Lausche, A. C.; Wang, S.; Khan, T. S.; Abild-Petersen, F.; Studt, F.; Norskov, J. K.; Bligaard, T., In Silico Search for Novel Methane Steam Reforming Catalysts. *New J. Phys.* **2013,** *15*, 125021.

[3] Hou, Z.; Gao, J.; Guo, J.; Liang, D.; Lou, H.; Zheng, X., Deactivation of Ni Catalysts During Methane Autothermal Reforming with Co2 and O2 in a Fluidized-Bed Reactor. *J. Catal.* **2007,** *250*, 331-341.

[4] Sirijaruphan, A.; Goodwin, J. G.; Rice, R. W., Investigation of the Initial Rapid Deactivation of Platinum Catalysts During the Selective Oxidation of Carbon Monoxide. *J. Catal.* **2004,** *221* (2), 288-293.

[5] Pereira, E. B.; Martin, G.-A., Morphology Changes and Deactivation of Alkali-Promoted Ni/Sio2 Catalysts During Carbon Monoxide Hydrogenation. *Appl. Catal., A* **1994,** *115*, 135-146.

[6] Crampton, A. S.; Rötzer, M. D.; Schweinberger, F. F.; Yoon, B.; Landman, U.; Heiz, U., Ethylene Hydrogenation on Supported Ni, Pd and Pt Nanoparticles: Catalyst Activity, Deactivation and the D-Band Model. *J. Catal.* **2016,** *333*, 51-58.

[7] Xu, Z.; Li, Y.; Zhang, J.; Chang, L.; Zhou, R.; Duan, Z., Bound-State Ni Species—a Superior Form in Ni-Based Catalyst for Ch4/Co2 Reforming. *Appl. Catal., A* **2001,** *210* (1-2), 45-53.

[8] Takenaka, S.; Ogihara, H.; Yamanaka, I.; Otsuka, K., Decomposition of Methane over Supported-Ni Catalysts: Effects of the Supports on the Catalytic Lifetime. *Appl. Catal., A* **2001,** *217* (1-2), 101-110.

[9] Jones, J.; Xiong, H. F.; Delariva, A. T.; Peterson, E. J.; Pham, H.; Challa, S. R.; Qi, G. S.; Oh, S.; Wiebenga, M. H.; Hernandez, X. I. P.; Wang, Y.; Datye, A. K., Thermally Stable Single-Atom Platinum-on-Ceria Catalysts Via Atom Trapping. *Science* **2016,** *353* (6295), 150-154.

[10] Li, Y.; Lu, G.; Ma, J., Highly Active and Stable Nano Nio–Mgo Catalyst Encapsulated by Silica with a Core–Shell Structure for Co 2 Methanation. *RSC Adv.* **2014,** *4* (34), 17420-17428.

[11] Matsubu, J. C.; Yang, V. N.; Christopher, P., Isolated Metal Active Site Concentration and Stability Control Catalytic Co2 Reduction Selectivity. *J. Am. Chem. Soc.* **2015,** *137* (8), 3076-3084.

[12] Matsubu, J. C.; Zhang, S.; DeRita, L.; Marinkovic, N. S.; Chen, J. G.; Graham, G. W.; Pan, X.; Christopher, P., Adsorbate-Mediated Strong Metal–Support Interactions in Oxide-Supported Rh Catalysts. *Nat. Chem.* **2017,** *9* (2), 120-127.

[13] Cargnello, M.; Doan-Nguyen, V. V. T.; Gordon, T. R.; Diaz, R. E.; Stach, E. A.; Gorte, R. J.; Fornasiero, P.; Murray, C. B., Control of Metal Nanocrystal Size Reveals Metal-Support Interface Role for Ceria Catalysts. *Science* **2013,** *341* (6147), 771-773.

[14] Ahmadi, M.; Mistry, H.; Cuenya, B. R., Tailoring the Catalytic Properties of Metal Nanoparticles Via Support Interactions. *J. Phys. Chem. Lett.* **2016,** *7* (17), 3519-3533.

[15] Campbell, C. T.; Sellers, J. R. V., Anchored Metal Nanoparticles: Effects of Support and Size on Their Energy, Sintering Resistance and Reactivity. *Faraday Discuss.* **2013,** *162*, 9-30.

[16] Farmer, J. A.; Campbell, C. T., Ceria Maintains Smaller Metal Catalyst Particles by Strong Metal-Support Bonding. *Science* **2010,** *329* (5994), 933-936.

[17] Sellers, J. R. V.; James, T. E.; Hemmingson, S. L.; Farmer, J. A.; Campbell, C. T., Adsorption Calorimetry During Metal Vapor Deposition on Single Crystal Surfaces: Increased Flux, Reduced Optical Radiation, and Real-Time Flux and Reflectivity Measurements. *Rev. Sci. Instrum.* **2013,** *84* (12), 123901.

[18] He, J. W.; Shea, W. L.; Jiang, X.; Goodman, D. W., Surface Chemistry of Monolayer Metallic Films on Re (0001) and Mo (110). *J. Vac. Sci. Technol., A* **1990,** *8* (3), 2435-2444.

[19] Brown, W. A.; Kose, R.; King, D. A., Femtomole Adsorption Calorimetry on Single-Crystal Surfaces. *Chem. Rev.* **1998,** *98*, 797-831.

[20] Dixon-Warren, S. J.; Kovar, M.; Wartnaby, C. E.; King, D. A., Pyroelectric Single Crystal Adsorption Microcalorimetry at Low Temperatures: Oxygen on Ni(100). *Surf. Sci.* **1994,** *307*, 16-22.

[21] Stuck, A.; Wartnaby, C. E.; Yeo, Y. Y.; Stuckless, J. T.; Al-Sarraf, N.; King, D. A., An Improved Single Crystal Adsorption Calorimeter. *Surf. Sci.* **1996,** *349*, 229-240.

[22] Borroni-Bird, C. E.; Al-Sarraf, N.; Andersson, S.; King, D. A., Single Crystal Adsorption Microcalorimetry. *Chem. Phys. Lett.* **1991,** *183*, 516-520.

[23] Lew, W.; Lytken, O.; Farmer, J. A.; Crowe, M. C.; Campbell, C. T., Improved Pyroelectric Detectors for Single Crystal Adsorption Calorimetry from 100 to 350 K. *Rev. Sci. Instrum.* **2010,** *81*, 024102.

[24] Sehested, J.; Gelten, J. A. P.; Helveg, S., Sintering of Nickel Catalysts: Effects of Time, Atmosphere, Temperature, Nickel-Carrier Interactions, and Dopants. *Appl. Catal., A* **2006,** *309* (2), 237-246.

[25] Xu, W. Q.; Liu, Z. Y.; Johnston-Peck, A. C.; Senanayake, S. D.; Zhou, G.; Stacchiola, D.; Stach, E. A.; Rodriguez, J. A., Steam Reforming of Ethanol on Ni/Ceo2: Reaction Pathway and Interaction between Ni and the Ceo2 Support. *ACS Catal.* **2013,** *3* (5), 975-984.

[26] Senanayake, S. D.; Rodriguez, J. A.; Stacchiola, D., Electronic Metal-Support Interactions and the Production of Hydrogen through the Water-Gas Shift Reaction and Ethanol Steam Reforming: Fundamental Studies with Well-Defined Model Catalysts. *Top. Catal.* **2013,** *56* (15-17), 1488-1498.

[27] Pacchioni, G., Electronic Interactions and Charge Transfers of Metal Atoms and Clusters on Oxide Surfaces. *Phys. Chem. Chem. Phys.* **2013,** *15* (6), 1737-1757.

[28] O'Brien, C. P.; Dostert, K. H.; Hollerer, M.; Stiehler, C.; Calaza, F.; Schauermann, S.; Shaikhutdinov, S.; Sterrer, M.; Freund, H. J., Supports and Modified Nano-Particles for Designing Model Catalysts. *Faraday Discuss.* **2016,** *188*, 309-321.

[29] Liu, Z. Y.; Grinter, D. C.; Lustemberg, P. G.; Nguyen-Phan, T. D.; Zhou, Y. H.; Luo, S.; Waluyo, I.; Crumlin, E. J.; Stacchiola, D. J.; Zhou, J.; Carrasco, J.; Busnengo, H. F.; Ganduglia-Pirovano, M. V.; Senanayake, S. D.; Rodriguez, J. A., Dry Reforming of Methane on a Highly-Active Ni-Ceo2 Catalyst: Effects of Metal-Support Interactions on C-H Bond Breaking. *Angew. Chem. Int. Ed.* **2016,** *55* (26), 7455-7459.

[30] Carrasco, J.; Barrio, L.; Liu, P.; Rodriguez, J. A.; Ganduglia-Pirovano, M. V., Theoretical Studies of the Adsorption of Co and C on Ni(111) and Ni/Ceo2 (111):

Evidence of a Strong Metal-Support Interaction. *J. Phys. Chem. C* **2013,** *117* (16), 8241-8250.

[31] Campbell, C. T., Catalyst-Support Interactions Electronic Perturbations. *Nat. Chem.* **2012,** *4* (8), 597-598.

[32] Zhou, Y. H.; Perket, J. M.; Crooks, A. B.; Zhou, J., Effect of Ceria Support on the Structure of Ni Nanoparticles. *J. Phys. Chem. Lett.* **2010,** *1* (9), 1447-1453.

[33] Carrasco, J.; Lopez-Duran, D.; Liu, Z. Y.; Duchon, T.; Evans, J.; Senanayake, S. D.; Crumlin, E. J.; Matolin, V.; Rodriguez, J. A.; Ganduglia-Pirovano, M. V., In Situ and Theoretical Studies for the Dissociation of Water on an Active Ni/Ceo2 Catalyst: Importance of Strong Metal-Support Interactions for the Cleavage of O-H Bonds. *Angew. Chem. Int. Ed.* **2015,** *54* (13), 3917-3921.

[34] Zhang, R.-j.; Xia, G.-f.; Li, M.-f.; Yu, W. U.; Hong, N. I. E.; Li, D.-d., Effect of Support on the Performance of Ni-Based Catalyst in Methane Dry Reforming. *J. Fuel Chem. Technol.* **2015,** *43* (11), 1359-1365.

[35] Hemmingson, S. L.; Campbell, C. T., Trends in Adhesion Energies of Metal Nanoparticles on Oxide Surfaces: Understanding Support Effects in Catalysis and Nanotechnology. *ACS Nano* **2017,** *11* (2), 1196-1203.

[36] Campbell, C. T.; Mao, Z. T., Chemical Potential of Metal Atoms in Supported Nanoparticles: Dependence Upon Particle Size and Support. *ACS Catal.* **2017,** *7* (12), 8460-8466.

[37] Tian, W.; Sun, H. P.; Pan, X. Q.; Yu, J. H.; Yeadon, M.; Boothroyd, C. B.; Feng, Y. P.; Lukaszew, R. A.; Clarke, R., Hexagonal Close-Packed Ni Nanostructures Grown on the (001) Surface of Mgo. *Appl. Phys. Lett.* **2005,** *86* (13), 131915.

[38] Mullins, D. R.; Radulovic, P. V.; Overbury, S. H., Ordered Cerium Oxide Thin Films Grown on Ru(0001) and Ni(111). *Surf. Sci.* **1999,** *429* (February), 186-98.

[39] Medford, A. J.; Vojvodic, A.; Hummelshoj, J. S.; Voss, J.; Abild-Pedersen, F.; Studt, F.; Bligaard, T.; Nilsson, A.; Norskov, J. K., From the Sabatier Principle to a Predictive Theory of Transition-Metal Heterogeneous Catalysis. *J. Catal.* **2015,** *328*, 36-42.

[40] Campbell, C. T., Finding the Rate-Determining Step in a Mechanism - Comparing Dedonder Relations with the "Degree of Rate Control". *J. Catal.* **2001,** *204* (2), 520-524.

[41] Kozuch, S.; Martin, J. M. L., The Rate‐Determining Step Is Dead. Long Live the Rate‐Determining State! *ChemPhysChem* **2011,** *12* (8), 1413-1418.

[42] Stegelmann, C.; Andreasen, A.; Campbell, C. T., Degree of Rate Control: How Much the Energies of Intermediates and Transition States Control Rates. *J. Am. Chem. Soc.* **2009,** *131* (23), 8077-8082.

[43] Campbell, C. T., The Degree of Rate Control: A Powerful Tool for Catalysis Research. *ACS Catal.* **2017,** *7* (4), 2770-2779.

[44] Cortright, R. D.; Dumesic, J. A.; Gates, B. C.; Knozinger, H., Kinetics of Heterogeneous Catalytic Reactions: Analysis of Reaction Schemes. *Adv, Catal.* **2001,** *46*, 161-264.

[45] Wei, J. M.; Iglesia, E., Isotopic and Kinetic Assessment of the Mechanism of Reactions of Ch4 with Co2 or H2o to Form Synthesis Gas and Carbon on Nickel Catalysts. *J. Catal.* **2004,** *224* (2), 370-383.

[46] Nesheim, J. C.; Lipscomb, J. D., Large Kinetic Isotope Effects in Methane Oxidation Catalyzed by Methane Monooxygenase: Evidence for C-H Bond Cleavage in a Reaction Cycle Intermediate. *Biochemistry* **1996,** *35* (31), 10240-10247.

[47] Ojeda, M.; Li, A. W.; Nabar, R.; Nilekar, A. U.; Mavrikakis, M.; Iglesia, E., Kinetically Relevant Steps and H-2/D-2 Isotope Effects in Fischer-Tropsch Synthesis on Fe and Co Catalysts. *J. Phys. Chem. C* **2010,** *114* (46), 19761-19770.

[48] Aparicio, L. M., Transient Isotopic Studies and Microkinetic Modeling of Methane Reforming over Nickel Catalysts. *J. Catal.* **1997,** *165* (2), 262-274.

[49] Farmer, J. A.; Baricuatro, J. H.; Campbell, C. T., Ag Adsorption on Reduced Ceo2(111) Thin Films. *J. Phys. Chem. C* **2010,** *114* (40), 17166-17172.

[50] Wilson, E. L.; Brown, W. A.; Thornton, G., Rairs Studies of Co Adsorption on Pd/Ceo(2-X)(111)/Pt(111). *Surf. Sci.* **2006,** *600* (12), 2555-2561.

[51] James, T. E.; Hemmingson, S. L.; Ito, T.; Campbell, C. T., Energetics of Cu Adsorption and Adhesion onto Reduced Ceo2 (111) Surfaces by Calorimetry. *J. Phys. Chem. C* **2015,** *119* (30), 17209-17217.

[52] Hemmingson, S. L.; Feeley, G. M.; Miyake, N. J.; Campbell, C. T., Energetics of 2d and 3d Gold Nanoparticles on Mgo(100): Influence of Particle Size and Defects on Gold Adsorption and Adhesion Energies. *ACS Catal.* **2017,** *7* (3), 2151-2163.

[53] Wu, M.-C.; Corneille, J. S.; He, J.-W.; Estrada, C. A.; Goodman, D. W., Preparation, Characterization, and Chemical Properties of Ultrathin Mgo Films on Mo(100). *J. Vac. Sci. Technol., A* **1992,** *10*, 1467.

[54] King, D. A.; Wells, M. G., Reaction Mechanism in Chemisorption Kinetics: Nitrogen on the {100} Plane of Tungsten. *Proc. R. Soc. A* **1974,** *339* (1617), 245-269.

[55] Campbell, C. T.; James, T. E., Ion Scattering Spectroscopy Intensities for Supported Nanoparticles: The Hemispherical Cap Model. *Surf. Sci.* **2015,** *641*, 166-169.

[56] Senanayake, S. D.; Evans, J.; Agnoli, S.; Barrio, L.; Chen, T. L.; Hrbek, J.; Rodriguez, J. A., Water-Gas Shift and Co Methanation Reactions over Ni-Ceo2(111) Catalysts. *Top. Catal.* **2011,** *54* (1-4), 34-41.

[57] Rodriguez, J. A.; Xu, W. Q.; Liu, Z. Y.; Senanayake, S.; Stacchiola, D., Steam Reforming of Ethanol on Ni-Ce-O Catalysts: Reaction Pathway and Interaction between Ni and the Ceo2 Components. *Abstracts of Papers of the American Chemical Society* **2014,** *248*.

[58] Ganduglia-Pirovano, M. V., The Non-Innocent Role of Cerium Oxide in Heterogeneous Catalysis: A Theoretical Perspective. *Catal. Today* **2015,** *253*, 20-32.

[59] Liu, Z. Y.; Duchon, T.; Wang, H. R.; Peterson, E. W.; Zhou, Y. H.; Luo, S.; Zhou, J.; Matolin, V.; Stacchiola, D. J.; Rodriguez, J. A.; Senanayake, S. D., Mechanistic Insights of Ethanol Steam Reforming over Ni-Ceox(111): The Importance of Hydroxyl Groups for Suppressing Coke Formation. *J. Phys. Chem. C* **2015,** *119* (32), 18248-18256.

[60] Liu, Z. Y.; Duchon, T.; Wang, H. R.; Grinter, D. C.; Waluyo, I.; Zhou, J.; Liu, Q.; Jeong, B.; Crumlin, E. J.; Matolin, V.; Stacchiola, D. J.; Rodriguez, J. A.; Senanayake, S. D., Ambient Pressure Xps and Irras Investigation of Ethanol Steam Reforming on Ni-Ceo2(111) Catalysts: An In situ Study of C-C and O-H Bond Scission. *Phys. Chem. Chem. Phys.* **2016,** *18* (25), 16621-16628.

[61] Lustemberg, P. G.; Ramirez, P. J.; Liu, Z. Y.; Gutierrez, R. A.; Grinter, D. G.; Carrasco, J.; Senanayake, S. D.; Rodriguez, J. A.; Ganduglia-Pirovano, M. V., Room-Temperature Activation of Methane and Dry Re-Forming with Co2 on Ni-Ceo2(111) Surfaces: Effect of Ce3+ Sites and Metal-Support Interactions on C-H Bond Cleavage. *ACS Catal.* **2016,** *6* (12), 8184-8191.

[62] Liu, Z. Y.; Lustemberg, P.; Gutierrez, R. A.; Carey, J. J.; Palomino, R. M.; Vorokhta, M.; Grinter, D. C.; Ramirez, P. J.; Matolin, V.; Nolan, M.; Ganduglia-Pirovano, M. V.; Senanayake, S. D.; Rodriguez, J. A., In Situ Investigation of Methane Dry Reforming on Metal/Ceria(111) Surfaces: Metal-Support Interactions and C-H Bond Activation at Low Temperature. *Angew. Chem. Int. Ed.* **2017,** *56* (42), 13041-13046.

[63] Liu, Z. Y.; Yao, S. Y.; Johnston-Peck, A.; Xu, W. Q.; Rodriguez, J. A.; Senanayake, S. D., Methanol Steam Reforming over Ni-Ceo2 Model and Powder Catalysts: Pathways to High Stability and Selectivity for H2/Co2 Production. *Catal. Today* **2018,** *311*, 74-80.

[64] Lustemberg, P. G.; Palomino, R. M.; Gutierrez, R. A.; Grinter, D. C.; Vorokhta, M.; Liu, Z. Y.; Ramirez, P. J.; Matolin, V.; Ganduglia-Pirovano, M. V.; Senanayake, S. D.; Rodriguez, J. A., Direct Conversion of Methane to Methanol on Ni-Ceria Surfaces: Metal-Support Interactions and Water-Enabled Catalytic Conversion by Site Blocking. *J. Am. Chem. Soc.* **2018,** *140* (24), 7681-7687.

[65] Voychok, D.; Guild, C. J.; Llorca, J.; Palomino, R. M.; Waluyo, I.; Rodriguez, J. A.; Suib, S. L.; Senanayake, S. D., Structural and Chemical State of Doped and Impregnated Mesoporous Ni/Ceo2 Catalysts for the Water-Gas Shift. *Appl. Catal., A* **2018,** *567*, 1-11.

[66] Lustemberg, P. G.; Feria, L.; Ganduglia-Pirovano, M. V., Single Ni Sites Supported on Ceo2 (111) Reveal Cooperative Effects in the Water-Gas Shift Reaction. *J. Phys. Chem. C* **2019,** *123* (13), 7749-7757.

[67] Akri, M.; Zhao, S.; Li, X. Y.; Zang, K. T.; Lee, A. F.; Isaacs, M. A.; Xi, W.; Gangarajula, Y.; Luo, J.; Ren, Y. J.; Cui, Y. T.; Li, L.; Su, Y.; Pan, X. L.; Wen, W.; Pan, Y.; Wilson, K.; Qiao, B. T.; Ishii, H.; Liao, Y. F.; Wang, A. Q.; Wang, X. D.; Zhang, T., Atomically Dispersed Nickel as Coke-Resistant Active Sites for Methane Dry Reforming. *Nat. Commun.* **2019,** *10*.

[68] Farrauto, R.; Hwang, S.; Shore, L.; Ruettinger, W.; Lampert, J.; Giroux, T.; Liu, Y.; Ilinich, O., New Material Needs for Hydrocarbon Fuel Processing: Generating Hydrogen for the Pem Fuel Cell. *Annu. Rev. Mater. Res.* **2003,** *33*, 1-27.

[69] Campbell, C. T.; Peden, C. H. F., Chemistry - Oxygen Vacancies and Catalysis on Ceria Surfaces. *Science* **2005,** *309* (5735), 713-714.

[70] Rocchini, E.; Trovarelli, A.; Llorca, J.; Graham, G. W.; Weber, W. H.; Maciejewski, M.; Baiker, A., Relationships between Structural/Morphological Modifications and Oxygen Storage-Redox Behavior of Silica Ceria. *J. Catal.* **2000,** *194*, 461-78.

[71] Kundakovic, L.; Flyzani-Stephanopoulos, J., Cu and Ag-Modified Cerium Oxide Catalysts for Methane Oxidation. *J. Catal.* **1998,** *179*, 203-21.

[72] Schwartz, J. M.; Schmidt, L. D., Microstructures of Pt-Ce and Rh-Ce Particles on Alumina and Silica. *J. Catal.* **1992,** *138*, 283-93.

[73] Campbell, C. T., The Energetics of Supported Metal Nanoparticles: Relationships to Sintering Rates and Catalytic Activity. *Acc. Chem. Res.* **2013,** *46* (8), 1712-1719.

[74] Kresse, G.; Hafner, J., Ab Initio Molecular-Dynamics for Liquid-Metals. *Phys. Rev. B* **1993,** *47* (1), 558–561.

[75] Kresse, G.; Furthmüller, J., Efficient Iterative Schemes for Ab Initio Total-Energy Calculations Using a Plane-Wave Basis Set. *Phys. Rev. B* **1996,** *54*, 11169.

[76] Kresse, G.; Joubert, D., From Ultrasoft Pseudopotentials to the Projector Augmented-Wave Method. *Phys. Rev. B* **1999,** *59* (3), 1758–1775.

[77] Dudarev, S. L.; Botton, G. A.; Savrasov, S. Y.; Humphreys, C. J.; Sutton, A. P., Electron-Energy-Loss Spectra and the Structural Stability of Nickel Oxide: An Lsda+U Study. *Phys. Rev. B* **1998,** *57* (3), 1505-1509.

[78] Perdew, J. P.; Burke, K.; Ernzerhof, M., Generalized Gradient Approximation Made Simple. *Phys. Rev. Lett.* **1996,** *77* (18), 3865-3868.

[79] Fabris, S.; Vicario, G.; Balducci, G.; de Gironcoli, S.; Baroni, S., Electronic and Atomistic Structures of Clean and Reduced Ceria Surfaces. *J. Phys. Chem. B* **2005,** *109* (48), 22860-22867.

[80] Castleton, C. W. M.; Kullgren, J.; Hermansson, K., Tuning Lda+U for Electron Localization and Structure at Oxygen Vacancies in Ceria. *J. Chem. Phys.* **2007,** *127* (24), 244704.

[81] Andersson, D. A.; Simak, S. I.; Johansson, B.; Abrikosov, I. A.; Skorodumova, N. V., Modeling of Ceo2, Ce2o3, and Ceo2-X in the Lda+U Formalism. *Phys. Rev. B* **2007,** *75* (3), 035109.

[82] Da Silva, J. L. F.; Ganduglia-Pirovano, M. V.; Sauer, J.; Bayer, V.; Kresse, G., Hybrid Functionals Applied to Rare-Earth Oxides: The Example of Ceria. *Phys. Rev. B* **2007,** *75* (4), 045121.

[83] Du, D.; Wolf, M. J.; Hermansson, K.; Broqvist, P., Screened Hybrid Functionals Applied to Ceria: Effect of Fock Exchange. *Phys. Rev. B* **2018,** *97* (23), 235203.

[84] Loschen, C.; Carrasco, J.; Neyman, K. M.; Illas, F., First-Principles Lda + U and Gga + U Study of Cerium Oxides: Dependence on the Effective U Parameter. *Phys. Rev. B* **2007,** *75* (3), 035115.

[85] Grimme, S.; Antony, J.; Ehrlich, S.; Krieg, H., A Consistent and Accurate Ab Initio Parametrization of Density Functional Dispersion Correction (Dft-D) for the 94 Elements H-Pu. *J. Chem. Phys.* **2010,** *132* (15), 154104.

[86] Grimme, S.; Ehrlich, S.; Goerigk, L., Effect of the Damping Function in Dispersion Corrected Density Functional Theory. *J. Comput. Chem.* **2011,** *32* (7), 1456-1465.

[87] Venables, J. A., Atomic Processes in Crystal Growth. *Surf. Sci.* **1994,** *299/300*, 798.

[88] Hemmingson, S. L.; James, T. E.; Feeley, G. M.; Tilson, A. M.; Campbell, C. T., Adsorption and Adhesion of Au on Reduced Ceo2(111) Surfaces at 300 and 100 K. *J. Phys. Chem. C* **2016,** *120* (22), 12113-12124.

[89] Castellani, N. J.; Branda, M. A.; Neyman, K. M.; Illas, F., Density Functional Theory Study of the Adsorption of Au Atom on Cerium Oxide: Effect of Low-Coordinated Surface Sites. *J. Phys. Chem. C* **2009,** *113* (12), 4948-4954.

[90] Hernandez, N. C.; Grau-Crespo, R.; de Leeuw, N. H.; Sanz, J. F., Electronic Charge Transfer between Ceria Surfaces and Gold Adatoms: A Gga Plus U Investigation. *Phys. Chem. Chem. Phys.* **2009,** *11* (26), 5246-5252.

[91] Zhang, C.; Michaelides, A.; King, D. A.; Jenkins, S. J., Structure of Gold Atoms on Stoichiometric and Defective Ceria Surfaces. *J. Chem. Phys.* **2008,** *129* (19).

[92] Zhang, C. J.; Michaelides, A.; King, D. A.; Jenkins, S. J., Anchoring Sites for Initial Au Nucleation on Ceo2{111}: O Vacancy Versus Ce Vacancy. *J. Phys. Chem. C* **2009,** *113* (16), 6411-6417.

[93] Camellone, M. F.; Fabris, S., Reaction Mechanisms for the Co Oxidation on Au/Ceo2 Catalysts: Activity of Substitutional Au3+/Au+ Cations and Deactivation of Supported Au+ Adatoms. *J. Am. Chem. Soc.* **2009,** *131* (30), 10473-10483.

[94] Lustemberg, P. G.; Pan, Y.; Shaw, B. J.; Grinter, D.; Pang, C.; Thornton, G.; Perez, R.; Ganduglia-Pirovano, M. V.; Nilius, N., Diffusion Barriers Block Defect Occupation on Reduced Ceo2(111). *Phys. Rev. Lett.* **2016,** *116* (23).

[95] Pan, Y.; Nilius, N.; Freund, H. J.; Paier, J.; Penschke, C.; Sauer, J., Titration of Ce 3 + ions in the Ceo2(111) Surface by Au Adatoms. *Phys. Rev. Lett.* **2013,** *111* (20).

[96] Rodriguez, J. A.; Wang, X.; Liu, P.; Wen, W.; Hanson, J. C.; Hrbek, J.; Perez, M.; Evans, J., Gold Nanoparticles on Ceria: Importance of O Vacancies in the Activation of Gold. *Top. Catal.* **2007,** *44* (1-2), 73-81.

[97] Pan, Y.; Cui, Y.; Stiehler, C.; Nilius, N.; Freund, H. J., Gold Adsorption on Ceo2 Thin Films Grown on Ru(0001). *J. Phys. Chem. C* **2013,** *117* (42), 21879-21885.

[98] Rodriguez, J. A.; Perez, M.; Evans, J.; Liu, G.; Hrbek, J., Reaction of So2 with Au/Ceo2 (111): Importance of O Vacancies in the Activation of Gold. *J. Chem. Phys.* **2005,** *122*, 241101.

[99] Kozlov, S. M.; Neyman, K. M., O Vacancies on Steps on the Ceo2(111) Surface. *Phys. Chem. Chem. Phys.* **2014,** *16* (17), 7823-7829.

[100] James, T. E.; Hemmingson, S. L.; Campbell, C. T., Energy of Supported Metal Catalysts: From Single Atoms to Large Metal Nanoparticles. *ACS Catal.* **2015,** *5* (10), 5673-5678.

[101] Romeo, M.; Bak, K.; El Fallah, J.; Le Normand, F.; Hilaire, L., Xps Study of the Reduction of Cerium Dioxide. *Surf. Interface Anal.* **1993,** *20* (6), 508-512.

[102] Tanuma, S.; Powell, C. J.; Penn, D. R., Calculations of Electron Inelastic Mean Free Paths for 31 Materials. *Surf. Interface Anal.* **1988,** *11* (11), 577-589.

[103] Grosvenor, A. P.; Biesinger, M. C.; Smart, R. S.; McIntyre, N. S., New Interpretations of Xps Spectra of Nickel Metal and Oxides. *Surf. Sci.* **2006,** *600* (9), 1771-1779.

[104] Zhou, Y. H.; Zhou, J., Interactions of Ni Nanoparticles with Reducible Ceo2(111) Thin Films. *J. Phys. Chem. C* **2012,** *116* (17), 9544-9549.

[105] Monkhorst, H. J.; Pack, J. D., Special Points for Brillouin-Zone Integrations. *Phys. Rev. B* **1976,** *13*, 5188-5192.

[106] Tang, W.; Sanville, E.; Henkelman, G., A Grid-Based Bader Analysis Algorithm without Lattice Bias. *J. Phys. Condens. Matter* **2009,** *21* (8), 084204.

[107] Janthon, P.; Luo, S.; Kozlov, S. M.; Viñes, F.; Limtrakul, J.; Truhlar, D. G.; Illas, F., Bulk Properties of Transition Metals: A Challenge for the Design of Universal Density Functionals. *J. Chem. Theory Comput.* **2014,** *10* (9), 3832-3839.

[108] Zhang, G.-X.; Reilly, A. M.; Tkatchenko, A.; Scheffler, M., Performance of Various Density-Functional Approximations for Cohesive Properties of 64 Bulk Solids. *New J. Phys.* **2018,** *20*, 063020.

[109] Kim, H. Y.; Henkelman, G., Co Oxidation at the Interface of Au Nanoclusters and the Stepped-Ceo2 (111) Surface by the Mars–Van Krevelen Mechanism. *J. Phys. Chem. Lett.* **2013,** *4* (1), 216-221.

[110] Ganduglia-Pirovano, M. V.; Hofmann, A.; Sauer, J., Oxygen Vacancies in Transition Metal and Rare Earth Oxides: Current State of Understanding and Remaining Challenges. *Surf. Sci. Rep.* **2007,** *62* (6), 219-270.

[111] Murgida, G. E.; Ganduglia-Pirovano, M. V., Evidence for Subsurface Ordering of Oxygen Vacancies on the Reduced Ceo2(111) Surface Using Density-Functional and Statistical Calculations. *Phys. Rev. Lett.* **2013,** *110* (24).

[112] Han, Z.-K.; Yang, Y.-Z.; Zhu, B.; Ganduglia-Pirovano, M. V.; Gao, Y., Unraveling the Oxygen Vacancy Structures at the Reduced Ceo2(111) Surface. *Phys. Rev. Mater.* **2018,** *2* (3), 035802.

[113] Paier, J.; Penschke, C.; Sauer, J., Oxygen Defects and Surface Chemistry of Ceria: Quantum Chemical Studies Compared to Experiment. *Chem. Rev.* **2013,** *113* (6), 3949-3985.

[114] Hailstone, R. K.; DiFrancesco, A. G.; Leong, J. G.; Allston, T. D.; Reed, K. J., A Study of Lattice Expansion in Ceo2 Nanoparticles by Transmission Electron Microscopy. *J. Phys. Chem. C* **2009,** *113* (34), 15155-15159.

[115] Campbell, C. T., Bimetallic Surface Chemistry. *Annu. Rev. Phys. Chem.* **1990,** *41* (775-837), 775-837.

[116] Campbell, C. T.; Parker, S. C.; Starr, D. E., The Effect of Size-Dependent Nanoparticle Energetics on Catalyst Sintering. *Science* **2002,** *298* (5594), 811-814.

[117] Parker, S. C.; Campbell, C. T., Kinetic Model for Sintering of Supported Metal Particles with Improved Size-Dependent Energetics and Applications to Au on Tio2(110). *Phys. Rev. B* **2007,** *75* (3).

[118] Goodman, D. W., Model Studies in Catalysis Using Surface Science Probes. *Chem. Rev.* **1995,** *95*, 523-536.

[119] Fan, M. S.; Abdullah, A. Z.; Bhatia, S., Catalytic Technology for Carbon Dioxide Reforming of Methane to Synthesis Gas. *ChemCatChem* **2009,** *1*, 192-208.

[120] Zuo, Z.; Liu, S.; Wang, Z.; Liu, C.; Huang, W.; Huang, J.; Liu, P., Dry Reforming of Methane on Single-Site Ni/Mgo Catalysts: Importance of Site Confinement. *ACS Catal.* **2018,** *8*, 9821-9835.

[121] Pakhare, D.; Spivey, J., A Review of Dry (Co2) Reforming of Methane over Noble Metal Catalysts. *Chem. Soc. Rev.* **2014,** *43*, 7813-7837.

[122] Guo, J.; Lou, H.; Zhao, H.; Chai, D.; Zheng, X., Dry Reforming of Methane over Nickel Catalysts Supported on Magnesium Aluminate Spinels. *Appl. Catal., A* **2004,** *273*, 75-82.

[123] Liu, H.; Teng, B.; Fan, M.; Wang, B.; Zhang, Y.; Harris, H. G., Ch4 Dissociation on the Perfect and Defective Mgo(001) Supported Ni4. *Fuel* **2014,** *123*, 285-292.

[124] Montoya, J. A.; Romero-Pascual, E.; Gimon, C.; Del Angel, P.; Monzon, A., Methane Reforming with Co2 over Ni/Zro2–Ceo2 Catalysts Prepared by Sol–Gel. *Catal. Today* **2000,** *63* (1), 71-85.

[125] Li, S.; Gong, J., Strategies for Improving the Performance and Stability of Ni-Based Catalysts for Reforming Reactions. *Chem. Soc. Rev.* **2014,** *43* (21), 7245-7256.

[126] Li, D.; Nakagawa, Y.; Tomishige, K., Methane Reforming to Synthesis Gas over Ni Catalysts Modified with Noble Metals. *Appl. Catal., A* **2011,** *408* (1-2), 1-24.

[127] Requies, J.; Cabrero, M. A.; Barrio, V. L.; Güemez, M. B.; Cambra, J. F.; Arias, P. L.; Pérez-Alonso, F. J.; Ojeda, M.; Peña, M. A.; Fierro, J. L. G., Partial Oxidation of Methane to Syngas over Ni/Mgo and Ni/La2o3 Catalysts. *Appl. Catal., A* **2005,** *289* (2), 214-223.

[128] Li, D.; Atake, I.; Shishido, T.; Oumi, Y.; Sano, T.; Takehira, K., Self-Regenerative Activity of Ni/Mg (Al) O Catalysts with Trace Ru During Daily Start-up and Shut-Down Operation of Ch4 Steam Reforming. *J. Catal.* **2007,** *250* (2), 299-312.

[129] Zuo, Z.; Shen, C.; Tan, P.; Huang, W., Ni Based on Dual-Support Mg-Al Mixed Oxides and Sba-15 Catalysts for Dry Reforming of Methane. *Catal. Commun.* **2013,** *41*, 132-135.

[130] Hu, Y. H.; Ruckenstein, E., High-Resolution Transmission Electron Microscopy Study of Carbon Deposited on the Nio/Mgo Solid Solution Catalysts. *J. Catal.* **1999,** *184* (1), 298-302.

[131] Chen, Y.-G.; Tomishige, K.; Yokoyama, K.; Fujimoto, K., Catalytic Performance and Catalyst Structure of Nickel–Magnesia Catalysts for Co2 Reforming of Methane. *J. Catal.* **1999,** *184* (2), 479-490.

[132] Hu, Y. H.; Ruckenstein, E., Binary Mgo-Based Solid Solution Catalysts for Methane Conversion to Syngas. *Catalysis Reviews* **2002,** *44* (3), 423-453 %@ 0161-4940.

[133] Hu, Y. H.; Ruckenstein, E., The Characterization of a Highly Effective Nio/Mgo Solid Solution Catalyst in the Co2 Reforming of Ch4. *Catal. Lett.* **1997,** *43* (1-2), 71-77.

[134] Ruckenstein, E.; Hu, Y. H., The Effect of Precursor and Preparation Conditions of Mgo on the Co2 Reforming of Ch4 over Nio/Mgo Catalysts. *Appl. Catal., A* **1997,** *154* (1-2), 185-205.

[135] Djaidja, A.; Libs, S.; Kiennemann, A.; Barama, A., Characterization and Activity in Dry Reforming of Methane on Nimg/Al and Ni/Mgo Catalysts. *Catal. Today* **2006,** *113* (3-4), 194-200.

[136] Fatsikostas, A. N.; Kondarides, D. I.; Verykios, X. E., Production of Hydrogen for Fuel Cells by Reformation of Biomass-Derived Ethanol. *Catal. Today* **2002,** *75* (1-4), 145-155.

[137] Ni, M.; Leung, D. Y. C.; Leung, M. K. H., A Review on Reforming Bio-Ethanol for Hydrogen Production. *Int. J. Hydrogen Energy* **2007,** *32* (15), 3238-3247.

[138] Frusteri, F.; Freni, S.; Spadaro, L.; Chiodo, V.; Bonura, G.; Donato, S.; Cavallaro, S., H2 Production for Mc Fuel Cell by Steam Reforming of Ethanol over Mgo Supported Pd, Rh, Ni and Co Catalysts. *Catal. Commun.* **2004,** *5* (10), 611-615.

[139] Ruckenstein, E.; Hu, Y. H., Carbon Dioxide Reforming of Methane over Nickel/Alkaline Earth Metal Oxide Catalysts. *Appl. Catal., A* **1995,** *133* (1), 149-161.

[140] Heiz, U.; Vanolli, F.; Trento, L.; Schneider, W. D., Chemical Reactivity of Size-Selected Supported Clusters: An Experimental Setup. *Rev. Sci. Instrum.* **1997,** *68* (5), 1986-1994.

[141] Heiz, U.; Vanolli, F.; Sanchez, A.; Schneider, W. D., Size-Dependent Molecular Dissociation on Mass-Selected, Supported Metal Clusters. *J. Am. Chem. Soc.* **1998,** *120* (37), 9668-9671.

[142] Sao-Joao, S.; Giorgio, S.; Mottet, C.; Goniakowski, J.; Henry, C. R., Interface Structure of Ni Nanoparticles on Mgo (1 0 0): A Combined Hrtem and Molecular Dynamic Study. *Surf. Sci.* **2006,** *600* (7), L86-L90.

[143] Lin, C.; Xu, Y. H.; Naramoto, H.; Wei, P.; Kitazawa, S.; Narumi, K., Morphology Evolution of Thin Ni Film on Mgo (100) Substrate. *J. Phys. D* **2002,** *35* (15), 1864.

[144] Benedetti, S.; Myrach, P.; Bona, A. D.; Valeri, S.; Nilius, N.; Freund, H. J., Growth and Morphology of Metal Particles on Mgo/Mo(001): A Comparative Stm and Diffraction Study. *Phys. Rev. B* **2011,** *83*, 125423.

[145] Pacchioni, G.; Rösch, N., Supported Nickel and Copper Clusters on Mgo (100): A First - Principles Calculation on the Metal/Oxide Interface. *J. Chem. Phys.* **1996,** *104* (18), 7329-7337.

[146] López, N.; Illas, F., Ab Initio Modeling of the Metal− Support Interface: The Interaction of Ni, Pd, and Pt on Mgo (100). *J. Phys. Chem. B* **1998,** *102* (8), 1430-1436.

[147] Paz-Borbón, L. O.; Baletto, F., A Dft Study on the O2 Adsorption Properties of Supported Ptni Clusters. *Inorganics* **2017,** *5* (3), 43.

[148] Guo, Y.-P.; Li, W.-Y.; Feng, J., Reaction Pathway of Ch4/Co2 Reforming over Ni8/Mgo (100). *Surf. Sci.* **2017,** *660*, 22-30.

[149] Guo, Y.; Feng, J.; Li, W., Effect of the Ni Size on Ch4/Co2 Reforming over Ni/Mgo Catalyst: A Dft Study. *Chin. J. Chem. Eng.* **2017,** *25* (10), 1442-1448.

[150] Giordano, L.; Pacchioni, G.; Ferrari, A. M.; Illas, F.; Rösch, N., Electronic Structure and Magnetic Moments of Co4 and Ni4 Clusters Supported on the Mgo (0 0 1) Surface. *Surf. Sci.* **2001,** *473* (3), 213-226 %@ 0039-6028.

[151] Giordano, L.; Pacchioni, G.; Illas, F.; Rösch, N., Adsorption Properties of Ni4 and Ni8 Clusters Supported on Regular and Defect Sites of the Mgo (001) Surface. *Surf. Sci.* **2002,** *499* (1), 73-84.

[152] Dong, Y. F.; Wang, S. J.; Mi, Y. Y.; Feng, Y. P.; Huan, A. C. H., First-Principle Studies on Initial Growth of Ni on Mgo(001) Surface. *Surf. Sci.* **2006,** *600,* 2154-2162.

[153] Sicolo, S.; Giordano, L.; Pacchioni, G., Adsorption of Late Transition Metal Atoms on Mgo/Mo (100) and Mgo/Ag (100) Ultrathin Films: A Comparative Dft Study. *J. Phys. Chem. C* **2009,** *113* (38), 16694-16701 %@ 1932-7447.

[154] Matsunaka, D.; Shibutani, Y., Electronic States and Adhesion Properties at Metal/Mgo Incoherent Interfaces: First-Principle Calculations. *Phys. Rev. B* **2008,** *77*, 165435.

[155] Venables, J. A.; Spiller, G. D. T., Nucleation and Growth of Thin Films. In *Surface Mobilities on Solid Materials*, Springer: 1983; pp 341-404.

[156] Campbell, C. T., Ultrathin Metal Films on Oxide Surfaces: Structural, Electronic and Chemisorptive Properties. *Surf. Sci. Rep.* **1997,** *227*, 1-111.

[157] Haynes, W. M., *Handbook of Chemistry and Physics*. CRC Press: 2014.

[158] Mao, Z.; Lustemberg, P. G.; Rumptz, J. R.; Ganduglia-Pirovano, M. V.; Campbell, C. T., Ni Nanoparticles on Ceo2(111): Energetics, Electron Transfer and Structure by Ni Adsorption Calorimetry, Spectroscopies and Dft. *ACS Catal.* **2020**, Just Accepted Manuscript.

[159] Ernst, K. H.; Ludviksson, A.; Zhang, R.; Yoshihara, J.; Campbell, C. T., Growth Model for Metal Films on Oxide Surfaces: Cu on Zno (0001)-O. *Phys. Rev. B* **1993,** *47* (20), 13782.

[160] Albertini, O. R.; Liu, A. Y., Site-Dependent Magnetism of Ni Adatoms on Mgo/Ag(001). *Phys. Rev. B* **2015,** *91*, 214423.

[161] Eberhardt, W., Clusters as New Materials. *Surf. Sci.* **2002,** *500* (1-3), 242-270.

[162] Haruta, M., Catalysis of Gold Nanoparticles Deposited on Metal Oxides. *Cattech* **2002,** *6* (3), 102-115.

[163] Rodriguez, J. A.; Liu, G.; Jirsak, T.; Hrbek, J.; Chang, Z.; Dvorak, J.; Maiti, A., Activation of Gold on Titania: Adsorption and Reaction of So2 on Au/Tio2 (110). *J. Am. Chem. Soc.* **2002,** *124* (18), 5242-5250.

[164] Valden, M.; Pak, S.; Lai, X.; Goodman, D. W., Structure Sensitivity of Co Oxidation over Model Au/Tio2 Catalysts. *Catal. Lett.* **1998,** *56*, 7-10.

[165] Valden, M.; Pak, S.; Lai, X.; Goodman, D. W., Structure Sensitivity of Co Oxidation over Model Au/Tio 2 2 Catalysts. *Catal. Lett.* **1998,** *56* (1), 7-10.

[166] Judai, K.; Abbet, S.; Worz, A. S.; Heiz, U.; Henry, C. R., Low-Temperature Cluster Catalysis. *J. Am. Chem. Soc.* **2004,** *126* (9), 2732-2737.

[167] Lee, S.; Fan, C.; Wu, T.; Anderson, S. L., Co Oxidation on Au N/Tio2 Catalysts Produced by Size-Selected Cluster Deposition. *J. Am. Chem. Soc.* **2004,** *126* (18), 5682-5683.

[168] Liu, P.; Rodriguez, J. A., Water-Gas-Shift Reaction on Metal Nanoparticles and Surfaces. *J. Chem. Phys.* **2007,** *126* (16).

[169] Rodriguez, J. A.; Liu, P.; Hrbek, J.; Evans, J.; Perez, M., Water Gas Shift Reaction on Cu and Au Nanoparticles Supported on Ceo2 (111) and Zno $(000\bar{1})$: Intrinsic Activity and Importance of Support Interactions. *Angew. Chem. Int. Ed.* **2007,** *46* (8), 1329-1332.

[170] Heiz, U.; Bullock, E. L., Fundamental Aspects of Catalysis on Supported Metal Clusters. *J. Mater. Chem.* **2004,** *14* (4), 564-577.

[171] Haruta, M.; Kobayashi, T.; Sano, H.; Yamada, N., Novel Gold Catalysts for the Oxidation of Carbon Monoxide at a Temperature Far Below 0 C. *Chem. Lett.* **1987,** *16* (2), 405-408.

[172] Haruta, M., Size-and Support-Dependency in the Catalysis of Gold. *Catal. Today* **1997,** *36*, 153.

[173] Van Hardeveld, R.; Hartog, F., The Statistics of Surface Atoms and Surface Sites on Metal Crystals. *Surf. Sci.* **1969,** *15* (2), 189-230.

[174] Lopez, N.; Janssens, T. V. W.; Clausen, B. S.; Xu, Y.; Mavrikakis, M.; Bligaard, T.; Norskov, J. K., On the Origin of the Catalytic Activity of Gold Nanoparticles for Low-Temperature Co Oxidation. *J. Catal.* **2004,** *223* (1), 232-235.

[175] Jaramillo, T. F.; Jørgensen, K. P.; Bonde, J.; Nielsen, J. H.; Horch, S.; Chorkendorff, I., Identification of Active Edge Sites for Electrochemical H2 Evolution from Mos2 Nanocatalysts. *Science* **2007,** *317* (5834), 100-102.

[176] Heiz, U.; Sanchez, A.; Abbet, S.; Schneider, W. D., Catalytic Oxidation of Carbon Monoxide on Monodispersed Platinum Clusters: Each Atom Counts. *J. Am. Chem. Soc.* **1999,** *121* (13), 3214-3217.

[177] Kyriakou, G.; Boucher, M. B.; Jewell, A. D.; Lewis, E. A.; Lawton, T. J.; Baber, A. E.; Tierney, H. L.; Flytzani-Stephanopoulos, M.; Sykes, E. C. H., Isolated Metal Atom Geometries as a Strategy for Selective Heterogeneous Hydrogenations. *Science* **2012,** *335* (6073), 1209-1212.

[178] Dean, J.; Taylor, M. G.; Mpourmpakis, G., Unfolding Adsorption on Metal Nanoparticles: Connecting Stability with Catalysis. *Sci. Adv.* **2019,** *5* (9), eaax5101.

[179] Larsen, J. H.; Ranney, J. T.; Starr, D. E.; Musgrove, J. E.; Campbell, C. T., Adsorption Energetics for Ag on Mgo(100). *Phys. Rev. B* **2001,** *63*, 195410.

[180] Alcoutlabi, M.; McKenna, G. B., Effects of Confinement on Material Behaviour at the Nanometre Size Scale. *J. Phys. Condens. Matter* **2005,** *17* (15), R461.

[181] Campbell, C. T.; Starr, D. E., Metal Adsorption and Adhesion Energies on Mgo(100). *J. Am. Chem. Soc.* **2002,** *124*, 9212-18.

[182] Sharp, J. C.; Yao, Y. X.; Campbell, C. T., Silver Nanoparticles on Fe3o4(111): Energetics by Ag Adsorption Calorimetry and Structure by Surface Spectroscopies. *J. Phys. Chem. C* **2013,** *117* (47), 24932-24936.

[183] Ranney, J. T.; Starr, D. E.; Musgrove, J. E.; Bald, D. J.; Campbell, C. T., A Microcalorimetric Study of the Heat of Adsorption of Copper on Well-Defined Oxide Thin Film Surfaces: Mgo(100), P(2x1)-Oxide on Mo(100), and Disordered W Oxide. *Faraday Discuss.* **1999,** *114*, 195-208.

[184] Strayer, M. E.; Senftle, T. P.; Winterstein, J. P.; Vargas-Barbosa, N. M.; Sharma, R.; Rioux, R. M.; Janik, M. J.; Mallouk, T. E., Charge Transfer Stabilization of Late Transition Metal Oxide Nanoparticles on a Layered Niobate Support. *J. Am. Chem. Soc.* **2015,** *137* (51), 16216-16224.

[185] O’Connor, N. J.; Jonayat, A. S. M.; Janik, M. J.; Senftle, T. P., Interaction Trends between Single Metal Atoms and Oxide Supports Identified with Density Functional Theory and Statistical Learning. *Nat. Catal.* **2018,** *1* (7), 531-539.

[186] Avanesian, T.; Christopher, P., Scaled Degree of Rate Control: Identifying Elementary Steps That Control Differences in Performance of Transition-Metal Catalysts. *ACS Catal.* **2016,** *6* (8), 5268-5272.

[187] Dix, S. T.; Scott, J. K.; Getman, R. B.; Campbell, C. T., Using Degrees of Rate Control to Improve Selective N-Butane Oxidation over Model Mof-Encapsulated Catalysts: Sterically-Constrained Ag3pd(111). *Faraday Discuss.* **2016,** *188*, 21-38.

[188] Meskine, H.; Matera, S.; Scheffler, M.; Reuter, K.; Metiu, H., Examination of the Concept of Degree of Rate Control by First-Principles Kinetic Monte Carlo Simulations. *Surf. Sci.* **2009,** *603* (10-12), 1724-1730.

[189] Kozuch, S.; Shaik, S., How to Conceptualize Catalytic Cycles? The Energetic Span Model. *Acc. Chem. Res.* **2011,** *44* (2), 101-110.

[190] Uhe, A.; Kozuch, S.; Shaik, S., Automatic Analysis of Computed Catalytic Cycles. *J. Comput. Chem.* **2011,** *32* (5), 978-985.

[191] Mao, Z. T.; Campbell, C. T., Apparent Activation Energies in Complex Reaction Mechanisms: A Simple Relationship Via Degrees of Rate Control. *ACS Catal.* **2019,** *9* (10), 9465-9473.

[192] Parmon, V. N., Rate-Determining Steps, Rate-Determining Parameters, and Apparent Activation Energy of Stepwise Reactions. 1. Stepwise Non-Catalytic Reactions Linear in Respect to Intermediates. *React. Kinet. Catal. Lett.* **2003,** *78* (1), 139-150.

[193] Motagamwala, A. H.; Dumesic, J. A., Analysis of Reaction Schemes Using Maximum Rates of Constituent Steps. *Proc. Natl. Acad. Sci. U.S.A* **2016,** *113* (21), E2879-E2888.

[194] Motagamwala, A. H.; Ball, M. R.; Dumesic, J. A.; Doherty, M. F.; Segalman, R. A.; Kane, R. S., Microkinetic Analysis and Scaling Relations for Catalyst Design. *Annu. Rev. Chem. Biomol. Eng.* **2018,** *9*, 413-450.

[195] Atkins, P.; de Paula, J., *Physical Chemistry*. 8th ed.; W. H. Freeman: New York, 2006.

[196] Stegelmann, C.; Schiodt, N. C.; Campbell, C. T.; Stoltze, P., Microkinetic Modeling of Ethylene Oxidation over Silver. *J. Catal.* **2004,** *221* (2), 630-649.

[197] Saavedra, J.; Doan, H. A.; Pursell, C. J.; Grabow, L. C.; Chandler, B. D., The Critical Role of Water at the Gold-Titania Interface in Catalytic Co Oxidation. *Science* **2014,** *345* (6204), 1599-1602.

[198] Kunkes, E. L.; Studt, F.; Abild-Pedersen, F.; Schlogl, R.; Behrens, M., Hydrogenation of Co2 to Methanol and Co on Cu/Zno/Al2o3: Is There a Common Intermediate or Not? *J. Catal.* **2015,** *328*, 43-48.

[199] Engelin, C.; Jensen, T.; Rodriguez-Rodriguez, S.; Fristrup, P., Mechanistic Investigation of Palladium-Catalyzed Allylic C-H Activation. *ACS Catal.* **2013,** *3* (3), 294-302.

[200] Lupp, D.; Christensen, N. J.; Fristrup, P., Synergy between Experimental and Theoretical Methods in the Exploration of Homogeneous Transition Metal Catalysis. *Dalton Trans.* **2014,** *43* (29), 11093-11105.

[201] Westheimer, F. H., The Magnitude of the Primary Kinetic Isotope Effect for Compounds of Hydrogen and Deuterium. *Chem. Rev.* **1961,** *61* (3), 265-273.

[202] Mao, Z. T.; Campbell, C. T., The Degree of Rate Control of Catalyst-Bound Intermediates in Catalytic Reaction Mechanisms: Relationship to Site Coverage. *J. Catal.* **2020,** *381*, 53-62.

[203] Parkin, G., Temperature-Dependent Transitions between Normal and Inverse Isotope Effects Pertaining to the Interaction of H-H and C-H Bonds with Transition Metal Centers. *Acc. Chem. Res.* **2009,** *42* (2), 315-325.

[204] Gomez-Gallego, M.; Sierra, M. A., Kinetic Isotope Effects in the Study of Organometallic Reaction Mechanisms. *Chem. Rev.* **2011,** *111* (8), 4857-4963.

[205] Sibbald, P. A.; Rosewall, C. F.; Swartz, R. D.; Michael, F. E., Mechanism of N-Fluorobenzenesulfonimide Promoted Diamination and Carboamination Reactions: Divergent Reactivity of a Pd(Iv) Species. *J. Am. Chem. Soc.* **2009,** *131* (43), 15945-15951.

[206] Sorokin, A.; Robert, A.; Meunier, B., Intramolecular Kinetic Isotope Effects in Alkane Hydroxylations Catalyzed by Manganese and Iron Porphyrin Complexes. *J. Am. Chem. Soc.* **1993,** *115* (16), 7293-7299.

[207] Jung, H. H.; Floreancig, P. E., Mechanistic Analysis of Oxidative C–H Cleavages Using Inter-and Intramolecular Kinetic Isotope Effects. *Tetrahedron* **2009,** *65* (52), 10830-10836.

[208] Simmons, E. M.; Hartwig, J. F., On the Interpretation of Deuterium Kinetic Isotope Effects in C?H Bond Functionalizations by Transition-Metal Complexes. *Angew. Chem. Int. Ed.* **2012,** *51* (13), 3066-3072.

[209] Studt, F.; Behrens, M.; Kunkes, E. L.; Thomas, N.; Zander, S.; Tarasov, A.; Schumann, J.; Frei, E.; Varley, J. B.; Abild-Pedersen, F.; Norskov, J. K.; Schlogl, R., The Mechanism of Co and Co2 Hydrogenation to Methanol over Cu-Based Catalysts. *ChemCatChem* **2015,** *7* (7), 1105-1111.

[210] Medford, A. J.; Shi, C.; Hoffmann, M. J.; Lausche, A. C.; Fitzgibbon, S. R.; Bligaard, T.; Norskov, J. K., Catmap: A Software Package for Descriptor-Based Microkinetic Mapping of Catalytic Trends. *Catal. Lett.* **2015,** *145* (3), 794-807.

[211] Yang, Y.; Mims, C. A.; Disselkamp, R. S.; Mei, D.; Kwak, J.; Szanyi, J.; Peden, C. H. F.; Campbell, C. T., Isotope Effects in Methanol Synthesis and the Reactivity of Copper Formates on a Cu/Sio2 Catalyst. *Catal. Lett.* **2008,** *125*, 201-208.

[212] McNaught, A. D.; Wilkinson, A., *Iupac Compendium of Chemical Terminology, 2nd Ed.* Blackwell Scientific Publications: Oxford, 1997.

[213] Kozuch, S., Steady State Kinetics of Any Catalytic Network: Graph Theory, the Energy Span Model, the Analogy between Catalysis and Electrical Circuits, and the Meaning of "Mechanism". *ACS Catal.* **2015,** *5* (9), 5242-5255.

[214] Bures, J.; Armstrong, A.; Blackmond, D. G., Curtin-Hammett Paradigm for Stereocontrol in Organocatalysis by Diarylprolinol Ether Catalysts. *J. Am. Chem. Soc.* **2012,** *134* (15), 6741-6750.

[215] Argyle, M. D.; Chen, K. D.; Bell, A. T.; Iglesia, E., Effect of Catalyst Structure on Oxidative Dehydrogenation of Ethane and Propane on Alumina-Supported Vanadia. *J. Catal.* **2002,** *208* (1), 139-149.

[216] Pestman, R.; Chen, W.; Hensen, E., Insight into the Rate-Determining Step and Active Sites in the Fischer-Tropsch Reaction over Cobalt Catalysts. *ACS Catal.* **2019,** *9* (5), 4189-4195.

[217] Green, I. X.; Tang, W. J.; Neurock, M.; Yates, J. T., Spectroscopic Observation of Dual Catalytic Sites During Oxidation of Co on a Au/Tio2 Catalyst. *Science* **2011,** *333* (6043), 736-739.

[218] Gokhale, A. A.; Dumesic, J. A.; Mavrikakis, M., On the Mechanism of Low-Temperature Water Gas Shift Reaction on Copper. *J. Am. Chem. Soc.* **2008,** *130* (4), 1402-1414.

[219] Tang, C.; Zhang, R.; Lu, W. B.; He, L. B.; Jiang, X.; Asiri, A. M.; Sun, X. P., Fe-Doped Cop Nanoarray: A Monolithic Multifunctional Catalyst for Highly Efficient Hydrogen Generation. *Adv. Mater.* **2017,** *29* (2).

[220] Grabow, L. C.; Gokhale, A. A.; Evans, S. T.; Dumesic, J. A.; Mavrikakis, M., Mechanism of the Water Gas Shift Reaction on Pt: First Principles, Experiments, and Microkinetic Modeling. *J. Phys. Chem. C* **2008,** *112* (12), 4608-4617.

[221] Kozuch, S.; Shaik, S., A Combined Kinetic-Quantum Mechanical Model for Assessment of Catalytic Cycles: Application to Cross-Coupling and Heck Reactions. *J. Am. Chem. Soc.* **2006,** *128* (10), 3355-3365.

[222] Kozuch, S.; Shaik, S., Kinetic-Quantum Chemical Model for Catalytic Cycles: The Haber-Bosch Process and the Effect of Reagent Concentration. *J. Phys. Chem. A* **2008,** *112* (26), 6032-6041.

[223] Solel, E.; Tarannam, N.; Kozuch, S., Catalysis: Energy Is the Measure of All Things. *Chem. Commun.* **2019,** *55* (37), 5306-5322.

[224] Jorgensen, M.; Gronbeck, H., Connection between Macroscopic Kinetic Measurables and the Degree of Rate Control. *Catal. Sci. Technol.* **2017,** *7* (18), 4034-4040.

[225] Medford, A. J.; Chuan, S.; Hoffmann, M. J.; Lausche, A. C.; Fitzgibbon, S. R.; Bligaard, T.; Norskov, J. K. Catmap Tutorials: Generating an Input File. https://catmap.readthedocs.io/en/latest/tutorials/generating_an_input_file.html.

[226] Madon, R. J.; Iglesia, E., Catalytic Reaction Rates in Thermodynamically Non-Ideal Systems. *J. Mol. Catal. A: Chem.* **2000,** *163* (1-2), 189-204.

[227] Kozuch, S.; Martin, J. M. L., What Makes for a Bad Catalytic Cycle? A Theoretical Study on the Suzuki-Miyaura Reaction within the Energetic Span Model. *ACS Catal.* **2011,** *1* (4), 246-253.

[228] Wang, S. G.; Vorotnikov, V.; Vlachos, D. G., Coverage-Induced Conformational Effects on Activity and Selectivity: Hydrogenation and Decarbonylation of Furfural on Pd(111). *ACS Catal.* **2015,** *5* (1), 104-112.

[229] Yang, B.; Burch, R.; Hardacre, C.; Headdock, G.; Hu, P., Origin of the Increase of Activity and Selectivity of Nickel Doped by Au, Ag, and Cu for Acetylene Hydrogenation. *ACS Catal.* **2012,** *2* (6), 1027-1032.

[230] Garcia-Muelas, R.; Li, Q.; Lopez, N., Density Functional Theory Comparison of Methanol Decomposition and Reverse Reactions on Metal Surfaces. *ACS Catal.* **2015,** *5* (2), 1027-1036.

[231] Michel, C.; Zaffran, J.; Ruppert, A. M.; Matras-Michalska, J.; Jedrzejczyk, M.; Grams, J.; Sautet, P., Role of Water in Metal Catalyst Performance for Ketone Hydrogenation: A Joint Experimental and Theoretical Study on Levulinic Acid Conversion into Gamma-Valerolactone. *Chem. Commun.* **2014,** *50* (83), 12450-12453.

[232] Yang, B.; Cao, X. M.; Gong, X. Q.; Hu, P., A Density Functional Theory Study of Hydrogen Dissociation and Diffusion at the Perimeter Sites of Au/Tio2. *Phys. Chem. Chem. Phys.* **2012,** *14* (11), 3741-3745.

[233] Garza, A. J.; Bell, A. T.; Head-Gordon, M., Mechanism of Co2 Reduction at Copper Surfaces: Pathways to C-2 Products. *ACS Catal.* **2018,** *8* (2), 1490-1499.

[234] Larmier, K.; Chizallet, C.; Cadran, N.; Maury, S.; Abboud, J.; Lamic-Humblot, A. F.; Marceau, E.; Lauron-Pernot, H., Mechanistic Investigation of Isopropanol Conversion on Alumina Catalysts: Location of Active Sites for Alkene/Ether Production. *ACS Catal.* **2015,** *5* (7), 4423-4437.

[235] Choksi, T.; Greeley, J., Partial Oxidation of Methanol on Moo3 (010): A Dft and Microkinetic Study. *ACS Catal.* **2016,** *6* (11), 7260-7277.

VITA

Zhongtian Mao received the degree of Bachelor of Science from the Department of Chemistry at Fudan University, China. He joined Professor Charles T. Campbell’s group at the University of Washington in 2015. During his five-year pursuit for the doctoral degree, his research interest includes studying the energetics and structures of late-transition metal nanoparticles supported on metal oxide surfaces using single crystal adsorption calorimetry and other surface spectroscopies, and understanding complex catalyzed reaction mechanisms with microkinetic modeling and degree of rate control analysis.